

Special Issue Reprint

Bioactive Compounds from Natural Sources

Discovery, Evaluation and Applications

Edited by
Tao Liu and Xuexiang Chen

mdpi.com/journal/molecules

Bioactive Compounds from Natural Sources: Discovery, Evaluation and Applications

Bioactive Compounds from Natural Sources: Discovery, Evaluation and Applications

Tao Liu
Xuexiang Chen



Basel • Beijing • Wuhan • Barcelona • Belgrade • Novi Sad • Cluj • Manchester

Tao Liu
School of Basic
Medical Sciences
Guangdong Pharmaceutical
University
Guangdong
China

Xuexiang Chen
School of Public Health
Guangzhou Medical
University
Guangzhou
China

Editorial Office

MDPI AG
Grosspeteranlage 5
4052 Basel, Switzerland

This is a reprint of the Special Issue, published open access by the journal *Molecules* (ISSN 1420-3049), freely accessible at: www.mdpi.com/journal/molecules/special_issues/7F7K75GFPY.

For citation purposes, cite each article independently as indicated on the article page online and as indicated below:

Lastname, A.A.; Lastname, B.B. Article Title. <i>Journal Name</i> Year , <i>Volume Number</i> , Page Range.
--

ISBN 978-3-7258-1706-1 (Hbk)

ISBN 978-3-7258-1705-4 (PDF)

<https://doi.org/10.3390/books978-3-7258-1705-4>

© 2024 by the authors. Articles in this book are Open Access and distributed under the Creative Commons Attribution (CC BY) license. The book as a whole is distributed by MDPI under the terms and conditions of the Creative Commons Attribution-NonCommercial-NoDerivs (CC BY-NC-ND) license (<https://creativecommons.org/licenses/by-nc-nd/4.0/>).

Contents

About the Editors	vii
Preface	ix
Jing Xia, Bo Hu, Mengyu Qian, Jiayue Zhang and Lin Wu Benzophenone Rhamnosides and Chromones from <i>Hypericum seniawinii</i> Maxim. Reprinted from: <i>Molecules</i> 2022 , <i>27</i> , 7056, doi:10.3390/molecules27207056	1
Jie Wang, Hancong Liu, Liuchong Zhu, Jingyi Wang, Xiongming Luo and Wenbin Liu et al. Prodigiosin from <i>Serratia Marcescens</i> in Cockroach Inhibits the Proliferation of Hepatocellular Carcinoma Cells through Endoplasmic Reticulum Stress-Induced Apoptosis Reprinted from: <i>Molecules</i> 2022 , <i>27</i> , 7281, doi:10.3390/molecules27217281	11
Tao Hou, Shenglan Guo, Zhuokun Liu, Hongyu Lin, Yu Song and Qiqi Li et al. Novel Pectic Polysaccharides Isolated from Immature Honey Pomelo Fruit with High Immunomodulatory Activity Reprinted from: <i>Molecules</i> 2022 , <i>27</i> , 8573, doi:10.3390/molecules27238573	28
Tao Liu, Ziyang Peng, Wei Lai, Yan Shao, Qing Gao and Miaoxin He et al. The Efficient Synthesis and Anti-Fatigue Activity Evaluation of Macamides: The Unique Bioactive Compounds in Maca Reprinted from: <i>Molecules</i> 2023 , <i>28</i> , 3943, doi:10.3390/molecules28093943	47
Siyuan Ma, Mengling Weng, Ting Yang, Li Ge and Kedi Yang Triterpenes and Pheophorbides from <i>Camellia ptilosperma</i> and Their Cytotoxicity, Photocytotoxicity, and Photodynamic Antibacterial Activity Reprinted from: <i>Molecules</i> 2023 , <i>28</i> , 7058, doi:10.3390/molecules28207058	60
Xueyan Lv, Lili Lv, Shichen Li, Chengcheng Ding, Bingchuan Yang and Chen Ma A Direct Method for Synthesis of Quinoxalines and Quinazolinones Using Epoxides as Alkyl Precursor Reprinted from: <i>Molecules</i> 2023 , <i>28</i> , 7391, doi:10.3390/molecules28217391	77
Xiuxiu Huang, Wenqing Dong, Xiao Luo, Lu Xu and Yinan Wang Target Screen of Anti-Hyperuricemia Compounds from Cortex Fraxini In Vivo Based on ABCG2 and Bioaffinity Ultrafiltration Mass Spectrometry Reprinted from: <i>Molecules</i> 2023 , <i>28</i> , 7896, doi:10.3390/molecules28237896	94
Ruijie Liu, Jingjing Gu, Yilin Ye, Yuxin Zhang, Shaoxing Zhang and Qiange Lin et al. A Natural Compound Containing a Disaccharide Structure of Glucose and Rhamnose Identified as Potential N-Glycanase 1 (NGLY1) Inhibitors Reprinted from: <i>Molecules</i> 2023 , <i>28</i> , 7758, doi:10.3390/molecules28237758	105
Ran Liu, Lili Lv, Bingchuan Yang, Ziyi Gu, Chenglong Li and Xueyan Lv et al. Transition-Metal-Free One-Pot Synthesis of Fused Benzofuranamines and Benzo[b]thiophenamines Reprinted from: <i>Molecules</i> 2023 , <i>28</i> , 7738, doi:10.3390/molecules28237738	119
Jiangtao Fan, Xiong Huang, Mengke Dou, Shuqin Tang, Gang Wang and Yijun Fan et al. Structural Characterization and Immunoenhancing Properties of Polysaccharide CPTM-P1 from <i>Taxus media</i> Reprinted from: <i>Molecules</i> 2024 , <i>29</i> , 1370, doi:10.3390/molecules29061370	131

About the Editors

Tao Liu

Dr. Liu Tao obtained his Ph.D. in Biochemical Engineering from the Institute of Process Engineering at the Chinese Academy of Sciences in 2011. Since then, he has been working as an associate researcher and master's supervisor at Guangdong Pharmaceutical University. He is currently affiliated with the School of Basic Medical Sciences and the Guangdong Provincial Key Laboratory of Pharmaceutical Bioactive Substances. His research primarily focuses on bioactive drug discovery and evaluation; protein engineering technology, with an emphasis on collagen; and AI-driven bio-manufacturing. He has published over 60 academic papers. Additionally, Dr. Liu has filed six invention patents, four of which have been granted. In recognition of his contributions to the field, he received the Second Prize of the Guangdong Provincial Natural Science Award in 2022.

Xuexiang Chen

Xuexiang Chen, Ph.D., is an associate professor. She graduated from South China Agricultural University (SCAU) in 2016 with a Ph.D. degree in Food Science (Food Nutrition and Chemistry). She carried out her Ph.D. joint cultivation at University of Massachusetts, Amherst, U.S.A. from July 2015 to July 2016. She joined the Department of Nutrition and Food Hygiene, School of Public Health, Guangzhou Medical University, Guangzhou, China in October 2016. She is a member of the Department of Nutrition and Food Hygiene, Guangzhou Medical University.

She is mainly engaged in teaching and scientific research related to food nutrition and hygiene, and her main research interests include (1) studying the chemopreventive effects of food functional active factors on diseases; (2) studying the absorption and metabolism of nutrient factors in the intestine and their protective effects on the intestinal mucosa; and (3) the interaction between plant polyphenols and human intestinal microorganisms. In recent years, she has published more than 30 papers, including 10 papers as the first author or correspondent in the *Journal of Agriculture and Food Chemistry*, *Food & Function*, *Food Bioscience*, *Food Science and Human Wellness*, and other authoritative journals on food and nutrition. Moreover, she has presided over and participated in more than 10 national, provincial, and municipal research projects.

Preface

Bioactive compounds from natural sources are highly valued for their potential health benefits and therapeutic applications. Derived from plants, animals, and microorganisms, these compounds exhibit a wide range of biological activities that can be leveraged for drug development, disease prevention, and health enhancement. Through bioactivity-guided isolation techniques, metabolomics, and genomics, we can discover and identify the molecular targets and mechanisms of action of these compounds.

The Special Issue “Bioactive Compounds from Natural Sources: Discovery, Evaluation, and Applications” is a curated collection of ten scholarly papers exploring the discovery, evaluation, and innovative application of bioactive compounds from natural sources such as plants, marine organisms, and microorganisms. Research has identified new benzophenone glycosides and known compounds in *Hypericum seniawinii* Maxim., demonstrating neuroprotective and anti-inflammatory effects. Prodigiosin from *Serratia marcescens* was found to have antitumor properties against hepatocellular carcinoma cells. A novel pectic polysaccharide from honey pomelo fruit exhibited significant immunomodulatory activity. Efficient synthesis of macamides showed their anti-fatigue potential. Compounds from *Camellia ptilosperma* leaves demonstrated cytotoxic, photocytotoxic, and antibacterial activities. An iodine-mediated one-pot synthesis method for heterocycles showed pharmaceutical potential. Another synthesis protocol for benzofuran and benzo[b]thiophen derivatives emphasized green chemistry. Virtual screening identified natural compounds as potential antiviral and anticancer inhibitors. Fraxin was identified as an active compound against hyperuricemia using bioaffinity ultrafiltration mass spectrometry. Lastly, a polysaccharide from *Taxus media* exhibited immunoenhancing properties, suggesting applications in immunotherapy and functional foods.


Targeted at researchers, academics, students, and professionals in the pharmaceutical and biotechnology industries, as well as policymakers and healthcare providers, this Special Issue serves as a valuable resource for those interested in the health benefits of natural products. We hope this collection will stimulate ongoing and future research, fostering a deeper understanding of nature’s chemical diversity.

Tao Liu and Xuexiang Chen

Editors

Article

Benzophenone Rhamnosides and Chromones from *Hypericum seniawinii* Maxim.

Jing Xia, Bo Hu, Mengyu Qian, Jiayue Zhang and Lin Wu * 

Inflammation and Immune Mediated Diseases Laboratory of Anhui Province, School of Pharmacy, Anhui Medical University, Hefei 230032, China

* Correspondence: wulin@ahmu.edu.cn; Tel./Fax: +86-0551-65169750

Abstract: Two new benzophenone glycosides, hypersens A and B, along with four known compounds, (S)-(+)-5,7-dihydroxy-2-(1-methylpropyl) chromone (3), 5,7-dihydroxy-2-isopropylchromone (4), urachromone B (5), and 3-8'' bisapigenin (6), were isolated from *Hypericum seniawinii*. The structures of new compounds (1 and 2) were elucidated according to comprehensive spectroscopic data analyses. The absolute configurations of 1 and 2 were determined by electronic circular dichroism (ECD) calculations. All isolated compounds were evaluated for their neuroprotective effect using corticosterone-induced PC12 cell injury. In addition, compounds 1–6 were evaluated for their anti-inflammatory activity in lipopolysaccharide-induced RAW 264.7 cells. Compound 6 was a biflavonoid and significantly inhibited the production of nitric oxide with an IC₅₀ value of 11.48 ± 1.23 μM.

Keywords: *Hypericum seniawinii*; Hypericaceae; benzophenone rhamnosides; anti-inflammatory activity; neuroprotective activity



Citation: Xia, J.; Hu, B.; Qian, M.; Zhang, J.; Wu, L. Benzophenone Rhamnosides and Chromones from *Hypericum seniawinii* Maxim.. *Molecules* **2022**, *27*, 7056. <https://doi.org/10.3390/molecules27207056>

Academic Editors: Tao Liu and Xuexiang Chen

Received: 30 September 2022

Accepted: 17 October 2022

Published: 19 October 2022

Publisher's Note: MDPI stays neutral with regard to jurisdictional claims in published maps and institutional affiliations.



Copyright: © 2022 by the authors. Licensee MDPI, Basel, Switzerland. This article is an open access article distributed under the terms and conditions of the Creative Commons Attribution (CC BY) license (<https://creativecommons.org/licenses/by/4.0/>).

1. Introduction

Hypericum seniawinii Maxim. (Hypericaceae) is a perennial herbaceous plant, and widely distributed in temperate regions [1]. It has been used as a folk medicine for the treatment of inflammation and infectious diseases in China [2]. Previous studies on the chemical constituent and bioactivities of this herb are minimal. However, the genus *Hypericum*, consisting of about 500 species, is an important resource of medicinal and cosmetic plants [3]. The genus *Hypericum* has been reported to contain phloroglucinol derivatives, flavonoids and xanthonoids [4–7], and other miscellaneous compounds [8] which exhibit various pharmacological activities, such as antioxidative, antitumor, antiviral, anti-inflammatory, and antifungal activities [9,10].

As a part of our investigation on bioactive compounds from natural sources [11–13], phytochemical investigation on this species was conducted. As a result, two new benzophenone glycosides (1 and 2), along with four known compounds (3–6), were isolated and characterized from *H. seniawinii*. Benzophenones glycosides isolated from the genus *Hypericum* have been reported to show various activities, such as antibacterial and anti-inflammatory activities [14]. The anti-inflammatory and neuroprotective activities of all compounds were investigated. Compounds 1–6 exhibited neuroprotective effects against corticosterone-induced PC12 cell injury. Moreover, all compounds reduced the lipopolysaccharide (LPS)-induced production of nitric oxide (NO) at the concentration of 10 μM. Among these, 6 showed a significant inhibitory effect with an IC₅₀ value of 11.48 ± 1.23 μM.

2. Results and Discussion

Hypersen A (1) was obtained as yellow gum. Its molecular formula was established as C₂₆H₃₀O₁₂ based on its HR-ESI-MS (Figures S1–S3, Supplementary Materials) ion at 535.1776 [M + H]⁺ (calcd 535.1810), indicating 12 sites of unsaturation. The ¹H NMR data (Table 1) showed a set of 1,3,5-trisubstituted benzene ring signals (δ_H 6.61 (2H, d, J = 2.3 Hz), 6.38 (1H, t, J = 2.3 Hz)), a 1,2,4,6-tetrasubstituted benzene ring (δ_H 6.23 (1H, brs) and 6.08 (1H,

d, $J = 2.1$ Hz)), and characteristic resonances of a rhamnopyranosyl moiety (Figure 1) at δ_{H} 5.28 (1H, d, $J = 2.0$ Hz), and 1.09 (3H, d, $J = 6.3$ Hz). In addition, the ^1H and ^{13}C NMR spectra (Figures S4 and S5) revealed the presence of an acetyl group (δ_{H} 2.01 (3H, s), δ_{C} 171.9 and 20.9), and a 2-methylbutyryl group (δ_{H} 2.35 (1H, m), 1.46 (1H, m), 1.61 (1H, m), 0.88 (3H, t, $J = 7.5$ Hz) and 1.10 (3H, d, $J = 6.3$ Hz)). The presence of a carbonyl (δ_{C} 199.2) and the HMBC (heteronuclear multiple-bond correlation) correlations (Figure 2) of H-6 to C-7 (δ_{C} 199.2), and H-1'' (δ_{H} 5.28 (1H, d, $J = 2.0$ Hz)) to C-2' (δ_{C} 158.6) suggested that **1** was a benzophenone glycoside. Comparing the NMR data (Figures S6–S8) of compound **1** with those of the known analogue petiolin G [15] reveals they have similar structures, except for additional signals due to a 2-methylbutyryl group in **1**. The 2-methylbutyryl group located at C-3'' (δ_{C} 72.6) in **1** is based on the HMBC correlation from H-3'' (δ_{H} 4.33 (1H, dd, $J = 9.9, 3.3$ Hz)) to C-1''' (δ_{C} 177.0). The HMBC correlation (Figure 2) of H-4'' (δ_{H} 5.01 (1H, t, $J = 9.9$ Hz)) to acetoxy carbonyl carbon (δ_{C} 171.9) indicated that the acetoxy group was attached to C-4''. The acidic hydrolysis of compound **1** shows that L-rhamnose was the sole sugar moiety. The β -glycosidic linkage was derived from the ROESY correlations (Figure 2) from H-1'' (δ_{H} 5.28 (1H, d, $J = 2.0$ Hz)) to H-2'' (δ_{H} 3.71 (1H, dd, $J = 3.3, 2.0$ Hz)), H-3'' (δ_{H} 4.33 (1H, dd, $J = 9.9, 3.3$ Hz)), and H-5'' (δ_{H} 3.58 (1H, m)). The relative configuration of H₃-5''' (δ_{H} 1.10 (3H, d, $J = 6.3$ Hz)) was unable to be determined in this case, due to the flexible side chain. Thus, the absolute configuration of the sugar moiety of **1** was further confirmed by comparing its calculated ECD spectrum with that of the experimental ECD spectrum (Figure 3). Finally, the structure of **1** was established as 2',3,4',5,6'-pentahydroxybenzophenone-2'-O-(4''-acetoxy-3''-methylbutyrate)- β -L-rhamnoside (Figure 1).

Table 1. ^1H (500 MHz) and ^{13}C (125 MHz) NMR data for **1** and **2** in methanol- d_4 .

1			2	
No.	δ_{H} (J in Hz)	δ_{C}	δ_{H} (J in Hz)	δ_{C}
1		143.9		144.7
2,6	6.61 (2H, d, $J = 2.3$ Hz)	107.9	6.59 (2H, d, $J = 2.3$ Hz)	108.1
3,5		159.8		159.6
4	6.38 (1H, t, $J = 2.3$ Hz)	107.7	6.37 (1H, t, $J = 2.3$ Hz)	107.6
7		199.2		199.5
1'		109.1		108.0
2'		158.6		159.7
3'	6.23 (1H, brs)	94.9	6.32 (1H, brs)	96.1
4'		164.1		165.3
5'	6.08 (1H, d, $J = 2.1$ Hz)	98.0	6.07 (1H, d, $J = 2.1$ Hz)	98.2
6'		164.0		164.4
1''	5.28 (1H, d, $J = 2.0$ Hz)	99.5	5.16 (1H, d, $J = 2.0$ Hz)	100.8
2''	3.71 (1H, dd, $J = 3.3, 2.0$ Hz)	69.0	3.36 (1H, m)	69.6
3''	4.33 (1H, dd, $J = 9.9, 3.3$ Hz)	72.6	4.58 (1H, dd, $J = 9.8, 3.3$ Hz)	74.2
4''	5.01 (1H, t, $J = 9.9$ Hz)	71.8	3.47 (1H, t, $J = 9.8$ Hz)	71.3
5''	3.58 (1H, m)	68.8	3.55 (1H, m)	71.2
6''	1.09 (3H, d, $J = 6.3$ Hz)	17.8	1.23 (3H, d, $J = 6.1$ Hz)	18.0
1'''		177.0		177.7
2'''	2.35 (1H, m)	42.1	2.42 (1H, m)	42.3
3'''	1.46 (1H, m)	27.9	1.69 (1H, m)	27.8
	1.61 (1H, m)		1.48 (1H, m)	
4'''	0.88 (3H, t, $J = 7.5$ Hz)	11.9	0.93 (3H, t, $J = 7.5$ Hz)	11.9
5'''	1.10 (3H, d, $J = 6.3$ Hz)	16.6	1.16 (3H, d, $J = 7.0$ Hz)	16.9
-Ac		171.9		
	2.01 (3H, s)	20.9		

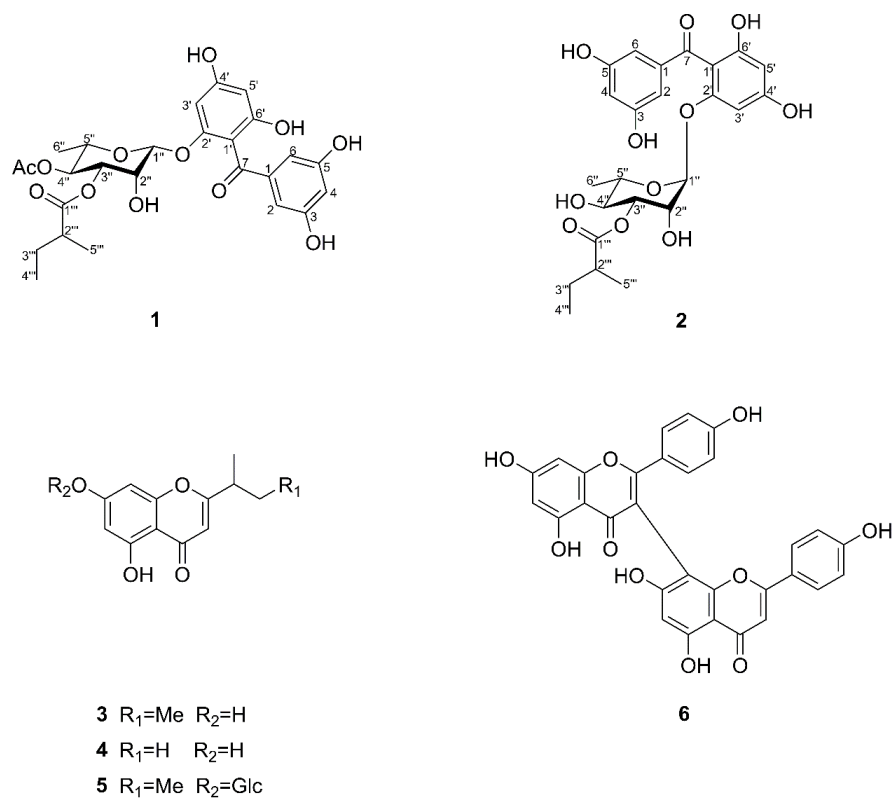


Figure 1. Structures of compounds 1–6.

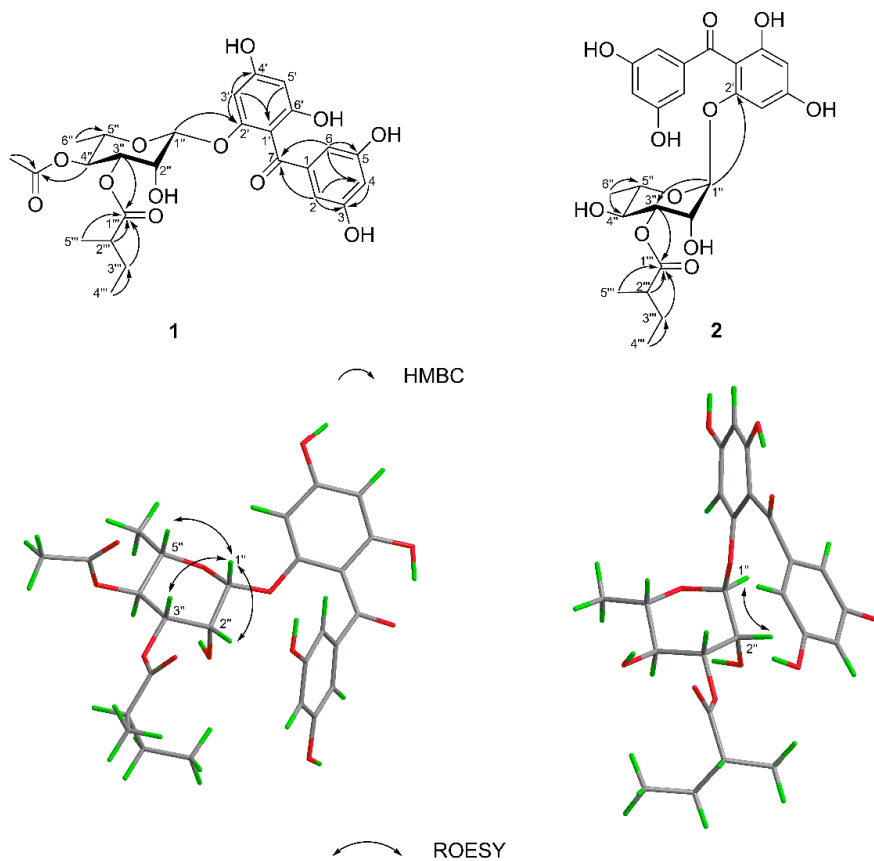


Figure 2. Key 2D correlations of 1 and 2.

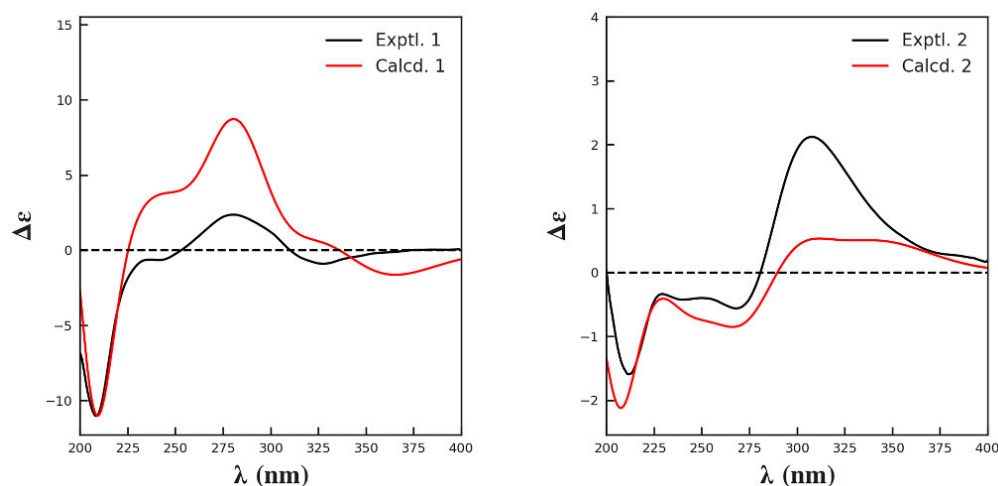


Figure 3. Experimental and calculated ECD spectra of **1** and **2**.

Hypersen B (**2**) was isolated as yellow gum. Its molecular formula was established as $C_{24}H_{28}O_{11}$ by HR-ESI-MS (Figures S9–S11, Supplementary Materials), with a sodium adduct molecular ion peak at m/z 515.1533 $[M + Na]^+$ (calcd for $[M + Na]^+$ 515.1524), which required 11 sites of unsaturation. A comparison of the NMR spectroscopic data (Figures S12–S17) (Table 1) of **2** with those of **1** indicated that they are closely related in structure. The difference was the absence of an acetyl group in **2**, which was further confirmed by the molecular formula and the chemical shift of H-4'' (δ_H 5.01 in **1**; δ_H 3.47 in **2**). The L-form of the rhamnose moiety of **2** was assigned by the same procedure as described for **1**. The α -glycosidic linkage was determined by the ROESY cross-peaks (Figure 2) between H-1'' (δ_H 5.16 (1H, d, $J = 2.0$ Hz)) and H-2'' (δ_H 3.36 (1H, m)). The absolute configuration of the sugar moiety of **2** was also determined by the calculation of the ECD spectrum (Figure 3). Accordingly, the structure of **2** was determined as 2',3,4',5,6'-pentahydroxybenzophenone-2'-O-(3''-methylbutyrate)- α -L-rhamnoside.

In addition to the new compounds **1** and **2**, four known compounds were also isolated from this plant. Their structures were identified as (*S*)-(+)-5,7-dihydroxy-2-(1-methylpropyl) chromone (**3**) [16], 5,7-dihydroxy-2-isopropylchromone (**4**) [16], urachromone B (**5**) [17], and 3-8'' bisapigenin (**6**) [18], respectively, by comparing their NMR and specific rotation data with those in the literature.

The extracts from the genus *Hypericum* have previously been used for the treatment of depression [19]. All isolates were evaluated for their protective effects on corticosterone-induced PC12 cell injury. As shown in Figure 4, compounds **1–6** (10 μ M) exhibited neuroprotective activity with cell viabilities of $79.27 \pm 1.70\%$, $78.92 \pm 2.09\%$, $82.02 \pm 2.87\%$, $81.35 \pm 2.90\%$, $83.35 \pm 1.62\%$, and $70.91 \pm 5.06\%$, respectively ($62.00 \pm 1.92\%$ for the model).

The anti-inflammatory activity of all isolated compounds in LPS-induced RAW 264.7 cells was investigated. The cytotoxicity of compounds **1–6** against RAW 264.7 cells was evaluated using the Cell Counting Kit-8 (CCK-8) assay [20]. None of the compounds were cytotoxic to RAW 264.7 cells at a concentration of 50 μ M. As depicted in Table 2, all compounds (10 μ M) exhibited inhibitory effects on NO production in LPS-induced RAW 264.7 cells. Among these, compound **6** exhibited the strongest inhibitory effect with an IC_{50} value of 11.48 ± 1.23 μ M. Therefore, the effect of compound **6** on tumor necrosis factor- α (TNF- α), interleukin-1 β (IL-1 β), and interleukin-6 (IL-6) production in LPS-induced RAW 264.7 cells was detected via enzyme-linked immunosorbent assay (ELISA). Moreover, the effect of compound **6** on mRNA expression levels of TNF- α , IL-1 β , and IL-6 in LPS-induced RAW 264.7 cells was also measured. As shown in Figure 5, compound **6** inhibited the production of TNF- α , IL-1 β and IL-6 by down-regulating the mRNA expressions of TNF- α , IL-1 β , and IL-6.

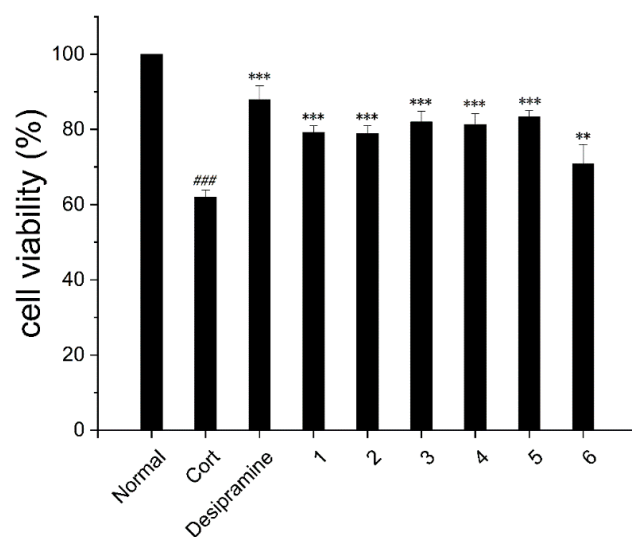


Figure 4. Neuroprotective effects of compounds 1–6 (10 μ M) against CORT-induced injury in PC12 cells. Desipramine was used as the positive control (10 μ M). ### $p < 0.001$ vs. normal. ** $p < 0.01$, and *** $p < 0.001$ vs. desipramine-treated group.

Table 2. Anti-inflammatory activity of compounds 1–6 in LPS-induced RAW 264.7 cells.

Compound	Inhibition of NO Production (%) (10 μ M)	IC ₅₀ (μ M)
1	19.21 \pm 3.15	>20
2	14.55 \pm 3.14	>20
3	14.26 \pm 1.33	>20
4	7.57 \pm 4.03	>20
5	18.92 \pm 1.01	>20
6	35.51 \pm 6.13	11.48 \pm 1.23
Indomethacin	36.68 \pm 1.33	15.04 \pm 3.31

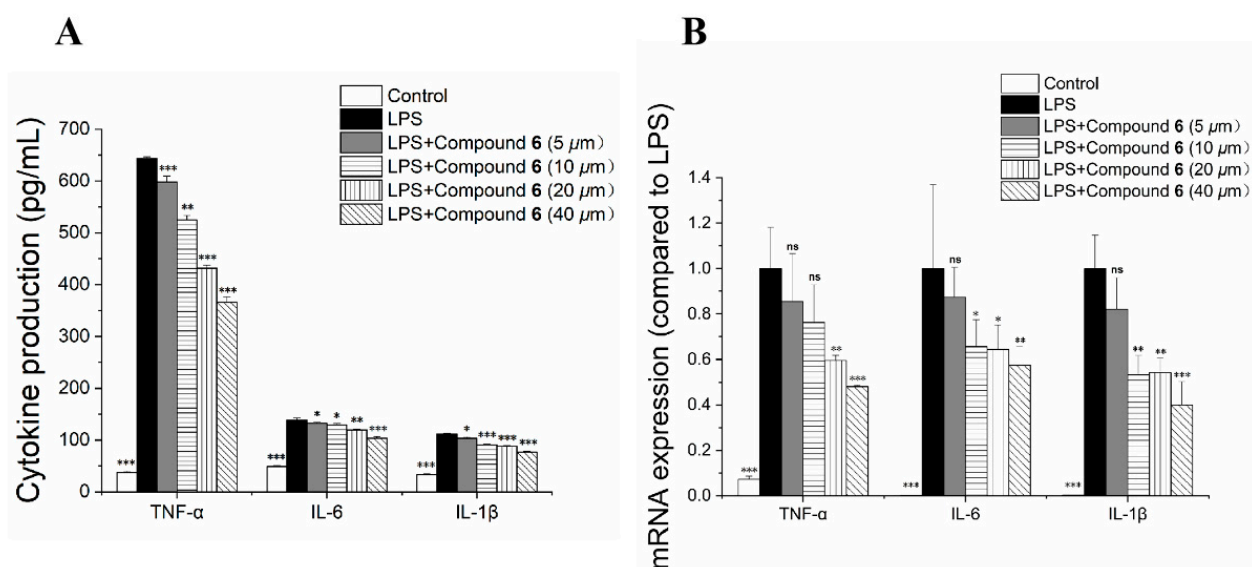


Figure 5. Effect of compound 6 on the production of TNF- α , IL-1 β , and IL-6 (A), and the mRNA expression levels of TNF- α , IL-1 β and IL-6 (B) in RAW 264.7 cells. RAW 264.7 cells were pretreated with different concentrations of compound 6 for 1 h and then stimulated with LPS (1 μ g/mL) for 24 h. * $p < 0.05$, ** $p < 0.01$, and *** $p < 0.001$ vs. LPS-treated group, ns = not significant.

3. Experimental

3.1. General Experimental Procedures

UV data were collected using a Shimadzu UV-1600PC spectrophotometer (Shimadzu Co., Kyoto, Japan). ECD spectra were measured on a Chirascan circular-dichroism spectrometer (Applied Photophysics Ltd., Surrey, UK). NMR spectra were recorded on a Bruker 500 spectrometer (Bruker Co., Billerica, MA, USA) with TMS as the internal standard. HRES-IMS spectra were recorded on an Agilent Technologies 6224 TOF liquid chromatograph mass spectrometer instrument (Agilent Technologies, Santa Clara, CA, USA). Column chromatography (CC) was performed on silica gel (Qingdao marine Chemical Co., Ltd., Qingdao, China), ODS (40–63 μm , Fuji, Chiryu, Japan), Amberlite XAD7HP (0.56–0.71 mm, Rohm and Hass Co., Philadelphia, PA, USA), CHEETAH Flashchromatography (Agela Technologies Co., Ltd., Tianjin, China), and Sephadex LH-20 (Pharmacia, Sweden). Preparative HPLC separations were performed on a Shimadzu LC-20AR instrument (Shimadzu Co., Kyoto, Japan) using a shim-pack RP-C18 column (20 \times 150 mm). Analytical and semipreparative HPLC were performed utilizing a Thermo Scientific Ultimate 3000 instrument (Thermo Fisher Scientific Inc., Waltham, MA, USA) equipped with a DAD detector, using a shim-pack VP-ODS column (4.6 \times 250 mm) and a SP ODS-A column (10 \times 250 mm), respectively.

3.2. Plant Material

The air-dried aerial parts of *Hypericum seniawinii* Maxim. (Hypericaceae) were collected from Yuexi county, Anqing city, Anhui Province, China, in June 2018. A voucher specimen (No. XJ201806) has been deposited in the School of Pharmacy, Anhui Medical University.

3.3. Extraction and Isolation

The air-dried aerial parts of *H. seniawinii* (500 g) were powdered and extracted with CH_2Cl_2 . After removing the solvent, the CH_2Cl_2 extract (20 g) was eluted by a gradient of Petroleum ether/EtOAc (12:1 to 1:4) on a silica gel column for a total of six fractions (Fr. A–F). Fr. D (286 mg) was subjected to a silica gel column and eluted with Petroleum ether/EtOAc (10:1 to 1:2) to obtain two subfractions (Fr. D.1–2). Fr. D.1 (75.8 mg) was chromatographed over a Sephadex LH-20 column (i.d. 200 \times 1.5 cm), eluting with MeOH to give four fractions (Fr. D.1.1–4). Fr. D.1.3 (5.2 mg) was further separately subjected to preparative HPLC using MeOH/ H_2O (70:30, 10 mL/min) to give compound **3** (5 mg t_{R} = 10.2 min) and **4** (1.3 mg t_{R} = 7.7 min). Fr. F (9 g) was absorbed on XAD7HP macroporon resin eluted with MeOH- H_2O (10:90 to 90:10) to generate fractions (Fr. F.1–8). Fr. F.5 (735 mg) was then applied onto an ODS column (i.d. 30 \times 3 cm) using a step gradient of MeOH/ H_2O (30:70 to 100:0) to give ten fractions (Fr. F.5.1–10). Fr. F.5.2 (55 mg) was submitted to Sephadex LH-20 column (i.d. 100 \times 1.5 cm), eluting with CH_2Cl_2 /MeOH (1:1) to obtain three subfractions (Fr. F.5.2.1–3). Fr. F.5.2.2 (15.6 mg) was purified by preparative HPLC with MeOH/ H_2O (40:60, 10 mL/min) to afford compound **2** (1.8 mg t_{R} = 15.3 min). Fr. F.5.4 (78.7 mg) was subjected to a silica gel column and eluted with CH_2Cl_2 /MeOH (30:1 to 1:1) to give five subfractions (Fr. F.5.4.1–5). The purification of Fr. F.5.4.3 (25.8 mg) and Fr. F.5.4.5 (10.7 mg) was then subjected to preparative HPLC with MeOH/ H_2O (45:55, 10 mL/min) to obtain compounds **1** (9.9 mg t_{R} = 28.5 min) and **5** (3.3 mg t_{R} = 21.6 min). Fr. F.8 (1.0265 g) was fractionated over flash chromatography eluting with MeOH/ H_2O (55:45, 10 mL/min), Fr. F.8.8 (52.4 mg) was subjected to a Sephadex LH-20 column (i.d. 100 \times 1.5 cm) to yield compound **6** (12.7 mg, t_{R} = 7.6 min).

3.3.1. Hypersen A (1)

Yellow gum; $[\alpha]_{\text{D}}^{20}$ -32 (c 0.15, MeOH); UV (MeOH) λ_{max} (log ϵ) 218 (3.90), 282 (4.14), 306 (4.19) nm; ECD (MeOH) λ_{max} (mdeg) 209 (-12.54), 279 ($+2.43$), 329 (-0.97) nm; ^1H NMR and ^{13}C NMR data, Table 1; HR-ESI-MS m/z 535.1776 $[\text{M} + \text{H}]^+$ (calcd for $\text{C}_{26}\text{H}_{31}\text{O}_{12}$, 535.1810).

3.3.2. Hypersen B (2)

Yellow gum; $[\alpha]_D^{20}$ -2 (c 0.10, MeOH); UV (MeOH) λ_{\max} ($\log \epsilon$) 206 (4.16), 281 (3.42), 306 (3.46) nm; ECD (MeOH) λ_{\max} (mdeg) 210 (-1.71), 273 (-0.59), 308 ($+2.158$) nm; ^1H NMR and ^{13}C NMR data, Table 1; HR-ESI-MS m/z 515.1533 $[\text{M} + \text{Na}]^+$ (calcd for $\text{C}_{24}\text{H}_{28}\text{O}_{11}\text{Na}$, 515.1524).

3.4. ECD Calculations

According to the relative configuration of each compound deduced from the coupling constant and ROESY spectrum, systematic conformational searches were performed with Confab [21]. The initial conformations were optimized and re-optimized with the Molclus program (version 1.9.9.5) [22] by invoking the xtb program (version 6.4) [23,24] and ORCA-5.0 [25,26] at the B97-3c level. The program ORCA-5.0 was used to calculate the ECD spectra at the PBE0/def2-SV(P) level with a CPCM solvent model (methanol).

3.5. Hydrolysis of Compounds 1 and 2

The compound (0.5 mg) was treated with 3 M hydrochloric acid (0.5 mL) at 90 °C for 2 h. After neutralization with 3 M ammonium hydroxide, the reactants were dried by evaporation of the solvent. L-cysteine methyl ester (0.5 mg) and pyridine (0.2 mL) were added, and then stirred at 60 °C for 1 h. Finally, phenyl isothiocyanate solution (0.5 mL) was added and stirred at 60 °C for 1 h. [27]. The residue of each sample was subjected to analytical HPLC (with MeCN/ H_2O (25:75, 1.0 mL/min) using a C18 RP column (4.6 mm \times 250 mm, 5 μm , Thermo Fisher Scientific Inc., Waltham, MA, USA). The configuration of the sugars was determined by comparing their retention times with that of derived L-rhamnose ($t_R = 20.2$ min).

3.6. Biological Assay

3.6.1. Cytotoxicity Assay

The cytotoxicity was measured by the Cell Counting Kit-8 assay (CCK-8, Beyotime, Shanghai, China). RAW 264.7 mouse macrophages were purchased from Procell Life Science & Technology Co. Ltd. (Wuhan, China, Product No. CL-0190) and PC12 (rat adrenal pheochromocytoma cell line) from the Beijing Stem Cell Bank (BSCS) (Beijing, China, Accession No. TCR 9). Both types of cells were cultured in DMEM supplemented with 10% fetal bovine serum and inoculated in 96-well plates at a density of 5×10^3 cells/well. Then, the cells were treated with compounds (3.125, 6.25, 12.5, 25, 50 μM) for 24 h. CCK-8 solution (100 μL) was added to each well, and the cells were further incubated for 1.5 h. The absorbance (OD values) was measured on a microplate spectrophotometer (Synergy HTX, Biotek, Shoreline, WA, USA) at 450 nm (wavelength).

3.6.2. Neuroprotective Assay

The neuroprotection was analyzed using the CCK-8 colorimetric assay. Compounds were dissolved in dimethyl sulfoxide (DMSO) (50 mM) solution. CORT (400 μM) served as an injury model group. PC12 cells were divided into no treatment (normal group), CORT (400 μM) (negative control group), CORT (400 μM) plus desipramine (10 μM) (positive control group), and CORT (400 μM) plus compounds (10 μM). Cell suspension (100 μL) was seeded in 96-well plates (5×10^3 cells/well). The cells were then incubated for 24 h, and 10% CCK-8 (100 μL) medium was added to each well and incubated further for 2 h. The absorbance was measured at 450 nm using a BioTek Synergy HTX multimode reader.

3.6.3. NO Production

RAW 264.7 macrophages were seeded in 48-well plates, pretreated with compounds (10 μM) for 1 h, and subsequently incubated with LPS (1.0 $\mu\text{g}/\text{mL}$) (*Escherichia coli*, Sigma-Aldrich, St. Louis, MO, USA) for 24 h. Griess reagent (Beyotime, Shanghai, China) was used to measure NO production. The absorbance was determined at 540 nm using a BioTek Synergy HTX multimode reader.

3.6.4. Determination of IL-6, TNF- α , and IL-1 β

The concentrations of IL-1 β , IL-6, and TNF- α in the supernatants of RAW 264.7 cells were investigated by ELISA (ELISA LAB, Wuhan, China) according to the manufacturer's protocols.

3.6.5. mRNA Expressions of IL-6, IL-1 β , and TNF- α

Sample RNA was extracted utilizing the triol method (Accurate Biology, Changsha, China). The RNA concentration of each sample was determined on the DS-11 Spectrophotometer (Denovix Inc., Wilmington, DE, USA) and verified for purity. cDNA synthesis was performed using a 5 \times Evo M-MLV RT Master Mix kit (Accurate Biology, Changsha, China). The relative levels of selected mRNAs were measured using a SYBR Green qPCR Kit (Accurate Biology, Changsha, China) and a CFX96 Real-time RT-PCR detection system (Bio-Rad Laboratories, Inc., Berkeley, CA, USA). The mRNA expression values were normalized by internal control β -actin. Primer sequences: β -actin (forward, 5'-AGTGTGACGTTGACATCCGT-3'; reverse, 5'-TGCTAGGAGCCAGAGCAGTA-3'); TNF- α (forward, 5'-CACCACCATCAAGGACTCAA-3'; reverse, 5'-AGGCAACCTGACCACTCTCC-3'); IL-6 (forward, 5'-CTTTGAAGTTGACGGACCC-3'; reverse, 5'-TGAGTGATACTGCCTGCCTG-3'); IL-1 β (forward, 5'-GAGGATACCACTCCCAACAGACC-3'; reverse, 5'-AAGTGCATCATCGTTGTTTCATACA-3').

3.6.6. Statistical Analysis

IBM SPSS 25.0 software (Armonk, NY, USA) was used for the statistical analysis. Data are presented as mean \pm SD ($n = 3$).

4. Conclusions

In summary, two new benzophenone glycosides (**1** and **2**), along with four known compounds (**3–6**) were isolated from the aerial parts of *H. seniawinii*. The absolute configurations of the sugar moiety of benzophenone glycosides were determined by hydrolysis and the calculation of the ECD spectrum. The neuroprotective and anti-inflammatory activities of these compounds were evaluated. Based on the results, compound **6** possessed a significant inhibitory effect on the production of NO, TNF- α , IL-1 β , and IL-6 in LPS-induced RAW 264.7 cells. This study will enrich the chemical diversity of *H. seniawinii* and facilitate the development of inflammatory inhibitors and neuroprotective agents.

Supplementary Materials: The following supporting information can be downloaded at: <https://www.mdpi.com/article/10.3390/molecules27207056/s1>. Figure S1: HRESIMS data of compound **1**; Figure S2: UV spectrum of compound **1** in CH₃OH; Figure S3: CD spectrum of compound **1** in CH₃OH; Figure S4: ¹H NMR spectrum of compound **1** (500 MHz, Methanol-*d*₄); Figure S5: ¹³C NMR spectrum of compound **1** (125 MHz, Methanol-*d*₄); Figure S6: HSQC spectrum of compound **1** (500 MHz, Methanol-*d*₄); Figure S7: HMBC spectrum of compound **1** (500 MHz, Methanol-*d*₄); Figure S8: ROESY spectrum of compound **1** (500 MHz, Methanol-*d*₄); Figure S9: HRESIMS data of compound **2**; Figure S10: UV spectrum of compound **2** in CH₃OH; Figure S11: CD spectrum of compound **2** in CH₃OH; Figure S12: ¹H NMR spectrum of compound **2** (500 MHz, Methanol-*d*₄); Figure S13: ¹³C NMR spectrum of compound **2** (125 MHz, Methanol-*d*₄); Figure S14: HSQC spectrum of compound **2** (500 MHz, Methanol-*d*₄); Figure S15: HMBC spectrum of compound **2** (500 MHz, Methanol-*d*₄); Figure S16: ROESY spectrum of compound **2** (500 MHz, Methanol-*d*₄); Figure S17: ¹H-¹H COSY spectrum of compound **2** (500 MHz, Methanol-*d*₄).

Author Contributions: Conceptualization, L.W.; data curation, B.H., M.Q. and J.Z.; writing—original draft, J.X. All authors have read and agreed to the published version of the manuscript.

Funding: This work was financially supported by the National Natural Science Foundation of China (No. 31800279).

Institutional Review Board Statement: Not applicable.

Informed Consent Statement: Not applicable.

Data Availability Statement: The data presented in this study are available in supplementary material.

Acknowledgments: We appreciate the support from Pharmaceutical peak discipline project of Anhui province.

Conflicts of Interest: The authors declare no conflict of interest.

Sample Availability: Compounds were deposited in the School of Pharmacy, Anhui Medical University.

References

- Meseguer, A.S.; Aldasoro, J.J.; Sanmartín, I. Bayesian inference of phylogeny, morphology and range evolution reveals a complex evolutionary history in St. John's wort (*Hypericum*). *Mol. Phylogenet. Evol.* **2013**, *67*, 379–403. [CrossRef] [PubMed]
- Zhang, R.F.; Ji, Y.N.; Morcol, T.; Lin, F.K.; Gu, R.H.; Kennelly, E.J.; Long, C.N. UPLC-QToF-MS chemical profiling and characterization of antiproliferative and anti-inflammatory compounds from seven *Hypericum* species in China. *Ind. Crops Prod.* **2021**, *173*, 114156. [CrossRef]
- Silva, A.R.; Taofiq, O.; Ferreira, I.C.F.R.; Barros, L. *Hypericum* genus cosmeceutical application—A decade comprehensive review on its multifunctional biological properties. *Ind. Crops Prod.* **2021**, *159*, 113053. [CrossRef]
- Barnes, J.; Anderson, L.A.; Phillipson, J.D. St John's wort (*Hypericum perforatum* L.): A review of its chemistry, pharmacology and clinical properties. *J. Pharm. Pharmacol.* **2001**, *53*, 583–600. [CrossRef]
- Morshedloo, M.R.; Ebadi, A.; Maggi, F.; Fattahi, R.; Yazdani, D.; Jafari, M. Chemical characterization of the essential oil compositions from Iranian populations of *Hypericum perforatum* L. *Ind. Crops Prod.* **2015**, *76*, 565–573. [CrossRef]
- Wang, J.; Shi, M.; Wang, J.; Li, J.; Ji, T. Polycyclic Polypropenylated Acylphloroglucinol Derivatives from *Hypericum acmosepalum*. *Molecules* **2018**, *24*, 50. [CrossRef]
- Bennett, G.J.; Lee, H.H. Xanthenes from *guttiferae*. *Phytochemistry* **1989**, *28*, 967–998. [CrossRef]
- Rouis, Z.; Laamari, A.; Abid, N.; Elaissi, A.; Cioni, P.L.; Flamini, G.; Aouni, M. Chemical composition and larvicidal activity of several essential oils from *Hypericum* species from Tunisia. *Parasitol. Res.* **2013**, *112*, 699–705. [CrossRef]
- Zhao, H.Z.; Wu, L.; Zhang, Y.; Feng, S.; Ding, Y.; Deng, X.; Feng, R.; Li, J.; Ma, T.T.; Huang, C. Betulinic acid prevents liver fibrosis by binding Lck and suppressing Lck in HSC activation and proliferation. *J. Ethnopharmacol.* **2022**, *296*, 115459. [CrossRef]
- Zhang, R.; Ji, Y.; Zhang, X.; Kennelly, E.J.; Long, C. Ethnopharmacology of *Hypericum* species in China: A comprehensive review on ethnobotany, phytochemistry and pharmacology. *J. Ethnopharmacol.* **2020**, *254*, 112686. [CrossRef]
- Deng, X.; Wang, X.R.; Wu, L. Triketone-terpene meroterpenoids from the leaves of *Rhodomyrtus tomentosa*. *Fitoterapia* **2020**, *143*, 104585. [CrossRef] [PubMed]
- Deng, X.; Xia, J.; Qian, M.Y.; Wang, X.R.; Hu, B.; Liu, X.S.; Wu, L. Ascyrones A–E, type B bicyclic polypropenylated acylphloroglucinol derivatives from *Hypericum ascyron*. *Chin. J. Nat. Med.* **2022**, *20*, 473–480. [CrossRef]
- Deng, X.; Xia, J.; Hu, B.; Hou, X.C.; Pu, X.D.; Wu, L. Hyjapones A–D, trimethylated acylphloroglucinol meroterpenoids from *Hypericum japonicum* thunb. With anti-inflammatory activity. *Phytochemistry* **2022**, *202*, 113308. [CrossRef]
- Bridi, H.; Meirelles, G.C.; von Poser, G.L. Structural diversity and biological activities of phloroglucinol derivatives from *Hypericum* species. *Phytochemistry* **2018**, *155*, 203–232. [CrossRef] [PubMed]
- Tanaka, N.; Kubota, T.; Kashiwada, Y.; Takaishi, Y.; Kobayashi, J. Petiolins F–I, benzophenone rhamnosides from *Hypericum pseudopetiolum* var. *kiusianum*. *Chem. Pharm. Bull.* **2009**, *57*, 1171–1173. [CrossRef] [PubMed]
- Qiu, D.; Zhou, M.; Lin, T.; Chen, J.J.; Wang, G.H.; Huang, Y.J.; Jiang, X.; Tian, W.J.; Chen, H.F. Cytotoxic Components from *Hypericum elodeoides* Targeting RXR α and Inducing HeLa Cell Apoptosis through Caspase-8 Activation and PARP Cleavage. *J. Nat. Prod.* **2019**, *82*, 1072–1080. [CrossRef] [PubMed]
- Chen, X.Q.; Li, Y.; Cheng, X.; Wang, K.; He, J.; Pan, Z.H.; Li, M.M.; Peng, L.Y.; Xu, G.; Zhao, Q.S. Polycyclic Polypropenylated Acylphloroglucinols and Chromone O-Glucosides from *Hypericum henryi* subsp. *uraloides*. *Chem. Biodivers.* **2010**, *7*, 196–204. [CrossRef] [PubMed]
- Jiang, L.; Numonov, S.; Bobakulov, K.; Qureshi, M.N.; Zhao, H.; Aisa, H.A. Phytochemical Profiling and Evaluation of Pharmacological Activities of *Hypericum scabrum* L. *Molecules* **2015**, *20*, 11257–11271. [CrossRef]
- Linde, K.; Berner, M.; Egger, M.; Mulrow, C. St John's wort for depression: Meta-analysis of randomised controlled trials. *Br. J. Psychiatry* **2005**, *186*, 99–107. [CrossRef]
- Baatar, D.; Siddiqi, M.Z.; Im, W.T.; Ul Khaliq, N.; Hwang, S.G. Anti-Inflammatory Effect of Ginsenoside Rh-2-Mix on Lipopolysaccharide-Stimulated RAW 264.7 Murine Macrophage Cells. *J. Med. Food* **2018**, *21*, 951–960. [CrossRef]
- O'Boyle, N.M.; Vandermeersch, T.; Flynn, C.J.; Maguire, A.R.; Hutchison, G.R. Confab-Systematic generation of diverse low-energy conformers. *J. Cheminform.* **2011**, *3*, 8. [CrossRef] [PubMed]
- Lu, T. Molclus Program Version 1.9.9.5. Available online: www.keinsci.com/research/molclus.html (accessed on 15 September 2022).
- Grimme, S. Exploration of Chemical Compound, Conformer, and Reaction Space with Meta-Dynamics Simulations Based on Tight-Binding Quantum Chemical Calculations. *J. Chem. Theory Comput.* **2019**, *15*, 2847–2862. [CrossRef] [PubMed]

24. Grimme, S.; Bannwarth, C.; Shushkov, P. A Robust and Accurate Tight-Binding Quantum Chemical Method for Structures, Vibrational Frequencies, and Noncovalent Interactions of Large Molecular Systems Parametrized for All spd-Block Elements ($Z = 1-86$). *J. Chem. Theory Comput.* **2017**, *13*, 1989–2009. [CrossRef] [PubMed]
25. Neese, F.; Wennmohs, F.; Becker, U.; Riplinger, C. The ORCA quantum chemistry program package. *J. Chem. Phys.* **2020**, *152*, 224108. [CrossRef] [PubMed]
26. Neese, F. Software update: The ORCA program system, version 4.0. *WIREs Comput. Mol. Sci.* **2018**, *8*, 1327. [CrossRef]
27. Ngo, T.H.; Uprety, A.; Ojha, M.; Kil, Y.S.; Choi, H.; Kim, S.Y.; Nam, J.W. Stability of valeriana-type iridoid glycosides from rhizomes of *Nardostachys jatamansi* and their protection against H₂O₂-induced oxidative stress in SH-SY5Y cells. *Phytochemistry* **2022**, *203*, 113375. [CrossRef]

Article

Prodigiosin from *Serratia Marcescens* in Cockroach Inhibits the Proliferation of Hepatocellular Carcinoma Cells through Endoplasmic Reticulum Stress-Induced Apoptosis

Jie Wang^{1,2,†}, Hancong Liu^{1,2,†}, Liuchong Zhu^{1,2,†}, Jingyi Wang¹, Xiongming Luo^{1,2}, Wenbin Liu^{1,2} and Yan Ma^{1,2,*}

¹ School of Biosciences & Biopharmaceutics, Guangdong Pharmaceutical University, Guangzhou 510000, China

² Guangdong Provincial Key Laboratory of Pharmaceutical Bioactive Substances, 280 Wai Huan Dong Road, Guangzhou Higher Education Mega Center, Guangzhou 510000, China

* Correspondence: mayan@gdpu.edu.cn

† These authors contributed equally to this work.

Abstract: Hepatocellular carcinoma (HCC) is the most common primary liver malignant tumor, and the targeted therapy for HCC is very limited. Our previous study demonstrated that prodigiosin (PG), a secondary metabolite from *Serratia marcescens* found in the intestinal flora of cockroaches, inhibits the proliferation of HCC and increases the expression of CHOP, a marker protein for endoplasmic reticulum stress (ERS)-mediated apoptosis, in a dose-dependent manner. However, the mechanisms underlying the activity of PG in vivo and in vitro are unclear. This study explored the molecular mechanisms of PG-induced ERS against liver cancer in vitro and in vivo. The apoptosis of hepatocellular carcinoma cells induced by PG through endoplasmic reticulum stress was observed by flow cytometry, colony formation assay, cell viability assay, immunoblot analysis, and TUNEL assay. The localization of PG in cells was observed using laser confocal fluorescence microscopy. Flow cytometry was used to detect the intracellular Ca²⁺ concentration after PG treatment. We found that PG could promote apoptosis and inhibit the proliferation of HCC. It was localized in the endoplasmic reticulum of HepG2 cells, where it induces the release of Ca²⁺. PG also upregulated the expression of key unfolded response proteins, including PERK, IRE1 α , Bip, and CHOP, and related apoptotic proteins, including caspase3, caspase9, and Bax, but down-regulated the expression of anti-apoptotic protein Bcl-2 in liver cancer. Alleviating ERS reversed the above phenomenon. PG had no obvious negative effects on the functioning of the liver, kidney, and other main organs in nude mice, but the growth of liver cancer cells was inhibited by inducing ERS in vivo. The findings of this study showed that PG promotes apoptosis of HCC by inducing ERS.

Keywords: PG; endoplasmic reticulum stress; apoptosis; hepatocellular carcinoma



Citation: Wang, J.; Liu, H.; Zhu, L.; Wang, J.; Luo, X.; Liu, W.; Ma, Y. Prodigiosin from *Serratia Marcescens* in Cockroach Inhibits the Proliferation of Hepatocellular Carcinoma Cells through Endoplasmic Reticulum Stress-Induced Apoptosis. *Molecules* **2022**, *27*, 7281. <https://doi.org/10.3390/molecules27217281>

Academic Editor: George Grant

Received: 16 September 2022

Accepted: 24 October 2022

Published: 26 October 2022

Publisher's Note: MDPI stays neutral with regard to jurisdictional claims in published maps and institutional affiliations.



Copyright: © 2022 by the authors. Licensee MDPI, Basel, Switzerland. This article is an open access article distributed under the terms and conditions of the Creative Commons Attribution (CC BY) license (<https://creativecommons.org/licenses/by/4.0/>).

1. Introduction

In recent years, the incidence of primary liver cancer has been increasing worldwide. Hepatocellular carcinoma (HCC) has the highest incidence among primary liver malignancies, and its morbidity and mortality are roughly equivalent [1,2]. The molecular mechanism of HCC formation is very complex, and multiple signaling pathways are involved. These signaling pathways include the PI3K-AKT-mTOR signaling pathway, HGF/C-Met signaling pathway, Wnt/ β -catenin pathway, and Notch pathway. These pathways interact with each other and are closely related to the proliferation, survival, and metastasis of liver tumor cells [3–5]. Research on the molecular mechanism of liver cancer development can reveal new targets for liver cancer treatment without causing major side effects.

Endoplasmic reticulum stress (ERS) refers to nutrient deficiency, pH change, hypoxia, or oxidative stress, which disrupts the folding function of the endoplasmic reticulum, causing excessive accumulation of poorly folded proteins. The poorly folded protein enters the

endoplasmic reticulum, initiates unfolded protein response (UPR), and participates in several tumor biological processes, including metastasis, proliferation, and drug resistance of tumor cells. The proteins can also induce inflammatory immune responses but inhibit antitumor immune responses. ERS is present in many human solid tumors, including liver cancer, lung cancer, nasopharyngeal cancer, breast cancer, etc., and is closely related to drug resistance and poor prognosis of cancers [6,7]. ERS further promotes the release of inflammatory factors from tumor-associated macrophages and the infiltration of inflammatory cells. This forms a vicious cycle of ERS, inflammation, and tumorigenesis. However, very high or prolonged endoplasmic reticulum stress promotes the apoptosis of tumor cells by regulating the cellular survival pathway that inhibits cell survival and directly removes cells that have been irreversibly damaged [8,9].

Microbial secondary metabolites are natural products with numerous properties, including antibacterial and antitumor properties. Our previous study revealed that *Serratia marcescens* in the intestinal flora of cockroaches procure Prodigiosin (PG), a metabolite with a strong antitumor effect against nasopharyngeal carcinoma and cervical cancer cells [10]. PG is a natural red-pigmented secondary metabolite, mainly produced by *Serratia marcescens* and actinomycetes. The structure of the bioactive agent differs among different bacteria, but all have a 4-methoxy-2,2 pyrrole ring structure. This metabolite possesses antibacterial, anti-fungal, anti-malaria immunosuppressive, and antitumor properties. PG abnormally activates the Wnt/ β -catenin signaling pathway, reverses the abnormal expression of survivin in liver cancer cells, and promotes the apoptosis of these cells [11]. PG also inhibits the growth of human oral squamous cell carcinoma cells by targeting the autophagic cell death pathway. Hosseini's research results showed that PG had a great affinity for the anti-apoptotic member MCL-1 of the BCL-2 family, and it could activate the mitochondrial apoptosis pathway by destroying the MCL-1/BAK complex to cause apoptosis in melanoma cells [12]. Therefore, it is necessary to clarify the role of different molecular phenotypes in the PG-induced apoptosis of malignant tumor cells and the molecular mechanisms underlying this process, which can reveal new and more effective targets for treating tumors. Our previous research revealed that PG increased the expression of CHOP, a marker protein for ERS-mediated apoptosis of the liver cancer cells, in a concentration-dependent manner. ERS can have the dual effects of either promoting or inhibiting apoptosis, implying that the antitumor activity of PG is related to ERS. In the present study, we performed *in vitro* and *in vivo* experiments to further investigate the effects of PG on genetically diverse HCC using HepG2 and BEL7402 cells. The molecular mechanism underlying the effect of PG on HCC was also investigated.

2. Results

2.1. PG Inhibits the Proliferation and Viability but Promotes the Apoptosis of Hepatocellular Carcinoma Cells

The Cell Counting Kit-8 (CCK-8) assay revealed that (Figure 1A,B) PG inhibits the proliferation of HepG2 and BEL-7402 cells in a time and dose-dependent manner. The CCK-8 assay demonstrated that the IC₅₀ values of PG on HepG2 and BEL7402 cells at 48 h were 1.01 μ g/mL and 2.69 μ g/mL, respectively. The inhibitory effect of PG on the viability of HepG2 was stronger than that of Bel7402. Colony formation assay further showed that PG had a significant effect on the colony formation property of HepG2 and Bel7402 (Figures 1C and 2D). Flow cytometry showed that PG arrested the cell cycle of HCC in the G₀/G₁ phase (Figure 2A) and the toxicity of PG to HCC increased with the increase in concentration (Figure 2B).

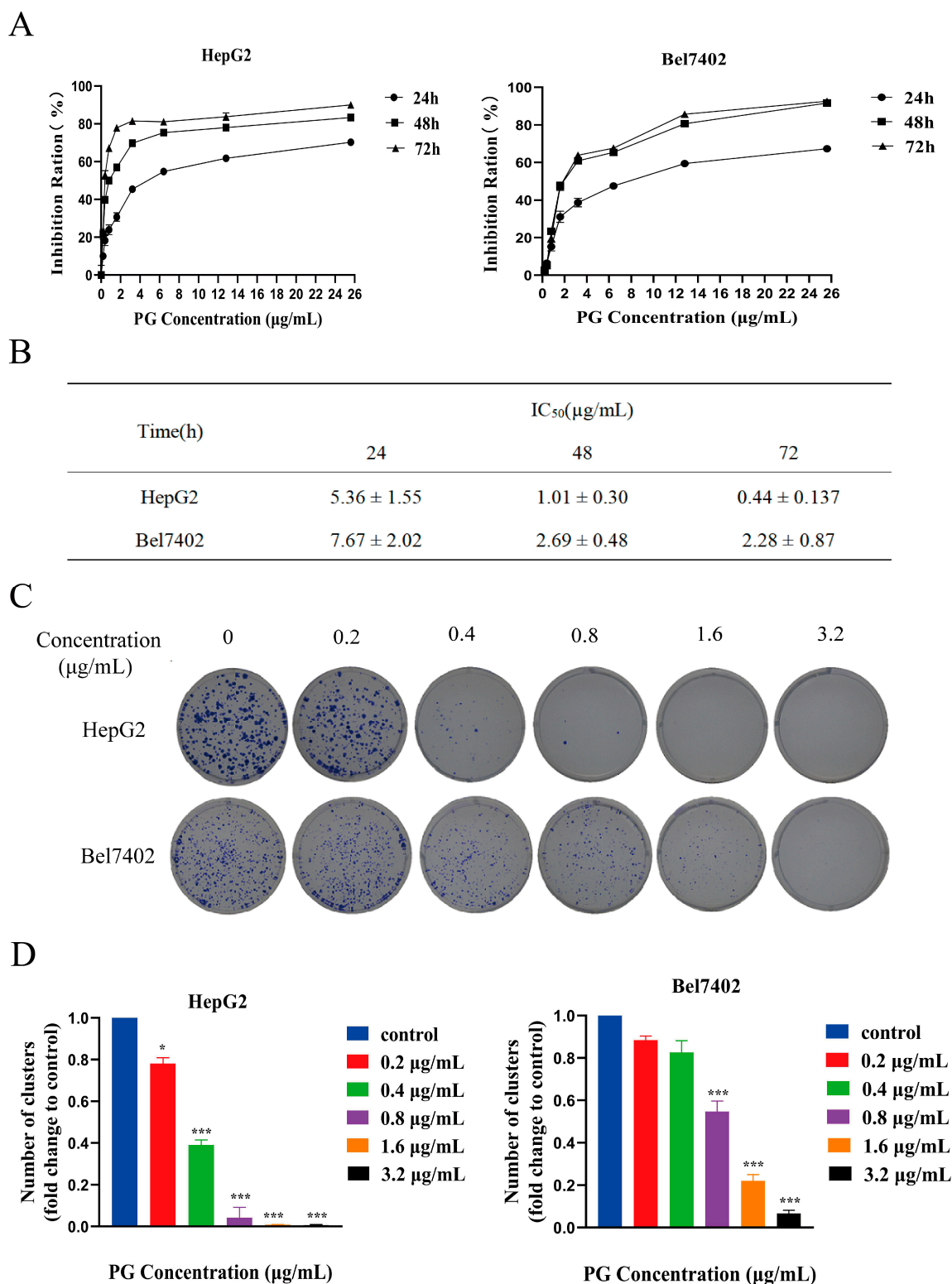


Figure 1. The effects of PG on the proliferation, cell cycle, and apoptosis of HepG2 and BEL7402 cells. (A). Inhibition rate of HepG2 and BEL7402 treated by PG for 24 h, 48 h and 72 h, respectively. (B). The IC₅₀ values of the cells treated with PG were at 24, 48 and 72 h, respectively. (C). The effect of PG on the colony formation property of HepG2 and BEL7402. (D) HepG2: PG (1.6 µg/mL), PG (0.8 µg/mL) and PG (0.4 µg/mL) vs. PG (0 µg/mL), * $p < 0.05$; *** $p < 0.001$, $n = 3$; Bel7402: PG (3.2 µg/mL), PG (1.6 µg/mL) and PG (0.8 µg/mL) vs. PG (0 µg/mL), *** $p < 0.001$, $n = 3$.

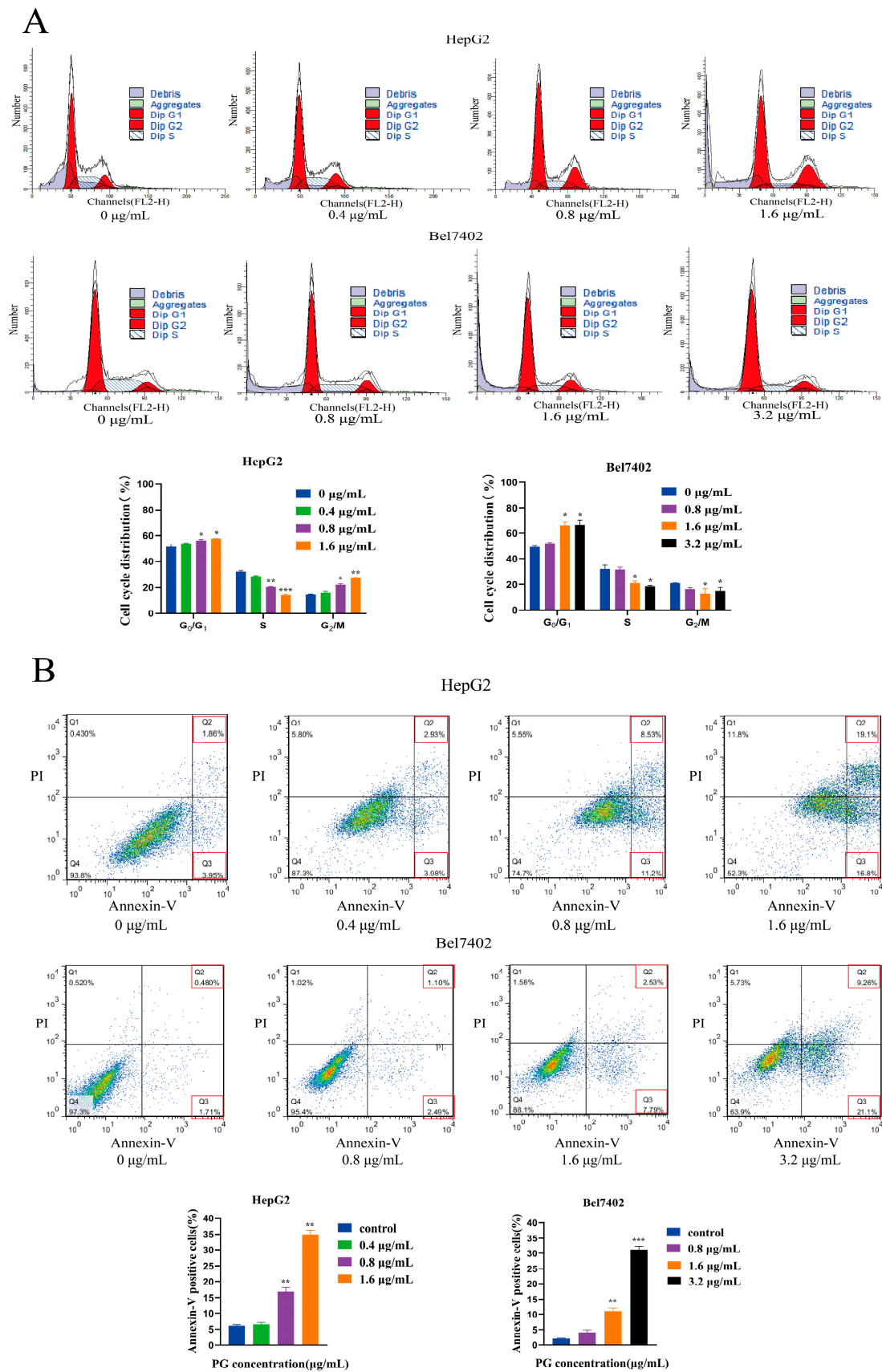


Figure 2. (A). Effect of PG on HepG2 and BEL7402 cell cycle. (B). Effect of PG on apoptosis of HePG2 and BEL7402 cells. The combined percentage of cells in Q2 and Q3 represents

Annexin V-positive cells. HepG2: PG (1.6 µg/mL), PG (0.8 µg/mL) and PG (0.4 µg/mL) vs. PG (0 µg/mL), * $p < 0.05$, ** $p < 0.01$, $n = 3$; Bel7402: PG (3.2 µg/mL), PG (1.6 µg/mL) and PG (0.8 µg/mL) vs. PG (0 µg/mL), * $p < 0.05$, ** $p < 0.01$ and *** $p < 0.001$, $n = 3$.

2.2. The Effect of Inhibiting ERS on Apoptosis of HCC Induced by PG

The effect of PG on apoptosis of HepG2 and Bel7402 was detected by TUNEL assay. The results showed that the fluorescence intensity of cells increased with the concentration of PG. However, ERS-inhibitor 4-Phenylbutyric acid (4-PBA) pretreatment reduced the fluorescence intensity of cells (Figure 3A,B). Western blotting revealed that PG treatment significantly increased the expression of Bax, caspase3, and caspase9 but decreased that of Bcl-2. However, 4-PBA pretreatment reversed the abnormal expression of the above proteins (Figure 3C,D). The results showed that PG regulated the expression of apoptotic and anti-apoptotic proteins in a dose-dependent manner, and inhibition of ER stress partially reversed the PG-induced apoptosis of HepG2 and Bel7402.

2.3. Effects of PG on ERS in HepG2 and Bel7402 Cells

Calnexin is an endoplasmic reticulum-bound chaperone protein and an endoplasmic reticulum stress-related unfolded response protein. It is a molecular chaperone that mainly participates in the folding and processing of protein nascent peptide chains. The cellular localization of PG in HepG2 cells was observed using a confocal laser fluorescence microscope (Figure 4A). We found that the correlation between PG and calnexin was stronger with the increase in PG concentration, indicating that more PG was localized in the ER. The endoplasmic reticulum also stores Ca^{2+} . Disrupting the Ca^{2+} balance in the endoplasmic reticulum induces ERS. The fluorescence intensity of HepG2 and Bel-7402 treated with different concentrations of PG was detected by flow cytometry (Figure 4B). We found that PG increased the expression of signal strength in a dose-dependent manner, suggesting that PG increases the Ca^{2+} in HepG2 and Bel-7402 cells. Western blot further revealed that PG increased the expression of PERK, IRE1 α , CHOP, and endoplasmic reticulum chaperone protein Bip in HepG2 and Bel7402 cells via the unfolded protein response signaling pathway (Figure 5A,B). PG treatment increased the protein expressions of PERK, IRE1 α , CHOP, and Bip, but 4-PBA pretreatment for 2 h reversed this phenomenon. The expression of ATF4, CHOP, XBP1, and Bip genes in HepG2 and Bel7402 after PG treatment was detected by real-time fluorescence quantitative PCR (Figure 5C). We found that PG increased the transcription of mRNAs. However, 4-PBA pretreatment reversed this phenomenon.

2.4. PG Reduced the Proliferation of HCC In Vivo

The nude mice model of HCC HepG2 was successfully constructed, and the subcutaneously transplanted tumor was dissected and weighed (Figure 6A). The tumor volume and weight were significantly smaller in the treatment group than that in the normal saline control group. The inhibitory rates of PG (2.5 mg/kg), PG (5 mg/kg), and the 4-PBA in combination with PG (5 mg/kg) were $35.6\% \pm 0.493$, $47.0\% \pm 0.419$ and $45.9\% \pm 0.169$, respectively. The biosafety of PG was also evaluated in vivo. PG had no significant effect on liver and kidney function (Figure 6B). The effect of PG on the functioning of the heart, liver, spleen, lung, and kidney was analyzed based on histomorphological analyses (Figure 7). Hematoxylin–eosin staining (HE staining) results showed well-arranged and dense myocardial myofilaments in the liver and kidney of nude mice were dense; the hepatic lobules and spleen nodules were normal with clear outlines; the alveoli and glomeruli were also generally normal. These results indicated that PG had no obvious toxic effect on liver and kidney function and other main organs of nude mice.

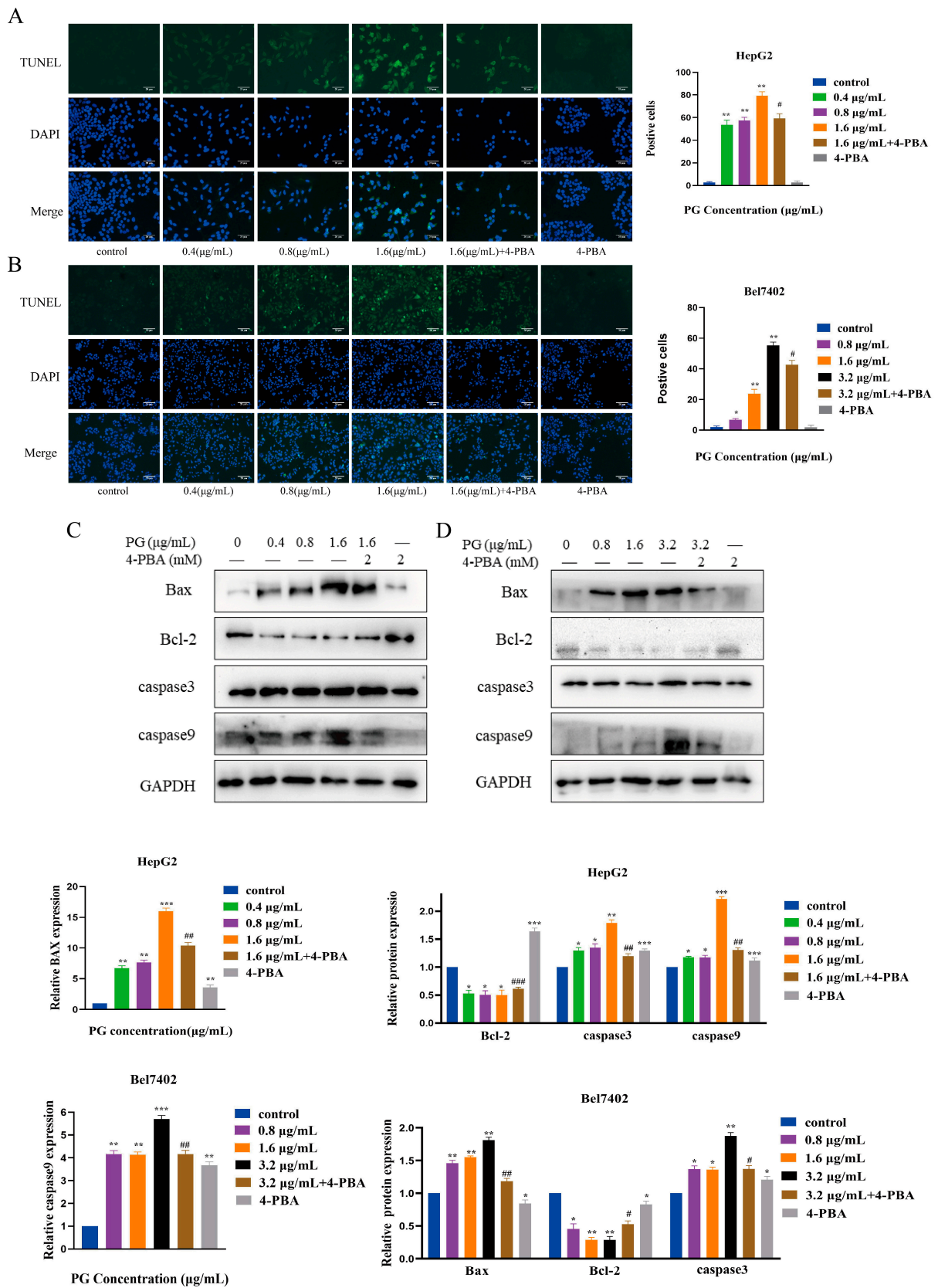
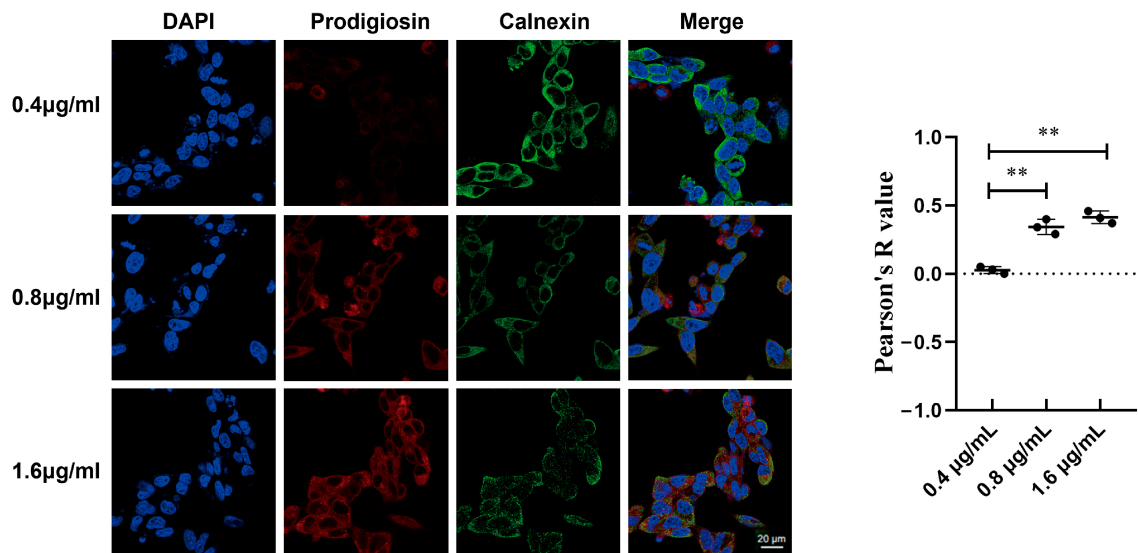


Figure 3. Induction of apoptosis by PG treatment of HCC cells. (A). TUNEL assay for the effect of 4-PBA pretreatment on the apoptotic effect of PG on HepG2 cells. (B). TUNEL assay for the effect of

4-PBA pretreatment on the apoptotic effect of PG on Bel7402; (C). Western blot for the effect of 4-PBA pretreatment on the expression of apoptotic proteins in HepG2; (D). Western blot for the effect of 4-PBA pretreatment on the expression of apoptotic proteins in Bel7402 cells. The treatments included PG (0.4 $\mu\text{g/mL}$, 0.8 $\mu\text{g/mL}$, 1.6 $\mu\text{g/mL}$, 3.2 $\mu\text{g/mL}$) vs. 0 $\mu\text{g/mL}$ of PG; 1.6 $\mu\text{g/mL}$ of PG vs. 1.6 $\mu\text{g/mL}$ of PG + 4-PBA; 3.2 $\mu\text{g/mL}$ PG vs. 3.2 $\mu\text{g/mL}$ of PG + 4-PBA; * $p < 0.05$, ** $p < 0.01$, *** $p < 0.001$, # $p < 0.05$, ## $p < 0.01$, ### $p < 0.001$, $n = 3$.

A



B

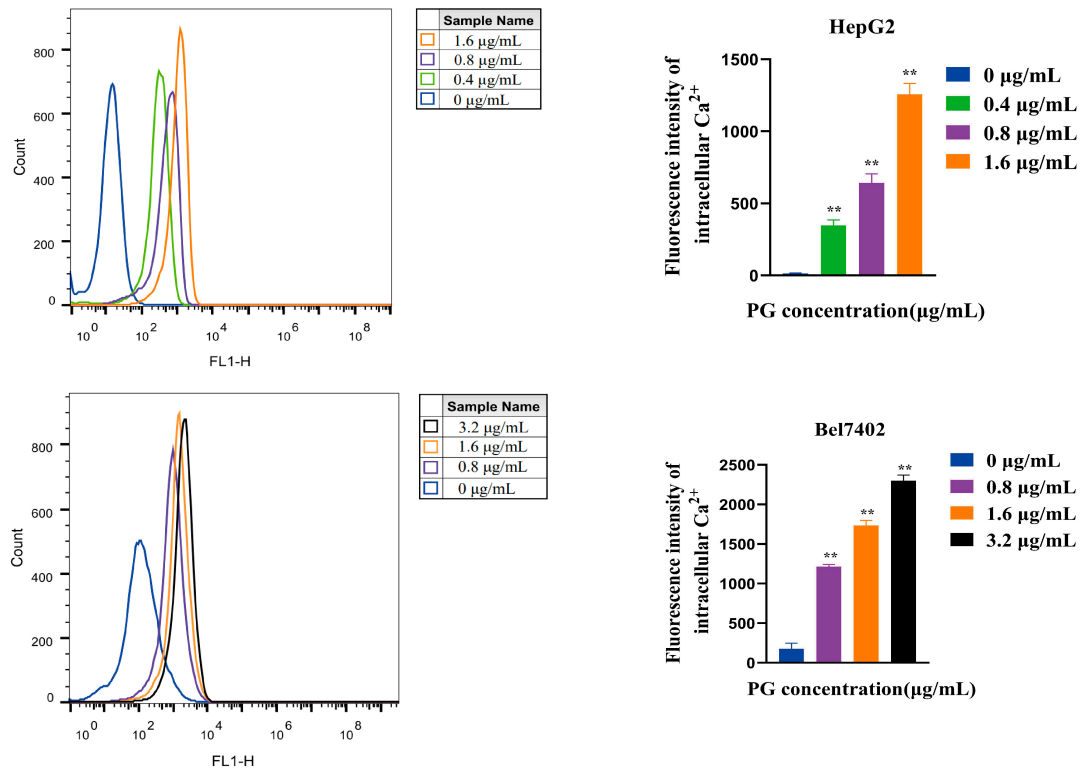


Figure 4. The effects of PG on ERS pathway in HepG2 and Bel7402 cells. (A). Localization of PG in HepG2 cells as observed under confocal laser fluorescence microscopy; (B). Flow cytometry for the effect of PG on Ca^{2+} concentration in HepG2 and Bel7402 cells. The treatments included PG (0.4 $\mu\text{g/mL}$, 0.8 $\mu\text{g/mL}$, 1.6 $\mu\text{g/mL}$, 3.2 $\mu\text{g/mL}$) vs. 0 $\mu\text{g/mL}$ of PG, ** $p < 0.01$, $n = 3$.

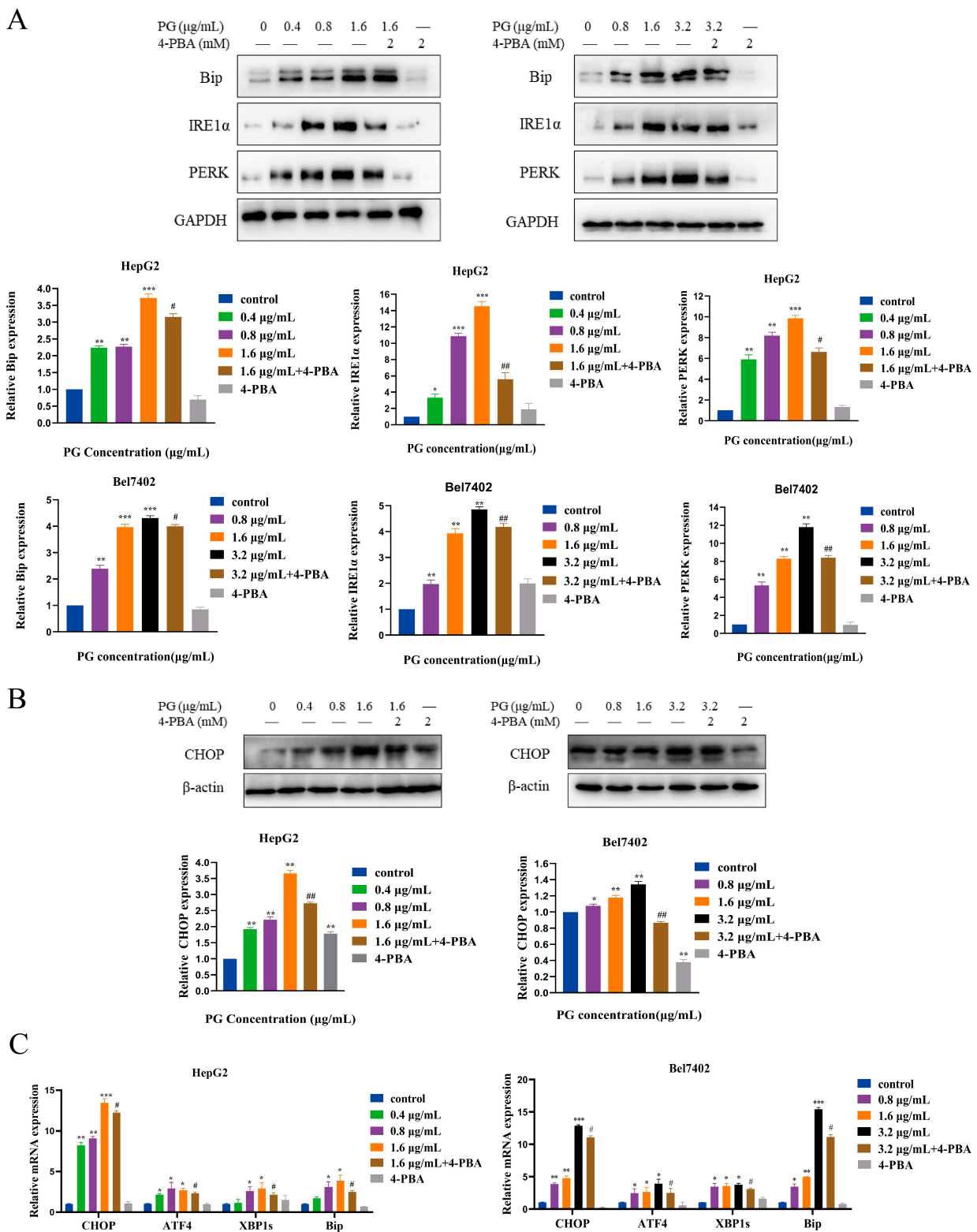


Figure 5. (A). Western blot assay on the expression of Bip, IRE1α, and PERK in HepG2 and Bel7402 cells; (B). Western blot assay for the expression of CHOP in HepG2 and Bel7402 cells; (C). RT-qPCR effect of 4-PBA pretreatment on the effect of PG on the expression of Bip, CHOP, ATF4, and XBP1 mRNA in HepG2 and Bel7402 cells. The treatments included PG (0.4 µg/mL, 0.8 µg/mL, 1.6 µg/mL, 3.2 µg/mL) vs. 0 µg/mL of PG; 1.6 µg/mL of PG vs. 1.6 µg/mL of PG + 4-PBA; 3.2 µg/mL PG vs. 3.2 µg/mL of PG + 4-PBA; * $p < 0.05$, ** $p < 0.01$, *** $p < 0.001$, # $p < 0.05$, ## $p < 0.01$, $n = 3$.

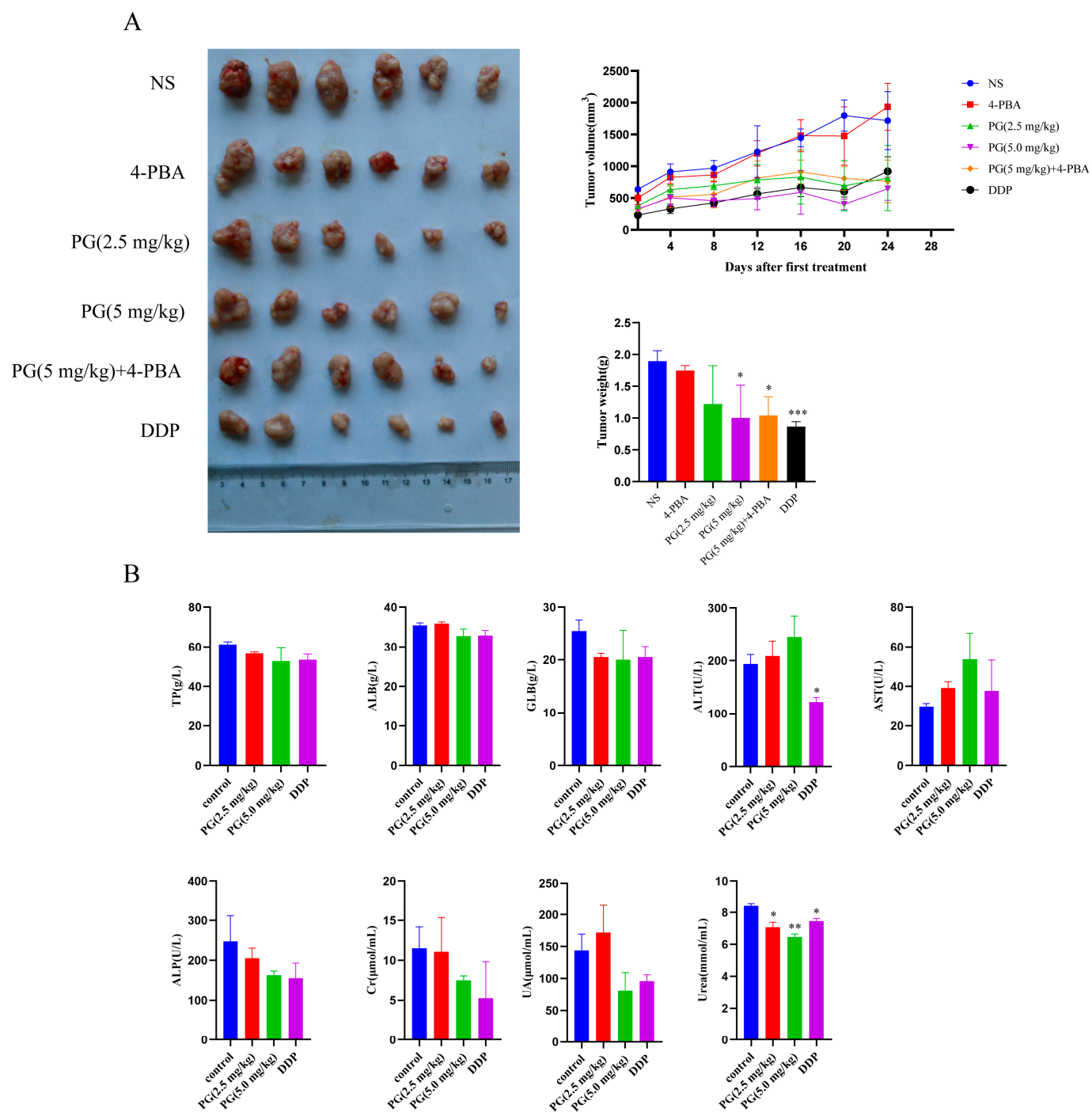


Figure 6. The effect of PG on the proliferation of hepatocellular carcinoma in vivo. (A). Effects of PG on the volume and weight of subcutaneously transplanted tumors; (B). The effect of PG on the liver and kidney function of nude mice with HepG2. The levels of total aspartate aminotransferase (AST), alanine aminotransferase (ALT), alkaline phosphatase (ALP), albumin (ALB), total protein (TP), creatinine (CR), uric acid (UA) and urea in the blood represent the liver and kidney function of nude mice. PG (2.5 mg/kg), PG (5 mg/kg), PG (5 mg/kg)+4-PBA, DDP vs. NS, * $p < 0.05$, ** $p < 0.01$, *** $p < 0.001$, $n = 6$.

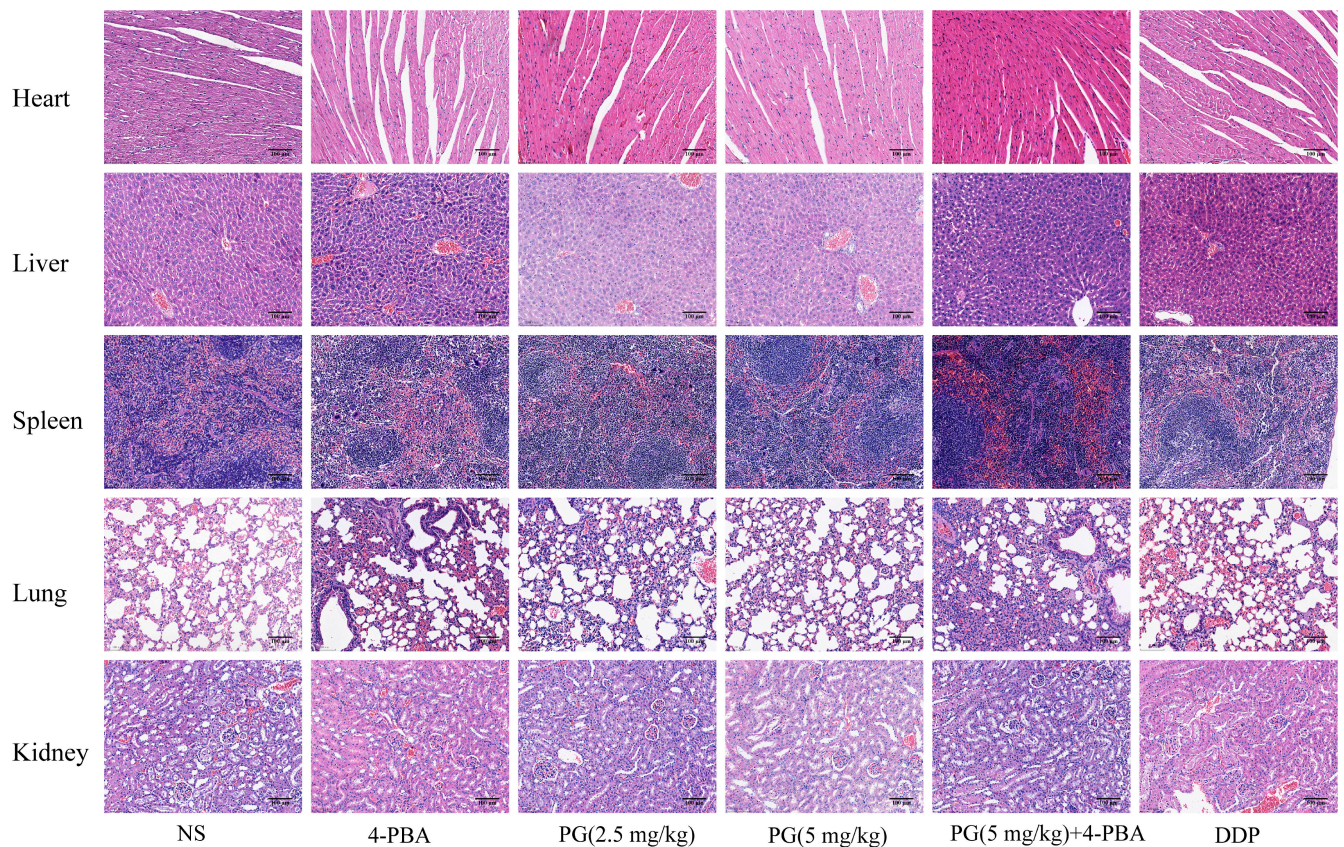


Figure 7. HE staining of heart, liver, spleen, lung, and kidney tissues of nude mice.

2.5. The Apoptosis-Inducing Effect of PG on Transplanted Tumors in Nude Mice

The effect of PG on the apoptosis of tumor tissue HepG2 cells was analyzed using the TUNEL assay (Figure 8A). The green fluorescence signal around the nuclei of tumor tissue increased with PG concentration. To observe the effect of PG-induced ERS on the apoptosis of tumor tissue, the expression of Bip, PERK, and caspase3 was detected using immunohistochemical analysis (Figure 8B). Compared with the control group, we found that PG increased the expression of Bip, PERK, and caspase3 in a concentration-dependent manner. However, 4-PBA pretreatment decreased the expression of these proteins. The expression of key proteins in the ERS pathway and apoptosis-related proteins in tumor tissues after PG treatment displayed a similar trend (Figure 8C).

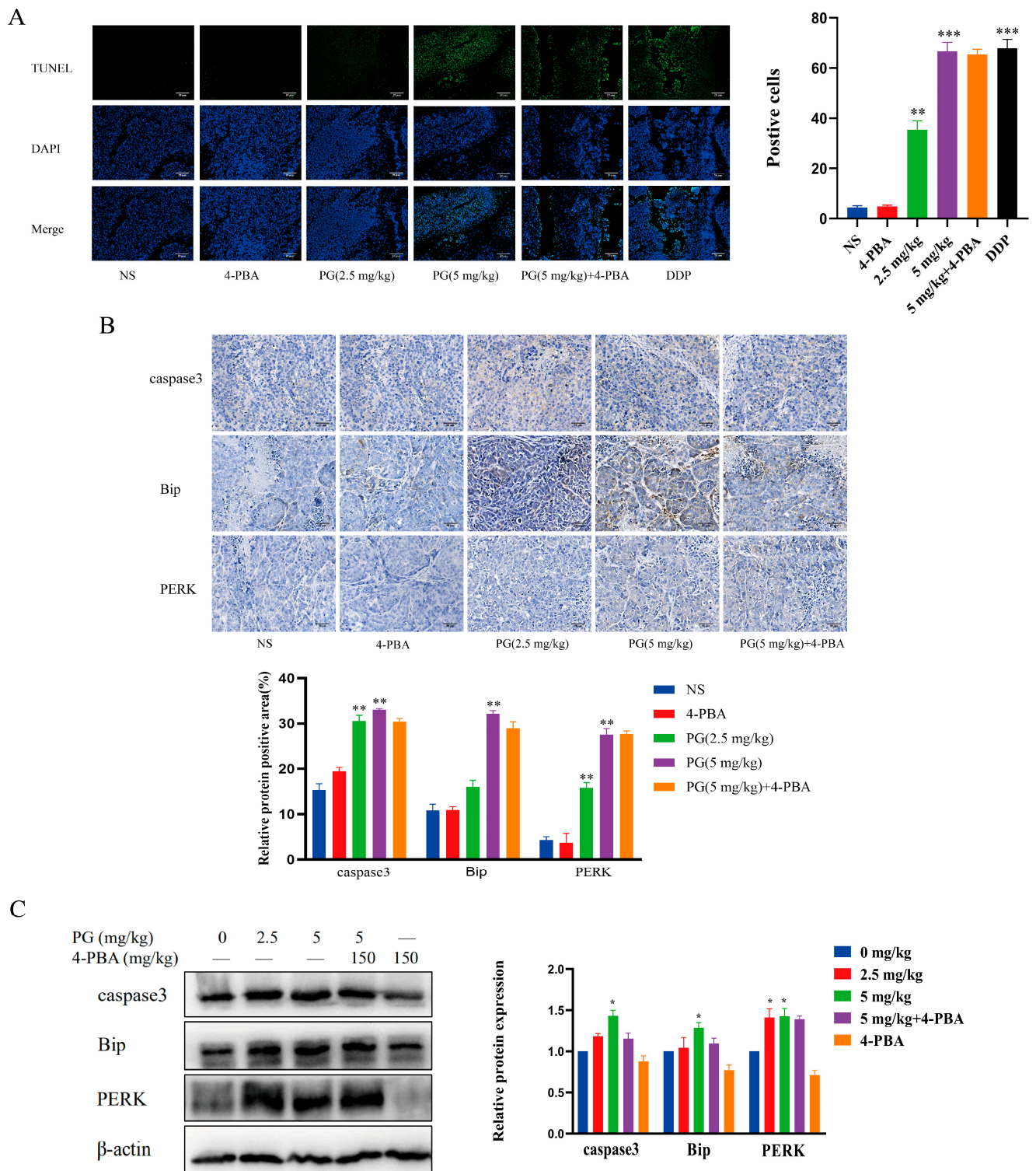


Figure 8. The effect of PG on the apoptosis in the tumor xenografts of HepG2 HCC model. (A). TUNEL assay for the apoptotic property of PG on HCC; (B). Immunohistochemical analysis for the effect of PG on the expression of caspase3, Bip and PERK in HCC tissue; (C). Western blot for the effect of PG on the expression of Bip, PERK, and caspase3 proteins in HCC tissues. PG (2.5 mg/kg), PG (5 mg/kg) vs. PG (0 mg/kg), * $p < 0.05$, ** $p < 0.01$, *** $p < 0.001$, $n = 3$; PG (5 mg/kg) vs. PG (5 mg/kg) + 4-PBA, $n = 3$.

3. Discussion

PG can promote the apoptosis of various tumor cells, such as lung, colon, oral, nasopharyngeal, breast, and liver cancer cells [13]. In recent years, the use of PG in combination with other cancer therapies has also been explored as a promising strategy for cancer treatment. It has been reported that PG inhibits autophagy to sensitize colorectal cancer cells to 5-fluorouracil, and the combination therapy significantly reduces the viability of cancer cells, partly through caspase-dependent apoptosis [14]. Furthermore, Shian-ren Lin [15] found that PG can induce autophagy, promote adriamycin influx and sensitize oral squamous carcinoma cells. A derivative of PG named obatoclax could promote the release of cytochrome C from the mitochondria of isolated leukemia cells. The combination of obatoclax and Ara C could synergistically induce apoptosis in leukemia cell lines and primary Acute Myelocytic Leukemia (AML) samples [16]. Several phase I and II clinical studies used a derivative of PG named obatoclax for cancer therapy on different patients [17–20]. Jelena's study showed that PG and its Br derivatives showed anticancer potential against all tumor cell lines and induced apoptosis, but their selectivity to healthy cell lines was low. The greater lipophilicity of Br derivatives of PG made them good targets for further structural optimization [12].

Additional evidence suggests that ERS-induced cellular dysfunction and cell death are primary contributors to many diseases [21], making modulation of the ERS pathway a potentially attractive therapeutic target. Moreover, this study further explored the mechanism of PG-mediated ERS-induced apoptosis of liver cancer cells and provided a theoretical basis for improving the anticancer effect of the drug.

In this study, the CCK-8 assay demonstrated that the IC₅₀ values of PG on HepG2 and BEL7402 cells at 48 h were different. The optimal drug concentration was selected according to the IC₅₀ value in subsequent experiments. The CCK-8 and cell colony formation assay results showed that PG could significantly inhibit the proliferation of HepG2 and Bel7402 cells, and HepG2 was more sensitive to PG than Bel7402 cells, which may be due to their different genetic backgrounds. Flow cytometry showed that PG blocked the cell cycle of HCC in the G₀/G₁ phase and induced apoptosis of HepG2 and Bel7402 cells in a dose-dependent manner. Another study showed that PG could reduce the expression of the anti-apoptotic protein survivin in liver cancer cells and activate caspase3, resulting in cell death [11]. However, its specific anti-hepatocellular carcinoma target and signal pathway are not clear.

In this study, we further observed the effect of PG on hepatocellular carcinoma cell apoptosis through ERS using the ERS inhibitor 4-PBA. TUNEL staining showed that the apoptosis of HCC cells decreased after 4-PBA pretreatment, and Western blot showed that the 4-PBA pretreatment reversed the expression change of the apoptotic proteins Bax, caspase3, caspase9, and anti-apoptotic protein Bcl-2. It has been reported that PG-induced apoptosis of tumor cells mainly occurs via the regulation of the mitochondrial apoptosis pathway. Cytochrome C released in the mitochondrial apoptosis pathway can activate caspase9 to shear apoptosis pathway caspase3, thus inducing apoptosis [22]. In melanoma cells, PG could bind to the BH3 domain and activate the mitochondrial apoptosis pathway by disrupting the McL-1/BAK complex, an anti-apoptotic member of the Bcl-2 family [23]. Our results suggest that PG induced the apoptosis of hepatocellular carcinoma cells by triggering ERS. Confocal laser fluorescence microscopy revealed that the action location of PG was co-located with calnexin in the endoplasmic reticulum of HepG2 cells. Further, flow cytometry detected an increase in Ca²⁺ concentration in hepatocellular carcinoma cells treated with PG. It has been reported [24] that acute release of Ca²⁺ in the endoplasmic reticulum can inhibit protein folding and trigger multiple signaling mechanisms to mediate mitochondrial apoptosis pathways. This study revealed that the endoplasmic reticulum was the active site of PG action in hepatocellular carcinoma cells, indicating that the mechanism of this substance is closely related to ER. Western blot analysis was then used to detect the expression of axon-related proteins in the unfolded protein signal branches PERK-eIF2 α -ATF4-CHOP and IRE1 α -XBP11-CHOP. The results showed that PG upreg-

ulated the expression of PERK, IRE1 α , Bip, and CHOP, but these expressions decreased significantly after 4-PBA pretreatment. The expression levels of the downstream transcription factors ATF4, CHOP, and XBP1 genes and the ER chaperone Bip gene of unfolded protein signal branch were also upregulated following PG exposure but downregulated by 4-PBA pretreatment. ERS-induced apoptosis occurs via the mitochondrial apoptotic pathway, which is regulated by the Bcl-2 protein family [25]. CHOP is one of the key pro-apoptotic factors of UPR, and its transcription is positively regulated by the PERK-ATF4 axis. Notably, CHOP can induce apoptosis by promoting the transcription of Bax and down-regulating the expression of Bcl-2 [26].

At present, most previous research on the antitumor activity of PG has been performed *in vitro*, with very few conducted *in vivo*. Our *in vivo* study demonstrated that PG has no obvious toxic effects on the main organs and related indicators of liver and kidney function in nude mice but inhibits tumor growth. These findings concur with Obayemi [27], who reported that PG does not cause toxic effects in mice. In our study, the expression of PERK and Bip proteins in the ERS pathway and the related apoptotic protein caspase3 increased with the drug concentration, but the expression levels of these proteins in the combined 4-PBA group decreased compared with the PG alone group. This finding of the *in vivo* experiments was consistent with the *in vitro* experiments, but the difference was not significant. Possibly, the difference in the effect of the drug between the *in vivo* and *in vitro* experiments was caused by variations in the absorption efficiency of the drug in animals. This study suggests that PG may exhibit anti-HCC activity by acting via ERS.

4. Materials and Methods

4.1. Cell lines and Laboratory Animals

HepG2 (HCC, ATCC HB-8065) and Bel7402 (HCC, SNL-148) were purchased from Guangdong Provincial Key Laboratory of Pharmaceutical Bioactive Substances. The cells were cultured at 37 °C in RPMI-1640 medium (Gibco) supplemented with 10% fetal bovine serum (Gemini) and a mixture of 1% penicillin and streptomycin (Hyclone) under 5% CO₂. A total of 36 4–6 weeks old SPF male BALB/C (nu/nu) nude mice weighing 16–20 g were purchased from Guangdong Medical Experimental Animal Center and were reared in an IVC system of the Animal Center of Guangdong Pharmaceutical University. The protocol for animal experiments was approved by the Guangdong Medical Experimental Animal Center (license number SCXK (Guangdong) 2018–0002). The animals were reared at 23–28 °C, at a relative humidity of 30–70%, and a light cycle of 12 h/d.

4.2. Antibodies and Reagents

Antibodies used in this study were anti PERK (Cell Signaling, D11A8), IRE1 α (Cell Signaling, 14C10), Bcl-2 (Cell Signaling, D55G8), Bip (Cell Signaling, C50B12), CHOP (Cell Signaling, L63F7), Bax (Cell Signaling, D2E11), caspase3 (Bioworld, BS6428), caspase9 (Bioworld, BS1731), β -Actin (Signaling, 8H10D10), Anti-GAPDH (Genomics, 5A12), and anti-Alexa Fluor 488 Labeled Goat Anti-Rabbit IgG (H+L) (Biyuntian, A0423). All these antibodies were purchased from Shanghai Biyuntian Biological Company. PG was isolated from *Serratia marcescens*, strain WA12-1-18, in the intestinal tract of cockroaches. The metabolite was extracted using 3.0 g/L of PBS from previously described [10]. Flou3-AM fluorescent probe, PVDF membrane, (2-(4-Amidinophenyl)-6-indolecarbamide dihydrochloride) DAPI, TUNEL apoptosis kit, and ECL kits were purchased from Shanghai Biyuntian Biological Company (Shanghai, China), whereas 4-PBA was purchased from Sigma Aldrich Company (St. Louis, MI, USA). A fluorescent quantitative PCR kit was purchased from Thermo Fisher Scientific (Waltham, MA, USA). Cell cycle and apoptosis kits were purchased from Beijing Sizhengbai Biotechnology Company (Beijing, China).

4.3. Cell Viability Assay

HepG2 and Bel7402 cells (5×10^3 cells/mL) in 100 μ L cell suspension were seeded into 96-well plates and incubated at 37 °C for 12 h under 5% CO₂. The cells were treated with

different PG concentrations (0.2, 0.4, 0.8, 1.6, 3.2, 6.4, 12.8 and 25.6 $\mu\text{g}/\text{mL}$) for 24, 48, and 72 h until the cell confluence reached about 80%. Each well was then washed twice with PBS. The absorbance at 450 nm was measured by Fully automatic enzyme labeling instrument (BioTek Instruments, Inc. USA) after adding CCK-8 (Biosharp) solution in the wells for a 1.5 h culture.

4.4. Colony Formation Assay

HepG2 and Bel7402 cells were seeded into 6-well plates (1000 cells/mL) and cultured at 37 °C for 24 h under 5% CO₂. The cells were treated with different PG concentrations (0.2, 0.4, 0.8, 1.6, and 3.2 $\mu\text{g}/\text{mL}$) for 1 h. The control group was treated with anhydrous ethanol. The culture was continued for 10 days after replacing the wells with a complete medium. Culturing was stopped when the confluence of the clone community cells in the control group grew above 80%, as observed under a microscope. After discarding the supernatant, the cells were fixed for 20 min using 1 mL of 4% paraformaldehyde. The cells were then stained using 1 mL of 0.1% crystal violet staining solution for 15 min at room temperature. The cells were photographed by digital camera (Nikon D3200, Tokyo, Japan), and the number of clonal colonies was counted. Number of clusters (Fold change to control) was calculated as: (Colony counts experiment group/Colony counts medium control group) \times 100%.

4.5. Cell Cycle and Apoptosis Assays Using Flow Cytometry

HepG2 and Bel7402 cells (100 μL ; 5×10^3 cells/mL) were added to 6-well plates and incubated at 37 °C for 12 h under 5%CO₂. When the cell confluence was about 80%, the cells were treated for 48 h with different PG concentrations (0.4, 0.8, 1.6, and 3.2 $\mu\text{g}/\text{mL}$). The control group was treated with anhydrous ethanol. The cells were then fixed with pre-cooled 70% ethanol at 4 °C overnight. The cells were stained using 400 μL of propidium iodide staining solution for 30 min at 37 °C before immediately detecting the cell cycle. For apoptosis rate detection, the cells were digested using trypsin without EDTA and suspended in Binding Buffer at a concentration of $1\text{--}5 \times 10^6/\text{mL}$. Thereafter, 100 μL of cell suspension was pipetted into a 5 mL flow tube. Annexin V-EGFP 5 μL was added to the flow tube and incubated in darkness for 5 min. The cells were then stained using 10 μL PI staining solution before adding 400 μL PBS. All sample flow detection was then performed immediately by flow cytometry (FACS Calibur; Becton, Dickinson and Company, Franklin Lakes, NJ, USA).

4.6. TUNEL Assay

When the cell confluence reached about 80%, the cells were pretreated with ERS-inhibitor 4-PBA (2 mm) for 2 h. The cells were then treated with different PG concentrations (0.4, 0.8, 1.6, and 3.2 $\mu\text{g}/\text{mL}$) for 48 h. The control group was treated with anhydrous ethanol. HepG2 and Bel7402 cells ($3 \times 10^4/\text{mL}$) were fixed with 4% paraformaldehyde, embedded in liquid paraffin, and stored in an oven at 62 °C for 1.5 h before gradient dewaxing. Thereafter, 50 μL of 20 $\mu\text{g}/\text{mL}$ of DNase-free protease K was added to the tissue for 20 min at 30 °C. TUNEL assay was performed following the manufacturer's instructions. The cell nuclei were then stained using DAPI and observed under a fluorescence microscope (OX31; Olympus, Tokyo, Japan) [28].

4.7. Immunoblot Analysis

For immunoblot assay, 20–30 μg of total cell extracts were separated in 10% or 12% SDS-PAGE and transferred onto the PVDF membranes. The membrane was then stained with primary antibodies against Bax, caspase3, caspase9, Bcl-2, PERK, IRE1 α , CHOP, and Bip at a 1:1000 dilution. After rinsing using PBS, the membrane we incubated with HRP-conjugated secondary antibodies goat anti-rabbit or anti-mouse was at a 1:2000 dilution. The proteins were detected using enhanced chemiluminescence.

4.8. The Localization of PG in Cells Using a Laser Confocal Fluorescence Microscopy

HepG2 cells (1.5×10^5 /mL) were seeded into laser confocal dishes and cultured with different PG concentrations (0.4, 0.8, and 1.6 $\mu\text{g}/\text{mL}$). After fixing with 4% paraformaldehyde for 20 min, the cells were incubated with 1% BSA for 30 min. The cells were then incubated overnight at 4 °C in calnexin diluted with 1% BSA and followed by Alexa Fluor 488-conjugated goat anti-rabbit secondary antibodies for 1 h. After DAPI staining for 5 min, the cells were washed three times with $1 \times \text{PBS}$, and added the fluorescence quenching agent. The intracellular calnexin protein was stained with green fluorescence. Since the PG itself had a spontaneous red fluorescence, the coincidence of the two can be used to determine co-localization. The cells were then observed and photographed using a laser confocal fluorescence microscope (FV3000; Olympus, Japan). Pearson's R value was calculated by using image J software (v1.8.0)

4.9. The measurement of Ca^{2+} Concentration in Cells Using Flow Cytometry

Briefly, 1 μM fluo-3 AM was added into HCC treated with different PG concentrations (0.4, 0.8, 1.6, and 3.2 $\mu\text{g}/\text{mL}$) for 50 min in the dark. The cells were then suspended in 300 μL PBS and then incubated for 15 min in the dark. The fluorescence intensity was detected using flow cytometry [29].

4.10. Real-Time PCR Analysis

HepG2 and Bel7402 cells (3×10^5 /mL) were pretreated with 4-PBA for 2 h, and thereafter with different PG concentrations (0.2, 0.4, 0.8, 1.6, 3.2 $\mu\text{g}/\text{mL}$). Anhydrous ethanol was used as the negative control. RNA was extracted from the cells and reverse-transcribed into cDNA. The primer sequences were as follows:

CHOP-forward primer: 5'-GGAGCATCAGTCCCCCACTT-3',
 CHOP-reverse primer: 5'-TGTGGGATTGAGGGTCACATC-3';
 ATF4-forward primer: 5'-GCTAAGGCGGGCTCCTCCGA-3',
 ATF4-reverse primer: 5'-ACCCAACAGGGCATCCAAGTCG-3';
 XBP1-forward primer: 5'-CCTGGTTGCTGAAGAGGAGG-3',
 XBP1-reverse primer: 5'-CCATGGGGAGATGTTCTGGAG-3';
 Bip-forward primer: 5'-TGACATTGAAGACTTCAAAGCT-3',
 Bip-reverse primer: 5'-CTGCTGTATCCTCTTACCAGT-3';
 GAPDH-forward primer: 5'-GGAGCGAGATCCCTCCAAAAT-3',
 GAPDH-reverse primer: 5'-GGCTGTTGTCATACTTCTCATGG-3'.

4.11. In Vivo Tumor Model

HepG2 cells (200 μL ; 2×10^7 /mL) were inoculated in the right lower axilla of 36 nude mice. The mice were then randomly divided into 6 groups: normal saline group (1% ethanol), PG2.5 (2.5 mg/kg), PG5.0 (5 mg/kg), PG5.0 (5 mg/kg) +4-PBA (150 mg/kg), 4-PBA (150 mg/kg) and cis-platinum (DDP) (2 mg/kg). DDP was a positive group. When the tumor volume reached 100 mm^3 , the mice were injected intraperitoneally with saline (1% ethanol), PG2.5 (2.5 mg/kg), PG5.0 (5 mg/kg), PG5.0 (5 mg/kg) +4-PBA (150 mg/kg), 4-PBA (150 mg/kg) and DDP (2 mg/kg), once every four days for 24 days. The tumor volume was calculated as follows; $\text{TV} (\text{mm}^3) = (\text{LW}^2)/2$, where TV is the tumor volume, L is the tumor length, and W is the shortest tumor diameter, measured on a vernier scale.

4.12. Assessment of Liver and Kidney Function

Blood was collected from the eyeballs of nude mice, and the serum was taken after centrifugation and sent to Jiangsu Enzymatic Immunity Industry Co., Ltd. (Yancheng, China) for testing. AST (blood volume: 15 μL), ALT (blood volume: 15 μL), ALP (blood volume: 15 μL), ALB (blood volume: 5 μL), TP (blood volume: 6 μL), CR (blood volume: 5 μL), UA (blood volume: 5 μL), and urea (blood volume: 3 μL) content in the serum was then measured by automatic biochemical analyzer (BK-280; BIOBASE, Jinan, China).

4.13. Hematoxylin–Eosin Staining

Tissue sections embedded in paraffin were heated in an oven at 62 °C for 1.5 h, dewaxed in water, and stained with hematoxylin for 5 min and eosin for 5 s. After dehydrating the tissue sections in serial alcohol concentrations, the tissue slices were sealed with neutral gum and photographed under a microscope (SQS-40P, Discover echo, San Diego CA, USA).

4.14. Statistical Analysis

Continuous normally distributed data were expressed as means of at least three independent experiments \pm SEM/SD. The data were analyzed using SPSS software, V 22.0. Differences between two groups were analyzed using Student's *t*-test and One-way ANOVA for comparison between multiple groups. GraphPad Prism 8 (GraphPad Software Inc.) was used for the creation. $p < 0.05$ was considered statistically significant.

5. Conclusions

In conclusion, this study explored the mechanism of anti-liver cancer action of PG in vitro and in vivo. The findings enrich the current literature on the antitumor mechanism of PG and provide laboratory evidence for its application in precision medicine and personalized therapy in HCC.

Author Contributions: Conceptualization, Y.M.; Data curation, H.L., L.Z. and Y.M.; Formal analysis, L.Z. and X.L.; Funding acquisition, J.W. (Jie Wang); Methodology, J.W. (Jingyi Wang) and W.L.; Project administration, H.L.; Software, L.Z.; Writing—original draft, J.W. (Jie Wang); Writing—review and editing, J.W. (Jie Wang) and Y.M. All authors have read and agreed to the published version of the manuscript.

Funding: This work was funded by Guangdong Natural Science Foundation (No.2020A1515011097); Medical Science and Technology Research Fund project of Guangdong Province (No.B2022326); Guangzhou Science and technology planning project (No.202201010357).

Institutional Review Board Statement: All animal experimental protocols were approved by the Ethics Committee of Guangdong Pharmaceutical University (Approval code: gdpulac2019136. Approval date:2019-06-03), and strictly followed the ARRIVE guidelines.

Informed Consent Statement: Not applicable.

Data Availability Statement: Not applicable.

Conflicts of Interest: The authors declare no conflict of interest.

Sample Availability: Not available.


References

1. Pascual, S.; Herrera, I.; Irurzun, J. New advances in hepatocellular carcinoma. *World J. Hepatol.* **2016**, *8*, 421–438. [CrossRef] [PubMed]
2. El-Serag, H.B. Hepatocellular carcinoma. *N. Engl. J. Med.* **2011**, *365*, 1118–1127. [CrossRef] [PubMed]
3. Huntzicker, E.G.; Hötzel, K.; Choy, L.; Che, L.; Ross, J.; Pau, G.; Sharma, N.; Siebel, C.W.; Chen, X.; French, D.M. Differential effects of targeting Notch receptors in a mouse model of liver. *Hepatology* **2015**, *61*, 942–952. [CrossRef] [PubMed]
4. Lehmann, W.; Mossmann, D.; Kleemann, J.; Mock, K.; Meisinger, C.; Brummer, T.; Herr, R.; Brabletz, S.; Stemmler, M.P.; Brabletz, T. ZEB1 turns into a transcriptional activator by interacting with YAP1 in aggressive cancer types. *Nat. Commun.* **2016**, *7*, 10498. [CrossRef] [PubMed]
5. Zhou, D.; Conrad, C.; Xia, F.; Park, J.S.; Payer, B.; Yin, Y.; Lauwers, G.Y.; Thasler, W.; Lee, J.T.; Avruch, J.; et al. Mst1 and Mst2 maintain hepatocyte quiescence and suppress hepatocellular. *Cancer Cell* **2009**, *16*, 425–438. [CrossRef] [PubMed]
6. Yadav, R.K.; Chae, S.W.; Kim, H.R.; Chae, H.J. Endoplasmic reticulum stress and cancer. *J. Cancer Prev.* **2014**, *19*, 75–88. [CrossRef]
7. Chevet, E.; Hetz, C.; Samali, A. Endoplasmic reticulum stress-activated cell reprogramming in oncogenesis. *Cancer Rev.* **2015**, *5*, 586–597. [CrossRef]
8. Rutkowski, D.T.; Hegde, R.S. Regulation of basal cellular physiology by the homeostatic unfolded protein response. *J. Cell Biol.* **2010**, *189*, 783–794. [CrossRef]

9. Hetz, C. The unfolded protein response: Controlling cell fate decisions under ER stress and beyond. *Nat. Rev. Mol. Cell. Biol.* **2012**, *13*, 89–102. [CrossRef]
10. Lin, P.B.; Shen, J.; Ou, P.Y.; Liu, L.Y.; Chen, Z.Y.; Chu, F.J.; Wang, J.; Jin, X.B. Prodigiosin isolated from *Serratia marcescens* in the *Periplaneta americana* gut and its apoptosis inducing activity in HeLa cells. *Oncol. Rep.* **2019**, *41*, 3377–3385. [CrossRef]
11. Yenkeje, R.A.; Sam, M.R.; Esmaeillou, M. Targeting survivin with prodigiosin isolated from cell wall of *Serratia marcescens* induces apoptosis in hepatocellular carcinoma cells. *Hum. Exp. Toxicol.* **2017**, *36*, 402–411. [CrossRef]
12. Lazic, J.; Skaro Bogojevic, S.; Vojnovic, S.; Aleksic, I.; Milivojevic, D.; Kretzschmar, M.; Gulder, T.; Petkovic, M.; Nikodinovic-Runic, J. Synthesis, Anticancer Potential and Comprehensive Toxicity Studies of Novel Brominated Derivatives of Bacterial Biopigment Prodigiosin from *Serratia marcescens* ATCC 27117. *Molecules* **2022**, *27*, 3729. [CrossRef]
13. Choi, S.Y.; Lim, S.; Yoon, K.H.; Lee, J.I.; Mitchell, R.J.; Orcid, I.D. Biotechnological, Activities and Applications of Bacterial Pigments Violacein and Prodigiosin. *J. Biol. Eng.* **2021**, *15*, 10. [CrossRef] [PubMed]
14. Zhao, C.; Qiu, S.; He, J.; Peng, Y.; Xu, H.; Feng, Z.; Huang, H.; Du, Y.; Zhou, Y.; Nie, Y. Prodigiosin impairs autophagosome-lysosome fusion that sensitizes colorectal cancer cells to 5-fluorouracil-induced cell death. *Cancer Lett.* **2020**, *481*, 15–23. [CrossRef] [PubMed]
15. Lin, S.R.; Orcid, I.D.; Weng, C.F. PG-priming Enhances doxorubicin influx to trigger necrotic and autophagic cell death in oral squamous cell carcinoma. *J. Clin. Med.* **2018**, *7*, 375. [CrossRef] [PubMed]
16. Konopleva, M.; Watt, J.; Contractor, R.; Tsao, T.; Harris, D.; Estrov, Z.; Bornmann, W.; Kantarjian, H.; Viallet, J.; Samudio, I.; et al. Mechanisms of Antileukemic Activity of the Novel Bcl-2 Homology Domain-3 Mimetic GX15-070 (Obatoclax). *Cancer Res.* **2008**, *68*, 3413–3420. [CrossRef]
17. Schimmer, A.D.; Raza, A.; Carter, T.H.; Claxton, D.; Erba, H.; DeAngelo, D.J.; Tallman, M.S.; Goard, C.; Borthakur, G. A multicenter phase I/II study of obatoclax mesylate administered as a 3- or 24-hour infusion in older patients with previously untreated acute myeloid leukemia. *PLoS ONE* **2014**, *9*, e108694. [CrossRef]
18. Langer, C.J.; Albert, I.; Ross, H.J.; Kovacs, P.; Blakely, L.J.; Pajkos, G.; Somfay, A.; Zatloukal, P.; Kazarnowicz, A.; Moezi, M.M.; et al. Randomized phase II study of carboplatin and etoposide with or without obatoclax mesylate in extensive-stage small cell lung cancer. *Lung Cancer* **2014**, *85*, 420–428. [CrossRef]
19. Oki, Y.; Copeland, A.; Hagemester, F.; Fayad, L.E.; Fanale, M.; Romaguera, J.; Younes, A. Experience with obatoclax mesylate (GX15-070), a small molecule pan-Bcl-2 family antagonist in patients with relapsed or refractory classical Hodgkin lymphoma. *Blood* **2012**, *119*, 2171–2172. [CrossRef]
20. Arellano, M.L.; Borthakur, G.; Berger, M.; Luer, J.; Raza, A. A Phase II, Multicenter, Open-Label Study of Obatoclax Mesylate in Patients with Previously Untreated Myelodysplastic Syndromes With Anemia or Thrombocytopenia. *Clin. Lymphoma Myeloma Leuk.* **2014**, *14*, 534–539. [CrossRef]
21. Chow, C.Y.; Wang, X.; Riccardi, D.; Wolfner, M.F.; Clark, A.G. The genetic architecture of the genome-wide transcriptional response to ER stress in the mouse. *PLoS Genet.* **2015**, *11*, e1004924. [CrossRef] [PubMed]
22. Hasenjäger, A.; Gillissen, B.; Müller, A.; Normand, G.; Hemmati, P.G.; Schuler, M.; Dörken, B.; Daniel, P.T. Smac induces cytochrome c release and apoptosis independently from Bax/Bcl-xL in a strictly caspase-3-dependent manner in human carcinoma cells. *Oncogene* **2004**, *23*, 4523–4535. [CrossRef] [PubMed]
23. Hosseini, A.; Espona-Fiedler, M.; Soto-Cerrato, V.; Quesada, R.; Pérez-Tomás, R.; Guallar, V. Molecular interactions of prodiginines with the BH3 domain of anti-apoptotic Bcl-2 family members. *PLoS ONE* **2013**, *8*, e5756. [CrossRef] [PubMed]
24. Rizzuto, R.; Pinton, P.; Carrington, W.; Fay, F.S.; Fogarty, K.E.; Lifshitz, L.M.; Tuft, R.A.; Pozzan, T. Close contacts with the endoplasmic reticulum as determinants of mitochondrial Ca²⁺ responses. *Science* **1998**, *280*, 1763–1766. [CrossRef] [PubMed]
25. Tait, S.W.; Green, D.R. Mitochondria and cell death: Outer membrane permeabilization and beyond. *Nature Cell. Biol.* **2010**, *11*, 621–632. [CrossRef] [PubMed]
26. Tabas, I.; Ron, D. Integrating the mechanisms of apoptosis induced by endoplasmic reticulum stress. *Nature Cell. Biol.* **2011**, *13*, 184–190. [CrossRef]
27. Obayemi, J.D.; Salifu, A.A.; Eluu, S.C.; Uzonwanne, V.O.; Jusu, S.M.; Nwazojie, C.C.; Onyekanne, C.E.; Ojelabi, O.; Payne, L.; Moore, C.M.; et al. LHRH-Conjugated Drugs as Targeted Therapeutic Agents for the Specific Targeting and Localized Treatment of Triple Negative Breast Cancer. *Sci. Rep.* **2020**, *10*, 8212. [CrossRef]
28. Guo, W.; Wang, Y.; Wang, Z.; Wang, Y.P.; Zheng, H. Inhibiting autophagy increases epirubicin's cytotoxicity in breast cancer cells. *Cancer Sci.* **2016**, *11*, 1610–1621. [CrossRef] [PubMed]
29. Wang, J.; Ming, H.; Chen, R.; Ju, J.M.; Peng, W.D.; Zhang, G.X.; Liu, C.F. CIH-induced neurocognitive impairments are associated with hippocampal Ca(2+) overload, apoptosis, and dephosphorylation of ERK1/2 and CREB that are mediated by overactivation of NMDARs. *Brain Res.* **2015**, *1625*, 64–72. [CrossRef] [PubMed]

Article

Novel Pectic Polysaccharides Isolated from Immature Honey Pomelo Fruit with High Immunomodulatory Activity

Tao Hou ^{1,†}, Shenglan Guo ^{2,†}, Zhuokun Liu ¹, Hongyu Lin ¹, Yu Song ¹, Qiqi Li ³, Xin Mao ³, Wencan Wang ³ , Yong Cao ^{1,*} and Guo Liu ^{1,*}

¹ Guangdong Provincial Key Laboratory of Nutraceuticals and Functional Foods, College of Food Sciences, South China Agricultural University, Guangzhou 510642, China

² Guangzhou Shuke Industrial Co., Ltd., Guangzhou 510642, China

³ Chongqing Sweet Pet Products Co., Ltd., Chongqing 402160, China

* Correspondence: caoyong2181@scau.edu.cn (Y.C.); liuguo@scau.edu.cn (G.L.);

Tel./Fax: +86-020-8586234 (Y.C. & G.L.)

† These authors contributed equally to this work.

Abstract: A novel pectic polysaccharide (HPP-1) with high immunomodulatory activity was extracted and isolated from the immature honey pomelo fruit (*Citrus grandis*). Characterization of its chemical structure indicated that HPP-1 had a molecular weight of 59,024 D. In addition, HPP-1 was primarily composed of rhamnose, arabinose, fucose, mannose, and galactose at a molar ratio of 1.00:11.12:2.26:0.56:6.40. Fourier-transform infrared spectroscopy, periodic acid oxidation, and Smith degradation results showed that HPP-1 had α - and β -glycosidic linkages and 1 \rightarrow 2, 1 \rightarrow 4, 1 \rightarrow 6, and 1 \rightarrow 3 glycosidic bonds. ¹³C NMR and ¹H NMR analyses revealed that the main glycosides included 1,4-D-GalA, 1,6- β -D-Gal, 1,6- β -D-Man, 1,3- α -L-Ara, and 1,2- α -L-Rha. Immunomodulatory bioactivity analysis using a macrophage RAW264.7 model in vitro revealed that NO, TNF- α , and IL-6 secretions were all considerably increased by HPP-1. Moreover, RT-PCR results showed that HPP-1-induced iNOS, TNF- α , and IL-6 expression was significantly increased in macrophages. HPP-1-mediated activation in macrophages was due to the stimulation of the NF- κ B and MAPK signaling pathways based on western blot analyses. HPP-1 extracted from immature honey pomelo fruit has potential applications as an immunomodulatory supplement.

Keywords: immature honey pomelo fruit; pectic polysaccharides; structural characterization; immunomodulatory activity and mechanism



Citation: Hou, T.; Guo, S.; Liu, Z.; Lin, H.; Song, Y.; Li, Q.; Mao, X.; Wang, W.; Cao, Y.; Liu, G. Novel Pectic Polysaccharides Isolated from Immature Honey Pomelo Fruit with High Immunomodulatory Activity. *Molecules* **2022**, *27*, 8573. <https://doi.org/10.3390/molecules27238573>

Academic Editor: Tao Liu

Received: 1 November 2022

Accepted: 23 November 2022

Published: 5 December 2022

Publisher's Note: MDPI stays neutral with regard to jurisdictional claims in published maps and institutional affiliations.



Copyright: © 2022 by the authors. Licensee MDPI, Basel, Switzerland. This article is an open access article distributed under the terms and conditions of the Creative Commons Attribution (CC BY) license (<https://creativecommons.org/licenses/by/4.0/>).

1. Introduction

Immature honey pomelo (*Citrus grandis*) fruit (IPF) is a by-product of pomelo cultivation, which is in the middle of its growth cycle in April. A small proportion of IPF is used in traditional Chinese medicine, but the majority of IPF is discarded, which contributes to environmental pollution [1]. However, our previous research suggests that IPF is rich in bioactive substances such as essential oils, naringin, and pectin, which have considerable medicinal and commercial value. Essential oils and naringin have good antioxidant activity [2], yet research on the bioactive substances of IPF remains limited. Pectin, a polysaccharide straight-chain compound, is an abundant and multifunctional component of terrestrial plant cell walls. It has a high functional value (gelling, thickening, emulsification, and stabilization) and is widely used as a food and drug gelling agent [3,4]. Citrus pectin has strong biological activities, such as immunomodulatory [5,6], antioxidant [7], anti-inflammatory [8], anti-cancer [9], heavy metal adsorption [10], drug transport [11], and other properties [12]. Despite numerous studies on pectin, information on its structure and immune activity in IPF is limited.

Polysaccharides have been widely reported to stimulate macrophages, enhance their phagocytic function, and release various cytokines such as interleukins (IL-1 β , IL-6, IL-8)

and tumor necrosis factor (TNF- α), as well as nitric oxide and reactive oxygen species (ROS), thereby supporting the body's immunity [13–16]. Some plant polysaccharides increase the secretion of nitric oxide (NO) and the synthesis of cytokines, which in turn increase macrophage action against pathogenic microorganisms and tumorigenesis [6]. NO is considered to be the primary effector molecule produced by macrophages. When macrophages are stimulated and activated, they secrete a series of chemokines and cytokines. This plays an important role in activating the immune response and immunomodulation of the body [17]. TNF- α is a cytokine capable of killing tumors to cause hemorrhagic necrosis and has clear antitumor activity. Moreover, TNF- α is produced mainly from activated macrophages and is a very important cytokine in the antitumor immune response, and is a common and important indicator of macrophage activity [18]. IL-6 is a type of pleiotropic cytokine and it is involved in the body's immune defense, as well as in promoting the growth and differentiation of primary bone marrow-derived cells [19]. Polysaccharides may bind to specific membrane receptors in macrophages and activate immune response transduction pathways via various signals. Based on previous studies, activator protein 1 (AP-1) and MAPK activity in the macrophage RAW264.7 were stimulated by polysaccharides from *Platycodon grandiflorus* (PG). Moreover, further research revealed that PG activates three subsets of MAPKs (ERK1/2, SAPK/JNK, and p38 MAPK) through increasing the DNA-binding activity of AP-1 [20,21]. However, the exact molecular mechanism through which IPF pectin activates macrophages remains unclear.

In this study, a crude IPF pectin was obtained from the IPF residue after the extraction of essential oil and naringin. Honey pomelo pectic polysaccharides (HPP-1) were systematically purified using anion exchange and gel permeation chromatography. The structure characterization of HPP-1 was investigated systematically by UV spectroscopy, chromatography, mass spectrometry, nuclear magnetic resonance (NMR), and other analytical techniques, whereas the immune activity and pattern recognition receptors of HPP-1 was evaluated using a mouse macrophage RAW 264.7 immune model *in vitro*. We analyzed the effect of HPP-1 on the pinocytic and phagocytic capacity, production of TNF- α , NO, and IL-6, and relevant mRNA expression. Furthermore, western blots were used to reveal the mechanism of HPP-1 immunoreactivity. In addition, the possible signaling pathways involved in HPP-1 activating macrophages were discussed, and these should all help further clarify the structure-effective relationship of HPP-1. The results provide valuable information for the application of IPF extracts in immunomodulatory activity.

2. Results and Discussion

2.1. Extraction and Purification of Pectic Polysaccharides from IPF

Crude IPF pectin was obtained from the residue after essential separation with a yield of $20.23\% \pm 0.66\%$ (*w/w*). Crude pectin was composed of 71.17% total sugar (59.90% galacturonic acid), 1.93% protein, and 4.33% ash. The degree of esterification was 44.65%, indicating that the compound was a low-ester pectin. Based on previous reports, pectin with esterification below 10% has anti-cancer properties, whereas high-ester pectin has anti-inflammatory properties [8].

When the extracted pectin was purified, two independent peaks were revealed: HPP-a (eluted by 0.3 M NaCl) and HPP-b (eluted by 0.3 M NaOH, Figure 1A). When HPP-a was further purified, a single peak of HPP-1 was observed, which contained a galacturonic acid reaction, but without protein (Figure 1B). Furthermore, a >98%-pure HPP-1 fraction was obtained.

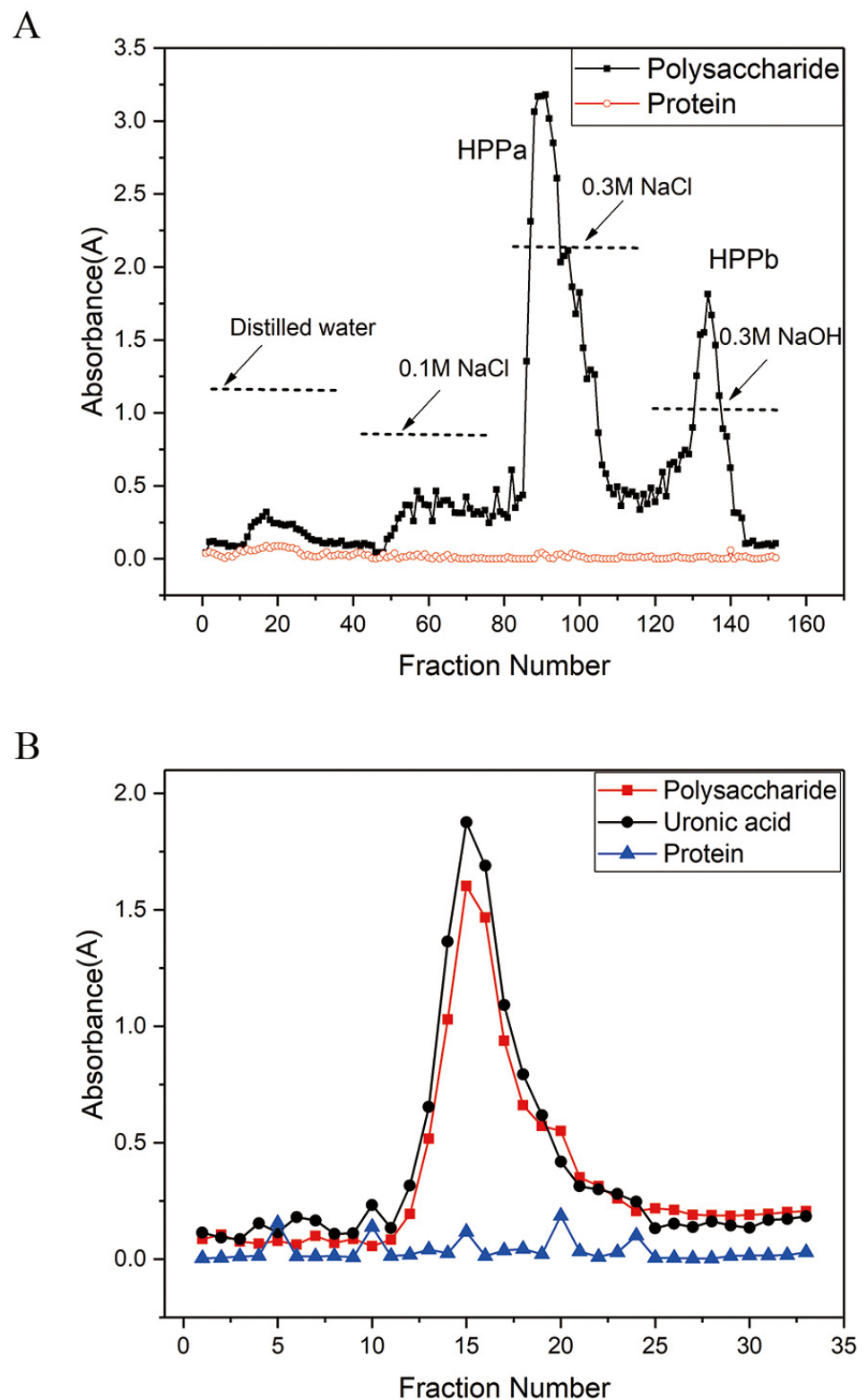


Figure 1. Chromatography of HPP-1 from honey pomelo pectin (HPP) by (A) DEAE-52 cellulose and (B) Superdex-G200.

2.2. Analysis of the HPP-1 Structure

2.2.1. UV Scan and Molecular Mass Detection

The UV spectral scan of HPP-1 revealed no evident characteristic absorption peaks of amino acids or proteins (i.e., near 260 and 280 nm; Figure 2A). However, these spectra were

consistent with the characteristic absorption spectral peaks of polysaccharides [22]. These results indicate that the separated HPP-1 fraction did not contain protein, suggesting that the protein in crude HPP could be completely removed during purification.

The structure of HPP-1 was further analyzed by GPC. The GPC results showed that HPP-1 had a single symmetric peak with a molecular mass of 59,024 Da (Figure 2B), indicating that HPP-1 has a small molecular mass. In general, the average molecular mass of pectin is between 50,000 and 150,000 Da [23]. It was hypothesized that pectin is a concentrated pectin fragment molecule, which requires further experimental confirmation.

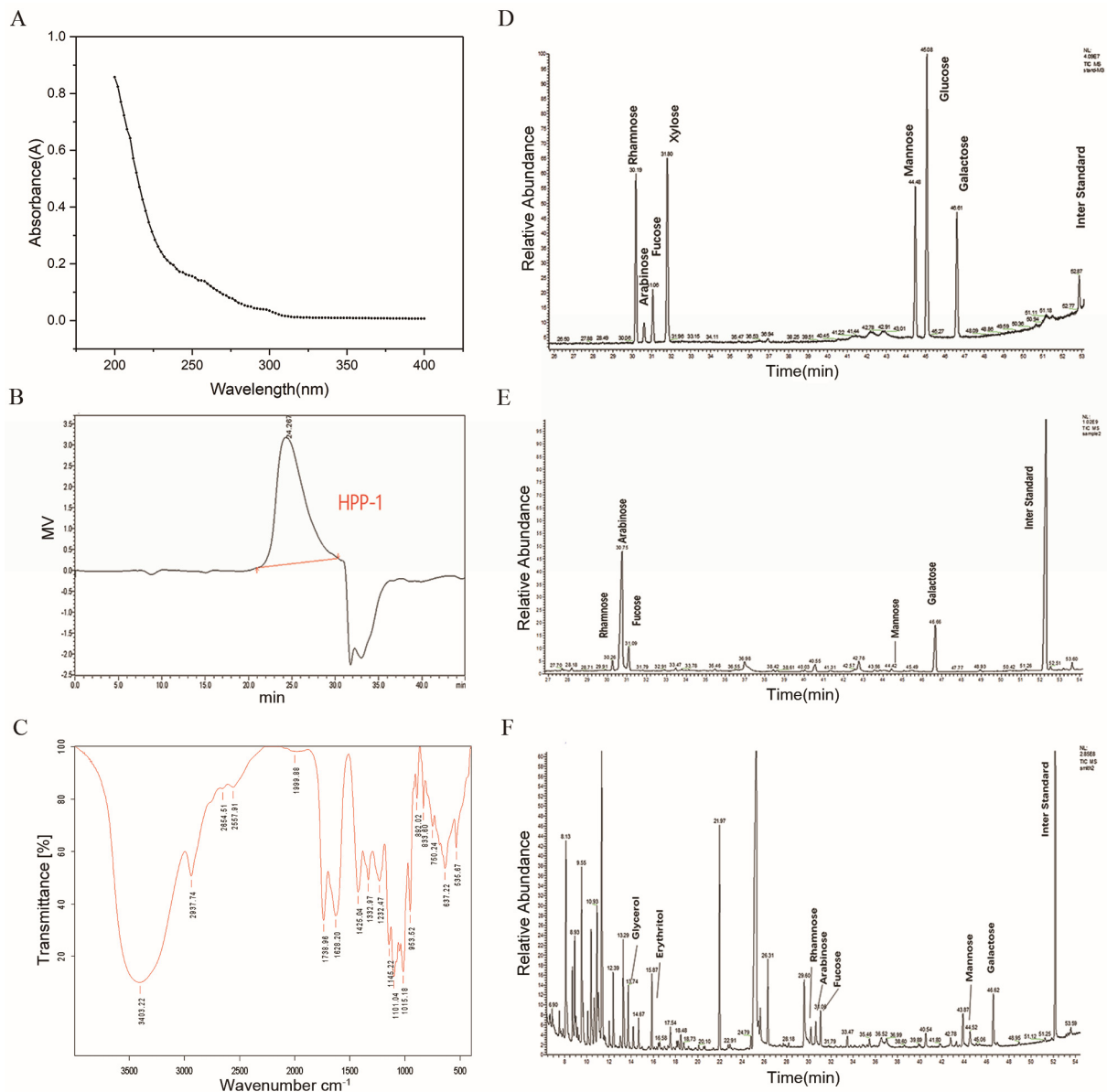
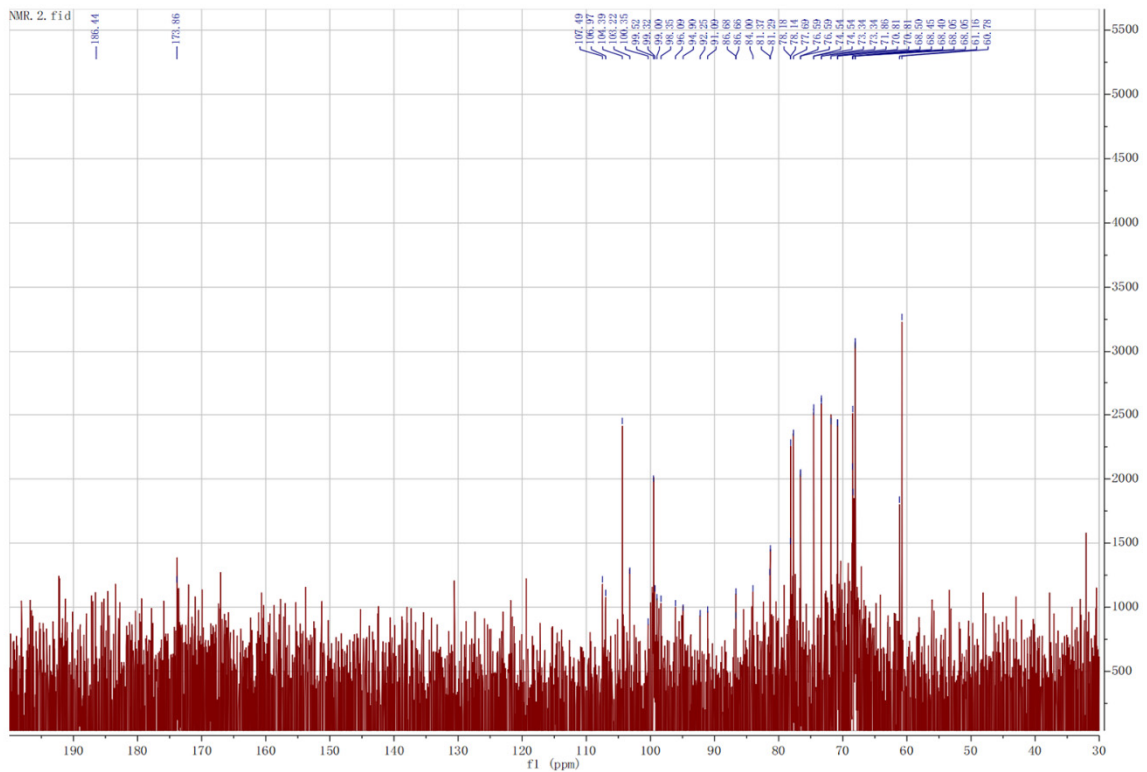


Figure 2. Cont.

G



H

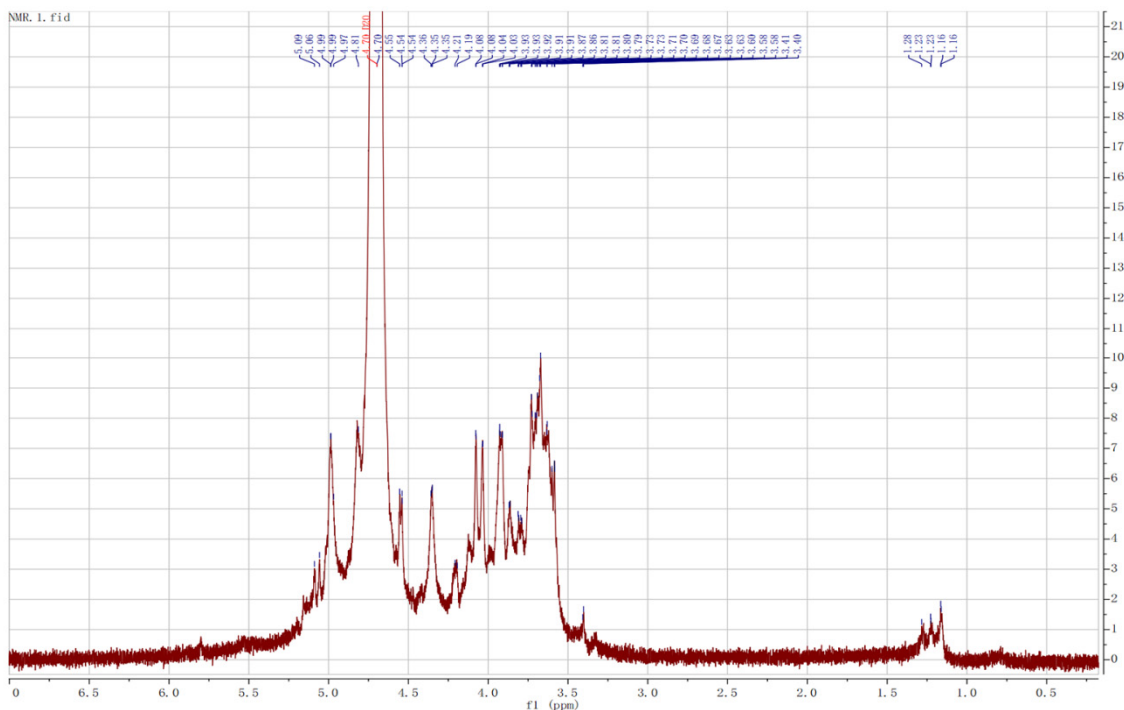


Figure 2. Chromatography results of HPP-1 obtained from (A) UV spectrum, (B) HPGPC, (C) FT-IR spectrum, gas chromatography-mass spectrometry (GC-MS) of (D) standard monosaccharide, and (E) monosaccharide composition of HPP-1. (F) GC of HPP-1 after Smith degradation. HPP-1 (G) ^{13}C NMR spectrum and (H) ^1H NMR spectrum.

2.2.2. FT-IR Spectrum

The FTIR spectrum of HPP-1 is shown in Figure 2C. Absorption peaks were observed at 3403.22 cm^{-1} , and the weak peaks at 2937.74 and 145.22 cm^{-1} correspond to characteristic absorption peaks of polysaccharides, which are associated with O-H, C-H, and C-O-C glycosidic stretching vibrations [24]. These results indicated that HPP-1 is a polysaccharide. Furthermore, absorption peaks at 1738.96 and 1628.20 cm^{-1} indicated the C=O stretching vibration of methylated carboxyl groups and free carboxyl groups on the HPP-1 sugar chain, respectively, and the absorption peak at 1015.18 cm^{-1} corresponded to pyranose structures [25]. The absorption peak at 1738.96 cm^{-1} likely represents the stretching vibration of uronic acid, whereas the peaks at 892.02 and 833.60 cm^{-1} represent β -D-mannitose and glycoside bonds in the alpha configuration, respectively [25]. Therefore, HPP-1 contains α -configurational and β -configurational glycosidic bonds.

2.2.3. Monosaccharide Composition Assay

The GC-MS results for the monosaccharide standard and HPP-1 are shown in Figures 2D and 2E, respectively.

By comparing the elution time of HPP-1 with that of monosaccharide standard, HPP-1 was composed of rhamnose (Rha), arabinose (Ara), fucose (Fuc), mannose (Man), and galactose (Gal), with a molar ratio of 1.00:11.12:2.26:0.56:6.40. The presence of mannose and fucose indicates the presence of an RG II region in HPP-1. Arabinose and galactose were the main components of HPP-1, and the arabinose and galactose contents were higher than those of rhamnose. This finding indicated that the RG I regional fragment existed simultaneously, and arabinose, galactose, and Arabian galactose were the main components of the RG I fragment branch chain [26].

2.2.4. Periodate Oxidation-Smith Degradation Analysis

Periodate oxidation revealed that 0.1150 mmol of periodate was consumed by HPP-1 and 0.0306 mmol of methane acid was produced, indicating the presence of (1 \rightarrow 6)-linked glucoside residues (Figure 2F). The consumption of sodium periodate was higher than that of formic acid, indicating additional (1 \rightarrow 2) and (1 \rightarrow 4) glycoside bond types [27].

Glycerol, erythritol, rhamnose, arabinose, fucose, mannose, and galactose were observed after HPP-1 underwent Smith degradation (Figure 2F). The formation of glycerol indicates (1 \rightarrow 2)-or (1 \rightarrow 6)-linked glycosidic bonds, whereas erythritol indicates (1 \rightarrow 4)-linked glycosidic bonds. In addition, the formation of rhamnose, arabinose, galactose, mannose, and galactose indicates the presence of (1 \rightarrow 3)-linked glycosidic bonds [18].

2.2.5. NMR Analysis

The ^{13}C NMR and ^1H NMR spectra of HPP-1 are shown in Figures 2G and 2H, respectively. The resonance signals between δ 95.0 and 110.0 in ^{13}C NMR belong to the anomeric carbon atoms of monosaccharides [24,28]. Five anomeric carbon atoms (99.51, 103.22, 104.39, 107.47, and 173.21 ppm) were detected in HPP-1. In ^1H NMR, the protons between δ 3.5 and 5.5 indicates anomeric hydrogen [18]. The chemical shift of α -configurational and β -configurational sugars was greater than 4.90 and less than 4.90 ppm, respectively, indicating the presence of α and β -configurations. This finding is consistent with the FTIR results. A small peak at δ 173.21 ppm indicated uronic acid, which was the main chain of the pectin structure, indicating the existence of 1,4-D-GalA [29]. The signals at δ 68.742 and δ 67.98 ppm, combined with infrared spectrum and monosaccharide composition, indicate the presence of 1,4- β -D-Gal and 1,6- β -D-Man [18]. The peaks at δ 107.47 and δ 82.36 ppm are characteristic of furanose (arabinose). Peaks at 16.73 and 16.49 ppm indicate hydrogen on rhamnose C6. Combined with previous reports [18,24,27,30], monosaccharide composition, and Smith degradation results, we identified 1,3- α -L-Ara and 1,2- α -L-Rha glycosylates in HPP-1.

1,4-D-GalA, 1,4-D-GalA-(1,2- α -Rha), 1,2- α -Rha, 1,2,4- α -Rha, 1,4- β -D-Gal, t- β -D-Gal, and α -L-Ara sugar residues were detected in pumpkin acid polysaccharides, which had

a pectic polysaccharide RG I structure similar to that of HPP-1 [29]. The structure of pectic polysaccharides has a structure–activity relationship with their immunomodulatory activity [6].

2.3. Immunomodulatory Activities of HPP-1 on RAW264.7 Cells

2.3.1. Effect of HPP-1 on RAW264.7 Cell Viability

After being treated with HPP-1 (10, 50, 100, 200, 400, 600, 800, and 1000 $\mu\text{g}/\text{mL}$) for 24 h [31], the results indicated that RAW 264.7 cells showed no toxicity at concentrations below 1000 $\mu\text{g}/\text{mL}$ of HPP-1 (Figure 3A). At concentrations of 600–1000 $\mu\text{g}/\text{mL}$, HPP-1 significantly improved cell viability and promoted macrophage proliferation.

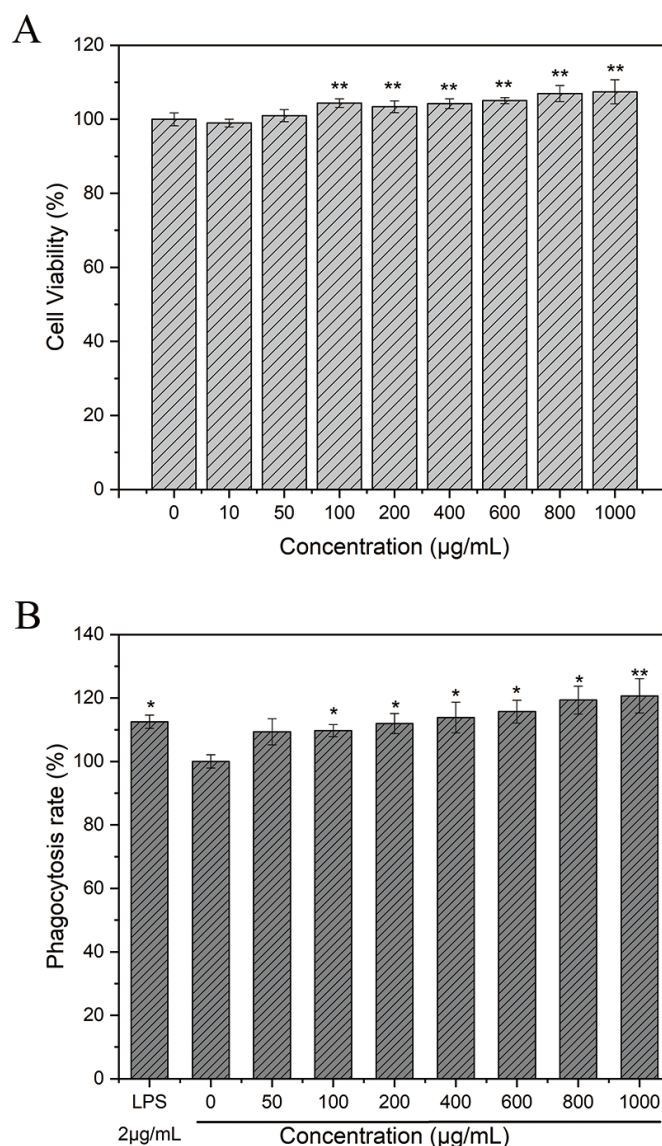


Figure 3. (A) Effect of HPP-1 on the viability of RAW 264.7 cells. (B) Effect of HPP-1 on the uptake of neutral red by RAW 264.7 cells. Significant differences with control cells were designated as * $p < 0.05$ or ** $p < 0.01$.

2.3.2. Effect of HPP-1 on the Phagocytic Capacities of RAW264.7 Cells

Neutral red is an effective acid–base indicator of living cells that can react with lysosomes to produce red substances [25]. The amount of neutral red entering the cell varies depending on the state of the living cell and can be used to assess the ability of macrophages to produce pinocytes.

After treatment with HPP-1, the intensity of neutral red cell absorption increased compared with that in the control group (Figure 3B). The phagocytic rate of cells at 200–1000 $\mu\text{g}/\text{mL}$ was significantly higher than that of the control group ($p < 0.05$). This result indicated that HPP-1 enhanced the phagocytic capacity of neutral red in murine macrophages. This finding is in accordance with previous findings, that is, polysaccharides from purple sweet potato and *Chrysanthemum indicum* stem polysaccharides could promote phagocytosis of neutral red by macrophages [32,33]. Acidic polysaccharides derived from *Cucurbita moschata* Duch, *Persimmon Leaves*, and *Helicteres Angustifolia* L. are pectic polysaccharides containing D-galacturonic acid, as previously reported. Furthermore, the improvements in macrophage phagocytic capacity were identified [34–36].

2.3.3. Effects of HPP-1 on Macrophage NO, TNF- α , and IL-6 Production

HPP-1 fractions stimulated NO and IL-6 secretion from macrophages at concentrations ranging from 1 to 1000 $\mu\text{g}/\text{mL}$ in a dose-dependent manner (Figure 4A–C). At increasing concentrations of HPP-1, TNF- α secretion showed an upward and then a downward trend. TNF- α is not only an important cytokine in immune regulation but is also a key cytokine involved in inflammation [37], cellular homeostasis, tumor progression, and insulin resistance in individuals with obesity and diabetes [38,39]. At 50 $\mu\text{g}/\text{mL}$ of HPP-1, the NO secretion level reached $27.06 \pm 1.60 \mu\text{M}$, which was significantly higher than that of the blank control ($p < 0.01$) and reached the NO secretion effect of $27.68 \pm 1.55 \mu\text{M}$ of the LPS-positive treatment group (2 $\mu\text{g}/\text{mL}$, Figure 4A). As HPP-1 concentrations increased, NO secretion significantly increased. When the concentration of HPP-1 reached 400 $\mu\text{g}/\text{mL}$, NO secretion in the experimental group was higher than that in the LPS-positive control group ($p < 0.01$). This finding is in accordance with those of previous studies [27,36].

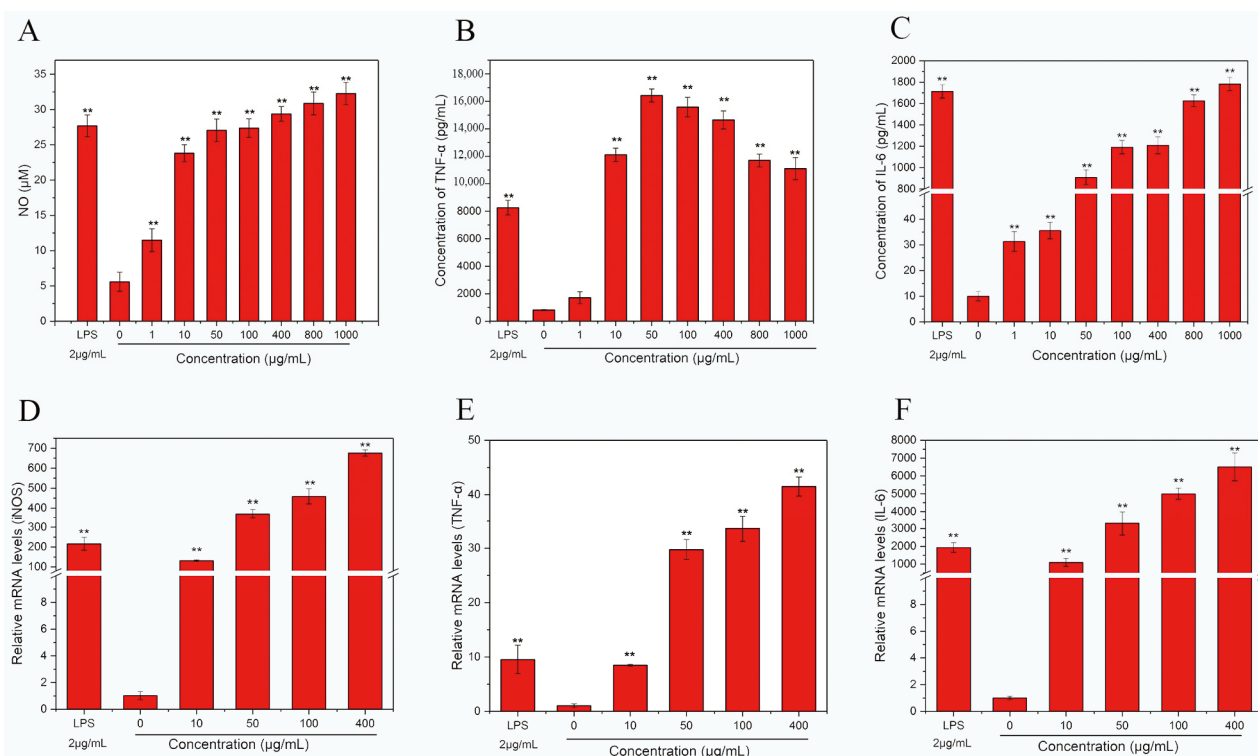


Figure 4. Effects of HPP-1 on cytokine secretion of (A) NO, (B) TNF- α , and (C) IL-6, mRNA levels of (D) iNOS, (E) TNF- α , and (F) IL-6. The group without HPP-1 was used as the negative control, and LPS (2 $\mu\text{g}/\text{mL}$) was used as the positive control. Significant differences with control cells were designated as ** $p < 0.01$.

Compared with the control group, increasing concentrations of HPP-1 from 1 to 1000 $\mu\text{g}/\text{mL}$ significantly promoted TNF- α secretion by macrophages (Figure 4B). TNF- α

secretion exceeded that of the positive and blank control groups at HPP-1 concentrations of 100–1000 $\mu\text{g}/\text{mL}$ ($p < 0.01$). The results showed that 50 $\mu\text{g}/\text{mL}$ HPP-1 stimulated the greatest secretion of $\text{TNF-}\alpha$ in macrophages, which was substantially higher than the amount stimulated by the same concentration of the purified fraction of fungal monkey head mushroom polysaccharide [24]. When the concentration was greater than 50 $\mu\text{g}/\text{mL}$, $\text{TNF-}\alpha$ secretion slowed but remained higher than that of the LPS-stimulated blank control group.

HPP-1 also increased macrophage IL-6 secretion at concentrations ranging from 1 to 1000 $\mu\text{g}/\text{mL}$ (Figure 4C). At concentrations of 1–10 $\mu\text{g}/\text{mL}$, the secretion of IL-6 was 30–40 times that of the blank control ($p < 0.01$). IL-6 secretion reached 1782.17 ± 63.12 pg/mL at HPP-1 concentrations of 1000 $\mu\text{g}/\text{mL}$, exceeding that of the positive control group (1713.09 ± 62.90 pg/mL).

2.3.4. Effects of HPP-1 on iNOS, $\text{TNF-}\alpha$, and IL-6 mRNA Levels in Macrophages

Expression of immune-related cytokines is associated with activation and immunomodulatory effects of macrophages [40].

HPP-1 increased the expression levels of iNOS, $\text{TNF-}\alpha$, and IL-6 in macrophages at concentrations of 10–400 $\mu\text{g}/\text{mL}$ in a dose-dependent manner (Figure 4D–F). At 50 $\mu\text{g}/\text{mL}$, the expression of iNOS, $\text{TNF-}\alpha$, and IL-6 was 370, 29 and 3300 times higher than that of the control group, respectively ($p < 0.01$), indicating that the HPP-1 fraction was more effective in upregulating the expression levels of iNOS, $\text{TNF-}\alpha$, and IL-6. When the stimulation concentration reached 400 $\mu\text{g}/\text{mL}$, the expression levels of iNOS, $\text{TNF-}\alpha$, and IL-6 were only 3–4 times higher than those in the LPS-positive group. High mRNA expression can induce the secretion of corresponding immune factors, thereby improving the immune capacity [41]. In addition, $\text{TNF-}\alpha$ expression was not positively correlated with $\text{TNF-}\alpha$ secretion concentration, probably because transcription is only the first step of $\text{TNF-}\alpha$ formation and is affected by post-transcriptional regulation [42,43]. Pectic polysaccharides from other plants have the same effects on macrophages. Gavlighi [44] used enzymatic extraction and purification of pectin polysaccharides from pomegranate peel. The fraction with the best immune effect significantly upregulated the expression levels of *iNOS*, *IL-1 β* , *TNF- α* , *IL-6*, and *IL-10* in a concentration-dependent manner. Moreover, western blotting showed that the immune effect fraction could affect the expression of cytokine levels and exert immunomodulatory effects related to the $\text{NF-}\kappa\text{B}$ and MAPK signaling pathways. The immunomodulatory molecular mechanism of HPP-1 must be further elucidated by studying signaling pathways.

2.4. Effect of HPP-1 on $\text{NF-}\kappa\text{B}$ and MAPKs Signaling Pathways in Murine Macrophages

Based on previous literature, several intracellular signal transduction routes have been shown to activate macrophages. $\text{NF-}\kappa\text{B}$ is an important gene expression regulator [45]. Macrophages usually remain in the cytoplasm because of their non-covalent binding to the $\text{NF-}\kappa\text{B}$ - $\text{I}\kappa\text{B}$ trimer. Upon activation of $\text{NF-}\kappa\text{B}$ signaling, $\text{I}\kappa\text{B}\alpha$ serine residues are phosphorylated, which causes $\text{NF-}\kappa\text{B}$ to separate from $\text{I}\kappa\text{B}\alpha$ and move to the nucleus as an activated transcription factor [46]. The binding sites of the p50–p65 dimer were revealed after $\text{I}\kappa\text{B}$ dissociation, allowing them to connect to the κB motif. The $\text{NF-}\kappa\text{B}$ p65 subunit then moves from the cytoplasm to the nucleus, inducing the transcription of a range of genes, including iNOS, ROS, and macrophage-related cytokines [47]. We used these samples to activate RAW 264.7 macrophage cells via western blot analysis to determine whether the $\text{NF-}\kappa\text{B}$ ($\text{NF-}\kappa\text{B}/\text{I}\kappa\text{B}\alpha$) signaling pathway was implicated in HPP-1 (10–400 $\mu\text{g}/\text{mL}$) or LPS (2 $\mu\text{g}/\text{mL}$). $\text{NF-}\kappa\text{B}$ and $\text{I}\kappa\text{B}\alpha$ protein levels increased in a dose-dependent manner with an increase in HPP-1 ($p < 0.01$), exhibiting significantly higher expression levels than those in the negative control group (Figure 5A,B; lane 2). Moreover, when the dose of HPP-1 reached 50 $\mu\text{g}/\text{mL}$, both protein expression levels were higher than those in the positive control group (Figure 5A,B; lane 1).

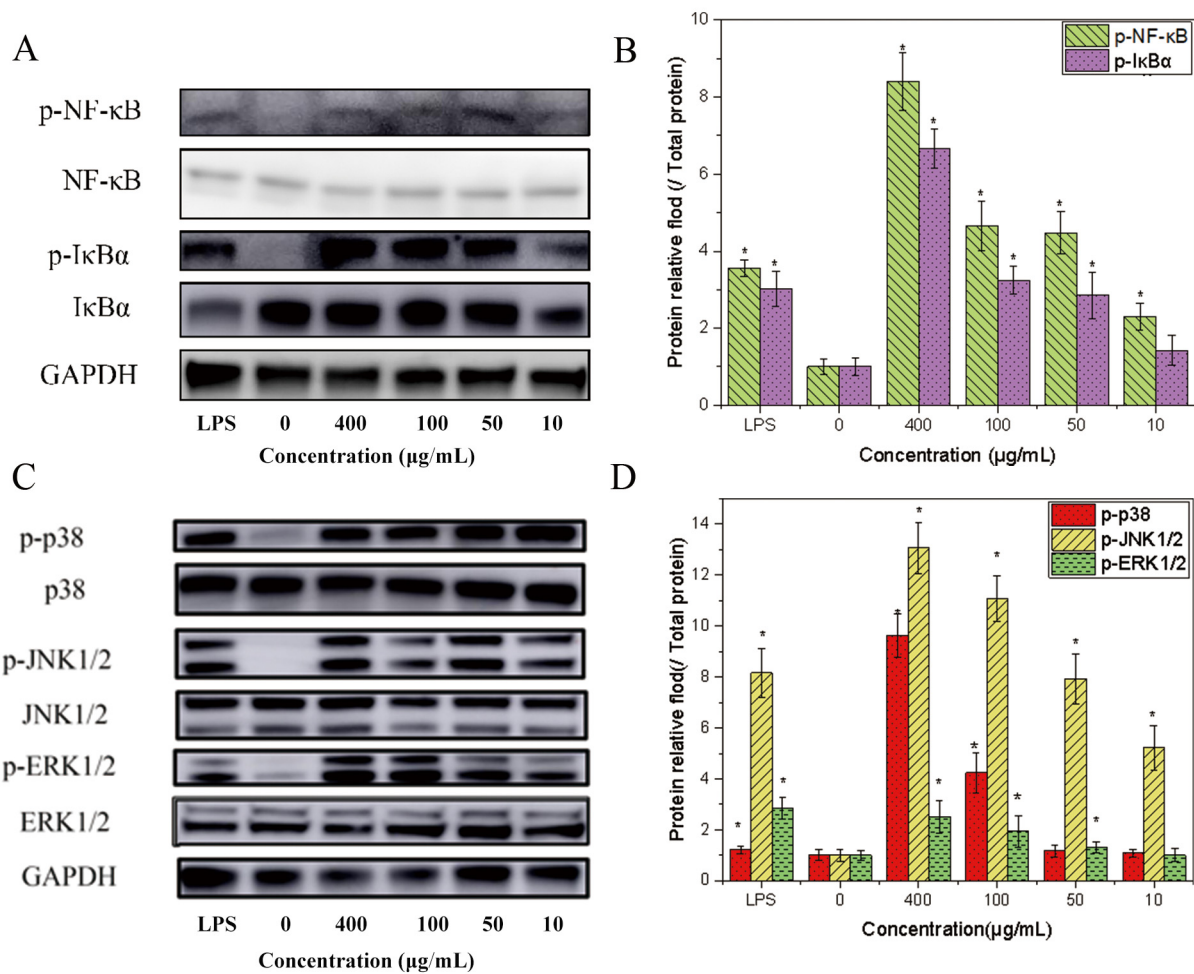


Figure 5. Effects of HPP-1 treatment on NF-κB and MAPK signaling pathways. (A) Representative Western blotting bands and (B) quantitative analysis of NF-κB/IκBα protein levels (values were normalized to the GAPDH level). (C) Representative Western blotting bands and (D) quantitative analysis of p-p38/p38, p-JNK1/2/pJNK, and p-ERK1/2/ERK1/2 protein levels. The group without HPP-1 was used as the negative control, and LPS (2 μg/mL) was used as the positive control. Significant differences with control cells were designated as * $p < 0.05$.

MAPKs are a group of serine/threonine-specific protein kinases that play a role in the activation of NF-κB and in cellular responses to diverse extracellular stimuli [48]. The MAPK family is divided into three subgroups: ERK1/2, p38, and JNK1/2 [48]. NF-κB is activated by several intracellular signaling pathways, including the MAPK pathway [48]. We evaluated the effect of HPP-1 on the MAPK signaling pathway by western blotting. The addition of HPP-1 (100–400 μg/mL, 50–400 μg/mL, and 10–400 μg/mL) significantly increased the phosphorylation levels of p38, ERK1/2, and JNK1/2 compared to those in the control group ($p < 0.01$, Figure 5C,D). However, for p38 and ERK1/2, no difference in phosphorylation levels was observed at low doses (10–50 μg/mL) of HPP-1, indicating that HPP-1 could stimulate the phosphorylation of JNK1/2 at relatively low concentrations. Furthermore, 100 μg/mL of HPP-1 increased the phosphorylation levels of p38 and JNK1/2 compared to the LPS control group, which showed stronger immune activation than related polysaccharides [14,44].

Collectively, these results indicate that HPP-1-mediated activation of macrophages is achieved by activation of the NF-κB and MAPK signaling pathways.

2.5. Pattern Recognition Receptors and Potential Molecular Mechanisms of HPP-1-Induced Macrophage Immunomodulation Activity

Plant polysaccharides interact with a variety of pattern recognition receptors on the surfaces of immune cells [38]. Pattern recognition receptors on macrophages can identify polysaccharides that activate macrophages to participate in immune regulation [49]. These receptors include complement receptor type 3 (CR3), Toll-like receptor (TLRs), β -glucan receptor (GR), mannose receptor (MR), and scavenger receptor (SR). When macrophage membrane receptors attach to glycosyl ligands on polysaccharides, a series of signaling cascades are activated [49]. NF- κ B, PI3K/Akt, MAPKs, and MyD88/IRAK-1/TRAF-6 appear to be important signaling pathways in the regulation of macrophage cell immunity [50]. Thus, we used these antibodies to evaluate whether the immunomodulatory effects involved the participation of TLR2, CR3, TLR4, MR, GR, and SR of HPP-1. Compared to the group treated only with HPP-1, NO, IL-6, and TNF- α , levels were significantly decreased following anti-GR therapy ($p < 0.01$, Figure 6A–C). However, no reduction in NO, TNF- α , and IL-6 levels was observed in the groups treated with anti-CR3, anti-TLR4, anti-TLR2, anti-MR, or anti-SR. This result indicates that macrophage GR is a receptor of HPP-1, causing transcriptional factors to be activated and cytokines to be expressed in the presence of HPP-1. In addition, HPP-1 may contain structural fragments similar to β -glucan and initiate the same effects as β -glucan, which is widely used as a natural bioactive modulator in tumor immunotherapy [51]. However, this finding warrants further investigation.

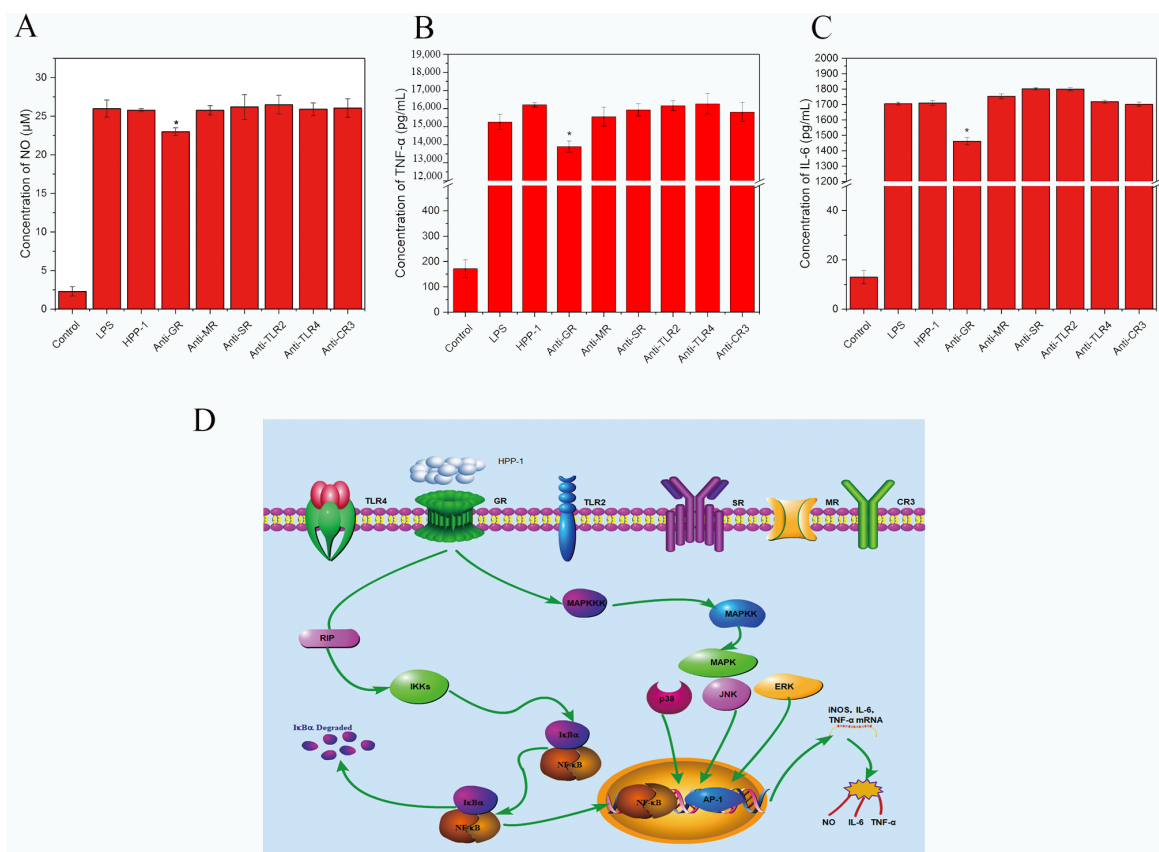


Figure 6. Effects of GR, MR, SR, TLR2, TLR4, and CR3 on the secretion of NO (A), TNF- α (B), and IL-6 (C) in RAW 264.7 cells. The group without HPP-1 was used as the negative control, and LPS (2 μ g/mL) was used as the positive control. Potential signal transduction pathways involved in macrophage activation by HPP-1 (D). Significant differences with control cells were designated as * $p < 0.05$.

The β -glucan receptor (GR) consists of the scavenger receptor (SR) [51], complement receptor type 3 (CR3) [52], lactosylceramide (Lac Cer) [53], and dendritic cell-associated C-type lectin-1 (Dectin-1) [54]. Moreover, Dectin-1 is a major β -glucan receptor in macrophages [55]. Dectin-1 pathways can activate numerous effects of polysaccharides on immunomodulation, anti-tumor processes, and anti-radiation functions [56].

Under stimulation by HPP-1, RAW 264.7, cells were likely turned on by MAPK/NF- κ B signaling pathways via GR to activate transcription factors such as mRNA encoding iNOS, TNF- α , and IL-6, which are responsible for increasing NO, TNF- α , and IL-6 secretion (Figure 6D).

3. Methods and Materials

3.1. Materials and Chemicals

Dried IPF was obtained from Li Pomelo Guangdong Agricultural Science and Technology Co., Ltd. (Meizhou, Guangdong, China) and was stored at room temperature.

The murine macrophage cell line (RAW 264.7) was purchased from Kunming Cell Bank of the Chinese Academy of Sciences Culture Collection. DEAE-52 cellulose and Sephadex G-200 were obtained from GE Healthcare Life Science (Piscataway, NJ, USA). Monosaccharide standards (glucuronic acid, rhamnose, arabinose, fucose, xylose, mannose, glucose, galactose, and inositol) and LPS were obtained from Sigma-Aldrich Company (St. Louis, MO, USA). Dulbecco's modified eagle's medium (DMEM), fetal bovine serum (FBS), phosphate buffer saline (PBS, pH 7.4), penicillin, and streptomycin were purchased from Gibco Life Technologies (Grand Island, NY, USA). Antibodies (anti-mannose receptor (anti-MR), anti-scavenger receptor I (anti-SR), anti-toll-like receptor 2 (anti-TLR2), anti-toll-like receptor 4 (anti-TLR4), anti-beta glucan receptor (anti-GR), anti-complement receptor 3 (anti-CR3), nuclear factor- κ -gene binding (NF- κ B), phospho-NF- κ B (p-NF- κ B), inhibitor of NF- κ B (I κ B α), phospho-I κ B α (p-I κ B α), extracellular regulated protein kinase (ERK1/2), phospho-ERK1/2 (p-ERK1/2), c-Jun N-terminal kinase (JNK1/2), phospho-JNK (p-JNK1/2), p38, phospho-p38 (p-p38), glyceraldehyde-3-phosphate dehydrogenase (GAPDH)) were obtained from Abcam, Inc. (Cambridge, MA, USA). Chemiluminescence (ECL) kit and NO-detecting kit were purchased from Beyotime Biotechnology Co., (Shanghai, China). Mouse IL-6 enzyme-linked immunosorbent assay (ELISA) kit and mouse TNF- α ELISA kit were obtained from Neobioscience Technology Co., Ltd. (Shenzhen, China). Standards of dextrans, uronic acid, phycite, glycerol, glycol reference, neutral red, 3-(4,5-dimethylthiazol-2-yl)-2,5-diphenyltetrazolium bromide (MTT) and Trizol were purchased from Macklin Biochemical Co., Ltd. (Shanghai, China). RNA Easy Fast Cell Kit, First Stand cDNA Synthesis Kit and FastStart Universal SYBR Green Master (ROX) were acquired from TIANGEN Biotech Co., Ltd. (Beijing, China).

3.2. Extraction of HPP

Approximately 1 kg of dried IPF fruit was ground into a 40 mesh powder and pre-treated to extract essential oils and naringin using a novel continuous phase-transition extraction device [57], based on our previously reported methodology [2]. The resulting IPF residue was subjected to acid extraction and alcohol precipitation to extract pectin [58]. In brief, deionized water was adjusted to pH 1.5 using 0.5 M HCl. The IPF residue and 0.3–0.4% sodium hexametaphosphate were added to deionized water (pH 1.5) at a 1:20 solid-to-liquid ratio. This mixture was extracted at 90 °C for 90 min and centrifuged (9000 rpm) at 4 °C for 20 min. The resulting filtrate was concentrated to half its original volume at 55 °C under reduced pressure. This solution was then passed through an electro dialysis device (HMTECH-1220, Hangzhou, China) to remove salt.

The demineralized solution was mixed two times the volume of 95% ethanol and kept at 4 °C for 4 h, after which the alcohol precipitate was collected and washed three times with 95% ethanol. Finally, the precipitate was freeze-dried to obtain crude pectin (HPP).

3.3. Purification of Crude Pectin

HPP was purified using anion DEAE-52 exchange column chromatography based on previous methods [21], with the following modifications. HPP (500 mg) was loaded onto a DEAE-52 cellulose ion exchange column (2.6 × 50 cm) after being dissolved in 40 mL of deionized water. The DEAE-52 column was eluted with deionized water, 0.1 M NaCl, 0.3 M NaCl, and 0.3 M NaOH solution. The flow rate was set at 1 mL/min. The resulting eluate (5 mL/tube) was collected, and the total sugar and galacturonic acid contents were tested. Samples containing sugar and galacturonic acid were collected in a bag for dialysis (10 kDa) and dialyzed for 48 h at 4 °C in deionized water. Sugar and galacturonic acid contents were determined using previously described methods [59]. Two subfractions of HPP-1 (HPP-a and HPP-b) were obtained and freeze-dried. HPP-a, the most abundant component, was further studied.

In 5 mL of deionized water, 50 mg of HPP-a was dissolved before being placed on a Sephadex G-200 column (2.6 × 60 cm) at a 0.5 mL/min flow of deionized water.

3.4. Analysis of the HPP-1 Chemical Structure

3.4.1. Ultraviolet Full Wavelength Scan

HPP-1 was dissolved in deionized water to a 0.1 mg/mL sample solution, and the protein content was measured using a UV3010 ultraviolet–visible spectrophotometer with continuous scanning at 200–400 nm based on previous methods [60].

3.4.2. HPGPC Molecular Mass Detection

The molecular mass of HPP-1 was quantified using high-performance gel permeation chromatography (HPGPC) as previously described [28]. HPP-1 and dextran standards 5–670 kDa were mixed with deionized water to obtain a 2.0 mg/mL solution. A chromatographic column (TSK G-5000 connection G-3000 PWXL gel column) with a mobile phase of 0.02 M KH₂PO₄ solution was used. The column temperature and flow rate were set to 35 °C and 0.6 mL/min, respectively. The injection volume was 10 µL.

3.4.3. Fourier Transform Infrared Spectroscopy (FT-IR) Analysis

The FT-IR spectrum of HPP-1 was obtained using a Nexus Fourier transform infrared spectrometer (Nicolet Nexus, Thermo Nicolet Company, Wilmington, DE, USA). Dry HPP-1 (1.0 mg) was mixed with 100 mg dried potassium bromide powder using an agate mortar. After grinding to a uniform consistency, the sample was pressed into thin slices using a tablet press and scanned from 4000 to 500 cm⁻¹.

3.4.4. Monosaccharide Composition

Pectic polysaccharides are composed of monosaccharides as structural units that are connected by glycosidic bonds. The glycosidic linkages were disrupted, and the derivatives were identified using high-temperature acid hydrolysis. The types of monosaccharide residues, their relative content, and their connection modes in pectic polysaccharides have been analyzed [30]. The composition of neutral sugars in HPP-1 was determined using gas chromatography–mass spectrometry [61]. In brief, 5.0 mg of the HPP-1 powder was added to 5.0 mL of 4 M trifluoroacetic acid and hydrolyzed in a sealed enclosure at 110 °C for 3 h. After hydrolysis, methanol (3.0 mL) was added, and the solution was concentrated under reduced pressure for 4–5 iterations. The HPP-1-concentrated solution was mixed with 10 mg of hydroxylamine hydrochloride and 1.0 mL of pyridine, and the resulting solution was heated at 90 °C for 30 min. Acetic anhydride (0.5 mL) was added to the mixture and the reaction was continued for an additional 30 min at 90 °C. The sample was then run through a chromatographic column (Agilent-technologies DB-5MS; 0.2 mm × 30 m × 0.25 µm, 110–160 °C at 2 °C/min, 160–220 °C at 1.5 °C/min, and then 220–260 °C at 5 °C/min, and kept at 250 °C for 5 min) equipped with a mass detector (MS) with a flow rate of 1.0 mL/min and an injection volume of 1 µL.

3.4.5. Periodic Acid Oxidation and Smith Degradation Analysis

The position of the glycosidic linkages in HPP-1 was investigated using the periodate oxidation-Smith degradation method. Periodate can selectively oxidize and break the 1,2-diol group of sugar to produce the corresponding polyformic acid. Different monosaccharide connections produce different products [62]. Smith degradation is a process in which the oxidation products of periodate are reverted to stable polyhydroxyl compounds, hydrolyzed, and derived, and the hydrolyzed products were identified.

The type and content of glycosidic bond were determined from HPP-1 using previously published methods [63]. In brief, 10.0 mg HPP-1 was dissolved in 10 mL of 30 mM sodium periodate solution. After the sample had fully reacted for 10 h, 2 mL of the resulting oxidation solution and 0.1 mL of ethylene glycol were mixed for 10 min. This solution was then titrated with a 0.005 M NaOH solution.

The remaining oxidation solution was added to 5 mL ethylene glycol and stirred for 30 min to terminate the periodate oxidation reaction. This mixture was placed in a dialysis bag (3 kDa), dialyzed with deionized water for 48 h, and then concentrated to 10 mL by rotary evaporation. NaBH₄ (35 mg) was added, and the sample solution was neutralized with 50% acetic acid to obtain a pH of 5.0. Next, the solution was dialyzed with deionized water for 48 h, and the composition was determined after hydrolysis and derivatization of the alcohol product using the aforementioned GC-MS.

3.4.6. NMR Analysis

Twenty milligrams of HPP-1 were dissolved in 1.0 mL of D₂O and placed in a nuclear magnetic tube. ¹H-NMR and ¹³C-NMR analyses were conducted using a Bruker AM-600 nuclear magnetic resonance instrument.

3.5. Immunomodulatory Activity of HPP-1

3.5.1. Cytotoxicity Test

The MTT assay was used to investigate the effect of HPP-1 components on the survival rate of macrophages [64]. In brief, 5×10^3 cells/mL of macrophages were inoculated in a 96-well cell plate and placed in a 37 °C and 5% CO₂ incubator for 24 h. After discarding the supernatant, cells were incubated for another 24 h. Then, 100 µL each of 0.5 mg/mL thiazole blue MTT solution and DMSO solution was added, and the absorbance (OD) was measured at 570 nm using a microplate ELISA reader (BioTek, Winooski, VT, USA).

3.5.2. Phagocytic Ability

The phagocytic activity of HPP-1 in RAW264.7 cells was investigated using a neutral red assay [65]. Briefly, 100 µL of 5×10^4 cells/mL macrophages were added to a 96-well cell culture plate. After culturing in a 5% CO₂ incubator at 37 °C for 24 h, the supernatant was discarded and 100 µL of 0.1% neutral red solution were added to each well. After incubation for 1 h at 37 °C, a new supernatant was discarded, and the cells were washed with PBS. Next, 100 µL of the cell lysate acetic acid-absolute ethanol (1:1, v/v) was added. After 2 h of incubation, the absorbance at 540 nm was measured using a microplate ELISA reader to estimate the phagocytic rate.

3.5.3. Effect of HPP-1 Components on the Secretion of NO, TNF-α, and IL-6

The Griess method was used to determine the amount of NO produced by the samples [66]. An ELISA reader was used to detect the absorbance of each well at a wavelength of 540 nm. The ELISA kit was used to detect immune factors secreted by RAW264.7 cells according to the manufacturer's instructions. Absorbance was measured at 450 nm using a microplate reader, and standard curves were used to calculate cytokine concentrations [67].

3.6. Immunomodulatory Mechanism of HPP-1

3.6.1. Effect of HPP-1 Components on the Expression of iNOS, TNF- α , and IL-6 mRNA

RT-PCR was used to assess the effects of HPP-1 components on the secretion of macrophage RAW264.7 immune factors at the RNA level [67]. The cells were lysed, and RNA was collected according to the manufacturer RNA total extract kit instructions. Five microliters of the resulting RNA were electrophoresed on a 1% agarose gel. Nanodrops were used to quantify RNA concentration and purity. Next, 3 μ g of complete total macrophage RNA was used for reverse transcription into cDNA.

SYBR Green prestaining was used for quantification [66]. The corresponding reagents were added to a PCR 8-tube to form a 20 μ L reaction system according to the manufacturer's instructions. Using GAPDH as the internal reference gene, the $2^{-\Delta\Delta C_t}$ method was used to analyze the expression of the target gene. Gene primer sequences for GAPDH, iNOS, IL-6, and TNF- α were obtained from the NCBI GenBank database (Table 1).

Table 1. Primers for qRT-PCR.

Primers		Sequences (5'—3')
GAPDH	Forward	AGGTCGGTGTGAACGGATTG
	Reverse	GGGGTCGTTGATGGCAACA
TNF- α	Forward	CAGGCGGTGCCTATGTCTC
	Reverse	CGATCACCCCGAAGTTCAGTAG
IL-6	Forward	CTGCAAGAGACTTCCATCCAG
	Reverse	AGTGGTATAGACAGGTCTGTGG
iNOS	Forward	GTTCTCAGCCCAACAATAACAAGA
	Reverse	GTGGACGGGTCGATGTCAC

3.6.2. Western Bolt Analysis

Western blot analyses were performed to quantify total protein and phosphorylated protein kinases [68]. A chemiluminescence (ECL) kit was used to perform densitometry of each protein.

3.6.3. Receptor of HPP-1 on RAW264.7 Cells Involving in Immunomodulation

RAW 264.7 cells (1×10^5 cells/mL) were loaded onto a 96-well plate to determine the mechanism by which HPP-1 modulates immunomodulatory function. After 24 h of incubation, the cells were pre-treated for 1 h with 5 g/mL of anti-MR, anti-GR, anti-SR, anti-CR3, anti-TLR4, and anti-TLR2 antibodies before being stimulated with 400 g/mL of HPP-1. The control group was treated with HPP-1 (400 μ g/mL) alone, and the positive group was treated with lipopolysaccharide LPS (2 μ g/mL). The negative control group consisted of serum-free culture medium. After culturing for 1 h, cell supernatants were collected, and NO and TNF- α levels were quantified as previously described [62] to determine the involved receptor.

3.7. Statistical Analysis

All experiments were repeated three times, and the results are presented as mean \pm SD. Data were analyzed using IBM SPSS 19.0 program (SPS Inc., Chicago, IL, USA). Differences among groups were assessed using one-way ANOVA. Results were considered significant at a p -value < 0.05 .

4. Conclusions

In this study, a novel pectic polysaccharide (HPP-1) with a molecular weight of 59,024 Da was identified. Mannose, rhamnose, galactose, arabinose, and fucose were the primary monosaccharide components of HPP-1. The presence of 1,4-D-Gal, 1,6-D-Man, 1,3-L-Ara, and 1,2-L-Rha connections was also confirmed. In vitro bioactivity experiments revealed that HPP-1 has significant immunomodulatory activity, which might be mediated via phagocytic promotion and might increase NO, IL-6, and TNF production. The

immunomodulatory effect of HPP-1 is primarily mediated through the NF- κ B and MAPK signaling pathways via the GR receptor. Therefore, HPP-1 has potential applications in immunological illness treatment and as a functional food.

Author Contributions: Conceptualization, T.H. and Y.C.; methodology, S.G. and T.H.; software, T.H.; validation, Z.L., S.G. and T.H.; formal analysis, H.L. and T.H.; investigation, S.G. and T.H.; resources, Y.S. and G.L.; data curation, S.G. and T.H.; writing—original draft preparation, S.G. and T.H.; writing—review and editing, G.L. and T.H.; visualization, Q.L. and T.H.; supervision, X.M. and T.H.; project administration, W.W. and T.H.; funding acquisition, Y.C. All authors have read and agreed to the published version of the manuscript.

Funding: This work was financially supported by the Guangdong Provincial Key Laboratory of Nutraceuticals and Functional Foods (2018B030322010) and Program for Guangdong Introducing Innovative and Entrepreneurial Teams (2019ZT08N291).

Institutional Review Board Statement: Not applicable.

Informed Consent Statement: Not applicable.

Data Availability Statement: The data supporting the findings of this study are available from the corresponding author upon reasonable request. Informed consent was obtained from all subjects involved in the study.

Acknowledgments: We express our gratitude to Yongsheng Li from Li Pomelo Guangdong Agricultural Science and Technology Co., Ltd. (Meizhou, China) for donating the immature honey Pomelo fruit used in this study.

Conflicts of Interest: The authors declare no conflict of interest.

References

1. Van Hung, P.; Nhi, N.H.Y.; Ting, L.Y.; Phi, N.T.L. Chemical Composition and Biological Activities of Extracts from Pomelo Peel By-Products under Enzyme and Ultrasound-Assisted Extractions. *J. Chem.* **2020**, *1*, 1043251. [CrossRef]
2. Liu, G.; Hou, T.; Guo, S.; Lin, H.; Chen, M.; Miao, J.; Liu, X.; Huang, Y.; Cao, Y.; Lan, Y.; et al. Comprehensive Utilization of Immature Honey Pomelo Fruit for the Production of Value-Added Compounds Using Novel Continuous Phase Transition Extraction Technology. *Biology* **2021**, *10*, 815. [CrossRef] [PubMed]
3. Nunes, C.; Silva, L.; Fernandes, A.P.; Guiné, R.P.F.; Domingues, M.R.M.; Coimbra, M.A. Occurrence of Cellobiose Residues Directly Linked to Galacturonic Acid in Pectic Polysaccharides. *Carbohydr. Polym.* **2012**, *87*, 620–626. [CrossRef]
4. Souto-Maior, J.F.A.; Reis, A.V.; Pedreiro, L.N.; Cavalcanti, O.A. Phosphated Crosslinked Pectin as a Potential Excipient for Specific Drug Delivery: Preparation and Physicochemical Characterization. *Polym. Int.* **2010**, *59*, 127–135. [CrossRef]
5. Xing, X.; Cui, S.W.; Nie, S.; Phillips, G.O.; Goff, H.D.; Wang, Q. A Review of Isolation Process, Structural Characteristics, and Bioactivities of Water-Soluble Polysaccharides from Dendrobium Plants. *Bioact. Carbohydr. Diet. Fibre* **2013**, *1*, 131–147. [CrossRef]
6. Ferreira, S.S.; Passos, C.P.; Madureira, P.; Vilanova, M.; Coimbra, M.A. Structure–Function Relationships of Immunostimulatory Polysaccharides: A Review. *Carbohydr. Polym.* **2015**, *132*, 378–396. [CrossRef]
7. Venzon, S.S.; Canteri, M.H.G.; Granato, D.; Demczuk, B., Jr.; Maciel, G.M.; Stafussa, A.P.; Haminiuk, C.W.I. Physicochemical Properties of Modified Citrus Pectins Extracted from Orange Pomace. *J. Food Sci. Technol.* **2014**, *52*, 4102–4112. [CrossRef]
8. Salman, H.; Bergman, M.; Djaldetti, M.; Orlin, J.; Bessler, H. Citrus Pectin Affects Cytokine Production by Human Peripheral Blood Mononuclear Cells. *Biomed. Pharmacother.* **2008**, *62*, 579–582. [CrossRef]
9. Platt, D.; Raz, A. Modulation of the Lung Colonization of B16-F1 Melanoma Cells by Citrus Pectin. *JNCI J. Natl. Cancer Inst.* **1992**, *84*, 438–442. [CrossRef]
10. Pérez Marín, A.B.; Ortuño, J.F.; Aguilar, M.I.; Meseguer, V.F.; Sáez, J.; Lloréns, M. Use of Chemical Modification to Determine the Binding of Cd(II), Zn(II) and Cr(III) Ions by Orange Waste. *Biochem. Eng. J.* **2010**, *53*, 2–6. [CrossRef]
11. Katav, T.; Liu, L.S.; Traitel, T.; Goldbart, R.; Wolfson, M.; Kost, J. Modified Pectin-Based Carrier for Gene Delivery: Cellular Barriers in Gene Delivery Course. *J. Control. Release* **2008**, *130*, 183–191. [CrossRef] [PubMed]
12. Maciel, V.; Yoshida, C.; Franco, T.T. Chitosan/Pectin Polyelectrolyte Complex as a PH Indicator. *Carbohydr. Polym.* **2015**, *132*, 537–545. [CrossRef] [PubMed]
13. Yu, Q.; Nie, S.P.; Wang, J.Q.; Yin, P.F.; Huang, D.F.; Li, W.J.; Xie, M.Y. Toll-like Receptor 4-Mediated ROS Signaling Pathway Involved in *Ganoderma Atrum* Polysaccharide-Induced Tumor Necrosis Factor- α Secretion during Macrophage Activation. *Food Chem. Toxicol.* **2014**, *66*, 14–22. [CrossRef]
14. Wang, M.; Yang, X.-B.; Zhao, J.-W.; Lu, C.-J.; Zhu, W. Structural Characterization and Macrophage Immunomodulatory Activity of a Novel Polysaccharide from *Smilax Glabra* Roxb. *Carbohydr. Polym.* **2017**, *156*, 390–402. [CrossRef] [PubMed]

15. Ma, L.; Jiao, K.; Luo, L.; Xiang, J.; Zhu, W. Characterization and Macrophage Immunomodulatory Activity of Two Polysaccharides from the Flowers of *Paonia Suffruticosa* Andr. *Int. J. Biol. Macromol.* **2018**, *124*, 955–962. [CrossRef]
16. Lee, J.S.; Kwon, D.S.; Lee, K.R.; Park, J.M.; Ha, S.J.; Hong, E.K. Mechanism of Macrophage Activation Induced by Polysaccharide from *Cordyceps Militaris* Culture Broth. *Carbohydr. Polym.* **2015**, *120*, 29–37. [CrossRef]
17. Xu, X.; Yan, H.; Zhang, X. Structure and Immuno-Stimulating Activities of a New Heteropolysaccharide from *Lentinula Edodes*. *J. Agric. Food Chem.* **2012**, *60*, 11560–11566. [CrossRef]
18. Liao, W.; Luo, Z.; Liu, D.; Ning, Z.; Yang, J.; Ren, J. Structure Characterization of a Novel Polysaccharide from *Dictyophora Indusiata* and Its Macrophage Immunomodulatory Activities. *J. Agric. Food Chem.* **2015**, *63*, 535–544. [CrossRef] [PubMed]
19. Schepetkin, I.A.; Xie, G.; Kirpotina, L.N.; Klein, R.A.; Jutila, M.A.; Quinn, M.T. Macrophage Immunomodulatory Activity of Polysaccharides Isolated from *Opuntia Polyacantha*. *Int. Immunopharmacol.* **2008**, *8*, 1455–1466. [CrossRef]
20. Meng, J.; Lien, E.; Golenbock, D.T. MD-2-Mediated Ionic Interactions between Lipid A and TLR4 Are Essential for Receptor Activation. *J. Biol. Chem.* **2010**, *285*, 8695–8702. [CrossRef]
21. Zheng, P.; Fan, W.; Wang, S.; Hao, P.; Wang, Y.; Wan, H.; Hao, Z.; Liu, J.; Zhao, X. Characterization of Polysaccharides Extracted from *Platycodon Grandiflorus* (Jacq.) A. DC. Affecting Activation of Chicken Peritoneal Macrophages. *Int. J. Biol. Macromol.* **2017**, *96*, 775–785. [CrossRef] [PubMed]
22. Yang, B.; Jiang, Y.; Zhao, M.; Chen, F.; Wang, R.; Chen, Y.; Zhang, D. Structural Characterisation of Polysaccharides Purified from Longan (*Dimocarpus Longan* Lour.) Fruit Pericarp. *Food Chem.* **2009**, *115*, 609–614. [CrossRef]
23. Maxwell, E.G.; Belshaw, N.J.; Waldron, K.W.; Morris, V.J. Pectin—An Emerging New Bioactive Food Polysaccharide. *Trends Food Sci. Technol.* **2012**, *24*, 64–73. [CrossRef]
24. Wang, M.; Liu, Y.; Qiang, M.; Wang, J. Structural Elucidation of a Pectin-Type Polysaccharide from *Hovenia Dulcis* Peduncles and Its Proliferative Activity on RAW264.7 Cells. *Int. J. Biol. Macromol.* **2017**, *104*, 1246–1253. [CrossRef]
25. Min, B.; Lim, J.; Ko, S.; Lee, K.-G.; Lee, S.H.; Lee, S. Environmentally Friendly Preparation of Pectins from Agricultural Byproducts and Their Structural/Rheological Characterization. *Bioresour. Technol.* **2011**, *102*, 3855–3860. [CrossRef] [PubMed]
26. Yan, J.; Shi, S.; Wang, H.; Liu, R.; Li, N.; Chen, Y.; Wang, S. Neutral Monosaccharide Composition Analysis of Plant-Derived Oligo- and Polysaccharides by High Performance Liquid Chromatography. *Carbohydr. Polym.* **2016**, *136*, 1273–1280. [CrossRef] [PubMed]
27. Wu, F.; Zhou, C.; Zhou, D.; Ou, S.; Huang, H. Structural Characterization of a Novel Polysaccharide Fraction from *Hericium Erinaceus* and Its Signaling Pathways Involved in Macrophage Immunomodulatory Activity. *J. Funct. Foods* **2017**, *37*, 574–585. [CrossRef]
28. Wang, J.; Ge, B.; Li, Z.; Guan, F.; Li, F. Structural Analysis and Immunoregulation Activity Comparison of Five Polysaccharides from *Angelica Sinensis*. *Carbohydr. Polym.* **2016**, *140*, 6–12. [CrossRef]
29. Zhao, J. Structural Analysis of Pumpkin Acidic Polysaccharides and Their Interactions with Functional Protein. Ph.D. Thesis, China Agricultural University, Beijing, China, 2017.
30. Liu, J.; Zhao, Y.; Wu, Q.; John, A.; Jiang, Y.; Yang, J.; Liu, H.; Yang, B. Structure Characterisation of Polysaccharides in Vegetable “Okra” and Evaluation of Hypoglycemic Activity. *Food Chem.* **2018**, *242*, 211–216. [CrossRef]
31. Yu, Y.; Shen, M.; Song, Q.; Xie, J. Biological Activities and Pharmaceutical Applications of Polysaccharide from Natural Resources: A Review. *Carbohydr. Polym.* **2018**, *183*, 91–101. [CrossRef]
32. Yin, M.; Zhang, Y.; Li, H. Advances in Research on Immunoregulation of Macrophages by Plant Polysaccharides. *Front. Immunol.* **2019**, *10*, 145. [CrossRef] [PubMed]
33. Trakoolpolpruek, T.; Moonmangmee, S.; Chanput, W. Structure-Dependent Immune Modulating Activity of Okra Polysaccharide on THP-1 Macrophages. *Bioact. Carbohydr. Diet. Fibre* **2019**, *17*, 100173. [CrossRef]
34. Sun, S.; Li, K.; Xiao, L.; Lei, Z.; Zhang, Z. Characterization of Polysaccharide from *Helicteres Angustifolia* L. and Its Immunomodulatory Activities on Macrophages RAW264.7. *Biomed. Pharmacother.* **2019**, *109*, 262–270. [CrossRef]
35. Song, Y.-R.; Han, A.-R.; Lim, T.-G.; Kang, J.-H.; Hong, H.-D. Discrimination of Structural and Immunological Features of Polysaccharides from *Persimmon* Leaves at Different Maturity Stages. *Molecules* **2019**, *24*, 356. [CrossRef]
36. Huang, L.; Zhao, J.; Wei, Y.; Yu, G.; Li, F.; Li, Q. Structural Characterization and Mechanisms of Macrophage Immunomodulatory Activity of a Pectic Polysaccharide from *Cucurbita Moschata* Duch. *Carbohydr. Polym.* **2021**, *269*, 118288. [CrossRef] [PubMed]
37. Wu, Y.; Zhou, B.P. TNF- α /NF-KB/Snail Pathway in Cancer Cell Migration and Invasion. *Br. J. Cancer* **2010**, *102*, 639–644. [CrossRef] [PubMed]
38. Balkwill, F. Tumour Necrosis Factor and Cancer. *Nat. Rev. Cancer* **2009**, *9*, 361–371. [CrossRef] [PubMed]
39. Hotamisligil, G.S.; Peraldi, P.; Budavari, A.; Ellis, R.; White, M.F.; Spiegelman, B.M. IRS-1-Mediated Inhibition of Insulin Receptor Tyrosine Kinase Activity in TNF- α - and Obesity-Induced Insulin Resistance. *Science* **1996**, *271*, 665–670. [CrossRef]
40. Wang, X.; Chen, Q.; Lü, X. Pectin Extracted from Apple Pomace and Citrus Peel by Subcritical Water. *Food Hydrocoll.* **2014**, *38*, 129–137. [CrossRef]
41. Du, Y.-Q.; Liu, Y.; Wang, J.-H. Polysaccharides from *Umbilicaria Esculenta* Cultivated in Huangshan Mountain and Immunomodulatory Activity. *Int. J. Biol. Macromol.* **2015**, *72*, 1272–1276. [CrossRef]
42. Dumitru, C.D.; Ceci, J.D.; Tsatsanis, C.; Kontoyiannis, D.; Stamatakis, K.; Lin, J.-H.; Patriotis, C.; Jenkins, N.A.; Copeland, N.G.; Kollias, G.; et al. TNF- α Induction by LPS Is Regulated Posttranscriptionally via a Tpl2/ERK-Dependent Pathway. *Cell* **2000**, *103*, 1071–1083. [CrossRef] [PubMed]

43. Tili, E.; Michaille, J.-J.; Cimino, A.; Costinean, S.; Dumitru, C.D.; Adair, B.; Fabbri, M.; Alder, H.; Liu, C.G.; Calin, G.A.; et al. Modulation of MiR-155 and MiR-125b Levels Following Lipopolysaccharide/TNF- α Stimulation and Their Possible Roles in Regulating the Response to Endotoxin Shock. *J. Immunol.* **2007**, *179*, 5082–5089. [CrossRef]
44. Ahmadi Gavlighi, H.; Tabarsa, M.; You, S.; Surayot, U.; Ghaderi-Ghahfarokhi, M. Extraction, Characterization and Immunomodulatory Property of Pectic Polysaccharide from Pomegranate Peels: Enzymatic vs. Conventional Approach. *Int. J. Biol. Macromol.* **2018**, *116*, 698–706. [CrossRef] [PubMed]
45. Yu, Q.; Nie, S.-P.; Wang, J.-Q.; Huang, D.-F.; Li, W.-J.; Xie, M.-Y. Signaling Pathway Involved in the Immunomodulatory Effect of Ganoderma Atrum Polysaccharide in Spleen Lymphocytes. *J. Agric. Food Chem.* **2015**, *63*, 2734–2740. [CrossRef]
46. Beinke, S.; Ley, S.C. Functions of NF-KappaB1 and NF-KappaB2 in Immune Cell Biology. *Biochem. J.* **2004**, *382*, 393–409. [CrossRef] [PubMed]
47. Wang, W.; Zou, Y.; Li, Q.; Mao, R.; Shao, X.; Jin, D.; Zheng, D.; Zhao, T.; Zhu, H.; Zhang, L.; et al. Immunomodulatory Effects of a Polysaccharide Purified from *Lepidium Meyenii* Walp. on Macrophages. *Process Biochem.* **2016**, *51*, 542–553. [CrossRef]
48. Campillo-Gimenez, L.; Renaudin, F.; Jalabert, M.; Gras, P.; Gosset, M.; Rey, C.; Sarda, S.; Collet, C.; Cohen-Solal, M.; Combes, C.; et al. Inflammatory Potential of Four Different Phases of Calcium Pyrophosphate Relies on NF-KB Activation and MAPK Pathways. *Front. Immunol.* **2018**, *9*, 2248. [CrossRef]
49. Liu, C.-P.; Zhang, X.; Tan, Q.-L.; Xu, W.-X.; Zhou, C.-Y.; Luo, M.; Li, X.; Huang, R.-Y.; Zeng, X. NF-KB Pathways Are Involved in M1 Polarization of RAW 264.7 Macrophage by Polyporus Polysaccharide in the Tumor Microenvironment. *PLoS ONE* **2017**, *12*, e0188317. [CrossRef]
50. Wang, Y.-Q.; Mao, J.-B.; Zhou, M.-Q.; Jin, Y.-W.; Lou, C.-H.; Dong, Y.; Shou, D.; Hu, Y.; Yang, B.; Jin, C.-Y.; et al. Polysaccharide from *Phellinus Ignarius* Activates TLR4-Mediated Signaling Pathways in Macrophages and Shows Immune Adjuvant Activity in Mice. *Int. J. Biol. Macromol.* **2019**, *123*, 157–166. [CrossRef]
51. Prabhudas, M.; Bowdish, D.; Drickamer, K.; Febbraio, M.; Herz, J.; Kobzik, L.; Krieger, M.; Loike, J.; Means, T.K.; Moestrup, S.K.; et al. Standardizing Scavenger Receptor Nomenclature. *J. Immunol.* **2014**, *192*, 1997–2006. [CrossRef]
52. Legentil, L.; Paris, F.; Ballet, C.; Trouvelot, S.; Daire, X.; Vetvicka, V.; Ferrières, V. Molecular Interactions of β -(1 \rightarrow 3)-Glucans with Their Receptors. *Molecules* **2015**, *20*, 9745–9766. [CrossRef] [PubMed]
53. Iwabuchi, K.; Masuda, H.; Kaga, N.; Nakayama, H.; Matsumoto, R.; Iwahara, C.; Yoshizaki, F.; Tamaki, Y.; Kobayashi, T.; Hayakawa, T.; et al. Properties and Functions of *Lactosylceramide* from Mouse Neutrophils. *Glycobiology* **2015**, *25*, 655–668. [CrossRef] [PubMed]
54. Batbayar, S.; Lee, D.H.; Kim, H.W. Immunomodulation of Fungal β -Glucan in Host Defense Signaling by Dectin-1. *Biomol. Ther.* **2012**, *20*, 433–445. [CrossRef] [PubMed]
55. Brown, G.D.; Taylor, P.R.; Reid, D.M.; Willment, J.A.; Williams, D.L.; Martinez-Pomares, L.; Wong, S.Y.C.; Gordon, S. Dectin-1 Is a Major Beta-Glucan Receptor on Macrophages. *J. Exp. Med.* **2002**, *196*, 407–412. [CrossRef] [PubMed]
56. Czop, J.K.; Austen, K.F. A Beta-Glucan Inhibitable Receptor on Human Monocytes: Its Identity with the Phagocytic Receptor for Particulate Activators of the Alternative Complement Pathway. *J. Immunol.* **1985**, *134*, 2588–2593. [PubMed]
57. Cao, Y.; DAI, W.; LIU, H.; Zhang, Y.; Guan, X.; Xu, H.; Liu, F. Multifunctional Continuous Phase Transition Extraction Apparatus. U.S. Patent 10,016,700, 10 July 2018.
58. Zhang, M.; Wu, W.; Ren, Y.; Li, X.; Tang, Y.; Min, T.; Lai, F.; Wu, H. Structural Characterization of a Novel Polysaccharide from *Lepidium Meyenii* (*Maca*) and Analysis of Its Regulatory Function in Macrophage Polarization in Vitro. *J. Agric. Food Chem.* **2017**, *65*, 1146–1157. [CrossRef]
59. Yang, B.; Jiang, Y.; Zhao, M.; Shi, J.; Wang, L. Effects of Ultrasonic Extraction on the Physical and Chemical Properties of Polysaccharides from Longan Fruit Pericarp. *Polym. Degrad. Stab.* **2008**, *93*, 268–272. [CrossRef]
60. Potthast, A.; Radosta, S.; Saake, B.; Lebioda, S.; Heinze, T.; Henniges, U.; Isogai, A.; Koschella, A.; Kosma, P.; Rosenau, T.; et al. Comparison Testing of Methods for Gel Permeation Chromatography of Cellulose: Coming Closer to a Standard Protocol. *Cellulose* **2015**, *22*, 1591–1613. [CrossRef]
61. Meng, M.; Cheng, D.; Han, L.; Chen, Y.; Wang, C. Isolation, Purification, Structural Analysis and Immunostimulatory Activity of Water-Soluble Polysaccharides from *Grifola Frondosa* Fruiting Body. *Carbohydr. Polym.* **2017**, *157*, 1134–1143. [CrossRef]
62. Jing, Y.; Huang, L.; Lv, W.; Tong, H.; Song, L.; Hu, X.; Yu, R. Structural Characterization of a Novel Polysaccharide from Pulp Tissues of *Litchi Chinensis* and Its Immunomodulatory Activity. *J. Agric. Food Chem.* **2014**, *62*, 902–911. [CrossRef]
63. Lai, P.K.-K.; Chan, J.Y.-W.; Wu, S.-B.; Cheng, L.; Ho, G.K.-W.; Lau, C.-P.; Kennelly, E.J.; Leung, P.-C.; Fung, K.-P.; Lau, C.B.-S. Anti-Inflammatory Activities of an Active Fraction Isolated from the Root of *Astragalus Membranaceus* in RAW 264.7 Macrophages. *Phytother. Res.* **2014**, *28*, 395–404. [CrossRef] [PubMed]
64. Zhang, Y.; Liu, X.; Wang, Y.; Jiang, P.; Quek, S. Antibacterial Activity and Mechanism of Cinnamon Essential Oil against *Escherichia Coli* and *Staphylococcus Aureus*. *Food Control.* **2016**, *59*, 282–289. [CrossRef]
65. Ren, Y.; Zheng, G.; You, L.; Wen, L.; Li, C.; Fu, X.; Zhou, L. Structural Characterization and Macrophage Immunomodulatory Activity of a Polysaccharide Isolated from *Gracilaria Lemaneiformis*. *J. Funct. Foods* **2017**, *33*, 286–296. [CrossRef]

66. Cheng, A.; Wan, F.; Wang, J.; Jin, Z.; Xu, X. Macrophage Immunomodulatory Activity of Polysaccharides Isolated from *Glycyrrhiza Uralensis* Fish. *Int. Immunopharmacol.* **2008**, *8*, 43–50. [CrossRef] [PubMed]
67. Lin, Z.; Liao, W.; Ren, J. Physicochemical Characterization of a Polysaccharide Fraction from *Platycladus Orientalis* (L.) Franco and Its Macrophage Immunomodulatory and Anti-Hepatitis B Virus Activities. *J. Agric. Food Chem.* **2016**, *64*, 5813–5823. [CrossRef]
68. Xiao, C.; Anderson, C.T. Roles of Pectin in Biomass Yield and Processing for Biofuels. *Front. Plant Sci.* **2013**, *4*, 67. [CrossRef]

Article

The Efficient Synthesis and Anti-Fatigue Activity Evaluation of Macamides: The Unique Bioactive Compounds in Maca

Tao Liu ¹ , Ziyang Peng ^{1,2}, Wei Lai ^{1,2}, Yan Shao ¹, Qing Gao ^{1,3}, Miaoxin He ^{1,3}, Wan Zhou ^{1,3}, Lirong Guo ^{1,3} , Jiyao Kang ⁴, Xiaobao Jin ¹  and Hui Yin ^{1,2,*} 

¹ Guangdong Provincial Key Laboratory of Pharmaceutical Bioactive Substances, School of Basic Medical Sciences, Guangdong Pharmaceutical University, Guangzhou 510006, China; liutao@gdpu.edu.cn (T.L.); 15812315359@163.com (Z.P.); laiwei1227@foxmail.com (W.L.); 2112240280@gdpu.edu.cn (M.H.)

² Department of Microbiology and Immunology, Guangdong Pharmaceutical University, Guangzhou 510006, China

³ School of Pharmacy, Guangdong Pharmaceutical University, Guangzhou 510006, China

⁴ National Key Laboratory of Biochemical Engineering, Institute of Process Engineering, Chinese Academy of Sciences, Beijing 100080, China; jykang@ipe.ac.cn

* Correspondence: huiyin0103@gdpu.edu.cn

Abstract: Macamides are a class of amide alkaloids that are only found in maca and are widely considered to be its bioactive marker compounds. More than thirty macamide monomers have been identified in recent years; however, it is difficult to obtain a single macamide monomer from the maca plant because of their similar structures and characteristics. We used the carbodiimide condensation method (CCM) to efficiently synthesize five typical macamides, including *N*-benzyl-hexadecanamide (NBH), *N*-benzyl-9Z,12Z,15Z-octadecanamide, *N*-(3-methoxybenzyl)-9Z,12Z-octadecanamide, *N*-benzyl-9Z,12Z-octadecanamide, and *N*-(3-methoxybenzyl)-9Z,12Z,15Z-octadecadienamide. All the synthesized macamides were purified by a one-step HPLC with a purity of more than 95%. NBH is the most abundant macamide monomer in natural maca, and it was selected to evaluate the anti-fatigue effects of macamides. The results indicated that NBH could enhance the endurance capacity of mice by increasing liver glycogen levels and decreasing blood urea nitrogen, lactate dehydrogenase, blood ammonia, and blood lactic acid levels. Macamides might be the active substances that give maca its anti-fatigue active function.

Keywords: macamides; bioactive marker compounds; synthesis; carbodiimide condensation method; anti-fatigue



Citation: Liu, T.; Peng, Z.; Lai, W.; Shao, Y.; Gao, Q.; He, M.; Zhou, W.; Guo, L.; Kang, J.; Jin, X.; et al. The Efficient Synthesis and Anti-Fatigue Activity Evaluation of Macamides: The Unique Bioactive Compounds in Maca. *Molecules* **2023**, *28*, 3943. <https://doi.org/10.3390/molecules28093943>

Academic Editor: David Barker

Received: 17 April 2023

Revised: 30 April 2023

Accepted: 5 May 2023

Published: 7 May 2023



Copyright: © 2023 by the authors. Licensee MDPI, Basel, Switzerland. This article is an open access article distributed under the terms and conditions of the Creative Commons Attribution (CC BY) license (<https://creativecommons.org/licenses/by/4.0/>).

1. Introduction

Lepidium meyenii walp. is an annual or biennial Andean crop, also known as maca in Peru, where it can be extensively grown at high altitudes (3500–4800 m). Its underground storage hypocotyls have been a traditional medicinal herb and dietary staple since pre-Columbian times [1]. The underground root of this plant is rich in macamides, maca alkaloids, glucosinolates, volatile oils, sterols, polyphenols, and macaenes [2,3]. A wide array of maca extracts has been obtained by petroleum ether [4], pentane [5], methanolic [6], alcoholic [7,8], or aqueous [9] extraction and widely used in pharmacological studies. Macamides, secondary amides with variable hydrocarbon chain lengths and levels of unsaturation, are formed by combining benzylamine and a fatty acid moiety. Macamides are considered functional components of the maca plant, unique to this species. Research in recent years has shown that macamides have a variety of pharmacological activities, including a vital effect on endurance capacity [10], neuroprotection [10,11], colitis [12], ovarian injury [13], and testicular function and spermatogenesis [14]. Moreover, some macamides act as irreversible inhibitors of fatty acid amide hydrolases (FAAH) and have

anti-fatigue properties [15]. However, the macamides content, especially highly unsaturated macamides, in maca is low, and the extraction steps are more tedious, making it problematic to obtain abundant and pure single macamides. Therefore, to further validate the biological activity and mechanisms of macamides, high-purity macamides should be employed instead of maca extracts. However, due to their special physicochemical properties, macamides cannot be easily isolated from maca.

The amides of these macamides are derivatives of oleic, linoleic, and linolenic acids combined with either benzylamine or 3-methoxybenzylamine [16] and contain an amide bond in their structure. Thus, an investigation of amide-bond synthetic methods could be useful in acquiring the desired macamides. Conventional amide-synthetic methods include a nucleophilic substitution of carboxylic acids (and their derivatives) with amines. Due to its low activity, the carboxylic acid typically converts to an activated derivative and then reacts with an amine to generate an amide.

In this study, the synthesis of the five main macamides was investigated using the CCM. Moreover, optimization of their purification processes was examined to increase both the purity and yield of these macamides. Additionally, the optimal synthetic conditions for these five macamides should use inexpensive raw materials and provide high product purity and yield. The structures of these macamides were established by spectrometric and spectroscopic methods, including ESI-MS, IR, ^1H NMR, and ^{13}C NMR. Although maca extracts in various solvents have occasionally been found to have anti-fatigue properties, there has not been much research on the anti-fatigue properties of pure components. In this experiment, NBH was selected, and extracts of macamides were used as controls to assess the anti-fatigue capacity of the synthetic macamides.

2. Results

2.1. Synthesis, Purification and Identification of Macamides

The macamide's structural formulas and synthetic reaction diagram are presented in Figures 1 and 2. Each macamide required different purification procedures, including an acid-base reaction, recrystallization, and silica gel column chromatography. The macamide purification method described herein is markedly different from the methods reported previously [17]. The results show that experiment 1 is comparable to experiment 5: the purity of **1** increased from 61.64% to 97.63%. To further investigate the effects of the acid-base reaction on the purity of **1**, the following experiment was carried out: *n*-hexane was washed with 10% sodium hydroxide and hydrochloric acid successively, and the lower aqueous layer was discarded. The *n*-hexane layer was washed again using the same steps as above, and it was then quantitatively analyzed by HPLC separately both before and after washing (Figure 3). This confirms that sodium hydroxide can reduce the impurity content (mainly fatty acids) and increase the macamide purity. This may be due to the fatty acid combining with sodium hydroxide, which could lead to decreased solubility of the impurities in *n*-hexane. In addition, alkaline substances in the reaction mixture, including triethylamine, were also easily removed by hydrochloric acid. Macamides are alkaloid amides which can combine with hydrochloric acid to form unstable compounds. When this compound dissolves in *n*-hexane, it can be cleaved into macamides. Macamides would easily dissolve in *n*-hexane. Thus, the acid-base reaction enhances macamide purity.

The pure precipitates were analyzed by HPLC-DAD, ESI-MS, IR, and NMR (^1H and ^{13}C). Macamides **1–5** were detected by HPLC-DAD, with the highest peak corresponding to the respective macamide (Figure 4). These macamide peaks accounted for more than 95% of the total. The molecular formulas of these compounds were determined to be $\text{C}_{23}\text{H}_{39}\text{NO}$, $\text{C}_{25}\text{H}_{37}\text{NO}$, $\text{C}_{26}\text{H}_{41}\text{NO}_2$, $\text{C}_{25}\text{H}_{39}\text{NO}$, and $\text{C}_{26}\text{H}_{39}\text{NO}_2$, respectively, using ESI-MS (Figures 5a and S1). The UV spectra of compounds **1–5** showed chromophores for a benzyl group (λ_{max} 210 nm), and the IR spectra revealed absorptions at ν_{max} 3302 cm^{-1} for N-H and ν_{max} 1453 cm^{-1} for a carbonyl group (Figures 5b and S2). The ^{13}C NMR spectra exhibited an amide carbonyl peak (δ_{C} 173.13) and peaks corresponding to monosubstituted or polysubstituted benzene rings, as well as two or three disubstituted double bonds (δ_{C}

131.99, 130.27, 129.12, 128.44, 127.63, 126.96; each d; C-9, C-10, C-12, C-13, C-15, C-16, respectively) (Figures 5c and S3). The ^1H NMR spectrum (Figures 5d and S4) exhibited two or three *cis*-coupled olefinic protons at δ 5.37 (d, $J = 4.0$ Hz, H-9) and 5.36 (m, H-10), four other olefinic protons between δ 5.31 and 5.34 (m, H-12, H-13, H-15, and H-16), a primary methyl group at δ 0.87 (t, $J = 4.0, 8.0$, H-16) or δ 0.97 (t, $J = 4.0, 8.0$, H-18), as well as other protons between δ 1.30 and 1.33, assigned to the methylene group. Compared with macamide 1 (NBH), the other four compounds (2–5) contain two or three unsaturated double bonds and a 6-substituted phenyl ring replacing the methoxy group, which is verified in IR, MS, ^1H , and ^{13}C NMR spectra (Supplementary data).

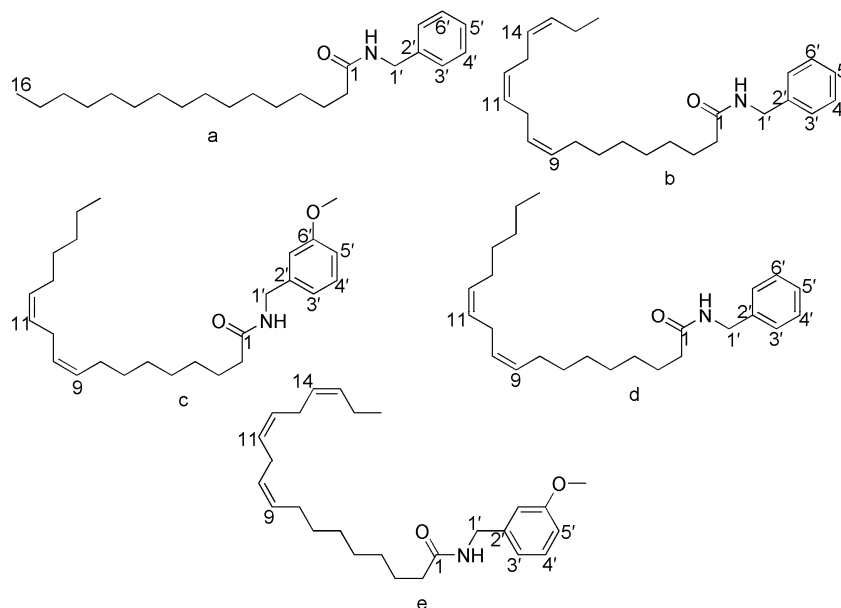


Figure 1. Structural formulas of five typical macamides. (a): N-benzyl-hexadecanamide (NBH), (b): N-benzyl-9Z,12Z,15Z-octadecatrienamide, (c): N-(3-methoxybenzyl)-9Z,12Z-octadecadienamide, (d): N-benzyl-9Z,12Z-octadecadienamide, (e): N-(3-methoxybenzyl)-9Z,12Z,15Z-octadecatrienamide.

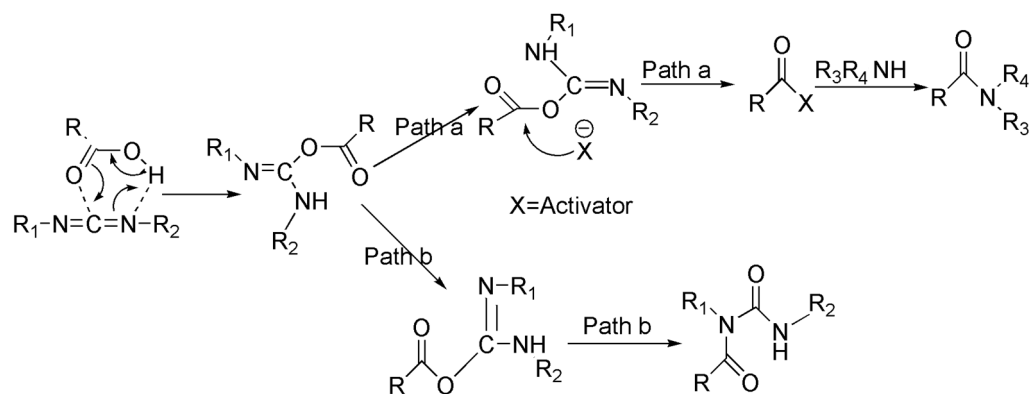


Figure 2. Diagram of the Synthetic reaction of macamides.

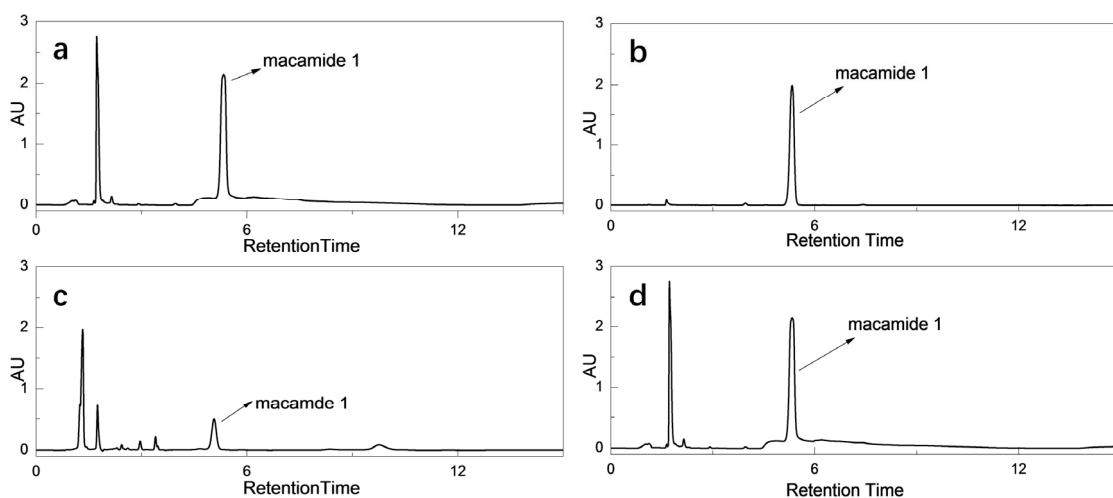


Figure 3. HPLC chromatograms of NBH samples: (a) the sample after acid-base reaction, (b) the sample after recrystallization, (c) the sample before the acid-base reaction, (d) the sample before recrystallization.

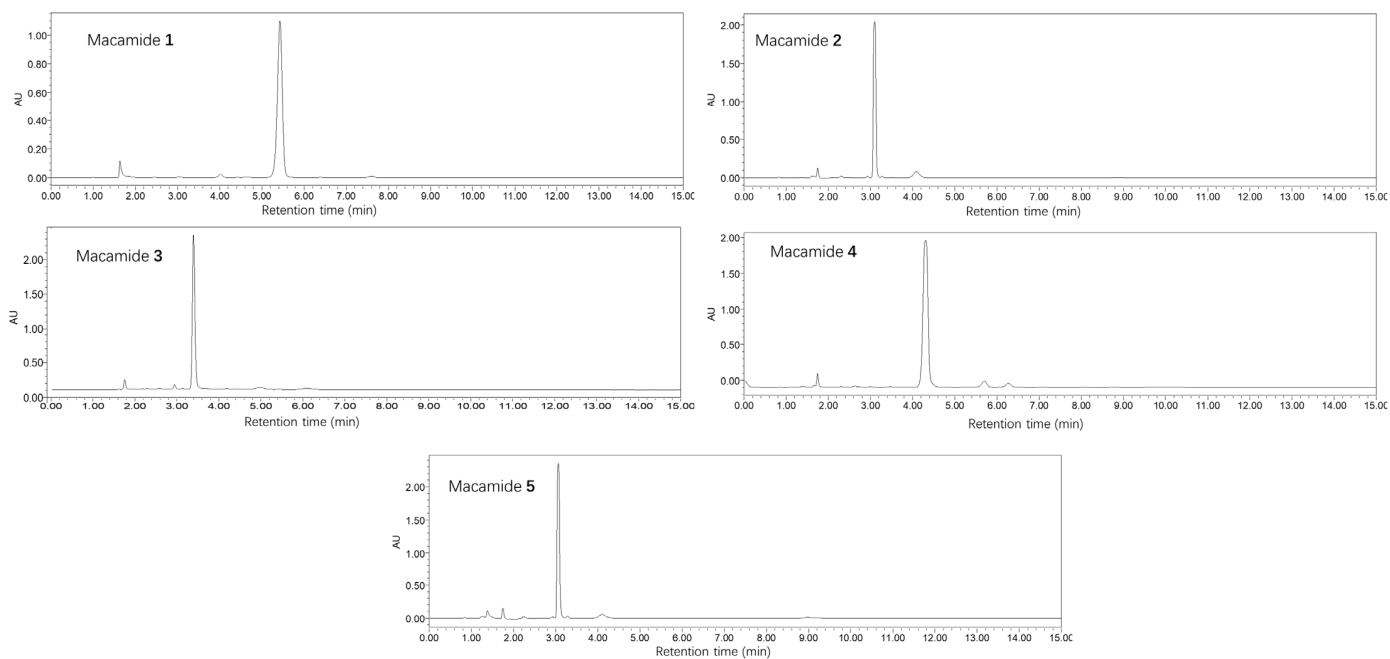


Figure 4. HPLC chromatograms of macamides 1–5.

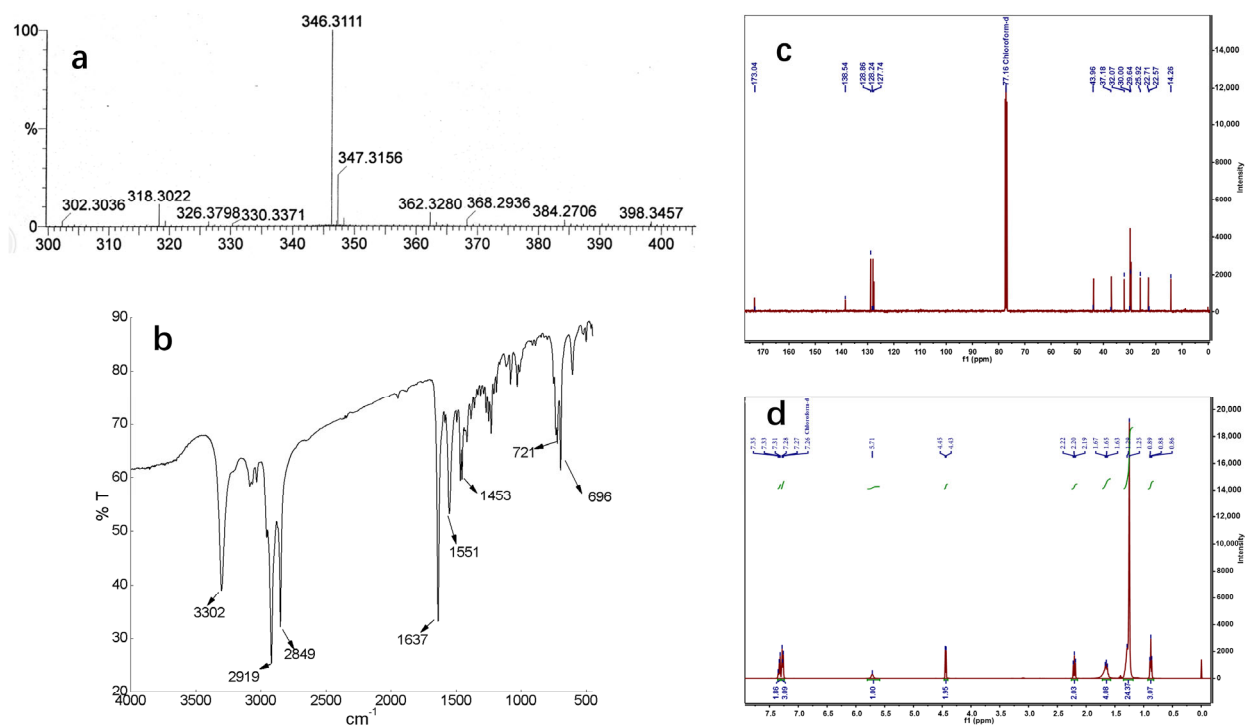


Figure 5. Characterization spectra of NBH. (a) Mass spectrum of NBH, (b) Infrared spectrum of NBH, (c) ^{13}C NMR spectrum of NBH, (d) ^1H NMR spectrum of NBH.

2.2. Anti-Fatigue Activity of NBH

2.2.1. Forced Swimming Test

It is widely accepted that exercise endurance is a direct and invariable factor in screening anti-fatigue agents, which is determined by the length of forced swimming time [9,18–20]. In this study, a forced swimming time (FST) model was developed to assess the fatigue-relieving effect of NBH by recording the swimming time of mice from the beginning of day 0; the swimming times of each group showed little difference. With constant NBH gavage, significant differences were observed in the NBH groups on day 28 ($p < 0.05$), and the increased ratio of swimming time was 105% (Figure 6). There was no significant difference between the control groups and the blank groups. The results showed that NBH played an important role in extending swimming time. Body weight was recorded on days 0, 7, 14, and 28. Compared to the normal increases, there were no significant differences in body weight changes between the two groups.

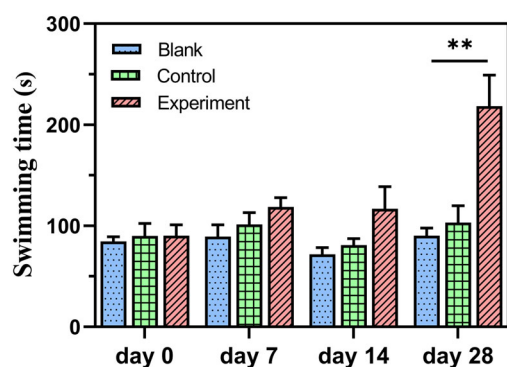


Figure 6. The effects of NBH on the forced swimming time to exhaustion in mice. The data were expressed as means \pm SD, with $n = 6$. The double asterisk ** indicates a highly significant difference ($p < 0.01$) compared to the blank group.

2.2.2. Effect of NBH on Biochemical Parameters Related to Fatigue

The FST results demonstrate that NBH plays a significant role in fatigue activity. Therefore, the biochemical parameters related to fatigue were measured to investigate a possible mechanism. For example, liver glycogen (LG), blood urea nitrogen (BUN), lactate dehydrogenase (LDH), blood ammonia (BA), and blood lactic acid (BLA) were measured [21].

Energy depletion and deficiencies can lead to fatigue and reduce the body's resistance. Liver glycogen (LG) is energy for exercise which is derived initially from the liver and converts lactate back to glycogen and releases glycogen into the blood [20]. Therefore, an increase in liver glycogen indicates enhanced exercise capacity and endurance capacity. The experimental results show that the content of the NBH group was significantly higher than that of the blank group, which was 241% (Figure 7a).

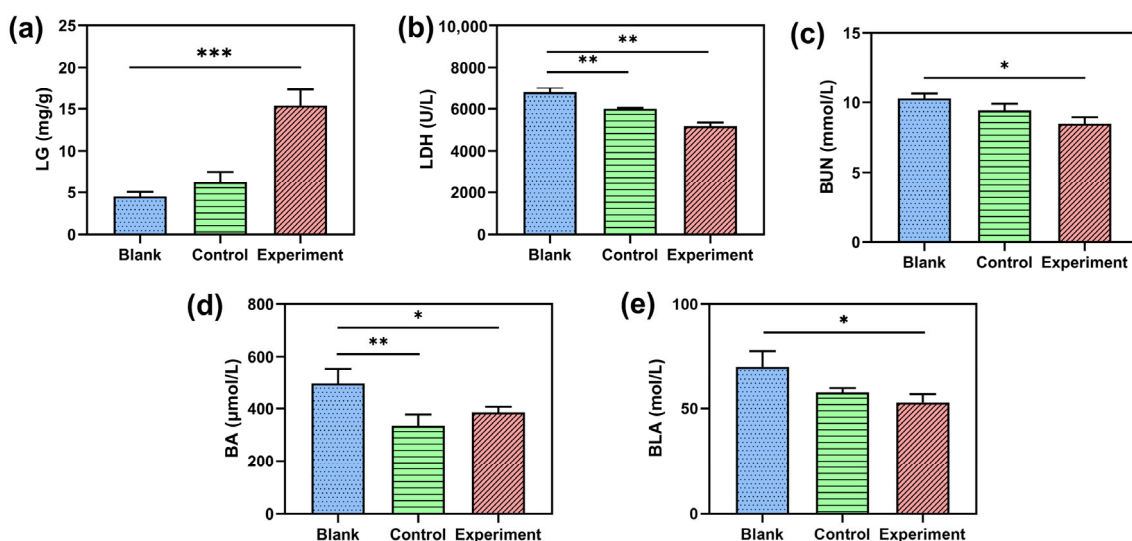


Figure 7. Effect of different supplementation on biochemical parameters in mice. (a): liver glycogen (LG); (b): lactic dehydrogenase (LDH); (c): blood urea nitrogen (BUN); (d): blood ammonia (BA); (e): blood lactic acid (BLA). (Data were expressed means \pm SD, $n = 6$, *, $p < 0.05$ compared with that in the blank group; **, $p < 0.01$ compared with that in the blank group; ***, $p < 0.001$ compared with that in the blank group).

BUN is another indicator of fatigue in the body. It is the metabolic outcome of protein and amino acids when the body suffers from exhaustive exercise, which is derived initially from the liver and later excreted out of the body through the kidneys [22]. In brief, the more exercise the body undergoes, the more vitally the BUN level increases. As shown in (Figure 7b), BUN levels in the NBH group were significantly reduced by 18% ($p < 0.05$). The experimental results show that NBH can effectively reduce the accumulated BUN. LDH is an enzyme that plays an important role in eliminating lactic acid and providing energy under anaerobic conditions [23]; in other words, the more severe the muscle damage, the higher the serum levels of LDH [24]. The activities of LDH in the control group and NBH group were significantly lower than that of the blank group, by 11% ($p < 0.01$) and 23% ($p < 0.01$), respectively (Figure 7c). This experiment shows that NBH can relieve fatigue caused by muscle damage. BA is a metabolite produced by the breakdown of amino acids in the body, which is translated into urea in the liver. The level of BA that was raised may be associated with the body's fatigue and liver glycogen decrease [25]. Compared with the blank group, the control group and NBH group showed significant differences, with the content of BA decreased by 30% ($p < 0.01$) and 21% ($p < 0.05$), respectively (Figure 7d). BLA, an important glycolysis product, is known to accumulate during intensive prolonged exercise [26]. In addition, with the repeated accumulation of lactic acid, there is eventually a decline of power output, leading to impairment of whole-body exercise performance; that

is, fatigue develops. As shown in Figure 7e, the NBH group decreased the BLA content by 24% ($p < 0.05$) lower than the blank group.

In summary, five fatigue-related biochemical markers were examined to assess NBH anti-fatigue activity. The findings imply that NBH could improve mice's endurance ability by raising the LG level and lowering the levels of BUN, LDH, BA, and BLA. For all four measures except LG, there were significant changes between the experimental group and the control group. These results demonstrated the anti-fatigue activity of NBH.

3. Discussion

A general method for amide synthesis involves the activation of a carboxylic fatty acid moiety with carbodiimide condensation agents (CCAs), followed by a reaction with an amine to generate the corresponding amide. CCAs, including *N,N'*-dicyclohexylcarbodiimide, *N,N'*-diisopropylcarbodiimide, and 1-(3-Dimethylaminopropyl)-3-ethylcarbodiimide hydrochloride (EDAC), are widely used in amide synthesis [27,28]. However, EDAC was chosen since it contributes to macamide purification. Subsequently, an acylation catalyst such as 4-dimethylaminopyridine (DMAP) or HOBt·H₂O was selected for addition. The main reason for this addition was that the intermediates formed by nucleophilic substitution reactions of CCAs were not stable, which led to rearrangement byproducts. Previous studies have been conducted on the synthesis of macamides. For example, *N*-benzyl-15Z-tetracosenamide was rapidly synthesized using *cis*-15-tetracosenoic acid, DMAP, and dicyclohexyl carbodiimide [29] but had low product yield and purity. Another synthetic method using palmitic acid, 1'-carbonyldiimidazole, and DMAP afforded *N*-benzylpalmitamide in large quantities [16]. However, product purification requires silica gel column chromatography, which is complicated and inefficient. A previous paper [30] described a purification method in which 10% sodium hydroxide and hydrochloric acid were added to the reaction solution, followed by stirring and discarding the lower aqueous layer. This resulted in a product NBH with higher yield and purity. However, this method could not be applied on an industrial scale because of the high cost of the reaction raw materials. Hence, the synthetic method should take into consideration the commercial availability of raw materials, the content and purity of products, and reaction time. The purification process is the key point of synthetic reactions, as it is used for removing byproducts, the remaining materials, and other impurities. In the present study, the reaction materials, including EDAC, HOBt·H₂O, triethylamine, and reaction byproducts, were water-soluble substances. Thus, extraction using organic solvents could easily reduce impurities and enrich the final product. For further purification, the acid-base reaction and recrystallization in the purification process first came up to increase product purity.

The effects of EDAC, HOBt·H₂O, triethylamine, and the acid-base reaction on the yield and purity of NBH (**1**) are shown in Table 1. These results show that under the same conditions, experiment 1 produces comparable results with experiments 2–4. The yield of **1** in experiment 1 is significantly higher than those without treatment with EDAC, HOBt·H₂O, and triethylamine. This is because EDAC, as a CCA, activates the carboxyl moiety of palmitic acid to form an intermediate by nucleophilic substitution. (Please see Supplementary Materials).

Because the intermediate is unstable, the use of HOBt as an acylation catalyst can keep the intermediate stable and stop it from generating related byproducts. In addition, using triethylamine as an acid-binding agent could accelerate the acylation reaction, which might mean that triethylamine could significantly improve the solubility of EDAC in DCM. In conclusion, EDAC, HOBt·H₂O, and triethylamine are necessary to obtain macamides and enhance their yield and purity. Macamides are easily recrystallized from *n*-hexane due to their poor solubility at low temperatures when compared with impurities. Based on the above inference, recrystallization was utilized to increase the product purity. The recrystallization conditions are at 4 °C. Finally, each layer in the experimental section was analyzed by HPLC-UV, both before and after recrystallization. These results indicate that the low-polar impurities remained in the solution, and the macamides were easily separated.

Due to their special physical properties, Macamides **2** and **4** should be recrystallized at $-20\text{ }^{\circ}\text{C}$. However, macamides **3** and **5** were difficult to recrystallize, thus necessitating purification using silica gel column chromatography. Thus, after the acid-base reaction, many impurities in the precipitate were removed, and the macamides could be easily afforded by silica gel column chromatography.

Table 1. Effects of EDAC, HOBt, triethylamine, and acid-base reactions on the yield and purity of macamide.

No.	EDAC	HOBt·H ₂ O	Triethylamine	Acid-Base Reaction	Precipitate Yield (%)	Purity (%)
1	Y *	Y	Y	Y	39.16	97.63
2	N **	Y	Y	Y	0	0
3	Y	N	Y	Y	0	0
4	Y	Y	N	Y	100.37	13.21
5	Y	Y	Y	N	64.25	61.64

* Y: addition; ** N: no addition.

FST is a reliable and valid model for evaluating anti-fatigue activity in mice, as several studies have reported a strong correlation between exercise endurance and the length of forced swim time [31]. Other biochemical parameters, such as muscle glycogen (MG), Adenosine Triphosphate (ATP), Adenosine Monophosphate (AMP), Methylendioxyamphetamine (MDA), Superoxide Dismutase (SOD), have also been utilized to assess fatigue and the anti-fatigue effects of various supplements [32,33]. These parameters can provide additional insights into the mechanism of action of macamides. For example, increasing levels of ATP, AMP, and muscle glycogen have been linked to improved endurance, while reducing the levels of MDA and SOD has been suggested to decrease fatigue and enhance fatigue resistance. Additionally, 5-HT is a major biochemical marker for assessing fatigue in different species, and its levels can be detected by ELISA and HPLC with electrochemical and fluorescence detection [34]. The results of this study showed that NBH extended swimming time in test mice, increased levels of LG and reduced levels of BUN, LDH, BA, and BLA, indicating its potential for decreasing physical fatigue and improving exercise capacity. We have demonstrated that NBH can effectively improve mice's endurance ability by altering several fatigue-related biochemical markers. However, it is important to note that the mechanism underlying this effect remains unclear. Future experiments could utilize techniques such as transcriptomics or metabolomics to gain a more comprehensive understanding of the molecular pathways involved in macamide's anti-fatigue activity. Unsaturated fatty acids are important components of macamides. The transportation, metabolism, and action of unsaturated fatty acids in the body are complicated. It is well known that the degree of unsaturation can influence their biological activities. Studies have shown that highly unsaturated fatty acids can exhibit potent anti-inflammatory and antioxidant effects, such as eicosapentaenoic acid (EPA) and docosahexaenoic acid (DHA) [35]. There are also different reports indicating that DHA and EPA play an important role in alleviating exercise fatigue. However, the administration of DHA/EPA-triglyceride (TG) and DHA-phospholipid (PL) rather than DHA-TG can significantly extend the time and distance to running exhaustion in mice [36]. Future studies could focus on this aspect to determine if there is a correlation between macamide unsaturation and anti-fatigue activity.

4. Materials and Methods

4.1. Materials and Chemicals

All solvents and reagents were commercially available. Palmitic acid (AR, 99.0% pure), linoleic acid (99.0% pure), linolenic acid (99.0% pure), 3-methoxybenzylamine (98% pure), benzylamine (99.0% pure), HOBt·H₂O (97% pure), EDAC (98.0% pure), and triethylamine (AR, 99.0% pure) were purchased from Aladdin (Shanghai, China). HPLC grade aceton-

trile, *n*-hexane, hydrochloric acid, sodium hydroxide, and dichloromethane (DCM) (used as analytical reagents for the purification of macamides) were purchased from Wenrui (Guangzhou, Guangdong, China). Ultrapure water (18.2 M Ω cm at 25 °C) (MilliQ Millipore, Billerica, MA, USA) was used for HPLC analysis and synthesis of macamides.

4.2. Instrumental and Chromatographic Conditions

HPLC analysis was carried out on a Waters Alliance 2695 HPLC system (Waters, Milford, MA, USA), which was equipped with an inline vacuum degasser, a quaternary gradient pump, an autosampler, a DAD (2998) detector, and a Waters SunFire^{TU} C18 column (4.6 \times 250 mm, 5 μ m) and a Waters SunFire^{TU} C18 column with a flow rate of 1 mL/min for 15 min. The isocratic elution system comprised acetonitrile (95%) and water (5%). The DAD detection wavelength was set as 210 nm. Gradient elution chromatography was applied to determine the macamides extract from the maca. The solvent system consisted of (A) distilled water and (B) acetonitrile, using a gradient of 50:50 to 5:95 in 25 min, and the UV detection wavelength was 210 nm. The sample volume was 10 μ L, and the flow rate was 1 mL/min. The injection volume of all samples was 10 μ L. The optimal MS parameters were as follows: positive ion mode for MS detection; desolvation gas (N₂) flow, 50 L/h; source voltage, 3 kV; transmission voltage, 30 V; all processes were controlled by Masslynx 4.1 software. In the HPLC-MS method, a Waters Acquity UPLC/Q-TOF Micro MS system equipped with an electrospray ionization (ESI) interface, working in positive ion mode, was used. Data processing was performed using Waters Masslynx 4.1 software. ¹H and ¹³C NMR spectra were recorded on a Bruker Avance III instrument (Bruker, Fällanden, Switzerland) at 400 MHz (¹H) and 100 MHz (¹³C) in CDCl₃, using the residual solvent signal as an internal standard. IR spectra were recorded on a Spectrum 100 FT-IR spectrometer (PerkinElmer, Rodgau, Germany).

4.3. The synthesis of Five Main Macamides

4.3.1. Preparation of NBH (1)

A DCM solution (50 mL) containing HOBT·H₂O (103 mg, 0.76 mmol), EDAC (146 mg, 0.76 mmol), and palmitic acid (195 mg, 0.76 mmol) was stirred at 24 °C for 20 h. A solution of benzylamine (83 μ L, 0.76 mmol) and triethylamine (264 μ L, 1.5 mmol) dissolved in DCM (10 mL) was then added to the reaction mixture. After 4 h, the final solution was evaporated to dryness. Subsequently, 10% hydrochloric acid (10 mL) and *n*-hexane (50 mL) were added and stirred under ultrasonic conditions (200 W) for 5 min. The *n*-hexane layer was washed successively with 10% sodium hydroxide and 10% hydrochloric acid (10 mL), and the lower aqueous layers were discarded. Finally, the *n*-hexane solution was cooled to 4 °C and allowed to recrystallize for 24 h. The recrystallized precipitate (39.16% yield, 97.63% pure) was obtained through vacuum filtration as a white powder and dried. IR ν_{\max} 3302, 2919, 2849, 1627, 1551, 1453, 721, 696 cm⁻¹; ¹H NMR (400 MHz, CDCl₃) and ¹³C NMR (100 MHz, CDCl₃) spectroscopic data of compound **1–5** were shown in Tables S1 and S2; MS, C₂₃H₃₉NO, [M + H]: 346.31. The spectroscopic data for the precipitate (MS, ¹H, and ¹³C NMR) correspond to the data previously published for NBH.

4.3.2. Preparation of *N*-Benzyl-9Z,12Z,15Z-octadecatrienamide (2)

Linolenic acid (233 μ L, 0.76 mol, 99.0% pure), HOBT·H₂O (103 mg, 0.76 mmol), and EDAC (146 mg, 0.76 mmol) were dissolved in DCM (50 mL). The reaction mixture was stirred at 25 °C for 20 h. Subsequently, benzylamine (83 μ L, 99.0% pure) and triethylamine (264 μ L, 1.5 mmol, 99.0% pure) were added to the resulting mixture. The same operating steps were followed for the preparation of NBH, except that the recrystallization temperature was –20 °C. Finally, the crystals were dried to yield the product as a brown powder (37.27% yield, 95.71% pure). IR ν_{\max} 3298, 2929, 2856, 1648, 1544, 1455, 730, 699 cm⁻¹; MS, C₂₅H₃₇NO, [M + H]: 368.30.

4.3.3. Preparation of *N*-(3-Methoxybenzyl)-9 Z ,12 Z -octadecadienamide (3)

Linoleic acid (236 μ L, 0.76 mol; 99.0% pure), HOBt·H₂O (103 mg, 0.76 mmol), and EDAC (146 mg, 0.76 mmol) were dissolved in DCM (50 mL). The reaction mixture was stirred at 24 °C for 20 h. Subsequently, 3-methoxybenzylamine (98 μ L, 98.0% pure) and triethylamine (264 μ L, 1.5 mmol, 99.0% pure) were added to the resulting mixture. The same operating steps were followed as for the preparation of NBH, except that the *n*-hexane solution was subjected to silica gel column chromatography (petroleum ether/ethyl acetate, 1:1) to yield the pure product as a colorless oil after solvent evaporation (31.25% yield, 96.21% pure). IR ν_{\max} 3288, 3008, 2928, 2855, 1646, 1254, 1154, 1052, 737, 694 cm^{-1} ; MS, C₂₆H₄₁NO₂, [M + H]: 400.32.

4.3.4. Preparation of *N*-Benzyl-9 Z ,12 Z -octadecadienamide (4)

Linoleic acid (236 μ L, 0.76 mol; 99.0% pure), HOBt·H₂O (103 mg, 0.76 mmol), and EDAC (146 mg, 0.76 mmol) were dissolved in DCM (50 mL). The reaction mixture was stirred at 24 °C for 20 h. Subsequently, benzylamine (83 μ L, 99.0% pure) and triethylamine (264 μ L, 1.5 mmol, 99.0% pure) were added to the resulting mixture. The same operating steps were followed for the preparation of NBH, except that the recrystallization temperature was −20 °C. Finally, the crystals were dried to yield the product as white oil (43.97% yield, 95.13% pure). IR ν_{\max} 3288, 3009, 2926, 2855, 1645, 1549, 1455, 1252, 1029, 726, 697 cm^{-1} ; MS, C₂₅H₃₉NO, [M + H]: 372.31.

4.3.5. Preparation of *N*-(3-Methoxybenzyl)-9 Z ,12 Z ,15 Z -octadecatrienamide (5)

Linolenic acid (233 μ L, 0.76 mol; 99.0% pure), HOBt·H₂O (103 mg, 0.76 mmol), and EDAC (146 mg, 0.76 mmol) were dissolved in DCM (50 mL). The reaction mixture was stirred at 24 °C for 20 h. Subsequently, 3-methoxybenzylamine (98 μ L, 98.0% pure) and triethylamine (264 μ L, 1.5 mmol, 99.0% pure) were added to the resulting mixture. The same operating steps were followed as for the preparation of NBH, except that the *n*-hexane solution was subjected to silica gel column chromatography (petroleum ether/ethyl acetate, 1:1) to yield the pure product as a light brown oil after solvent evaporation (30.79% yield, 95.92% pure). IR ν_{\max} 3300, 2931, 2856, 1647, 1265, 1154, 1051, 700 cm^{-1} ; MS, C₂₆H₃₉NO₂, [M + H]: 398.31.

4.4. The Preparation of Macamides-Rich Extracts

The dried maca powder (40 mesh) 1 g was mixed with diethyl ether 30 mL and then ultrasonic extracted for 30 min. The solution was centrifuged at 4000 rpm for 15 min, and then the supernatant was concentrated by a rotary vacuum evaporator to obtain a dry extract. A certain amount of diethyl ether extract of maca was further washed with ethanol 5 mL and 5 mL sodium hydroxide (1 mol/L) in a water bath at 50 °C for 50 min, and 2 mL carbonic acid was added to neutralize. Finally, the concentrated solution was dissolved with *n*-hexane 5 mL and water 30 mL by ultrasonic to obtain *n*-hexane content. Finally, the *n*-hexane layer was dried, and its macamide content was analyzed using HPLC [37,38].

4.5. Anti-Fatigue Activity of NBH

4.5.1. Animals and Groups

The following anti-fatigue activity experiment was designed mainly based on previous research [19,39,40]. Adult male C57 mice, weighing an average of 20 g, were obtained from Guangdong Medical Laboratory Animal Center (certificate number SCXK-2013-0002). The animals were housed under controlled conditions (room temperature of 24 °C, relative humidity of 38–60%, 12 h/12 h light/dark cycle) and had free access to food and water. All experiments were performed by the Animal Care and Use Committee of Guangdong Pharmaceutical University.

Before the experimental mice were forced to swim, the mice that failed to learn to swim were eliminated. After that, 18 mice were randomly divided into three groups: (1) blank group, treated with distilled water; (2) control group: treated with 1000 mg/kg extract of

maca; (3) experiment group (NBH): treated with 10 mg/kg. Oral gavage was performed at 2 p.m. for 28 days.

4.5.2. Forced Swimming Times and Biochemical Parameters

During 28 days of gavage, the body weight of each group of mice was measured before being forced to swim on days 0, 7, 14, and 28. The swimming test was as follows: each time mice had been orally gavaged, they were allowed to rest for 30 min and loaded with a tin wire (10% of body weight) attached to their tails. Then, the mice were individually dropped into a plastic swimming pool (50 cm × 50 cm × 40 cm) containing 35 cm deep water at 25 ± 1 °C. The exhaustive swimming time was immediately recorded when mice failed to rise to the surface of the water to breathe within 3 s. After the forced swimming test, the mice were allowed to rest for 30 min and then were anesthetized with ether. Blood samples were collected from the eyeball and centrifugated at 4000 rpm for 10 min, which was used for BUN, BLA, LDH, and BA determination. After the blood was obtained, the liver was immediately taken out and analyzed for HG. All kits were purchased from Nanjing Jiancheng Bioengineering Institute (Nanjing, China).

4.6. Statistical Analysis

Experimental data were represented as mean ± standard deviation. Differences between groups were estimated by one-way analysis of variance (ANOVA) using GraphPad Prism and Excel. Differences at $p < 0.05$ or $p < 0.01$ were considered significant.

5. Conclusions

We have successfully developed an efficient and simple synthetic protocol for the synthesis of the five main macamides, achieving a purity of over 95% and a yield of more than 30%. The macamides were identified using a combination of HPLC, MS, ¹H and ¹³C NMR, and IR techniques. By synthesizing macamides in large quantities rather than using maca extracts, they can be utilized in pharmacological experiments and for quality control of maca products. Furthermore, NBH is the representative monomer in macamides. Animal experiments demonstrated that it has anti-fatigue activity, which can be primarily attributed to its ability to raise the LG level and reduce the levels of BUN, LDH, BA, and BLA. NBH may be a promising candidate for alleviating fatigue for further study.

Supplementary Materials: The following supporting information can be downloaded at: <https://www.mdpi.com/article/10.3390/molecules28093943/s1>, Table S1: ¹H NMR spectrums data of macamides 1–5; Table S2: ¹³C NMR spectrums data of macamides 1–5; Figure S1: Mass spectrums of macamides 2–5; Figure S2: Infrared spectrums of macamides 2–5; Figure S3: ¹³C NMR spectrums of macamides 2–5; Figure S4: ¹H NMR spectrums of macamides 2–5.

Author Contributions: Conceptualization, T.L.; methodology; investigation, Z.P., W.L., Y.S., M.H. and Q.G.; data curation, L.G.; writing—original draft preparation, Y.S. and W.Z.; writing—review and editing, T.L. and J.K.; supervision, X.J.; project administration, H.Y.; funding acquisition, H.Y. All authors have read and agreed to the published version of the manuscript.

Funding: This research was funded by National Natural Science Foundation of China, grant number 82171700 and 81770527, and The APC was funded by National Natural Science Foundation of China, grant number 82171700.

Institutional Review Board Statement: All animal experimental protocols were approved by the Ethics Committee of Guangdong Pharmaceutical University (Approval code: gdpulac 2023053. Approval date: 2023-03-03), and strictly followed the ARRIVE guidelines.

Informed Consent Statement: Not applicable.

Data Availability Statement: Data sharing is not applicable to this article.

Conflicts of Interest: The authors declare no conflict of interest.

Sample Availability: Samples of the compounds Macamides 1–5 are available from the authors.

References


- Esparza, E.; Hadzich, A.; Kofer, W.; Mithöfer, A.; Cosio, E.G. Bioactive maca (*Lepidium meyenii*) alkalimides are a result of traditional Andean postharvest drying practices. *Phytochemistry* **2015**, *116*, 138–148. [CrossRef] [PubMed]
- Wang, S.; Zhu, F. Chemical composition and health effects of maca (*Lepidium meyenii*). *Food Chem.* **2019**, *288*, 422–443. [CrossRef]
- Tafari, S.; Cocchia, N.; Vasseti, A.; Carotenuto, D.; Esposito, L.; Maruccio, L.; Avallone, L.; Ciani, F. *Lepidium meyenii* (Maca) in male reproduction. *Nat. Prod. Res.* **2021**, *35*, 4550–4559. [CrossRef] [PubMed]
- Ai, Z.; Cheng, A.F.; Yu, Y.T.; Yu, L.J.; Jin, W. Antidepressant-Like Behavioral, Anatomical, and Biochemical Effects of Petroleum Ether Extract from Maca (*Lepidium meyenii*) in Mice Exposed to Chronic Unpredictable Mild Stress. *J. Med. Food* **2014**, *17*, 535–542. [CrossRef] [PubMed]
- Alasmari, M.; Böhlke, M.; Kelley, C.; Maher, T.; Pino-Figueroa, A. Inhibition of Fatty Acid Amide Hydrolase (FAAH) by Macamides. *Mol. Neurobiol.* **2019**, *56*, 1770–1781. [CrossRef]
- Lee, Y.-K.; Chang, Y.H. Physicochemical and antioxidant properties of methanol extract from Maca (*Lepidium meyenii* Walp.) leaves and roots. *Food Sci. Technol.* **2019**, *39*, 278–286. [CrossRef]
- Li, A.; Liu, J.; Ding, F.; Wu, X.; Pan, C.; Wang, Q.; Gao, M.; Duan, S.; Han, X.; Xia, K.; et al. Maca extracts regulate glucose and lipid metabolism in insulin-resistant HepG2 cells via the PI3K/AKT signalling pathway. *Food Sci. Nutr.* **2021**, *9*, 2894–2907. [CrossRef]
- Fei, W.; Hou, Y.; Yue, N.; Zhou, X.; Wang, Y.; Wang, L.; Li, A.; Zhang, J. The effects of aqueous extract of Maca on energy metabolism and immunoregulation. *Eur. J. Med. Res.* **2020**, *25*, 24. [CrossRef]
- Yang, Q.; Jin, W.; Lv, X.; Dai, P.; Ao, Y.; Wu, M.; Deng, W.; Yu, L. Effects of macamides on endurance capacity and anti-fatigue property in prolonged swimming mice. *Pharm. Biol.* **2016**, *54*, 827–834. [CrossRef]
- Zhou, Y.; Li, P.; Brantner, A.; Wang, H.; Shu, X.; Yang, J.; Si, N.; Han, L.; Zhao, H.; Bian, B. Chemical profiling analysis of Maca using UHPLC-ESI-Orbitrap MS coupled with UHPLC-ESI-Qq MS and the neuroprotective study on its active ingredients. *Sci. Rep.* **2017**, *7*, 44660. [CrossRef]
- Jiao, M.; Dong, Q.; Zhang, Y.; Lin, M.; Zhou, W.; Liu, T.; Yuan, B.; Yin, H. Neuroprotection of N-benzyl Eicosapentaenamide in Neonatal Mice Following Hypoxic-Ischemic Brain Injury. *Molecules* **2021**, *26*, 3108. [CrossRef] [PubMed]
- Zha, R.; Ge, E.; Guo, L.; Gao, Q.; Lin, Q.; Zhou, W.; Jin, X.; Xie, W.; Yin, H.; Liu, T. A newly identified polyunsaturated macamide alleviates dextran sulfate sodium-induced colitis in mice. *Fitoterapia* **2021**, *152*, 104916. [CrossRef] [PubMed]
- Guo, L.; Gao, Q.; Zhu, J.; Jin, X.; Yin, H.; Liu, T. A Docosahexaenoic Acid Derivative (N-Benzyl Docosahexaenamide) as a Potential Therapeutic Candidate for Treatment of Ovarian Injury in the Mouse Model. *Molecules* **2022**, *27*, 2754. [CrossRef] [PubMed]
- Yu, Z.; Liu, H.; Li, D.; Chen, X.; Ao, M.; Jin, W.; Yu, L. N-(3-Methoxybenzyl)-(9Z,12Z,15Z)-octadecatrienamide from maca (*Lepidium meyenii* Walp.) ameliorates corticosterone-induced testicular toxicity in rats. *Food Funct.* **2020**, *11*, 7762–7774. [CrossRef]
- Lamou, B.; Taiwe, G.S.; Hamadou, A.; Abene; Houlray, J.; Atour, M.M.; Tan, P.V. Antioxidant and Antifatigue Properties of the Aqueous Extract of *Moringa oleifera* in Rats Subjected to Forced Swimming Endurance Test. *Oxid. Med. Cell Longev.* **2016**, *2016*, 3517824. [CrossRef]
- Wu, H.; Kelley, C.J.; Pino-Figueroa, A.; Vu, H.D.; Maher, T.J. Macamides and their synthetic analogs: Evaluation of in vitro FAAH inhibition. *Bioorgan. Med. Chem.* **2013**, *21*, 5188–5197. [CrossRef]
- Fu, L.; Wei, J.; Gao, Y.; Chen, R. Antioxidant and antitumoral activities of isolated macamide and macaene fractions from *Lepidium meyenii* (Maca). *Talanta* **2021**, *221*, 121635. [CrossRef]
- Armario, A. The forced swim test: Historical, conceptual and methodological considerations and its relationship with individual behavioral traits. *Neurosci. Biobehav. Rev.* **2021**, *128*, 74–86. [CrossRef]
- Zhao, H.P.; Zhang, Y.; Liu, Z.; Chen, J.Y.; Zhang, S.Y.; Yang, X.D.; Zhou, H.L. Acute toxicity and anti-fatigue activity of polysaccharide-rich extract from corn silk. *Biomed. Pharmacother.* **2017**, *90*, 686–693. [CrossRef]
- Tan, W.; Yu, K.Q.; Liu, Y.Y.; Ouyang, M.Z.; Yan, M.H.; Luo, R.; Zhao, X.S. Anti-fatigue activity of polysaccharides extract from *Radix Rehmanniae Preparata*. *Int. J. Biol. Macromol.* **2012**, *50*, 59–62. [CrossRef]
- Li, Z.; Zhu, H.; Hua, H.; Liu, C.; Cheng, Y.; Guo, Y.; Du, P.; Qian, H. Anti-fatigue activity of *Brassica rapa* L. extract and correlation among biochemical changes in forced swimming mice. *Food Biosci.* **2022**, *47*, 101633. [CrossRef]
- Li, J.; Sun, Q.; Meng, Q.; Wang, L.; Xiong, W.; Zhang, L. Anti-fatigue activity of polysaccharide fractions from *Lepidium meyenii* Walp. (maca). *Int. J. Biol. Macromol.* **2017**, *95*, 1305–1311. [CrossRef] [PubMed]
- Zhu, H.; Wang, R.; Hua, H.; Cheng, Y.; Guo, Y.; Qian, H.; Du, P. The macamide relieves fatigue by acting as inhibitor of inflammatory response in exercising mice: From central to peripheral. *Eur. J. Pharmacol.* **2022**, *917*, 174758. [CrossRef] [PubMed]
- Huang, L.Z.; Huang, B.K.; Liang, J.; Zheng, C.J.; Han, T.; Zhang, Q.Y.; Qin, L.P. Antifatigue activity of the liposoluble fraction from *Acanthopanax senticosus*. *Phytother. Res.* **2011**, *25*, 940–943. [CrossRef] [PubMed]
- Trefts, E.; Williams, A.S.; Wasserman, D.H. Exercise and the Regulation of Hepatic Metabolism. *Prog. Mol. Biol. Transl. Sci.* **2015**, *135*, 203–225. [CrossRef]
- Zhao, X.N.; Liang, J.L.; Chen, H.B.; Liang, Y.E.; Guo, H.Z.; Su, Z.R.; Li, Y.C.; Zeng, H.F.; Zhang, X.J. Anti-Fatigue and Antioxidant Activity of the Polysaccharides Isolated from *Milletia speciosa* Champ. Leguminosae. *Nutrients* **2015**, *7*, 8657–8669. [CrossRef]
- Gbadebo, O.; Fox, K.; Sutton, G.; Murphy, P.V.; Smith, D.; O’Leary, P. Novel versatile synthesis method for amides, carbamates and ureas employing a Grignard base, an amine and an ester. *Results Chem.* **2022**, *4*, 100253. [CrossRef]
- Leggio, A.; Bagalà, J.; Belsito, E.L.; Comandè, A.; Greco, M.; Liguori, A. Formation of amides: One-pot condensation of carboxylic acids and amines mediated by TiCl₄. *Chem. Cent. J.* **2017**, *11*, 87. [CrossRef]

29. Zhao, J.; Muhammad, I.; Dunbar, D.C.; Mustafa, J.; Khan, I.A. New Alkamides from Maca (*Lepidium meyenii*). *J. Agric. Food Chem.* **2005**, *53*, 690. [CrossRef]
30. McCollom, M.M.; Villinski, J.R.; McPhail, K.L.; Craker, L.E.; Gafner, S. Analysis of macamides in samples of Maca (*Lepidium meyenii*) by HPLC-UV-MS/MS. *Phytochem. Anal.* **2005**, *16*, 463–469. [CrossRef]
31. Liu, R.; Zhang, P.; Zhang, Z.J.; Wang, B.; Zhang, Z.F. A practical model for efficient anti-fatigue design and selection of metallic materials: II. Parameter analysis and fatigue strength improvement. *J. Mater. Sci. Technol.* **2021**, *70*, 250–267. [CrossRef]
32. Lee, S.M.; Kim, Y.H.; Kim, Y.R.; Lee, B.-R.; Shin, S.; Kim, J.Y.; Jung, I.C.; Lee, M.Y. Anti-fatigue potential of Pinus koraiensis leaf extract in an acute exercise-treated mouse model. *Biomed. Pharmacother.* **2022**, *153*, 113501. [CrossRef] [PubMed]
33. Cai, M.; Zhu, H.; Xu, L.; Wang, J.; Xu, J.; Li, Z.; Yang, K.; Wu, J.; Sun, P. Structure, anti-fatigue activity and regulation on gut microflora in vivo of ethanol-fractional polysaccharides from *Dendrobium officinale*. *Int. J. Biol. Macromol.* **2023**, *234*, 123572. [CrossRef]
34. Chen, J.; Lu, X.; Chen, P.; Shen, Y.; Zheng, B.; Guo, Z. Anti-fatigue effect of glycoprotein from hairtail (*Trichiurus lepturus*) by-products in a behavioral mouse model. *Food Chem. X* **2023**, *18*, 100645. [CrossRef] [PubMed]
35. So, J.; Wu, D.; Lichtenstein, A.H.; Tai, A.K.; Matthan, N.R.; Maddipati, K.R.; Lamon-Fava, S. EPA and DHA differentially modulate monocyte inflammatory response in subjects with chronic inflammation in part via plasma specialized pro-resolving lipid mediators: A randomized, double-blind, crossover study. *Atherosclerosis* **2021**, *316*, 90–98. [CrossRef] [PubMed]
36. Wang, C.-C.; Shi, H.-H.; Zhang, L.-Y.; Ding, L.; Xue, C.-H.; Yanagita, T.; Zhang, T.-T.; Wang, Y.-M. The rapid effects of eicosapentaenoic acid (EPA) enriched phospholipids on alleviating exercise fatigue in mice. *RSC Adv.* **2019**, *9*, 33863–33871. [CrossRef]
37. Lin, L.; Huang, J.; Sun-Waterhouse, D.; Zhao, M.; Zhao, K.; Que, J. Maca (*Lepidium meyenii*) as a source of macamides and polysaccharide in combating of oxidative stress and damage in human erythrocytes. *Int. J. Food Sci. Technol.* **2018**, *53*, 304–312. [CrossRef]
38. Zhu, H.; Hu, B.; Hua, H.; Liu, C.; Cheng, Y.; Guo, Y.; Yao, W.; Qian, H. Macamides: A review of structures, isolation, therapeutics and prospects. *Food Res. Int.* **2020**, *138*, 109819. [CrossRef]
39. Jia, L.; Zhao, F. Evaluation of silymarin extract from *Silybum marianum* in mice: Anti-fatigue activity. *Food Sci. Hum. Well* **2022**, *11*, 914–921. [CrossRef]
40. Li, W.; Luo, C.; Huang, Y.; Zhan, J.; Lei, J.; Li, N.; Huang, X.; Luo, H. Evaluation of antifatigue and antioxidant activities of the marine microalgae *Isochrysis galbana* in mice. *Food Sci. Biotechnol.* **2020**, *29*, 549–557. [CrossRef]

Disclaimer/Publisher’s Note: The statements, opinions and data contained in all publications are solely those of the individual author(s) and contributor(s) and not of MDPI and/or the editor(s). MDPI and/or the editor(s) disclaim responsibility for any injury to people or property resulting from any ideas, methods, instructions or products referred to in the content.

Article

Triterpenes and Pheophorbides from *Camellia ptilosperma* and Their Cytotoxicity, Photocytotoxicity, and Photodynamic Antibacterial Activity

Siyuan Ma ^{1,†}, Mengling Weng ^{2,†}, Ting Yang ³, Li Ge ^{4,*} and Kedi Yang ^{1,4,*} 

¹ School of Chemistry & Chemical Engineering, Guangxi University, Nanning 530004, China; masiyuan@aliyun.com

² Key Laboratory of Sugarcane Biotechnology and Genetic Improvement (Guangxi), Ministry of Agriculture & Rural Affairs, Guangxi Key Laboratory of Sugarcane Genetic Improvement, Sugarcane Research Institute, Guangxi Academy of Agricultural Sciences, Nanning 530004, China

³ Guangxi Fangcheng Golden Camellia National Nature Reserve Management Center, Fangchenggang 538021, China

⁴ Medical College, Guangxi University, Nanning 530004, China

* Correspondence: geli_2009@163.com (L.G.); kdyang@163.com (K.Y.); Tel.: +86-771-3949953 (K.Y.)

† These authors contributed equally to this work.

Abstract: Phytochemical investigation of the leaves of *Camellia ptilosperma* S. Y. Liang et Q. D. Chen led to the isolation of ten undescribed compounds, including six new triterpenes (1–6) and four new pheophorbide-related compounds (7–10). Meanwhile, the cytotoxic activity of the six triterpenes against six cancer cell lines was evaluated by MTT assay. Compound 2 showed potent cytotoxicity toward HepG2 cells with an IC₅₀ value of 2.57 μM. Compounds 4 and 5 exhibited cytotoxicity against MDA-MB231 cells, with IC₅₀ values of 11.31 and 5.52 μM, respectively. Additionally, the cytotoxicity of four new pheophorbides against these cancer cells was evaluated both in the presence and absence of light treatment. Compound 7 exhibited exceptional photocytotoxicity against HeLa, MCF-7, and A549 cells, with IC₅₀ values of 0.43 μM, 0.28 μM, and 0.92 μM, respectively. Compound 10 demonstrated significant photodynamic cytotoxic activity against BEL-7402 and HepG2 cells with IC₅₀ values of 0.77 μM and 0.33 μM, respectively. The photodynamic antibacterial activity of 7–10 was also tested for *S. aureus*, *E. coli*, *K. pneumoniae*, and *P. aeruginosa* under direct illumination. Compounds 8 and 10 exhibited sensitivity to *E. coli* and demonstrated a photodynamic antibacterial effect, with a MIC value of 0.625 μM.

Keywords: *Camellia ptilosperma*; triterpene; pheophorbide; cytotoxicity; antibacterial activity; photodynamic therapy



Citation: Ma, S.; Weng, M.; Yang, T.; Ge, L.; Yang, K. Triterpenes and Pheophorbides from *Camellia ptilosperma* and Their Cytotoxicity, Photocytotoxicity, and Photodynamic Antibacterial Activity. *Molecules* **2023**, *28*, 7058. <https://doi.org/10.3390/molecules28207058>

Academic Editor: Kemal Husnu Can Baser

Received: 20 September 2023

Revised: 30 September 2023

Accepted: 10 October 2023

Published: 12 October 2023



Copyright: © 2023 by the authors. Licensee MDPI, Basel, Switzerland. This article is an open access article distributed under the terms and conditions of the Creative Commons Attribution (CC BY) license (<https://creativecommons.org/licenses/by/4.0/>).

1. Introduction

Yellow camellia, a member of the Theaceae family, is an evergreen shrub or dune-garunga that was first discovered in Fangchenggang, Guangxi, China in 1933. To date, more than 43 species, including 5 variants, of yellow camellias have been identified, with their primary distribution spanning southwest China and northern Vietnam [1]. Distinguished from common tea plants with their red, pink, and white flowers, yellow camellia has unique golden-yellow flowers due to which it is honored as ‘flora panda’ and ‘camellia queen’. The leaves and flowers of yellow camellias are commonly utilized in the preparation of a popular tea known as Jin-Hua-Cha among local communities. Furthermore, local communities have long employed yellow camellias as traditional remedies for conditions such as hypertension, sore throat, and cancer prevention. In 2010, the Chinese Ministry of Health included yellow camellia in the national list of new food resources, leading to the continued development of functional foods based on yellow camellia, and currently available products include oral solutions [2] and instant teas [3] with yellow

camellia. *Camellia ptilosperma*, a renowned species of yellow camellia, was discovered in 1982 in Chongzuo, Guangxi. Unlike other yellow camellia, which bloom from September to November, *C. ptilosperma* blooms from July to the following April [4].

The biological activity research on yellow camellia has mainly focused on *C. tungghinensis* and *C. nitidissima*, and has documented the diverse pharmacological properties of phytochemicals or crude extracts derived from yellow camellia, encompassing antioxidant activity [5,6], anti-hypertensive [7] and hyperlipidemic effects [8,9], hypoglycemic effects [10,11], antibacterial effects [12], anticancer activity [13–16], and anti-depressive effects [17,18].

The chemical composition of *C. ptilosperma* is currently unknown. In view of its potential medicinal and economic value, there is a need for phytochemical research on it. According to the literature reports, the leaves of plants in *Theaceae* contain mainly polyphenols, terpenes, flavonoids, tannins, and chlorophylls [19–22]. Although polyphenols, flavonoids, and tannins have been extensively studied [23–27], there have been no relevant reports on pheophorbide in the last 5 years. Chlorophyll and pheophorbide belong to the porphyrin group and are potential photosensitizers [28–30]. In the presence of light, they can produce free radicals or reactive oxygen species, which have a powerful killing effect on bacteria, microorganisms, and viruses [31,32]. Many triterpenoids have shown anti-tumor activity [33–35]. Therefore, this study focuses on the triterpenoids and pheophorbides in *C. ptilosperma*. In the biological activity experiment section, the cytotoxic activity of triterpenoids against cancer cells, photocytotoxicity against cancer cells, and the photodynamic antibacterial activity of pheophorbides were evaluated.

2. Results and Discussion

In this work, ten undescribed compounds, including six triterpenes (1–6, Figure 1) and four pheophorbides (7–10, Figure 1), were isolated from the leaves of *C. ptilosperma*. The cytotoxic activity of the six triterpenes against six cancer cell lines, namely Hela, MCF-7, BEL-7402, A549, HepG2, and MDA-MB-231, was evaluated by MTT assay. The photocytotoxic activity of four pheophorbides on the same human tumor cell lines was tested under both illuminated and non-illuminated conditions. Furthermore, the antimicrobial properties of pheophorbides were evaluated against a range of bacteria, including *S. aureus*, *E. coli*, *K. pneumoniae*, and *P. aeruginosa*.

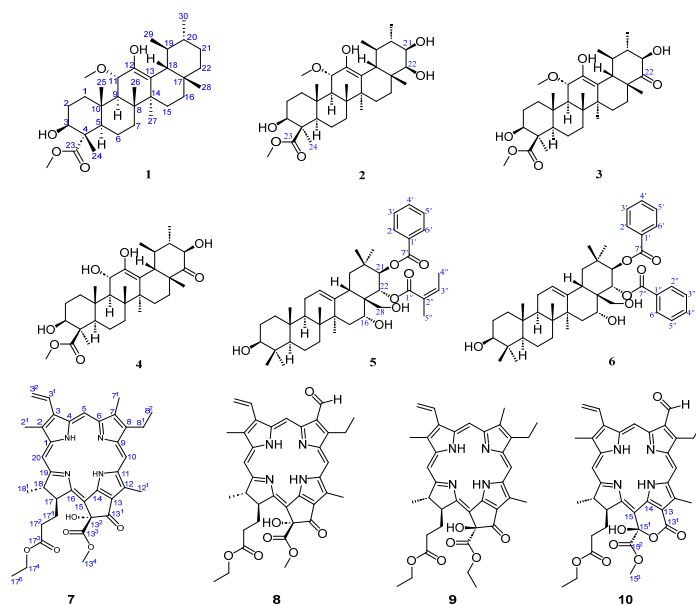


Figure 1. Structure of compounds 1–10 from the leaves of *C. ptilosperma*.

Compound **1** was obtained as a colorless solid. Its molecular formula was $C_{32}H_{52}O_5$ given by HR-ESI-MS (539.3718, $[M+Na]^+$, calcd. for $C_{32}H_{52}O_5Na$, 539.3712) with 7 degrees of unsaturation. Also, the Liebermann–Burchard reaction for **1** was positive, suggesting a triterpenoid structure. 1H NMR data (Table 1) demonstrated two distinctive methines at δ_H 0.92 (d, $J = 6.6$ Hz, H-29) and 0.93 (d, $J = 6.4$ Hz, H-30), which coincided with the ursane-type triterpene skeleton. The 1H and ^{13}C NMR data (Table 1) revealed the presence of the other five methyl groups (δ_H 0.80, 1.09, 1.13, 1.18, and 1.21), one oxygenated methine group at δ_H 4.00 (dd, $J = 11.5, 5.1$ Hz) and two methoxyl groups at δ_H 3.18 (s) and 3.73 (s). A hydroxy group was located in C-3 (δ_C 75.3) based on the HMBC correlations (Figure 2) between H-3 (δ_H 4.00), C-23 (δ_C 178.1), and C-24 (δ_C 11.0). The relative configuration of the 3-OH was a β -orientation, which was established from the trans-diaxial coupling constant of H-3 ($J = 11.5$ Hz) and the NOESY correlations (Figure 2) of the proton signals at H-3 (δ_H 4.00), H-5 (δ_H 1.55), and H-9 (δ_H 1.94), respectively. The hydroxy group attached to C-12 was confirmed by the HMBC correlations of 12-OH (δ_H 4.53) with C-11 (δ_C 76.4), C-12 (δ_C 141.7), and C-13 (δ_C 118.3). The cross-peak from δ_H 3.18 (3H, s) to δ_C 76.4 (C-11) in the HMBC spectrum indicated a methoxyl group attached to C-11. In addition, a β -oriented H-11 could be deduced from the large 3J values of 10.4 Hz and NOESY correlations of H-11 (δ_H 4.26) with H-25 (δ_H 1.13) and H-26 (δ_H 1.09). The presence of a methyl ester group at C-4 was confirmed by the HMBC correlations between 23-OCH₃ (δ_H 3.73) and C-23 (δ_C 178.1), as well as between H-3 (δ_H 4.00) and C-23 (δ_C 178.1). Thus, compound **1** was determined to be 11 α -methoxy-3 β ,12-dihydroxyurs-12-en-23-oic acid methyl ester.

Table 1. 1H (600 MHz) and ^{13}C (151MHz) NMR data for compounds **1–4** in $CDCl_3$.

No.	1		2		3		4	
	δ_H (J in Hz)	δ_C	δ_H (J in Hz)	δ_C	δ_H (J in Hz)	δ_C	δ_H (J in Hz)	δ_C
1	1.32 m 2.27 dt-like (13.6, 3.4)	38.6	1.21 m 2.34 dt-like (13.4, 3.5)	39.8	1.22 m 2.38 dt-like (13.3, 3.3)	39.9	1.22 m 2.40 dt-like (13.3, 3.5)	41.8
2	1.60–1.71 m	26.8	1.77 m 2.03 m	28.3	1.78 m 2.04 m	28.4	1.79 m 2.04 m	28.2
3	4.00 dd (11.5, 5.1)	75.3	3.11 dd (12.1, 4.3)	77.9	3.11 ddd (11.9, 11.9, 4.4)	77.9	3.11 td-like (11.7, 4.3)	77.8
4		54.2		49.3		49.4		49.2
5	1.55 m	51.1	0.95 m	56.7	0.97 m	56.8	0.97 m	56.6
6	1.01 m 1.55 m	21.3	1.66 m 1.82 m	19.9	1.67 m 1.84 m	19.8	1.68 m 1.85 m	19.9
7	1.31 m 1.53 m	33.7	1.35–1.48 m	34.2	1.40–1.49 m	34.5	1.38–1.51 m	34.2
8		43.1		42.7		42.5		42.4
9	1.94 d (10.4)	46.3	1.86 d (10.7)	45.3	1.89 d (10.7)	44.7	1.61 d (9.8)	53.3
10		37.7		38.5		38.6		38.5
11	4.26 d (10.4)	76.4	4.23 d (10.5)	76.5	4.27 d (10.7)	76.3	4.16 br d (10.7)	70.5
12		141.7		142.8		143.4		145.9
13		118.3		116.6		114.5		112.3
14		40.6		41.0		40.6		40.8
15	0.98 br d (13.5) 1.77 td-like (13.5, 5.1) 0.83 br d (13.5)	27.1	1.02 m 1.81 m	26.4	1.13 m 1.79 m	25.6	1.13 m 1.76 m	25.3
16	2.01 td-like (13.5, 4.8)	27.5	1.02 m 1.81 m	26.6	1.26 m 2.06 m	28.0	1.26 m 2.05 m	28.1
17		33.3		38.3		47.8		47.7
18	2.24 dd (11.4, 1.3)	47.6	2.62 br d (11.2)	41.8	2.75 d (11.6)	48.1	2.66 br d (11.6)	47.7
19	1.37 m	40.8	1.51 m	39.1	1.95 m	38.5	1.95 m	38.4
20	1.03 m	39.5	1.45 m	39.1	1.29 m	47.2	1.30 m	47.3
21	1.26 m 1.41 m	31.2	3.49 dd (10.5, 2.7)	73.5	4.05 dd (11.6, 3.0)	76.4	4.06 dd (11.6, 3.0)	76.4

Table 1. Cont.

	1		2		3		4	
No.	δ_H (J in Hz)	δ_C	δ_H (J in Hz)	δ_C	δ_H (J in Hz)	δ_C	δ_H (J in Hz)	δ_C
22	1.32–1.46 m	41.6	3.40 d (2.7)	78.7		215.3		215.2
23		178.1	1.42 s	23.8	1.43 s	23.8	1.44 s	23.8
24	1.18 s	11.0		178.4		178.3		178.3
25	1.13 s	16.6	0.95 s	14.0	0.97 s	14.0	0.98 s	14.3
26	1.09 s	18.0	1.12 s	18.0	1.12 s	18.1	1.10 s	18.0
27	1.21 s	24.0	1.19 s	24.1	1.29 s	23.6	1.28 s	23.8
28	0.80 s	28.5	0.96 s	21.9	1.09 s	20.1	1.09 s	20.3
29	0.92 d (6.6)	17.0	0.96 d (6.6)	16.8	1.02 d (6.7)	16.0	0.98 d (6.6)	15.8
30	0.93 d (6.4)	21.2	1.06 d (6.1)	16.0	1.20 d (6.3)	16.8	1.19 d (6.3)	16.7
3-OH					3.39 d (11.9)		3.39 d (12.0)	
12-OH	4.53 br s		4.69 br s		4.76 s		4.88 br s	
21-OH					3.79 d (3.0)		3.80 d (3.0)	
11-OCH ₃	3.18 s	51.3	3.14 s	51.1	3.14 s	50.8		
23-OCH ₃	3.73 s	52.2						
24-OCH ₃			3.69 s	51.3	3.70 s	51.3	3.71 s	51.4

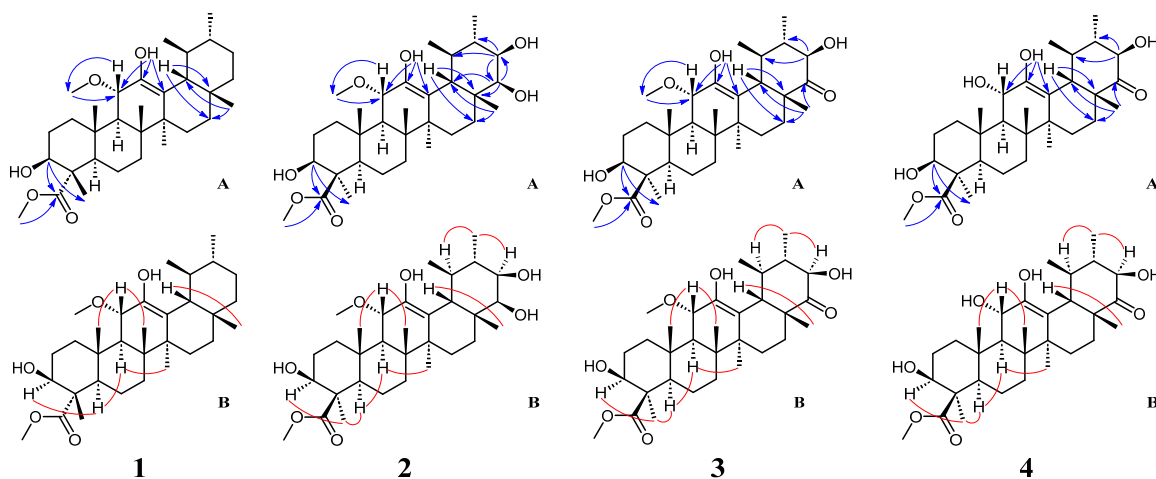


Figure 2. Key HMBC (A) and NOESY (B) correlations of compounds 1–4.

Compound 2 was isolated as a white powder and showed a molecular formula of $C_{32}H_{52}O_7$ by HR-ESI-MS (m/z 571.3605, $[M+Na]^+$, calcd. 571.3611). Its 1H and ^{13}C NMR data (Table 1) closely resembled those of compound 1 except for the presence of two hydroxy groups at C-21 (δ_C 73.5) and C-22 (δ_C 78.7), respectively, as well as a relative difference in the configuration of the methyl and methyl ester attached to C-4. The positions of the two additional hydroxy groups were confirmed by the HMBC correlations (Figure 2) from H-21 (δ_H 3.49) to C-20 (δ_C 39.1), C-22 (δ_C 78.7), and C-29 (δ_C 16.8) and from H-22 (δ_H 3.40) and C-21 (δ_C 73.5), C-17 (δ_C 38.3), and C-21 (δ_C 73.5). Cross-peaks (Figure 2) between resonances at δ_H 3.49 (H-21), δ_H 1.06 (H₃-30), and δ_H 1.51 (H-19) in the NOESY spectrum confirmed the β -orientation of the hydroxy group at C-21. A small coupling constant of 2.7 Hz between H-21 and H-22 suggested that two protons were in the *cis*-form and that the 22-OH should be β -oriented. Observation of NOESY correlations of H₃-23 (δ_H 1.42) with H-3 (δ_H 3.11) and H-5 (δ_H 0.95) indicated the α -configuration of the methyl group at C-4. Therefore, compound 2 was identified as 11 α -methoxy-3 β ,12,21 β ,22 β -tetrahydroxyurs-12-en-24-oic acid methyl ester.

Compound 3 was obtained as a pale powder and displayed a molecular formula of $C_{32}H_{50}O_7$ (m/z 569.3452, $[M+Na]^+$, calcd. 569.3454) based on the HR-ESI-MS data. The 1H and ^{13}C NMR data (Table 1) were very similar to compound 2 except for the absence of the hydroxy group at C-22, replaced by the carbonyl group, which was confirmed by the HMBC correlation (Figure 2) of H-28 (δ_H 1.09) to C-22 (δ_C 215.3). Therefore, compound 3 was established as 11 α -methoxy-3 β ,12,21 β -trihydroxy-22-oxours-12-en-24-oic acid methyl ester.

Compound **4** was obtained as a white powder. The molecular formula was identified as $C_{31}H_{48}O_7$ by HR-ESI-MS (m/z 555.3298, $[M+Na]^+$, calcd. 555.3298). The NMR spectroscopic data (Table 1) of **4** closely resembled those of **3** and differed only in the substitution at the C-11 position, where a hydroxyl group attached at C-11 in **4** instead of a methoxyl group in **3**. It was confirmed by the HMBC correlations (Figure 2) of H-11 (δ_H 4.16) with C-9 (δ_C 53.3) and C-12 (δ_C 145.9). The NOESY (Figure 2) cross-peaks of H-11 (δ_H 4.16) with H-25 (δ_H 0.98) and H-26 (δ_H 1.10) indicated that the hydroxy group at C-11 was an α -configuration. As a result, compound **4** was elucidated as 3 β ,11 α ,12,21 β -tetrahydroxy-22-oxours-12-en-24-oic acid methyl ester.

Compound **5** was isolated as a white powder. Its molecular formula was determined as $C_{42}H_{60}O_7$ based on HR-ESI-MS results (m/z 699.4236, $[M+Na]^+$, calcd. 699.4237), indicating 13 degrees of unsaturation. Also, the Liebermann–Burchard reaction for **5** was positive, suggesting a triterpenoid. The NMR data (Table 2) displayed the presence of eight singlets of the methyl group (at δ_H 0.79, 0.91, 0.94, 0.96, 1.00, 1.18, 1.47, and 1.67), a distinctive proton at δ_H 2.77 (*dd*, $J = 14.3, 4.2$ Hz, H-18), and two characteristic unsaturated carbons at δ_C 124.0 (C-12) and 140.6 (C-13), revealing an oleanane-type skeleton. In addition, the HSQC spectrum showed two oxymethine protons connected to the carbons C-3 (δ_C 78.9) and C-16 (δ_C 69.9), respectively, and two methylene protons attached to the carbon C-28 (δ_C 63.6) appeared as a doublet of doublets at δ_H 2.93/3.30 (each *d*, $J = 11.5$ Hz). Three hydroxy groups attached to C-3, C-16, and C-28, respectively, were confirmed by the HMBC correlations (Figure 3) of H-3 (δ_H 3.24) with C-24 (δ_C 15.6) and C-23 (δ_C 28.1), of H-15 (δ_H 1.37), H-18 (δ_H 2.77), and H-22 (δ_H 5.55) with C-16 (δ_C 69.9), and of H-22 (δ_H 5.55) with C-28 (δ_C 63.6) successively. A typical coupling constant of H-3 ($J = 11.5$ Hz) and the NOESY correlations (Figure 3) of H-3 with H-23 (δ_H 1.00) and H-5 (δ_H 0.76) indicated the axial orientation of H-3 and β -configuration of OH-3. The NEOSY correlations of H-15 β (δ_H 1.37) with H-26 (δ_H 0.91) and H-16 (δ_H 3.97) indicated that the hydroxy group at C-16 was α -configuration. Moreover, the 1H and ^{13}C NMR spectra showed five aromatic protons at δ_H 7.98 (H-2' and H-6', *d*, $J = 7.7$ Hz), 7.53 (H-4', *t*, $J = 7.3$ Hz), and 7.41 (H-3' and H-5', *dd*, $J = 7.7, 7.3$ Hz), six aromatic carbons at δ_C 128.3 (C-3' and C-5'), 129.5 (C-2' and C-6'), 130.3 (C-1'), and 132.3 (C-4'), and an ester carbonyl at δ_C 166.3 (C-7'). These data and HMBC correlations, together with the NOESY correlations of H-21 (δ_H 6.01) with H₃-29 (δ_H 0.96) and H-19 α (δ_H 2.62), confirmed the presence of a β -oriented benzoyloxy at C-21. Meanwhile, the NMR spectra also showed another ester carbonyl at δ_C 169.3 (C-1''), two olefinic carbons at 126.9 (C-2'') and 139.7 (C-3''), and two methyl groups at 15.6 (C-4'') and 20.3 (C-5''). These NMR data and NOESY correlations of H-22 (δ_H 5.55) with H-18 (δ_H 2.77) and H₃-30 (δ_H 1.18), together with HMBC correlation results demonstrated an α -configuration of the angeloyloxy group at C-22 [36]. Hence, compound **5** was identified as 21 β -benzoyloxy-22 α -angeloylolean-12-ene-3 β ,16 α ,28-triol.

Table 2. 1H (600 MHz) and ^{13}C (151MHz) NMR data for compounds **5** and **6** in $CDCl_3$.

No.	5		6	
	δ_H (<i>J</i> in Hz)	δ_C	δ_H (<i>J</i> in Hz)	δ_C
1	1.00 m 1.65 m	38.6	1.01 m 1.64 m	38.6
2	1.54–1.66 m	27.2	1.55–1.67 m	27.1
3	3.24 <i>dd</i> (11.5, 4.3)	78.9	3.23 <i>dd</i> (11.6, 4.4)	79.0
4		38.8		38.8
5	0.76 <i>br d</i> (11.8)	55.1	0.76 <i>br d</i> (10.9)	55.2
6	1.40 m 1.56 m	18.3	1.40 m 1.56 m	18.3
7	1.30 m 1.57 m	32.7	1.31 m 1.57 m	32.7
8		41.0		41.0

Table 2. Cont.

No.	5		6	
	δ_H (J in Hz)	δ_C	δ_H (J in Hz)	δ_C
9	1.64 m	46.5	1.64 m	46.5
10		36.9		36.9
11	1.88–1.96 m	23.5	1.88–1.97 m	23.5
12	5.48 t (3.3)	124.8	5.50 t (3.3)	125.1
13		140.6		140.7
14		39.7		39.7
15	1.37 m	33.7	1.38 m	33.7
16	1.70 m		1.70 m	
17	3.97 br s	69.9	4.02 br s	69.8
18		47.7		47.7
19	2.77 dd (14.3, 4.2)	39.2	2.82 dd (14.4, 4.7)	39.2
20	1.32 m		1.32 m	
21	2.62 dd (14.3, 13.2)	46.4	2.66 dd (14.4, 13.9)	46.4
22		36.1		36.1
23	6.01 d (10.2)	78.7	6.19 d (10.2)	78.6
24	5.55 d (10.2)	73.1	5.66 d (10.2)	74.5
25	1.00 s	28.1	1.00 s	28.1
26	0.79 s	15.6	0.79 s	15.6
27	0.94 s	15.6	0.94 s	15.6
28	0.91 s	16.7	0.91 s	16.7
29	1.47 s	27.1	1.47 s	27.1
30	2.93 d (11.5)	63.6	2.97 d (11.5)	63.6
31	3.30 d (11.5)		3.32 d (11.5)	
32	0.96 s	29.1	0.96 s	29.1
33	1.18 s	19.5	1.18 s	19.5
34	1'	130.3		130.1
35	2', 6'	7.98 d (7.7)	7.91 d (7.8)	129.7
36	3', 5'	7.41 dd (7.7, 7.3)	7.32 dd (7.8, 7.2)	128.4
37	4'	7.53 t (7.3)	7.46 t (7.2)	132.3
38	7'			166.3
39	1''	169.3		129.0
40	2''	126.9	7.88 d (7.8)	129.5
41	3''	5.91 br q (7.2)	7.33 dd (7.8, 7.2)	128.2
42	4''	1.77 br d (7.2)	7.42 t (7.2)	132.0
43	5''	1.67 br s	7.33 dd (7.8, 7.2)	128.2
44	6''		7.88 d (7.8)	129.5
45	7''			166.5

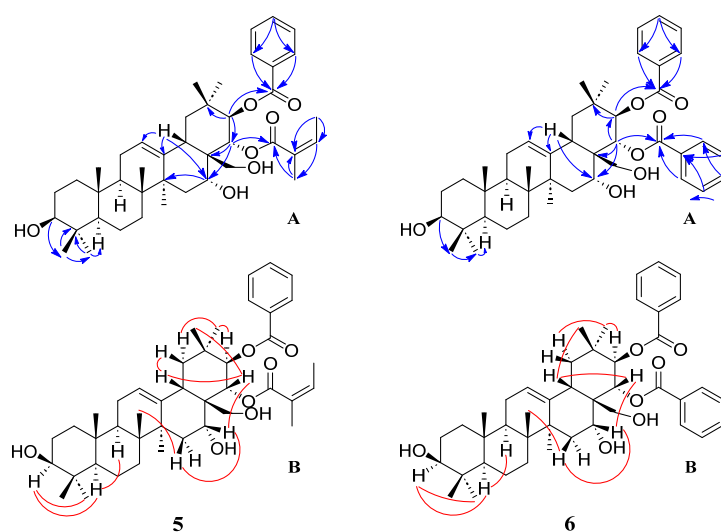


Figure 3. Key HMBC (A) and NOESY (B) correlations of compounds 5 and 6.

Compound **6** was obtained as a white amorphous powder and possessed a molecular formula of $C_{44}H_{58}O_7$ based on HR-ESI-MS analysis (m/z 721.4092 $[M+Na]^+$, calcd. 721.4080). The NMR data of **6** (Table 2) were similar to those of **5**. The inspection of the

NMR data showed a benzoyloxy substituent at C-22 in compound **6** instead of an angeloyloxy group at C-22 in **5**. The cross-peaks (Figure 3) of H-22 (δ_{H} 5.66) with H₃-30 (δ_{H} 1.18) and H-18 (δ_{H} 2.82) in the NOESY spectrum confirmed the β -orientation of the benzoyloxy group. Thus, compound **6** was ascertained as 21 β ,22 α -dibenzoyloxyolean-12-ene-3 β ,16 α ,28-triol. This structure was previously reported but no NMR spectroscopic data were available before [37]. This work reports its NMR data for the first time.

Compound **7** was obtained as a dark green amorphous solid with a molecular formula C₃₇H₄₀N₄O₆ measured by HR-ESI-MS (m/z 637.3029, [M+H]⁺, calcd. for C₃₇H₄₁N₄O₆, 637.3026). The ¹H NMR spectrum (Table 3) of **7** indicated the presence of seven methyl groups at δ_{H} 1.12 (CH₃-17⁵, t, J = 7.1 Hz), 1.69 (CH₃-8², t, J = 7.7 Hz), 1.69 (CH₃-18¹, d, J = 7.3 Hz), 3.23 (CH₃-7¹, s), 3.42 (CH₃-2¹, s), 3.65 (CH₃-13⁴, s), and 3.71 (CH₃-12¹, s), and three olefinic protons at δ_{H} 9.42 (H-5, s), 9.57 (H-10, s), and 8.61 (H-20, s), respectively. A monosubstituted vinyl proton signal appeared at δ_{H} 6.18 (dd, J = 11.5, 1.2 Hz), 6.29 (dd, J = 17.8, 1.2 Hz), and 7.99 (dd, J = 17.8, 11.5 Hz). The peaks of two interchangeable hydrogens showed at δ_{H} 0.42 and −1.73 (both br s), which disappeared with the addition of D₂O to the sample. The ¹³C NMR (Table 4) and DEPT spectra displayed two methylene carbons at δ_{C} 30.2 (C-17¹) and 31.2 (C-17²), an oxymethylene carbon at δ_{C} 60.4 (C-17⁴), a methyl carbon at δ_{C} 14.1 (C-17⁵), and an ester carbonyl carbon at δ_{C} 173.0 (C-17³). An ethyl propanoate moiety attached to C-17 (δ_{C} 50.2) was confirmed by the analysis of the ¹H-¹H COSY spectrum and HMBC correlation (Figure 4). In addition, a carboxylic acid methyl ester unit and a hydroxyl group connected to C-13² (δ_{C} 89.1) were also confirmed based on the NMR data analyses. A $J_{\text{H-17-H-18}}$ value of 8.5 Hz suggested the *trans*-orientation of the CH₃-18¹ and ethyl propanoate units in the D ring. The *R*-configuration of the carboxylic acid methyl ester unit was assigned to C-13² based on the downfield signal at δ_{H} 4.69 (H-17), in contrast with δ_{H} 4.16 ppm for the *S*-configuration, as concluded by Nakatani [38], which proposed an α -oriented hydroxyl group at C-13². Consequently, the more downfield shift of H-17 caused by the deshielding effect of the hydroxyl group also demonstrated that H-17 and HO-13² lay on the same side of the ring, so the relative configuration of CH₃-18 was established as α -orientation and that of the ethyl propanoate moiety at C-17 as β -orientation. Thus, compound **7** was identified as 13²(*R*)-hydroxypheophorbide-a ethyl ester.

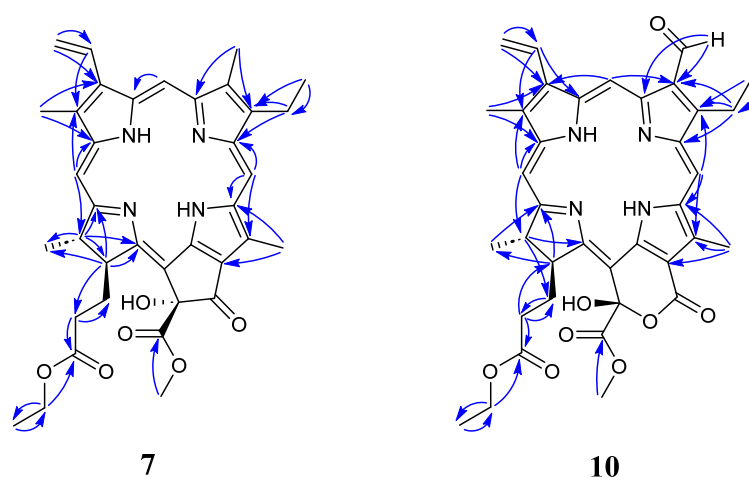
Table 3. ¹H (600 MHz) NMR data for compounds **7**–**10** in CDCl₃.

No.	7	8	9	10
2 ¹	3.42, s	3.39, s	3.43, s	3.37, s
3 ¹	7.99, dd (17.8, 11.5)	7.99, dd (17.8, 11.6)	8.03, dd (17.8, 11.6)	7.90, dd (17.8, 11.6)
3 ²	6.18, dd (11.5, 1.2)	6.23, d, (11.6)	6.20, dd (11.6, 1.3)	6.17, d (11.6)
5	6.29, dd (17.8, 1.2)	6.37, d, (17.8)	6.31, dd (17.8, 1.3)	6.35, d (17.8)
7 ¹	9.42, s	10.37, s	9.50, s	10.28, s
7 ²	3.23, s	11.11, s	3.28, s	11.00, s
8 ¹	3.68, q (7.7)	4.01, m	3.73, q (7.7)	3.91, q (7.5)
8 ²	1.69, t (7.7)	1.80, t (7.7)	1.71, t (7.7)	1.75, t (7.5)
10	9.57, s	9.64, s	9.64, s	9.65, s
12 ¹	3.71, s	3.69, s	3.74, s	3.83, s
13 ⁴	3.65, s	3.66, s	4.09, m	
13 ⁵			4.25, m	
15 ³			0.90, t (7.1)	
17	4.69, br d (8.5)	4.67, br dd (8.5, 2.2)	4.17, br dd (9.2, 2.5)	3.79, s
17 ¹	2.12, m	2.09, m	2.27, m	4.09, br d (9.2)
	2.27, m	2.28, m	2.94, m	1.85, m
	2.04, m	2.09, m	2.25, m	2.62, m
17 ²	2.44, m	2.46, m	2.52, m	2.27, m
17 ⁴	4.02, m	4.04, m	4.10, q (7.1)	2.51, m
17 ⁵	1.12, t (7.1)	1.14, t (7.1)	1.15, t (7.1)	3.95–4.09, m
18	4.49, br q (7.3)	4.49, br q (7.3)	4.50, br q (7.3)	1.11, t (7.1)
18 ¹	1.69, d (7.3)	1.71, d (7.3)	1.60, d (7.3)	4.45, br q (7.1)
20	8.61, s	8.59, s	8.65, s	1.62, d (7.1)
13 ² -OH	5.35, br s	5.36, br s	5.51, br s	8.64, s
15 ¹ -OH				6.34, br s
NH ¹	−1.73, 0.42 (br s)	−1.62, 0.44 (br s)	−1.84, 0.26 (br s)	−1.17, −0.71 (br s)

¹ Interchangeable proton.

Table 4. ^{13}C (151 MHz) NMR data for compounds 7–10 in CDCl_3 .

No.	7	8	9	10
1	142.1	143.6	142.0	143.1
2	131.9	132.3	131.8	131.9
2 ¹	12.1	12.1	12.1	12.0
3	136.3	137.9	136.3	137.8
3 ¹	129.0	128.6	129.1	128.4
3 ²	122.9	123.7	122.9	123.6
4	136.4	137.0	136.2	137.0
5	97.9	102.0	98.0	103.8
6	155.6	151.2	155.3	151.4
7	136.5	133.0	136.5	132.9
7 ¹	11.3	187.7	11.3	187.6
8	145.3	159.4	145.3	159.4
8 ¹	19.5	19.1	19.5	19.1
8 ²	17.5	19.4	17.5	19.5
9	151.0	147.1	151.3	146.1
10	104.3	106.7	104.2	106.4
11	137.7	137.7	137.8	141.7
12	129.6	132.9	129.5	131.5
12 ¹	12.3	12.5	12.3	12.5
13	126.3	127.1	127.0	112.3
13 ¹	192.0	192.0	192.2	160.5
13 ²	89.1	89.0	88.9	
13 ³	173.5	173.1	172.3	
13 ⁴	53.8	53.9	62.8	
13 ⁵			14.0	
14	150.2	151.1	150.0	136.7
15	107.6	107.4	107.8	102.0
15 ¹				100.5
15 ²				170.6
15 ³				54.3
16	161.9	164.7	162.4	169.0
17	50.2	50.4	51.8	53.9
17 ¹	30.2	30.0	31.1	31.3
17 ²	31.2	31.3	31.6	32.2
17 ³	173.0	172.9	173.6	173.1
17 ⁴	60.4	60.5	60.5	60.5
17 ⁵	14.1	14.1	14.1	14.1
18	50.8	50.8	50.4	50.2
18 ¹	22.7	22.7	22.8	22.2
19	172.8	174.6	172.4	173.3
20	93.4	93.7	93.6	94.1

**Figure 4.** Key HMBC correlations of compounds 7 and 10.

Compound **8** was isolated as a dark green amorphous solid and showed a molecular formula of $\text{C}_{37}\text{H}_{38}\text{N}_4\text{O}_7$ based on HR-ESI-MS analysis (m/z 673.2635, $[\text{M}+\text{Na}]^+$, calcd.

673.2638). ^1H and ^{13}C NMR data (Tables 3 and 4) for **8** were very similar to those of compound **7**. Compared with **7**, compound **8** had an aldehyde group at position C-7 instead of a methyl group in **7**, confirmed by the HMBC correlations of H-7¹ (δ_{H} 11.11) with C-7 (δ_{C} 133.0) and C-6 (δ_{C} 151.2). Therefore, compound **8** was established as 7-formyl-13²-hydroxypheophorbide-a ethyl ester.

Compound **9** was obtained as a dark green powder with the molecular formula of ($\text{C}_{38}\text{H}_{42}\text{N}_4\text{O}_6$) deduced by HR-ESI-MS analysis (m/z 651.3179, $[\text{M}+\text{H}]^+$, calcd. 651.3183). Its ^1H and ^{13}C NMR data (Tables 3 and 4) were similar to those of compound **7**, the main distinction being the substituent groups and their configuration at position C-13². The relative up-field shift of H-17 at δ_{H} 4.17, as mentioned in the structural elucidation of **7**, indicated the OH-13² as β -configuration. Also, an ethyl formate unit with α -orientation was assigned to C-13² based on the NMR data analyses. Thus, compound **9** was designated to be 13³-ethoxypheophorbide-a ethyl ester.

Compound **10** was obtained as a dark green powder and had a molecular formula of $\text{C}_{37}\text{H}_{38}\text{N}_4\text{O}_8$ as determined by its HR-ESI-MS results (m/z 667.2759, $[\text{M}+\text{H}]^+$, calcd. 667.2768). Compounds **10** and **8** showed similar ^1H and ^{13}C NMR data (Tables 3 and 4) and 2D NMR data. The main differences between **10** and **8** were observed from the chemical shift changes at C-13 (δ_{C} 112.3 for **10** vs. δ_{C} 127.1 for **8**) and C-13¹ (δ_{C} 160.5 for **10** vs. δ_{C} 192.0 for **8**), indicating that compound **10** should have a six-membered lactone ring in its skeleton structure. Furthermore, the downfield shift of H-17 (δ_{H} 4.67), which arose from the inductive effect of OH-15¹, suggested that OH-15¹ was β -oriented. Thus, compound **10** was designated as 7-formyl-15¹-hydroxypurpurin-7-lactone ethyl methyl diester.

The compounds **1–6** isolated from the leaves of *C. ptilosperma* in the present study were tested in terms of their cytotoxicity against six human cancer lines, namely Hela, MCF-7, BEL-7402, A549, HepG2, and MB-231, by MTT assay (Table 5). Compound **2** showed potent cytotoxicity toward HepG2 cells with an IC_{50} value of $2.57 \pm 0.29 \mu\text{M}$. In particular, the inhibitory effect of compound **2** was comparable to that of the positive control drug. Compounds **4** and **5** exhibited moderate cytotoxicity against MDA-MB-231 cells, with IC_{50} values of 11.31 ± 3.05 and $5.52 \pm 0.13 \mu\text{M}$, respectively. All the compounds were found to exhibit lower or no inhibitory activity against Hela, MCF-7, BEL-7402, and A549 cancer cells. The results indicated that triterpenoids were highly selective in inhibiting tumor cells.

Table 5. Cytotoxicity (IC_{50} , $\mu\text{M} \pm \text{SD}$, $n = 3$) of compounds **1–6** and doxorubicin against six cancer lines.

Compounds	1	2	3	4	5	6	Doxorubicin
Hela	>50	>50	>50	>50	>50	>50	5.19 ± 0.26
MCF-7	>50	22.18 ± 8.95	30.93 ± 5.10	19.62 ± 2.16	>50	>50	12.03 ± 1.15
BEL-7402	37.20 ± 5.46	>50	>50	>50	>50	20.04 ± 3.46	4.82 ± 0.76
A549	14.08 ± 1.16	>50	>50	48.02 ± 12.14	>50	>50	8.05 ± 1.12
HepG2	29.07 ± 5.69	2.57 ± 0.29	>50	42.63 ± 3.97	>50	>50	2.49 ± 0.36
MDA-MB231	>50	27.05 ± 7.18	19.09 ± 0.75	11.31 ± 3.05	5.52 ± 0.13	>50	7.96 ± 1.17

Preliminary SAR (structure–activity relationship) analysis indicated that ursane-type triterpenes were more cytotoxic than oleanane-type triterpenes, and the presence of benzoyloxy and angeloyloxy groups reduced cytotoxicity against these cancer cells. Overall, among the isolated ursane-type compounds, the presence or absence of methoxy or hydroxyl groups at the position of C-11 and hydroxyl or carbonyl groups at the position of C-22 has no significant effect on cytotoxicity. Compared to the reported triterpenoids isolated from *camellias* [39–42], the triterpenoids isolated from *C. ptilosperma* in this study showed more potent cytotoxicity against hepatocellular carcinoma and lung cancer cells.

The cytotoxicity for compounds **7–10** in the absence of direct illumination was assayed against six tumor cell lines, Hela, MCF-7, BEL-7402, A549, HepG2, and MB-231, by the MTT method (Table 6). Compounds **8** and **9** exhibited limited or negligible cytotoxic activity against all tested cell lines. In contrast, compound **7** exhibited moderate inhibitory

activity against MCF-7 cells, yielding an IC_{50} value of $5.26 \pm 0.71 \mu\text{M}$, while compound **10** demonstrated moderate cytotoxicity against BEL-7402 and HepG2 cells, with IC_{50} values of 7.68 ± 1.87 and $3.77 \pm 0.49 \mu\text{M}$, respectively. The findings for compounds **7** and **10**, observed in the absence of direct illumination, indicate that the cytotoxicity of pheophorbide-related compounds may involve mechanisms distinct from the previously reported photodynamic action.

Table 6. Cytotoxicity (IC_{50} , $\mu\text{M} \pm \text{SD}$, $n = 3$) of compounds **7–10** against six cancer cell lines in darkness.

Compounds	7	8	9	10
Hela	18.19 ± 3.62	18.08 ± 2.48	59.26 ± 5.50	35.41 ± 7.62
MCF-7	5.26 ± 0.71	46.26 ± 4.81	59.08 ± 3.09	76.84 ± 4.93
BEL-7402	22.72 ± 4.98	51.04 ± 6.36	75.07 ± 9.73	7.68 ± 1.87
A549	20.48 ± 2.16	76.43 ± 8.75	27.13 ± 6.08	39.31 ± 3.23
HepG2	60.53 ± 9.40	12.65 ± 4.96	53.57 ± 10.28	3.77 ± 0.49
MDA-MB231	25.92 ± 3.30	37.50 ± 5.09	22.06 ± 1.51	40.06 ± 8.33

Furthermore, the photocytotoxicity of compounds **7–10** was assessed against the above tumor cell lines when exposed to light radiation (Figure 5). Four compounds demonstrated heightened inhibition of proliferation in all tested cell lines when subjected to illumination, and this effect intensified with longer light exposure times. Notably, compound **7** exhibited exceptional photocytotoxicity against Hela, MCF-7, and A549 cells, with IC_{50} values of $0.43 \pm 0.15 \mu\text{M}$, $0.28 \pm 0.05 \mu\text{M}$, and $0.92 \pm 0.21 \mu\text{M}$, respectively. Compound **10** demonstrated significant photodynamic cytotoxic activity against BEL-7402 and HepG2 cells with IC_{50} values of $0.77 \pm 0.34 \mu\text{M}$ and $0.33 \pm 0.04 \mu\text{M}$, respectively. Conversely, compounds **8** and **9** exhibited limited photodynamic activity across all tested cell lines, despite a noticeable improvement in inhibition effects under light radiation. These results suggest that certain pheophorbide-related compounds derived from *C. ptilosperma* have the potential to serve as potent photosensitizers for photodynamic therapy (PDT).

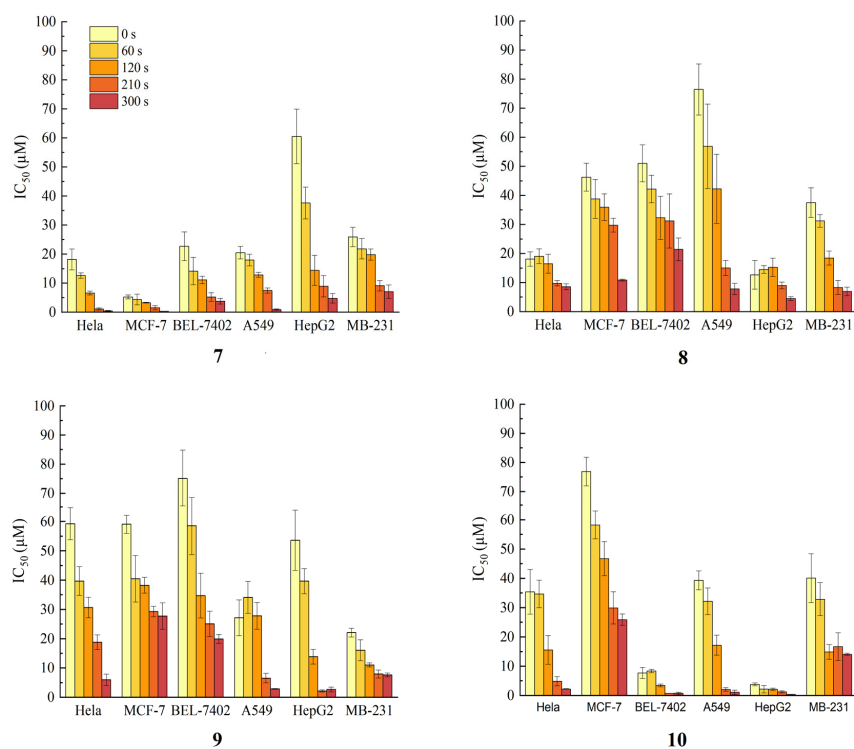


Figure 5. Cytotoxicity for Hela, MCF-7, BEL-7402, A549, HepG2, and MDA-MB-231 cells exposed to compounds **7–10** under photo-irradiation.

Pheophorbide is one of the classes of porphyrins. Porphyrins are a family of heteromeric macrocyclic organic compounds containing four pyrrole rings linked by naturally occurring methine bridges, capable of generating singlet oxygen in the presence of light and oxygen, effectively killing tumor cells. [43–45]. Both natural and synthetic porphyrins exhibit photocytotoxicity. Thomas et al. [46] designed and prepared an N-fused porphyrin (NCP), displaying an IC₅₀ value of 6 μM. Hynek et al. [47] synthesized porphyrin derivatives containing methyl, isopropyl, and phenyl groups, and strong photocytotoxicity against HeLa cells with an IC₅₀ value of 0.45 μM was shown. However, the porphyrins isolated in this study were less effective in inhibiting tumor cells than other types of photocytotoxic compounds, such as metal complexes [48–50]. This also suggested that compounds 7–10 can be further structurally modified to increase their photocytotoxicity. Preliminary SAR (structure–activity relationship) analysis suggested that the length of side chain substituents, differences in functional groups, and chiral carbon configurations did not reflect a significant degree of photocytotoxicity.

Two Gram-positive bacteria (*S. aureus* and *E. coli*) and two Gram-negative bacteria (*K. pneumoniae* and *P. aeruginosa*) were selected to evaluate the antibacterial activity of compounds 7–10 using MIC values. In the absence of light exposure, compounds 7–10 exhibited no activity against the four bacteria at a concentration of 100 μM. However, when the bacteria were exposed to compounds 7–10 with 30 min of photo-irradiation, four of the pheophorbides displayed limited antibacterial activity against *S. aureus* and *E. coli* (Table 7). Notably, compounds 8 and 10 exhibited sensitivity to *E. coli* and demonstrated a photodynamic antibacterial effect, with a MIC value of 0.625 μM. Conversely, none of the tested compounds displayed any activity for the two Gram-negative bacteria, whether subjected to photo-irradiation or not.

Table 7. MICs (μM, n = 3) of compounds 7–10 against four bacteria.

Compounds	7	8	9	10	Positive Control
<i>S. aureus</i>	2.5	5.0	1.25	2.5	1.25 (ampicillin)
<i>E. coli</i>	5.0	0.625	2.5	0.625	2.50 (ampicillin)
<i>P. aeruginosa</i>	>10	>10	5.0	>10	0.625 (ceftazidime)
<i>K. pneumoniae</i>	>10	>10	>10	>10	1.25 (ceftazidime)

3. Experimental

3.1. General Experimental Procedures

HR-ESI-MS was measured on a Waters G2-XS Q-TOF mass spectrometer. All mass spectrometric data were obtained in positive ion mode using an ESI ion source, with a scan range from 100 to 1000 (*m/z*). NMR spectra were recorded on a Bruker AVANCE III HD 600 MHz spectrometer with TMS as the internal standard. Analytical HPLC was carried out on an SSI 1500 HPLC system equipped with a Model 201 UV detector and a Welch XB-C18 column (5 μm, 4.6 × 250 mm, 1.0 mL/min). Semipreparative HPLC was performed on a Laballiance HPLC system with a Welch XB-C18 column (5 μm, 10 × 250 mm, 4 mL/min) and a Model 500 UV detector. Silica gel (100–200 and 300–400 mesh, Qingdao Marine Chemical Inc., Qingdao, China), neutral alumina (100–200 mesh, Sinopharm Chemical Reagent Co., Ltd., Shanghai, China), and Sephadex LH-20 (20–150 μm, GE Healthcare, Boston, TX, USA) were used for column chromatography. Thin-layer chromatography (TLC) was performed on precoated silica gel G plates (Qingdao Marine Chemical Inc., Qingdao, China) and detected by heating after spraying a solution of 5% H₂SO₄ in EtOH. Photodynamic cytotoxicity and antibacterial activity evaluation used a 10 W halogen tungsten lamp (Philips, Amsterdam, The Netherlands) as the light source. All reagents used in the extraction and column chromatography process were analytically pure and in the HPLC analysis and preparation were of chromatographic purity.

HeLa, MCF-7, BEL-7402, A549, HepG2, and MDA-MB-231 cancer cells were provided by the Chinese Cell Resource Center (National Infrastructure of Cell-Line Resources, Shanghai, China). Penicillin–streptomycin solution (100X, Beyotime Biotechnology, Bei-

jing, China), fetal bovine serum (Gibco, Thornton, Australia), RPMI-1640, and DMEM cell culture media (Gibco, Beijing, China) were used for cell culture. The absorption values were recorded on a Synergy LX microplate reader. Tetrazolium bromide (MTT, Beyotime Biotechnology, Beijing, China) was used for cell colorimetry staining. *Staphylococcus aureus*, *Escherichia coli*, *Pseudomonas aeruginosa*, and *Klebsiella pneumoniae* were provided by the China Center for Type Culture Collection (CCTCC, Wuhan University, Wuhan, China).

3.2. Plant Material

The leaves of *C. ptilosperma* were picked in Daxin County, Chongzuo City, Guangxi Zhuang Region (China) in August 2019. A voucher specimen (No. 20190804-7014) representing this plant has been deposited at the Guangxi Institute of Botany, Chinese Academy of Sciences.

3.3. Extraction and Isolation

The dried leaves of *C. ptilosperma* (5.3 kg) were extracted three times with 95% EtOH (12 L each) at room temperature, and the combined solvent was evaporated in vacuo. The EtOH extract (1.4 kg) was suspended in water and successively partitioned with *n*-hexane and EtOAc three times (3 L each). Of these partitions, 412 g of EtOAc extract was subjected to a silica gel column and eluted with gradient mixtures of CH₂Cl₂-MeOH (from 200:1 to 5:1, *v/v*). Eluents were pooled based on TLC analysis to yield 12 combined fractions (Fr. 1-12). Further, Fr. 3 was chromatographed over a 100–200 mesh Al₂O₃ column and eluted with gradient mixtures of PE-EtOAc (20:1 to 8:1, *v/v*), and the eluents were pooled after TLC analysis to obtain six subfractions (Fr. 3.1–3.6). Fr. 3.1 was further separated on the LH-20 column and eluted with MeOH-CH₂Cl₂ (1:1, *v/v*) to yield three subfractions (Fr. 3.1.1–3.1.3.). Fr. 3.1.1 was purified by separation over a semi-preparative column, eluted with CH₃CN-H₂O (60:40, *v/v*) to yield compound **1** (*t*_R = 19.56 min, 7.0 mg). Fr. 3.1.2 was chromatographed on a semi-preparative, eluted with CH₃CN-H₂O (43:57 *v/v*) to give compound **2** (*t*_R = 23.33 min, 14.8 mg). Fr. 3.1.3 was subjected to a silica gel column (300–400 mesh) and eluted with a gradient of CH₂Cl₂-MeOH (40:1 to 10:1, *v/v*) to achieve three subfractions (Fr. 3.1.3.1–3.1.3.3). Fr. 3.1.3.1 was purified on a semi-preparative column, eluted with CH₃CN-H₂O (50:50 *v/v*) to give compounds **3** (*t*_R = 5.61 min, 6.8 mg) and **4** (*t*_R = 15.65 min, 3.5 mg). Fr. 3.1.3.2 was purified on a semi-preparative column with an elution of CH₃CN-H₂O (35:65 *v/v*) to obtain compounds **5** (*t*_R = 5.05 min, 13.7 mg) and **6** (*t*_R = 10.19 min, 3.0 mg).

Fr.1 was chromatographed on 300–400 mesh silica gel and eluted with PE/CH₂Cl₂ (40:1 and 20:1, *v/v*) to yield three fractions (Fr. 1.1 to Fr. 1.3). Fr. 1.1 was subjected to separation on the Sephadex LH-20 and eluted with CH₂Cl₂/MeOH (3:1, *v/v*) to yield a black eluate. This residue was purified on a semipreparative HPLC with acetonitrile as the mobile phase to obtain a mixture of **7** and **9**, and the mixture was eluted with 90% acetonitrile/10% MeOH to yield **7** (25.7 mg, *t*_R = 10.8 min) and **9** (16.9 mg, *t*_R = 11.1 min). Fr. 1.2 was isolated on the Sephadex LH-20 with the elution of CH₂Cl₂/MeOH (1:1, *v/v*) to give **8** (51.9 mg). Fr. 1.3 was purified using the Sephadex LH-20 and eluted with CH₂Cl₂/MeOH (1:1, *v/v*) to give **10** (10.0 mg).

3.3.1. Compound 1

Colorless solid; $[\alpha]_D^{20} + 9.08$ (*c* 0.5, CH₂Cl₂); UV (CH₂Cl₂) λ_{\max} (log ϵ) 201 (1.16) nm; HR-ESI-MS *m/z* 539.3718 [M+Na]⁺, calcd. for C₃₂H₅₂O₅Na, 539.3712; ¹H NMR (600 MHz) and ¹³C NMR (151 MHz) in CDCl₃ (see Table 1).

3.3.2. Compound 2

White powder; $[\alpha]_D^{20} + 4.36$ (*c* 0.5, CH₂Cl₂); UV (CH₂Cl₂) λ_{\max} (log ϵ) 199 (1.32) nm; HR-ESI-MS *m/z* 571.3605 [M+Na]⁺, calcd. for C₃₂H₅₂O₇Na, 571.3611; ¹H NMR (600 MHz) and ¹³C NMR (151 MHz) in CDCl₃ (see Table 1).

3.3.3. Compound 3

Pale powder; $[\alpha]_D^{20} + 3.01$ (*c* 0.5, CH₂Cl₂); UV (CH₂Cl₂) λ_{\max} (log ϵ) 201 (0.94) nm; HR-ESI-MS *m/z* 569.3452 [M+Na]⁺, calcd. for C₃₂H₅₀O₇Na, 569.3454; ¹H NMR (600 MHz) and ¹³C NMR (151 MHz) in CDCl₃ (see Table 1).

3.3.4. Compound 4

White powder; $[\alpha]_D^{20} + 15.27$ (*c* 0.5, CH₂Cl₂); UV (CH₂Cl₂) λ_{\max} (log ϵ) 192 (1.40) nm; HR-ESI-MS *m/z* 555.3298 [M+Na]⁺, calcd. for C₃₁H₄₈O₇Na, 555.3298; ¹H NMR (600 MHz) and ¹³C NMR (151 MHz) in CDCl₃ (see Table 1).

3.3.5. Compound 5

White powder; $[\alpha]_D^{20} - 4.21$ (*c* 0.5, CH₂Cl₂); UV (CH₂Cl₂) λ_{\max} (log ϵ) 225 (1.30), 262 (0.84), 279 (0.37) nm; HR-ESI-MS *m/z* 699.4236 [M+Na]⁺, calcd. for C₄₂H₆₀O₇Na, 699.4237; ¹H NMR (600 MHz) and ¹³C NMR (151 MHz) in CDCl₃ (see Table 2).

3.3.6. Compound 6

White powder; $[\alpha]_D^{20} + 2.90$ (*c* 0.5, CH₂Cl₂); UV (CH₂Cl₂) λ_{\max} (log ϵ) 230 (1.11), 275 (0.52), 281 (0.29) nm; HR-ESI-MS *m/z* 721.4092 [M+Na]⁺, calcd. for C₄₄H₅₈O₇Na, 721.4080; ¹H NMR (600 MHz) and ¹³C NMR (151 MHz) in CDCl₃ (see Table 2).

3.3.7. Compound 7

Dark green amorphous solid; $[\alpha]_D^{20} + 0.42$ (*c* 0.2, CH₂Cl₂); UV (CH₂Cl₂) λ_{\max} (log ϵ) 250 (1.06), 410 (2.80), 422 (2.93), 511 (0.40), 539 (0.27), 615 (0.27), 670 (1.53) nm; IR (ATR) ν_{\max} 3329, 3110, 1759, 1620, 1249; HR-ESI-MS *m/z* 637.3029 [M+H]⁺, calcd. for C₃₇H₄₁N₄O₆, 637.3026; ¹H NMR (600 MHz) and ¹³C NMR (151 MHz) in CDCl₃ (see Tables 3 and 4).

3.3.8. Compound 8

Dark green amorphous solid; $[\alpha]_D^{20} + 0.67$ (*c* 0.2, CH₂Cl₂); UV (CH₂Cl₂) λ_{\max} (log ϵ) 250 (1.22), 432 (2.71), 447 (2.90), 534 (0.36), 563 (0.23), 606 (0.21), 657 (0.92) nm; IR (ATR) ν_{\max} 3344, 3107, 2932, 1764, 1250; HR-ESI-MS *m/z* 673.2635 [M+Na]⁺, calcd. for C₃₇H₆₀N₄O₇Na, 673.2638; ¹H NMR (600 MHz) and ¹³C NMR (151 MHz) in CDCl₃ (see Tables 3 and 4).

3.3.9. Compound 9

Dark green powder; $[\alpha]_D^{20} + 0.09$ (*c* 0.2, CH₂Cl₂); UV (CH₂Cl₂) λ_{\max} (log ϵ) 252 (1.03), 420 (2.65), 439 (2.86), 520 (3.60), 552 (0.20), 609 (0.28), 662 (6.81) nm; IR (ATR) ν_{\max} 3320, 3123, 1742, 1230; HR-ESI-MS *m/z* 651.3179 [M+H]⁺, calcd. for C₃₈H₄₃N₄O₆, 651.3183; ¹H NMR (600 MHz) and ¹³C NMR (151 MHz) in CDCl₃ (see Tables 3 and 4).

3.3.10. Compound 10

Dark green powder; $[\alpha]_D^{20} + 0.50$ (*c* 0.2, CH₂Cl₂); UV (CH₂Cl₂) λ_{\max} (log ϵ) 247 (1.12), 428 (2.92), 433 (2.73), 525 (0.24), 566 (0.17), 606 (0.13), 662 (0.59) nm; IR (ATR) ν_{\max} 3358, 3109, 2920, 1777, 1238; HR-ESI-MS *m/z* 667.2759 [M+Na]⁺, calcd. for C₃₇H₃₉N₄O₈, 667.2768; ¹H NMR (600 MHz) and ¹³C NMR (151 MHz) in CDCl₃ (see Tables 3 and 4).

3.4. Biological Assay

3.4.1. Cytotoxicity Assays

The cytotoxic activity of compounds 1–6 against Hela, MCF-7, BEL-7402, A549, HepG2, and MDA-MB-231 cancer cell lines was evaluated using the MTT assay according to the reported method [51,52] with doxorubicin as a positive control drug. MCF-7 and BEL-7402 cells were cultured in RPMI-1640 medium containing 10% fetal bovine serum, and Hela, A549, HepG2, and MDA-MB-231 cells were cultured in DMEM medium containing 10% fetal bovine serum, all of which were incubated in a constant temperature incubator at 5% CO₂ at 37 °C. A549 in the logarithmic growth phase were inoculated into 96-well plates at a density of 4 × 10⁴ cells/mL. MCF-7, HepG2, BEL-7402, MDA-MB-231, and Hela were

inoculated at a density of 5×10^4 cells/mL, with 100 μ L in each well. After the cells were attached to the wall, the drug treatment was performed. Different concentrations (0.1, 0.5, 1.0, 5.0, 1.0, and 20.0 μ M) of doxorubicin (dissolved in PBS) and compounds 1–6 (1.0, 2.0, 5.0, 10.0, 25.0, and 50.0 μ M, dissolved in 0.1% DMSO/PBS) were administered. Three parallel tests were conducted for each concentration and the cells were cultured for 48 h. An amount of 10 μ L of MTT was added to each well, and the cells were incubated. After incubation for 4 h at 37 °C, the medium was aspirated and 150 μ L of DMSO solution was added and shaken for 10 min, the plate was shocked using an enzyme marker, and the absorbance value was detected at 490 nm to calculate the cell survival rate. The entire experiment was repeated three times.

3.4.2. Photocytotoxicity Assay

The cytotoxicity of compounds 7–10 with or without photo-irradiation was evaluated against the same six cancer cell lines by the MTT method. For the photodynamic cytotoxicity assay, a halogen tungsten lamp was employed as the irradiation source. The lamp was positioned immediately above the 96-well plate, maintaining a separation distance of 10 cm. The concentrations of the compounds 7–10 were set at 0.1, 0.5, 1.0, 5.0, 10.0, 50.0, and 100.0 μ M. Immediately after the addition of different concentrations of these compounds, the cells were exposed to continuous light for 0, 60, 120, 210, and 300 s. The subsequent experimental steps were the same as described in Section 3.4.1.

3.4.3. Photodynamic Antibacterial Activity Assay

The MIC (minimal inhibitory concentration) value was identified as the lowest concentration of the compound that inhibited visible bacterial growth following the incubation period. It was determined using the double dilution method. *S. aureus*, *E. coli*, *K. pneumoniae*, and *P. aeruginosa* were inoculated on Mueller–Hinton agar medium and incubated at 37 °C for 24 h. The concentration of the bacterial suspension was adjusted to 1.0×10^6 CFU/mL by the use of sterile saline solution and then the bacterial solution was inoculated on a 96-well plate with 100 μ L per-well.

Compounds 7–10 and positive control drugs were diluted to attain the final concentrations within the range of 0.625–10.0 μ M. These different concentrations of solutions and positive control drugs were inoculated into 96-well plates with an inoculation volume of 50 μ L per well, while for the blank control, only 50 μ L of culture medium was added. The solutions were then incubated at 37 °C for 24 h. All the above operations were carried out under light-protected conditions. Bacterial growth in the treated group was determined by comparing the characteristics of bacterial growth in the blank control group and recording the minimum concentration corresponding to bacterial growth.

In the photodynamic antibacterial test, the samples were exposed to continuous light irradiation for a duration of 30 min using a halogen tungsten lamp positioned 10 cm above the samples after administration. The other procedures were the same as in the light avoidance condition. The experiment was repeated three times.

3.5. Statistical Analysis

Data from the cytotoxicity assays were evaluated according to their means and standard deviations. The cytotoxic concentration at 50% was determined to compare with the control obtained from nonlinear regression. These analyses were performed using SPSS® Statistics 18.0 (IBM software, Armonk, NY, USA).

4. Conclusions

In summary, ten new compounds were isolated from the leaves of *Camellia ptilosperma*, including six triterpenes and four pheophorbides. The structures of the undescribed compounds were based on NMR and HR-ESI-MS spectroscopic data.

Meanwhile, the cytotoxic activity of the six triterpenes against six cancer cell lines was evaluated by MTT assay. Among them, compounds 1, 4, and 5 showed no significant

cytotoxicity against any of the six cell lines. Compound 2 exhibited potent cytotoxicity against HepG2 cells with an IC_{50} value of $2.57 \pm 0.29 \mu\text{M}$, which was close to that of the positive control drug doxorubicin, indicating that compound 2 significantly inhibited HepG2 proliferation. Compound 5 also showed notable cytotoxicity against MDA-MB231 cells with an IC_{50} value of $5.52 \pm 0.13 \mu\text{M}$, which was stronger than that of the positive control drug doxorubicin. Compounds 7–10, the four pheophorbides, did not exhibit more pronounced cytotoxicity and bacteriostatic activity in the absence of light. The cytotoxicity of all compounds increased significantly after exposure to light, in a manner shown to be time-dependent, and the IC_{50} values of compounds 7–10 were lower than that of the positive control drug for all cells after 300 s of irradiation. On the other hand, they displayed a certain degree of inhibitory effect against *S. aureus* and *E. coli* after 30 min of irradiation, and the MIC values of compounds 8 and 10 were lower than those of the positive control drug ampicillin. However, these compounds did not show any antibacterial activity against *P. aeruginosa* and *K. pneumoniae* in the presence or absence of light.

Therefore, compounds 2 and 5 are promising for the treatment of liver and breast tumors. Compounds 7–10 have potential as photosensitizers for the treatment of tumors and bacterial infections. It is hoped that our study can provide a new direction for the research on and application of *Camellia ptilosperma*. We look forward to investigating its exact mechanism of action in further studies.

Supplementary Materials: The following supporting information can be downloaded at: <https://www.mdpi.com/article/10.3390/molecules28207058/s1>, Figure S1 (S1-1 to S1-8): Spectroscopic data for compound 1; Figure S2 (S2-1 to S2-8): Spectroscopic data for compound 2; Figure S3 (S3-1 to S3-8): Spectroscopic data for compound 3; Figure S4 (S4-1 to S4-8): Spectroscopic data for compound 4; Figure S5 (S5-1 to S5-8): Spectroscopic data for compound 5; Figure S6 (S6-1 to S6-8): Spectroscopic data for compound 6; Figure S7 (S7-1 to S7-7): Spectroscopic data for compound 7; Figure S8 (S8-1 to S8-7): Spectroscopic data for compound 8; Figure S9 (S9-1 to S9-7): Spectroscopic data for compound 9; Figure S10 (S10-1 to S10-7): Spectroscopic data for compound 10; Figure S11: The scheme of extraction and isolation.

Author Contributions: Writing—original draft preparation, S.M.; data curation, M.W.; data curation, T.Y.; investigation, S.M. and L.G.; resources, L.G.; conceptualization, K.Y. All authors have read and agreed to the published version of the manuscript.

Funding: This work was financially supported by the General Program of the National Natural Science Foundation of China (no. 22078073).

Institutional Review Board Statement: Not applicable.

Informed Consent Statement: Not applicable.

Data Availability Statement: The data presented in this study are available in the Supplementary Materials.

Acknowledgments: We appreciate the support from the General Program of the National Natural Science Foundation of China.

Conflicts of Interest: The authors declare no conflict of interest.

Sample Availability: Compounds were deposited at the Medical College of Guangxi University.

References

1. Liang, S.Y. World list of yellow camellia plants. *Guangxi Forest. Sci.* **2007**, *142*, 221–223.
2. Ning, E.C.; Qin, X.M.; Yang, H.H. Research on a processing technique of camellia oral liquid. *Sci. Technol. Food Ind.* **2006**, *27*, 121–122.
3. Wei, L.; Ning, E.C.; Liu, Z.X.; Yang, J.W.; Tang, N.; Chen, Z.L. Development of *Camellia nitidissima* instant tea. *J. Anhui Agric. Sci.* **2011**, *39*, 238–240.
4. Liu, B.C.; Chen, J.Y.; Zhang, W.J.; Huang, Y.Z.; Zhao, Y.Q. Biochemical components evaluation and optimal harvest period of the leaves of *Camellia* Sect. *Chrysanthemum*. *Chin. J. Trop. Crops* **2021**, *42*, 159–167.

5. Song, L.X.; Wang, X.S.; Zheng, X.Q.; Huang, D.J. Polyphenolic antioxidant profiles of yellow camellia. *Food Chem.* **2011**, *129*, 351–357. [CrossRef]
6. Wei, J.B.; Li, X.; Song, H.; Liang, Y.H.; Pan, Y.Z.; Ruan, J.X.; Qin, X.; Chen, Y.X.; Nong, C.L.; Su, Z.H. Characterization and determination of antioxidant components in the leaves of *Camellia chrysantha* (Hu) Tuyama based on composition-activity relationship approach. *J. Food Drug Anal.* **2015**, *23*, 40–48. [CrossRef]
7. Oku, H.; Ogawa, Y.; Iwaoka, E.; Yamaguchi, Y.; Kagota, S.; Kazumasa, S.; Kunitomo, M.; Ishiguro, K. Preventive effects of the extract of kinka-cha, a folk tea, on a rat model of metabolic syndrome. *J. Nat. Med.* **2011**, *65*, 610–616. [CrossRef]
8. Zhang, H.L.; Wu, Q.X.; Wei, X.; Qin, X.M. Pancreatic lipase and cholesterol esterase inhibitory effect of *Camellia nitidissima* Chi flower extracts in vitro and in vivo. *Food Biosci.* **2020**, *37*, 100682. [CrossRef]
9. Chen, J.H.; Wu, X.H.; Zhou, Y.; He, J.H. *Camellia nitidissima* Chi leaf as pancreatic lipase inhibitors: Inhibition potentials and mechanism. *J. Food Biochem.* **2021**, *45*, e13837. [CrossRef] [PubMed]
10. Wang, W.X.; Liu, H.Y.; Wang, Z.N.; Qi, J.; Yuan, S.T.; Zhang, W.J.; Chen, H.J.; Finley, J.W.; Gu, L.W.; Jia, A.Q. Phytochemicals from *Camellia nitidissima* Chi inhibited the formation of advanced glycation end-products by scavenging methylglyoxal. *Food Chem.* **2016**, *205*, 204–211. [CrossRef]
11. Zhang, H.L.; Wu, Q.X.; Qin, X.M. *Camellia nitidissima* Chi flower extracts inhibit α -amylase and α -glucosidase: In vitro by analysis of optimization of addition methods, inhibitory kinetics and mechanisms. *Process Biochem.* **2019**, *86*, 177–185. [CrossRef]
12. Yang, R.; Guan, Y.; Zhou, J.W.; Sun, B.; Wang, Z.N.; Chen, H.J.; He, Z.C.; Jia, A.Q. Phytochemicals from *Camellia nitidissima* Chi flowers reduce the pyocyanin production and motility of *Pseudomonas aeruginosa* PAO1. *Front. Microbiol.* **2017**, *8*, 2640. [CrossRef]
13. Lin, J.N.; Lin, H.Y.; Yang, N.S.; Li, Y.H.; Lee, M.R.; Chuang, C.H.; Ho, C.T.; Kuo, S.C.; Way, T.D. Chemical constituents and anticancer activity of yellow camellias against MDA-MB-231 human breast cancer cells. *J. Agric. Food Chem.* **2013**, *61*, 9638–9644. [CrossRef] [PubMed]
14. Ma, S.Y.; Ge, L.; Li, Y.X.; Liao, N.Y.; Xie, J.Z.; Yang, K.D. Ursane-type triterpenes with a phenylpropanoid unit from *Camellia ptilosperma* and evaluation of their cytotoxic activities. *J. Nat. Prod.* **2023**, *86*, 1793–1800. [CrossRef] [PubMed]
15. Dai, L.; Li, J.L.; Liang, X.Q.; Li, L.; Feng, Y.; Liu, H.Z.; Wei, W.E.; Ning, S.F.; Zhang, L.T. Flowers of *Camellia nitidissima* cause growth inhibition, cell-cycle dysregulation and apoptosis in a human esophageal squamous cell carcinoma cell line. *Mol. Med. Rep.* **2016**, *14*, 1117–1122. [CrossRef]
16. Xu, Y.N.; Ma, S.Y.; Han, X.F.; Su, L.; Ge, L.; Chen, Q.H.; Mo, Q.F.; Yang, K.D. Triterpenes and saponins from leaves of *Camellia nitidissima*, and cytotoxic activities against Bel-7402 and SMMC-7721 human liver cancer cells. *Rec. Nat. Prod.* **2022**, *16*, 550–558.
17. He, D.Y.; Wang, X.T.; Zhang, P.; Luo, X.X.; Li, X.Y.; Wang, L.L.; Li, S.Y.; Xu, Y.P. Evaluation of the anxiolytic and antidepressant activities of the aqueous extract from *Camellia euphlebia* Merr. ex Sealy in mice. *J. Evid.-Based Complement. Altern. Med.* **2015**, *2015*, 618409.
18. Tsoi, B.; Gao, C.; Yan, S.Y.; Du, Q.H.; Yu, H.; Li, P.; Deng, J.G.; Shen, J.G. *Camellia nitidissima* Chi extract promotes adult hippocampal neurogenesis and attenuates chronic corticosterone-induced depressive behaviours through regulating Akt/GSK3 β /CREB signaling pathway. *J. Funct. Foods* **2022**, *95*, 105199. [CrossRef]
19. Yang, Z.; Chen, C.H.; Zhang, Y.Y.; Yang, Y.; Zhang, P.; Bao, G.H. Chemical composition and antibacterial activity of 12 medicinal plant ethyl acetate extracts using LC-MS feature-based molecular networking. *Phytochem. Anal.* **2022**, *33*, 473–489. [CrossRef]
20. Weinhold, A.; Doll, S.; Liu, M.; Schedl, A.; Poschl, Y.; Xu, X.L.; Neumann, S.; Dam, N.M. Tree species richness differentially affects the chemical composition of leaves, roots and root exudates in four subtropical tree species. *J. Ecol.* **2022**, *110*, 97–116. [CrossRef]
21. Hou, X.Y.; Du, H.Z.; Yang, R.; Qi, J.; Huang, Y.; Feng, S.Y.; Wu, Y.; Lin, S.S.; Liu, Z.X.; Jia, A.Q.; et al. The antitumor activity screening of chemical constituents from *Camellia nitidissima* Chi. *Int. J. Mol. Med.* **2018**, *41*, 2793–2801. [CrossRef] [PubMed]
22. Zhang, X.F.; Han, Y.Y.; Di, T.M.; Gao, L.P.; Xia, T. Triterpene saponins from tea seed pomace (*Camellia oleifera* Abel) and their cytotoxic activity on MCF-7 cells in vitro. *Nat. Prod. Res.* **2021**, *35*, 2730–2733. [CrossRef] [PubMed]
23. Ji, M.Y.; Gong, X.; Li, X.; Wang, C.C.; Li, M.H. Advanced Research on the antioxidant activity and mechanism of polyphenols from *Hippophae Species*—A review. *Molecules* **2020**, *25*, 917. [CrossRef] [PubMed]
24. Li, Q.L.; Wang, Y.H.; Mai, Y.X.; Li, H.Y.; Wang, Z.; Xu, J.W.; He, X.J. Health benefits of the flavonoids from onion: Constituents and their pronounced antioxidant and anti-neuroinflammatory capacities. *J. Agric. Food Chem.* **2020**, *68*, 799–807. [CrossRef] [PubMed]
25. Brighenti, V.; Iseppi, R.; Pinzi, L.; Mincuzzi, A.; Ippolito, A.; Messi, P.; Sanzani, S.M.; Rastelli, G.; Pellati, F. Antifungal activity and DNA topoisomerase inhibition of hydrolysable tannins from *Punica granatum* L. *Int. J. Mol. Sci.* **2021**, *22*, 4175. [CrossRef]
26. Chai, W.M.; Wei, Q.M.; Deng, W.L.; Zheng, Y.L.; Chen, X.Y.; Huang, Q.; Chong, O.Y.; Peng, Y.Y. Anti-melanogenesis properties of condensed tannins from *Vigna angularis* seeds with potent antioxidant and DNA damage protection activities. *Food Funct.* **2019**, *10*, 99–111. [CrossRef]
27. Magozwi, D.K.; Dinala, M.; Mokwana, N.; Siwe-Noundou, X.; Krause, R.W.M.; Sonopo, M.; McGaw, L.J.; Augustyn, W.A.; Tembu, V.J. Flavonoids from the genus *Euphorbia*: Isolation, structure, pharmacological activities and structure-activity relationships. *Pharmaceuticals* **2021**, *14*, 428. [CrossRef]
28. Lee, D.; Jang, S.Y.; Kwon, S.; Lee, Y.; Park, E.; Koo, H. Optimized combination of photodynamic therapy and chemotherapy using gelatin nanoparticles containing tirapazamine and pheophorbide a. *ACS Appl. Mater. Interfaces* **2021**, *13*, 10812–10821. [CrossRef]
29. Aksel, M.; Bozkurt-Girit, O.; Bilgin, M.D. Pheophorbide a-mediated sonodynamic, photodynamic and sonophotodynamic therapies against prostate cancer. *Photodiagn. Photodyn. Ther.* **2020**, *31*, 101909. [CrossRef]

30. Karg, C.A.; Wang, P.Y.; Kluibenschedl, F.; Muller, T.; Allmendinger, L.; Vollmar, A.M.; Moser, S. Phylloxanthobilins are abundant linear tetrapyrroles from chlorophyll breakdown with activities against cancer cells. *Eur. J. Org. Chem.* **2020**, *29*, 4499–4509. [CrossRef]
31. Gariboldi, M.B.; Marras, E.; Vaghi, I.; Margheritis, A.; Malacarne, M.C.; Caruso, E. Phototoxicity of two positive-charged diaryl porphyrins in multicellular tumor spheroids. *J. Photochem. Photobiol. B* **2021**, *225*, 112353. [CrossRef]
32. Schneider, L.; Kalt, M.; Larocca, M.; Babu, V.; Spingler, B. Potent PBS/polysorbate-soluble transplatin-derived porphyrin-based photosensitizers for photodynamic therapy. *Inorg. Chem.* **2021**, *60*, 9416–9426. [CrossRef] [PubMed]
33. Heliawati, L.; Khatimah, H.; Hermawati, E.; Syah, Y.M. Four dammarane triterpenes and their inhibitory properties against eight receptor tyrosine kinases. *Nat. Prod. Sci.* **2020**, *26*, 345–350. [CrossRef]
34. Farimani, M.M.; Abbas-Mohammadi, M. Two new polyhydroxylated triterpenoids from *Salvia urmiensis* and their cytotoxic activity. *Fitoterapia* **2016**, *30*, 2648–2654. [CrossRef]
35. Gao, X.H.; Wang, X.Y.; Zhou, J.S.; Zhang, Y.; Liu, H.C.; Zhou, B.; Yue, J.M. Rearranged dichapetalin-type triterpenoids with cytotoxic activity from *Dichapetalum gelonioides*. *Chin. J. Chem.* **2022**, *40*, 2531–2538. [CrossRef]
36. Lanzotti, V.; Termolino, P.; Dolci, M.; Curir, P. Paviosides A–H, eight new oleane type saponins from *Aesculus pavia* with cytotoxic activity. *Bioorg. Med. Chem.* **2012**, *20*, 3280–3286. [CrossRef]
37. Barua, A.; Dutta, S.; Pal, S. Triterpenoids XXX. The structure of barringtonol E. A new triterpenoid sapogenol from *barringtonia acutangula*. *J. Indian Chem. Soc.* **1967**, *991*, 937–940.
38. Nakatani, Y.; Ourisson, G.; Beck, J. Chemistry and biochemistry of Chinese drugs. VII.: Cytostatic pheophytins from silkworm excreta, and derived photocytotoxic pheophorbides. *Chem. Pharm. Bull.* **1981**, *29*, 2261–2269. [CrossRef]
39. Qi, J.; Shi, R.F.; Yu, J.M.; Li, Y.; Yuan, S.T.; Yang, J.Z.; Hu, J.M.; Jia, A.Q. Chemical constituents from leaves of *Camellia nitidissima* and their potential cytotoxicity on SGC7901 cells. *Chin. Herb. Med.* **2016**, *8*, 80–84. [CrossRef]
40. Thao, N.T.P.; Hung, T.M.; Lee, M.K.; Kim, J.C.; Min, B.S.; Bae, K. Triterpenoids from *Camellia japonica* and their cytotoxic activity. *Chem. Pharm. Bull.* **2010**, *58*, 121–124. [CrossRef]
41. Fan, L.M.; He, Y.F.; Xu, Y.J.; Li, P.H.; Zhang, J.S.; Zhao, J. Triterpenoid saponins in tea (*Camellia sinensis*) plants: Biosynthetic gene expression, content variations, chemical identification and cytotoxicity. *Int. J. Food Sci. Nutr.* **2021**, *72*, 308–323. [CrossRef] [PubMed]
42. Zhou, H.; Wang, C.Z.; Ye, J.Z.; Chen, H.X. New triterpene saponins from the seed cake of *Camellia Oleifera* and their cytotoxic activity. *Phytochem. Lett.* **2014**, *8*, 46–51. [CrossRef]
43. Lin, Y.Y.; Zhou, T.; Bai, R.R.; Xie, Y.Y. Porphyrins are able to generate monoclinic oxygen in the presence of light and oxygen, effectively killing tumour cells. *J. Enzyme Inhib. Med. Chem.* **2020**, *35*, 1080–1099. [CrossRef]
44. Chavda, J.; Rajwar, A.; Bhatia, B.; Gupta, I. Synthesis of novel zinc porphyrins with bioisosteric replacement of sorafenib: Efficient theranostic agents for anti-cancer application. *J. Inorg. Biochem.* **2023**, *22*, 112384. [CrossRef] [PubMed]
45. Pan, Z.H.; Fan, J.J.; Xie, Q.; Zhang, X.; Zhang, W.; Ren, Q.; Li, M.J.; Zheng, Q.S.; Lu, J.; Li, D. Novel sulfonamide porphyrin TBPoS-2OH used in photodynamic therapy for malignant melanoma. *Biomed. Pharmacother.* **2021**, *133*, 111042. [CrossRef] [PubMed]
46. Thomas, A.P.; Babu, P.S.S.; Nair, S.A.; Ramakrishnan, S.; Ramaiah, D.; Chandrashekar, T.K.; Srinivasan, A.; Pillai, M.R. meso-Tetrakis(*p*-sulfonatophenyl)N-confused porphyrin tetrasodium salt: A potential sensitizer for photodynamic therapy. *J. Med. Chem.* **2012**, *55*, 5110–5520. [CrossRef]
47. Hynek, J.; Koncosova, M.; Zelenka, J.; Krizova, I.; Ruml, T.; Kubat, P.; Demel, J.; Lang, K. Phosphinatophenylporphyrins tailored for high photodynamic efficacy. *Org. Biomol. Chem.* **2018**, *16*, 7274–7281. [CrossRef]
48. Steinke, S.J.; Gupta, S.; Piechota, E.J.; Moore, C.E.; Kodanko, J.J.; Turro, C. Photocytotoxicity and photoinduced phosphine ligand exchange in a Ru(II) polypyridyl complex. *Chem. Sci.* **2022**, *13*, 1933–1945. [CrossRef]
49. Upadhyay, A.; Gautam, S.; Ramu, V.; Kondaiah, P.; Chakravarty, A. Photocytotoxic cancer cell-targeting platinum(II) complexes of glucose-appended curcumin and biotinylated 1,10-phenanthroline. *Dalton Trans.* **2019**, *48*, 17556–17565. [CrossRef]
50. Banaspati, A.; Ramu, V.; Raza, M.K.; Goswami, T.K. Copper(II) curcumin complexes for endoplasmic reticulum targeted photocytotoxicity. *RSC Adv.* **2022**, *12*, 30722–30733. [CrossRef]
51. Ragasa, C.Y.; Cornelio, K.B. Triterpenes from *Euphorbia hirta* and their cytotoxicity. *Chin. J. Nat. Med.* **2013**, *11*, 528–533. [CrossRef]
52. Kikuchi, T.; Uchiyama, E.; Ukiya, M.; Tabata, K.; Kimura, Y.; Suzuki, T.; Akihisa, T. Cytotoxic and apoptosis-inducing activities of triterpene acids from *Poria cocos*. *J. Nat. Prod.* **2011**, *74*, 137–144. [CrossRef] [PubMed]

Disclaimer/Publisher’s Note: The statements, opinions and data contained in all publications are solely those of the individual author(s) and contributor(s) and not of MDPI and/or the editor(s). MDPI and/or the editor(s) disclaim responsibility for any injury to people or property resulting from any ideas, methods, instructions or products referred to in the content.

Article

A Direct Method for Synthesis of Quinoxalines and Quinazolinones Using Epoxides as Alkyl Precursor

Xueyan Lv ¹, Lili Lv ², Shichen Li ¹, Chengcheng Ding ¹, Bingchuan Yang ^{3,*} and Chen Ma ^{1,*}

¹ Key Laboratory of Special Functional Aggregated Materials, Ministry of Education, School of Chemistry and Chemical Engineering, Shandong University, Jinan 250100, China; lxy17852267584@163.com (X.L.); ray19940519@foxmail.com (S.L.); 202220349@mail.sdu.edu.cn (C.D.)

² China Petroleum Planning and Engineering Institute, Dongying 257237, China; lvlili@petrochina.com.cn

³ College of Chemistry and Chemical Engineering, Qilu Normal University, Jinan 250013, China

* Correspondence: yangbingchuan@lcu.edu.cn (B.Y.); chenma@sdu.edu.cn (C.M.)

Abstract: An iodine-mediated one-pot synthesis of pyrrolo/indolo [1,2-*a*]quinoxalines and quinazolin-4-one via utilizing epoxides as alkyl precursors under metal-free conditions has been described. Both 1-(2-aminophenyl)-pyrrole and 2-aminobenzamide could be applied to this protocol. A total of 33 desired products were obtained with moderate to good yields. This methodology was suitable for wide-scale preparation and the obtained products could be further modified into promising pharmaceutically active reagents.

Keywords: epoxide; pyrrolo [1,2-*a*]quinoxalines; quinazolin-4-one; transition-metal free

1. Introduction

N-heterocycles are inseparable from our life for use as drug molecules, functional materials and dyes [1–3]. Pyrrolo [1,2-*a*]quinoxalines and quinazolin-4-ones are two essential heterocyclic skeletons with outstanding biological properties for antimalarial, anticancer, anti-HIV, antibacterial, etc [4–14]. As shown in Figure 1, compound **I** exhibits excellent activity towards the 5-HT₃ receptor, and compounds **II** and **III** have anticancer and antileishmanial properties, respectively. Glycosminine (Figure 1, **IV**) and alkaloid bouchardatine (Figure 1, **V**) are present in natural products. Compound **VI** has anticonvulsant activity. Given their excellent applications, especially in medicinal chemistry, their efficient and green synthesis has been a long-pursued research topic in the field of organic synthetic chemistry. In 1966, Cheeseman and Tuck [15] first synthesized pyrrolo [1,2-*a*]quinoxalines using 1-(2-aminophenyl)-pyrrole as the starting material with aqueous formic acid under reflux conditions. Since then, a number of groups have made tremendous efforts to construct these compounds [16–25]. In 2022, Ma [16] reported a Cu(II)-catalyzed synthesis of pyrrolo[1,2-*a*]quinoxalines using *N,N*-dimethylethanolamine (DMEA) as a C1 synthon. In addition, the method of Ma's group was also applicable to the synthesis of quinazolin-4-one and benzo[4,5]imidazoquinazoline. During the preparation of our manuscript, by means of an I₂-DMSO synergistic system, Lin [17] reported a method for the synthesis of acyl-substituted pyrrolo[1,2-*a*]quinolines using epoxides as acyl precursors. As part of our research interest in the green synthesis of nitrogen-containing heterocycles under metal-free conditions, PEG-400 [18], DMF [19] and DMSO [20] as carbon synthons have been reported (Scheme 1).

On the other hand, the synthesis of quinazolin-4-ones has also attracted much attention from chemists. In traditional synthesis methods, quinazolinone was obtained by an acid/base facilitated condensation reaction of esters, aldehydes or carboxylic acids with amides by means of some homogeneous catalytic systems and expensive raw materials [26–30]. In 2018, Wang [31] reported a novel synthetic strategy for the synthesis of quinazolinones from olefins, carbon monoxide and amines over a heterogeneous Ru



Citation: Lv, X.; Lv, L.; Li, S.; Ding, C.; Yang, B.; Ma, C. A Direct Method for Synthesis of Quinoxalines and Quinazolinones Using Epoxides as Alkyl Precursor. *Molecules* **2023**, *28*, 7391. <https://doi.org/10.3390/molecules28217391>

Academic Editors: Tao Liu and Xuexiang Chen

Received: 29 September 2023

Revised: 24 October 2023

Accepted: 25 October 2023

Published: 2 November 2023



Copyright: © 2023 by the authors. Licensee MDPI, Basel, Switzerland. This article is an open access article distributed under the terms and conditions of the Creative Commons Attribution (CC BY) license (<https://creativecommons.org/licenses/by/4.0/>).

cluster/cerium oxide catalyst under acid/ base-free and oxidant-free conditions with H₂O as the only by-product. In 2019, Zheng [32] developed a visible light-mediated intramolecular C-N cross-coupling reaction to synthesize a series of fused *N*-substituted polycyclic quinazolinone derivatives under mild reaction conditions via long-lived photoactive photoisomer complexes. In 2023, Fan [33] reported a method for the synthesis of 5*H*-phthalazino[1,2-*b*]quinazolin-8(6*H*)-one derivatives via a *t*-BuOK-catalyzed intramolecular hydrogen amination reaction of quinazolinones. Also in 2023, Zhu [34] reported a cobalt homeostatic catalysis system for the synthesis of quinazolinones from the coupling of enaminones and oxadiazolones.

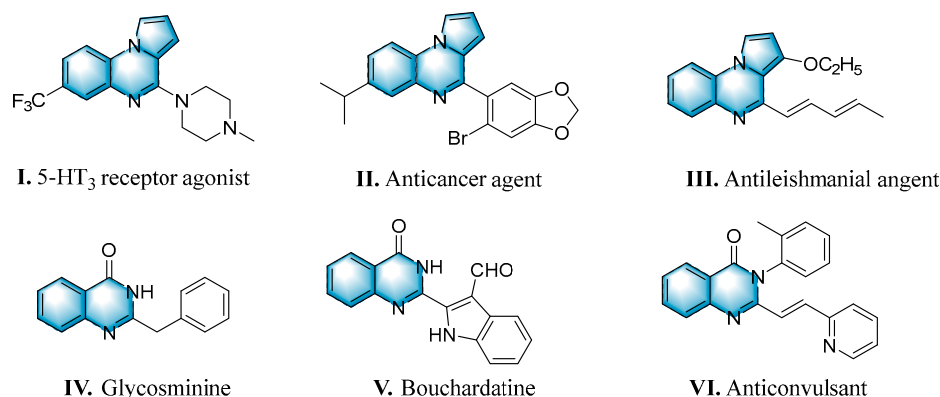
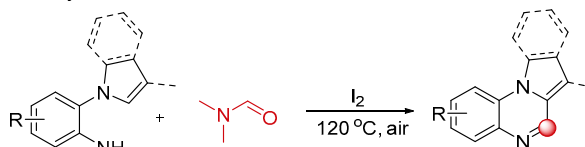


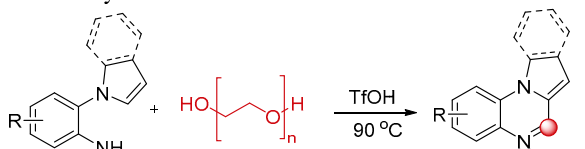
Figure 1. Drug Molecules Containing Quinoxalines and Quinazolines.

Our previous work

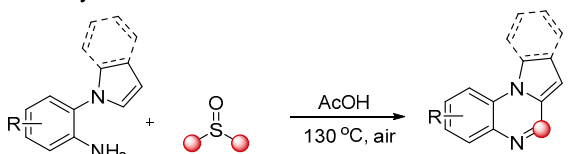
(a) DMF as carbon synthon:



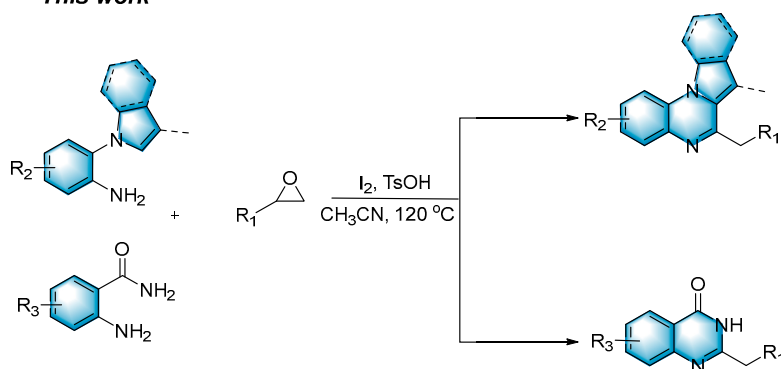
(b) PEG-400 as carbon synthon:



(c) DMSO as carbon synthon:



This work



Scheme 1. Synthesis of Pyrrolo[1,2-*a*]quinoxalines.

Epoxides are well-known electrophiles that can react with various nucleophiles. They are readily available from olefins or ketones and are usually air-stable and easily stored. The Meinwald rearrangement [35] is an acid-catalyzed rearrangement reaction in which epoxides form aldehydes or ketones via ring-opening followed by a 1,2-shift of the hydride or alkyl group. Aldehydes, especially enolizable aliphatic aldehydes, are susceptible to self-condensation which makes them unstable and hard to store in pure form. Therefore, it is more desirable to utilize epoxides to replace the original aldehydes. In 2023, Moran [36] synthesized a series of functionalized isochromans using epoxides as an alternative to aldehydes. In 2021, Feng [37] reported the first catalytic asymmetric multi-insertion olefin addition reaction triggered by an epoxy-vinyl Meinwald rearrangement using a chiral *N,N'*-dioxide/Sc^{III} complex catalyst. Encouraged by these discoveries and to further explore the applications of epoxides [38–42], herein, we developed a method for synthesizing pyrrolo[1,2-*a*]quinoxalines and quinazolin-4-ones via a tandem Meinwald rearrangement and cyclization in one pot.

2. Results and Discussion

2.1. Optimization

We commenced our exploration with 1-(2-aminophenyl)-pyrrole (**1a**; 0.5 mmol) and styrene oxide (**2a**; 1.0 mmol) as the model substrates. In the presence of I₂ (0.5 mmol) and AcOH (0.5 mmol) in CH₃CN (1.0 mL) at 120 °C, the target product 4-benzylpyrrolo[1,2-*a*]quinoxaline (**3a**) was obtained in 52% yield. Then, we screened several common Brønsted acids, such as HCOOH, trifluoromethanesulfonic acid (TfOH) and *p*-toluenesulfonic acid (TsOH) (Table 1, entries 1–5), and **3a** had the best yield (76%) when TsOH was used (Table 1, entry 5). In addition, we found that in the absence of iodine or acid, yields showed a significant decline (Table 1, entries 6–7). It can be noted that iodine and acid play a crucial role in this reaction system. Furthermore, when the acid was reduced to 0.5 equivalents, the yield decreased; when the acid equivalent was increased to 1.5 equivalents, the yield did not increase significantly (Table 1, entries 8–9). In addition, common solvents, such as 1,2-dichloroethane (DCE), EtOH, toluene, *N*-methylpyrrolidone (NMP) and PhCl, were selected, and CH₃CN was the best (Table 1, entries 10–14). Lowering the reaction temperature did not improve the reaction yield (Table 1, entries 15–16). For the sake of economy and safety, we did not raise the temperature further. We finally determined that subsequent experiments will be performed with I₂ (0.5 mmol) and TsOH (0.5 mmol) in CH₃CN at 120 °C for 4 h (Table 1, entry 5).

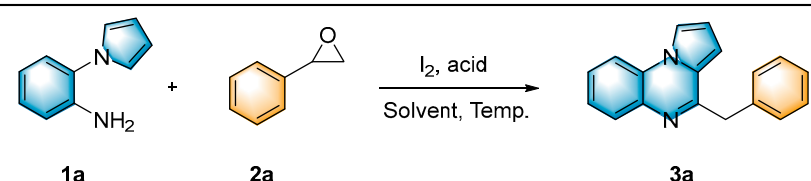
2.2. Scope of Substrates

With the optimal reaction conditions in hand, various substituted 1-(2-aminophenyl)-pyrroles were first explored, and the results are shown in Table 2. For monosubstituted 1-(2-aminophenyl)-pyrroles, some bearing electron-donating groups (EDGs), like methyl, methoxy or *tert*-butyl, work well in this method (**3b–3c**, **3e–3f** and **3k**). The method was also compatible with substrates containing electron-withdrawing groups (EWGs), such as fluoro, chloro, bromo and iodine (**3d**, **3g–3j** and **3l**). Disubstituted 1-(2-aminophenyl)-pyrroles were also well tolerated under these conditions; for 4,5-dimethyl-2-(1*H*-pyrrol-1-yl)aniline, 4,5-difluoro-2-(1*H*-pyrrol-1-yl)aniline and 4,5-dichloro-2-(1*H*-pyrrol-1-yl)aniline, the target products **3m**, **3n** and **3o** were obtained with the yields of 64%, 76% and 65%, respectively. When we replaced the pyrrole ring with indole, the reaction still proceeded with 35–48% yields (**3p–3r**). The reaction also proceeds smoothly when alkyl epoxides, such as 1,2-epoxybutane, were used (**3s**); when 3,4-epoxy-1-butene was used, the product **3t'** was expected to suffer a facile double-bond migration, affording the conjugated structure **3t**.

Inspired by the experimental results in Table 2, we then turned our focus to the synthesis of quinazolin-4-ones. We attempted to react 2-aminobenzamide (**4a**) with styrene oxide (**2a**) under optimal conditions and successfully obtained 2-benzylquinazolin-4(3*H*)-one (**5a**) in 70% yield (Table 3). Whether the R₃ group of 2-aminobenzamide was EDG or EWG participated successfully in the reaction with yields ranging from 58% to 74% (**5a–5j**).

Whether the R₃ group of the 2-aminobenzamide was an EDG or EWG and could smoothly participate in this reaction, were demonstrated with yields ranging from 58% to 74% (**5a–5j**). The reaction also performed well when styrene oxide (**2a**) was attached to EWGs, such as chloro and bromo (**5k–5l**). When we used 3,4-epoxy-1-butene to react with **4a**, the expected product quinazolinone **5m'** suffered an easy double-bond migration to give the conjugated product **5m**. Unfortunately, we did not obtain the desired products **5n** and **5o** when the R₄ group was replaced with an alkyl or aryl group.

Table 1. Optimization ^a.



Entry	Acid/Equiv.	Solvent	Temp. (°C)	Yield (%) ^b
1	AcOH/1.0	CH ₃ CN	120	52
2	HCOOH/1.0	CH ₃ CN	120	55
3	TFA/1.0	CH ₃ CN	120	56
4	TfOH/1.0	CH ₃ CN	120	63
5	TsOH/1.0	CH ₃ CN	120	76
6	TsOH/1.0	CH ₃ CN	120	27 ^c
7	-	CH ₃ CN	120	50
8	TsOH/0.5	CH ₃ CN	120	56r
9	TsOH/1.5	CH ₃ CN	120	71
10	TsOH/1.0	DCE	120	47
11	TsOH/1.0	EtOH	120	43
12	TsOH/1.0	toluene	120	trace
13	TsOH/1.0	NMP	120	48
14	TsOH/1.0	PhCl	120	26
15	TsOH/1.0	CH ₃ CN	100	62
16	TsOH/1.0	CH ₃ CN	80	58

^a Reaction conditions: **1a** (0.5 mmol, 1 equiv.), **2a** (1.0 mmol, 2 equiv.), I₂ (0.5 mmol, 1 equiv.) and acid in solvent (1.0 mL) were stirred in a sealed tube and allowed to react for 4 h. ^b Isolated yield. ^c Without I₂.

2.3. Large Scale Reaction and Synthetic Applications

Subsequently, several synthetic applications were performed to demonstrate the practicality of this methodology (Scheme 2). Under standard conditions, the gram-scale synthesis of **3a** and **5a** was carried out. Pleasantly, the desired product was successfully obtained in 60% and 62% yields, respectively, making the procedure suitable for a broad-scale preparation. Of these, **5a** can be used as a cardiovascular agent [14]. In addition, the 2-benzylquinazolin-4(3H)-one (**5a**) obtained in this protocol could be further modified into an active antiurease reagent [43], molecular antagonists of CCR₄ [44] and a photoluminescent probe [45]. The photoluminescent probe could be used for the label-free, highly selective and sensitive detection of Fe³⁺ and Ag⁺ metal ions.

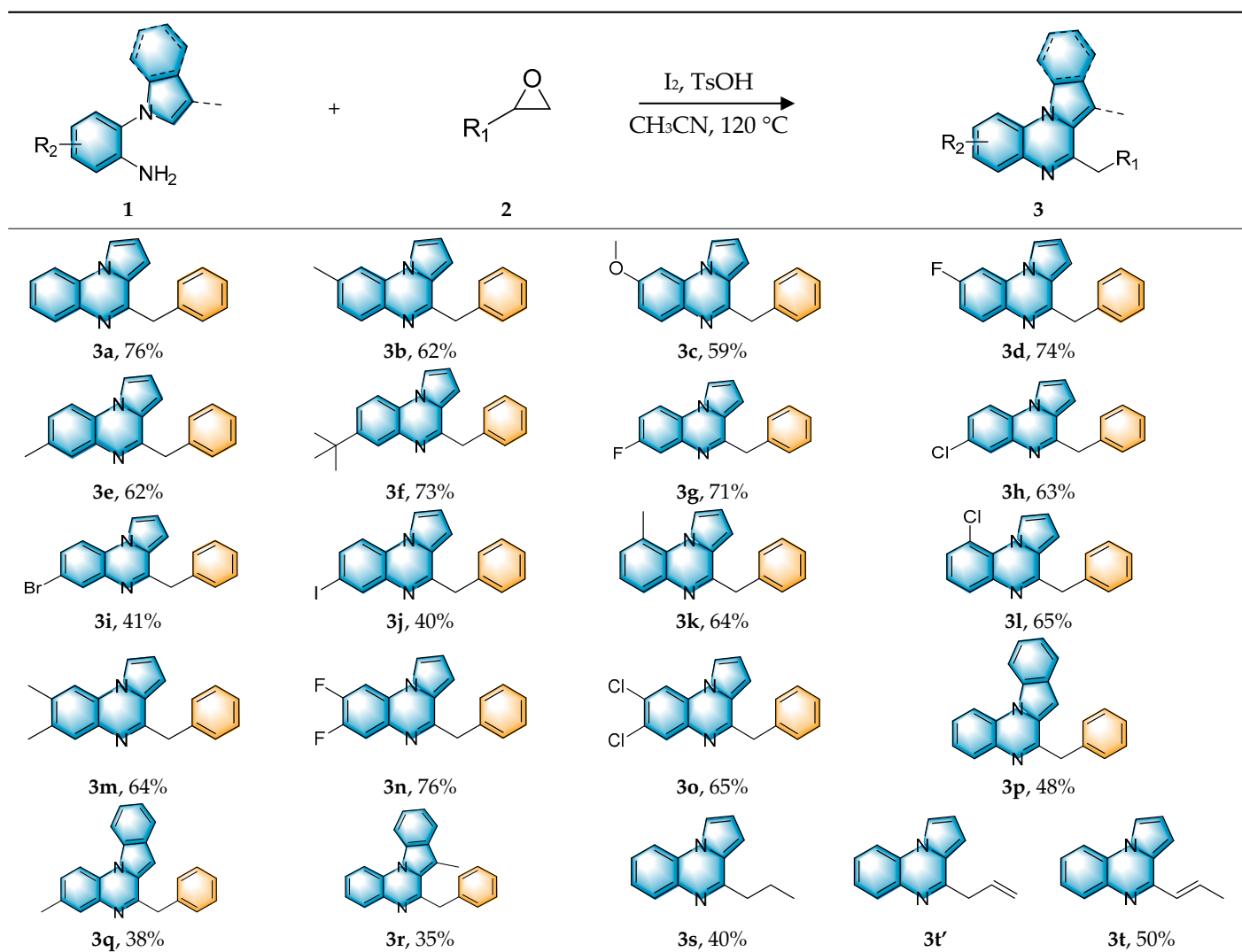
2.4. Mechanism Investigation

To shed light on the mechanism of the reaction, several control experiments were performed (Scheme 3). When the radical scavengers 2,2,6,6-tetramethylpiperidinyl-1-oxide (TEMPO, 3.0 equiv.) and 2,6-di-*tert*-butyl-4-methylphenol (BHT, 3.0 equiv.) were added to the reaction system under standard conditions, the desired product was obtained in 65% and 68% yields (Scheme 3a), respectively. This indicated that the conversion was a non-radical process. When the reaction was carried out without the addition of I₂, the yield exhibited a significant decrease (27%). When the reaction system was performed without the addition of TsOH, the target product was obtained with a 50% yield; we presumed that it is the I₂, as a Lewis acid, that plays a role in the conversion process (Table 1, entries 6–7). To

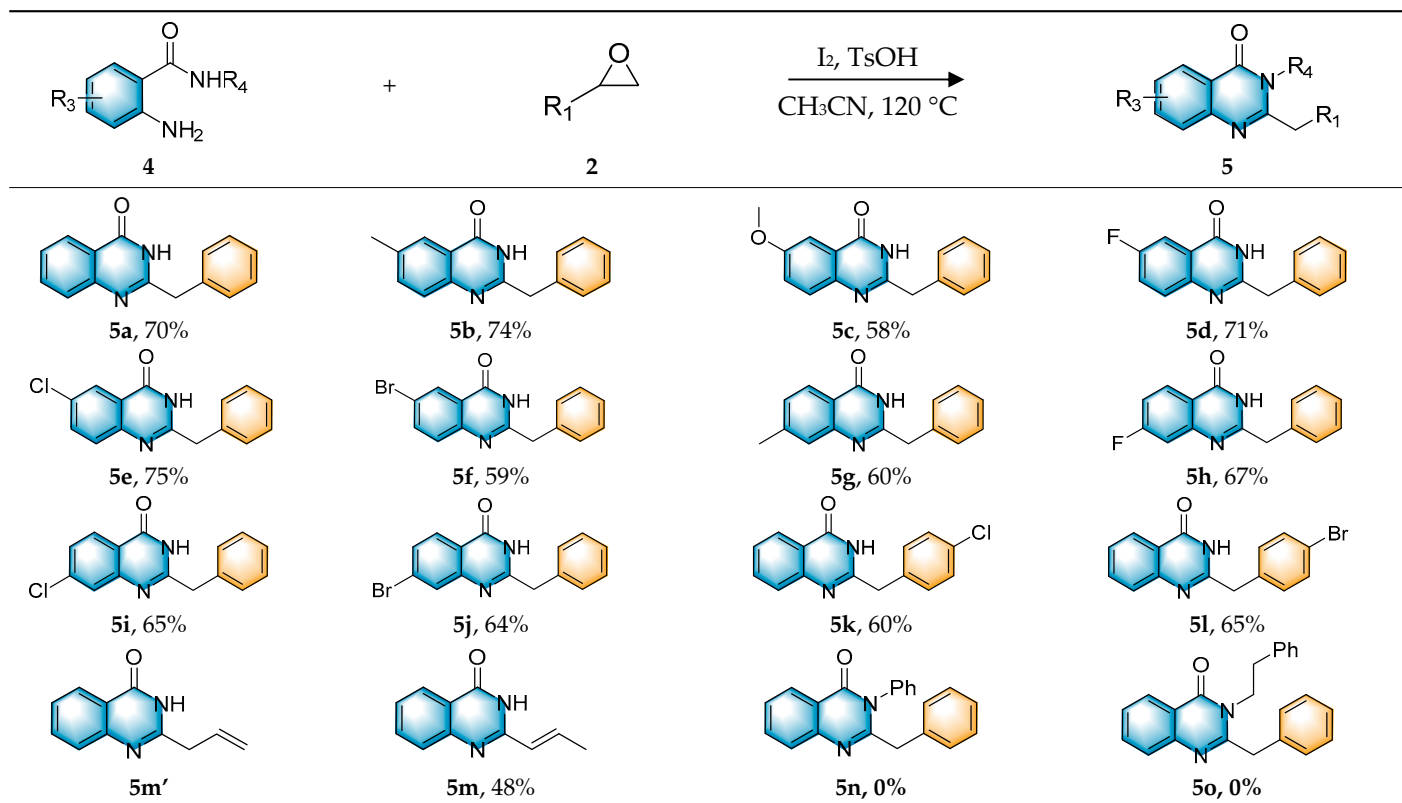
investigate the reaction mechanism in more depth, we used 2-phenylacetaldehyde to react with **1a** under standard conditions to obtain the target product in 65% yield (Scheme 3b). This indicated that 2-phenylacetaldehyde may be a key intermediate in the reaction. In the absence of I_2 , the yield decreased significantly, indicating that iodine plays a key role in the subsequent cyclization reaction. Under standard conditions, aniline and 1-(2-aminophenyl)-pyrrole were reacted with styrene oxide (**2a**), respectively, and the intermediate imide was detected with HRMS (Scheme 3c,d).

Based on the aforementioned control experiments and related literature studies, a plausible mechanism of this reaction is described in Scheme 4. Initially, in the presence of TsOH, styrene oxide (**2a**) underwent a Meinwald rearrangement to afford 2-phenylacetaldehyde. The 2-phenylacetaldehyde reacted with 1-(2-aminophenyl)-pyrrole (**1a**) accompanied by the elimination of H_2O to generate the intermediate imine **I**. Afterwards, intramolecular cyclization was accomplished with the assistance of molecular iodine to afford the dihydropyrrolo[1,2-*a*]quinoxaline **II**, which was ultimately aromatized to afford the target product **3a**.

Table 2. Substrate Scope of 2-(1*H*-Pyrrolo/indolo-1-yl)anilines ^{a,b}.

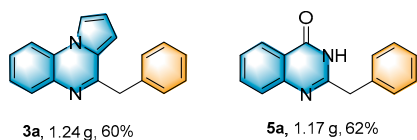


^a **1** (0.5 mmol, 1 equiv.), **2** (1.0 mmol, 2 equiv.), I_2 (0.5 mmol, 1 equiv.) and acid (0.5 mmol, 1 equiv.) in solvent (1.0 mL) were stirred in a sealed tube, and allowed to react for 4 h. ^b Isolated yield.

Table 3. Substrate Scope of 2-Aminobenzamide^{a,b}.

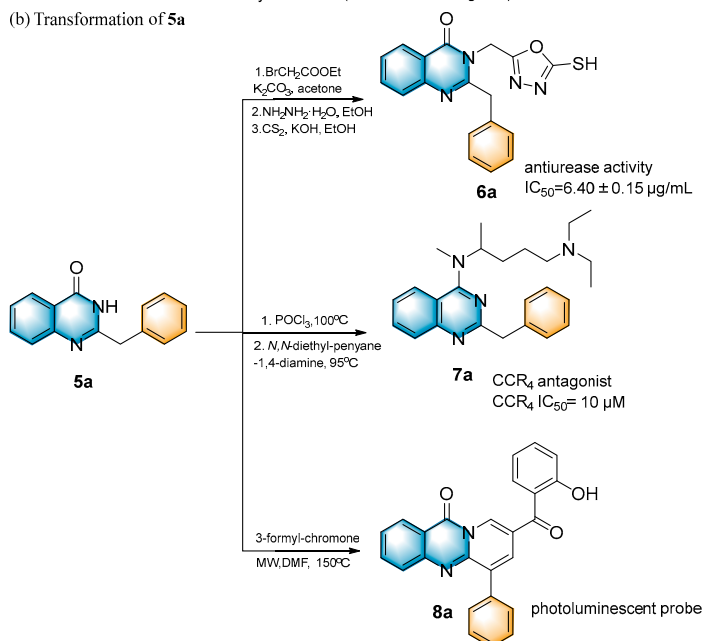
^a 4 (0.5 mmol, 1 equiv.), 2 (1.0 mmol, 2 equiv.), I_2 (0.5 mmol, 1 equiv.) and acid (0.5 mmol, 1 equiv.) in solvent (1.0 mL) were stirred in a sealed tube and allowed to react for 4 h. ^b Isolated yield.

(a) Gram-scale synthesis

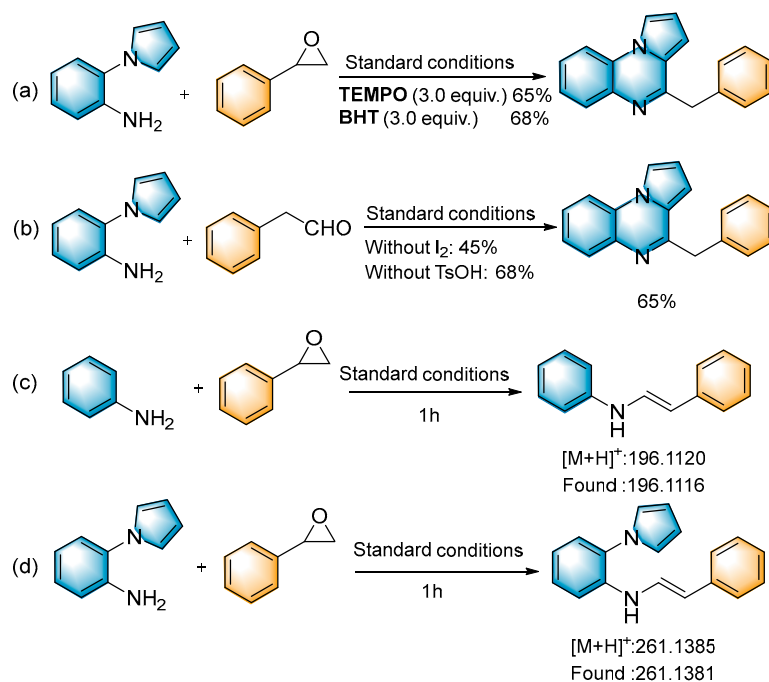


Deoxyvasicinone (Cardiovascular agents)

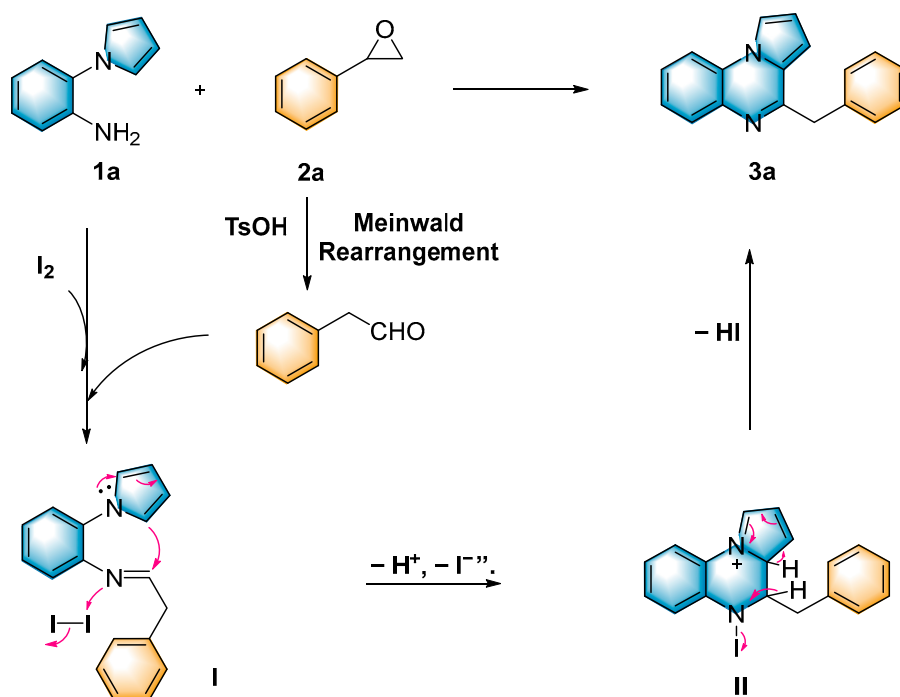
(b) Transformation of 5a



Scheme 2. Large-scale reaction and synthetic applications.



Scheme 3. Control experiments (a–d).



Scheme 4. Proposed Mechanism.

3. Materials and Methods

3.1. General Information

2-(1*H*-pyrrol-1-yl)anilines/2-(1*H*-indolo-1-yl)anilines and 2-aminobenzamides were obtained based on procedures reported in the literature [46,47]. All other reagents were market available and used with no further purification. We monitored the reactions using thin layer chromatography (TLC). Reactions requiring heat were performed in an oil bath. ¹H NMR (400 MHz or 500 MHz) and ¹³C NMR (100 MHz or 125 MHz) spectra were recorded on a Bruker spectrometer, with CDCl₃ or DMSO-*d*₆ as a solvent and tetramethylsilane (TMS)

as an internal standard (Supplementary Materials). HRMS spectra (ESI) were acquired on a Bruker impact II spectrograph in positive-ion mode with an ESI ion source.

3.2. General Experimental Procedures for 2-(1H-Pyrrol-1-yl) Anilines (1)

The substituted 2-nitroaniline (2.7626 g, 20 mmol, 1 equiv.) and 2, 5-dimethoxytetrahydrofuran (2.9075 g, 22 mmol, 1.1 equiv.) were mixed in HOAc (30 mL) and stirred vigorously under reflux conditions for 2–3 h. To neutralize the reaction mixture, Na₂CO₃ aqueous solution was added and extracted three times with EtOAc. The organic layer was then dried with anhydrous Na₂SO₄ and the residue was obtained after vacuum evaporation. Iron powder (4.4680 g, 80 mmol, 5 equiv.) and NH₄Cl (1.0698 g, 20 mmol, 1 equiv.) were added to the residue in water (40 mL) and refluxed for 4–9 h. When the reaction was complete, the mixture was extracted three times with EtOAc. The organic layer was then dried with anhydrous Na₂SO₄, and the residue was obtained after vacuum evaporation. The residue was subsequently purified by silica gel chromatography to yield the desirable compounds.

3.3. General Experimental Procedures for 2-(1H-Indolo-1-yl)anilines (1)

The substituted fluoro-2-nitrobenzene (2.8220 g, 20 mmol, 1 equiv.), indole (2.3430 g, 20 mmol, 1 equiv.) and NaOH (0.8000 g, 20 mmol, 1 equiv.) were mixed in DMSO (30 mL) and stirred at room temperature for 4 h. The reaction mixture was extracted with EtOAc (3 × 30 mL). The organic layer was then dried with anhydrous Na₂SO₄ and a solid was obtained after vacuum evaporation. Iron powder (5.6850 g, 100 mmol, 5 equiv.) and NH₄Cl (1.0700 g, 20 mmol, 1 equiv.) were added to the solvent and refluxed for 5–9 h. After cooling, the reaction mixture was extracted three times with EtOAc and brine solution and subsequently dried with anhydrous Na₂SO₄. After filtration, a vacuum was used to remove the solvent. The resulting solid was then purified by silica gel column chromatography to obtain the desired compound.

3.4. General Experimental Procedures for Compounds 3a–3t and 5a–5m

Various substituted amines (0.5 mmol, 1 equiv.), epoxides (1.0 mmol, 2 equiv.), iodine (0.1269 g, 0.5 mmol, 1 equiv.) and TsOH (0.0861 g, 0.5 mmol, 1 equiv.) were added to CH₃CN (1 mL) in a sealed tube. The reaction mixture was stirred vigorously at 120 °C for 4 h. After completion of the reaction, monitored by TLC, the reaction mixture was neutralized with Na₂S₂O₃ and extracted three times with EtOAc and H₂O, followed by drying with anhydrous Na₂SO₄. The product was purified by silica gel column chromatography to give the desired compounds 3a–3t and 5a–5m.

3.5. Characterization Data

4-benzylpyrrolo[1,2-a]quinoxaline (3a), purification on a silica gel (petroleum ether/ethyl acetate = 15:1) afforded compound 3a as a light yellow solid (98.2 mg, 76% yield); ¹H NMR (400 MHz, CDCl₃): δ 7.86–7.84 (m, 1 H), 7.65 (dd, *J* = 2.9, 1.4 Hz, 1 H), 7.60–7.57 (m, 1 H), 7.31–7.24 (m, 4 H), 7.14 (t, *J* = 8.0 Hz, 2 H), 7.10–7.03 (m, 1 H), 6.69 (dd, *J* = 4.0, 1.2 Hz, 1 H), 6.62–6.62 (m, 1 H), 4.23 (s, 2 H). ¹³C NMR (100 MHz, CDCl₃): δ 154.1, 136.9, 134.7, 128.5, 127.8, 127.8, 127.4, 126.1, 125.5, 124.7, 124.0, 113.2, 112.6, 112.5, 106.1, 41.5. HRMS (ESI-TOF): *m/z* [M + H]⁺ calcd for C₁₈H₁₅N₂⁺: 259.1229; found: 259.1233.

4-benzyl-8-methylpyrrolo[1,2-a]quinoxaline (3b), purification on a silica gel (petroleum ether/ethyl acetate = 15:1) afforded compound 3b as a yellow solid (84.4 mg, 62% yield); ¹H NMR (400 MHz, CDCl₃): δ 7.77 (d, *J* = 8.2 Hz, 1 H), 7.72 (dd, *J* = 2.7, 1.3 Hz, 1 H), 7.50 (s, 1 H), 7.32 (d, *J* = 7.4 Hz, 2 H), 7.20–7.10 (m, 4 H), 6.71 (dd, *J* = 4.0, 1.3 Hz, 1 H), 6.67 (dd, *J* = 4.0, 2.7 Hz, 1 H), 4.26 (s, 2 H), 2.43 (s, 3 H). ¹³C NMR (100 MHz, CDCl₃): δ 153.2, 137.1, 136.6, 132.8, 128.3, 127.8, 127.4, 126.0, 125.5, 125.3, 124.9, 112.8, 112.6, 112.5, 105.7, 41.5, 20.7. HRMS (ESI-TOF): *m/z* [M + H]⁺ calcd for C₁₉H₁₇N₂⁺: 273.1385; found: 273.1381.

4-benzyl-8-methoxypyrrolo[1,2-a]quinoxaline (3c), purification on a silica gel (petroleum ether/ethyl acetate = 8:1) afforded compound **3c** as a yellow solid (85.1 mg, 59% yield); ^1H NMR (400 MHz, CDCl_3): δ 7.77 (d, J = 8.9 Hz, 1 H), 7.57 (dd, J = 2.8, 1.3 Hz, 1 H), 7.29 (d, J = 6.8 Hz, 2 H), 7.14 (t, J = 7.4 Hz, 2 H), 7.08–7.03 (m, 2 H), 6.88 (dd, J = 8.9, 2.7 Hz, 1 H), 6.66–6.61 (m, 2 H), 4.21 (s, 2 H), 3.75 (s, 3 H). ^{13}C NMR (100 MHz, CDCl_3): δ 157.7, 151.5, 137.2, 129.8, 129.2, 127.8, 127.4, 126.9, 125.4, 124.7, 112.7, 112.6, 111.5, 105.5, 96.4, 54.6, 41.4. HRMS (ESI-TOF): m/z $[\text{M} + \text{H}]^+$ calcd for $\text{C}_{19}\text{H}_{17}\text{ON}_2^+$: 289.1335; found: 289.1339.

4-benzyl-8-fluoropyrrolo[1,2-a]quinoxaline (3d), purification on a silica gel (petroleum ether/ethyl acetate = 15:1) afforded compound **3d** as a yellow solid (102.3 mg, 74% yield); ^1H NMR (400 MHz, CDCl_3): δ 7.63 (dd, J = 2.8, 1.3 Hz, 1 H), 7.56–7.50 (m, 2 H), 7.31 (d, J = 7.2 Hz, 2 H), 7.16 (t, J = 7.5 Hz, 2 H), 7.11–7.00 (m, 2 H), 6.74 (d, J = 4.0 Hz, 1 H), 6.64 (dd, J = 4.1, 2.7 Hz, 1 H), 4.22 (s, 2 H). ^{13}C NMR (100 MHz, CDCl_3): δ 158.7 (d, $J_{\text{C-F}}$ = 243.4 Hz), 155.4, 136.7, 136.0 (d, $J_{\text{C-F}}$ = 11.4 Hz), 127.65 (d, $J_{\text{C-F}}$ = 34.6 Hz), 125.6, 124.5, 122.86 (d, $J_{\text{C-F}}$ = 2.3 Hz), 113.9 (d, $J_{\text{C-F}}$ = 22.2 Hz), 113.7 (d, $J_{\text{C-F}}$ = 21.1 Hz), 113.6, 113.5, 113.4, 112.7, 106.4, 41.4. ^{19}F NMR (377 MHz, CDCl_3): δ –116.7 (s). HRMS (ESI-TOF): m/z $[\text{M} + \text{H}]^+$ calcd for $\text{C}_{18}\text{H}_{14}\text{FN}_2^+$: 277.1135; found: 277.1132.

4-benzyl-7-methylpyrrolo[1,2-a]quinoxaline (3e), purification on a silica gel (petroleum ether/ethyl acetate = 15:1) afforded compound **3e** as a yellow solid (84.4 mg, 62% yield); ^1H NMR (400 MHz, CDCl_3): δ 7.67 (d, J = 1.5 Hz, 2 H), 7.52 (d, J = 8.3 Hz, 1 H), 7.31 (d, J = 7.2 Hz, 2 H), 7.18–7.12 (m, 3 H), 7.08 (t, J = 7.3 Hz, 1 H), 6.70 (dd, J = 4.0, 1.3 Hz, 1 H), 6.63 (dd, J = 4.0, 2.7 Hz, 1 H), 4.24 (s, 2 H), 2.36 (s, 3 H). ^{13}C NMR (100 MHz, CDCl_3): δ 154.1, 137.0, 134.8, 133.8, 128.5, 127.8, 127.4, 127.2, 125.5, 124.7, 124.1, 112.9, 112.3, 112.2, 105.7, 41.5, 20.0. HRMS (ESI-TOF): m/z $[\text{M} + \text{H}]^+$ calcd for $\text{C}_{19}\text{H}_{17}\text{N}_2^+$: 273.1385; found: 273.1384.

4-benzyl-7-(tert-butyl)pyrrolo[1,2-a]quinoxaline (3f), purification on a silica gel (petroleum ether/ethyl acetate = 20:1) afforded compound **3f** as a yellow solid (114.8 mg, 73% yield); ^1H NMR (400 MHz, CDCl_3): δ 7.90 (s, 1 H), 7.68 (dd, J = 2.8, 1.3 Hz, 1 H), 7.59 (d, J = 8.6 Hz, 1 H), 7.40 (dd, J = 8.6, 2.3 Hz, 1 H), 7.30 (d, J = 6.8 Hz, 2 H), 7.14 (t, J = 7.5 Hz, 2 H), 7.08–7.04 (m, 1 H), 6.69 (d, J = 4.0 Hz, 1 H), 6.63 (dd, J = 4.0, 2.7 Hz, 1 H), 4.25 (s, 2 H), 1.30 (s, 9 H). ^{13}C NMR (100 MHz, CDCl_3): δ 154.0, 147.3, 137.0, 134.5, 127.7, 127.4, 125.5, 125.0, 124.7, 124.0, 123.8, 112.9, 112.4, 112.1, 105.8, 41.6, 33.7, 30.4. HRMS (ESI-TOF): m/z $[\text{M} + \text{H}]^+$ calcd for $\text{C}_{22}\text{H}_{23}\text{N}_2^+$: 315.1855; found: 315.1859.

4-benzyl-7-fluoropyrrolo[1,2-a]quinoxaline (3g), purification on a silica gel (petroleum ether/ethyl acetate = 20:1) afforded compound **3g** as a yellow solid (98.1 mg, 71% yield); ^1H NMR (400 MHz, CDCl_3): δ 7.67 (dd, J = 2.8, 1.3 Hz, 1 H), 7.59 (dd, J = 9.0, 5.0 Hz, 1 H), 7.53 (dd, J = 9.5, 2.9 Hz, 1 H), 7.32 (d, J = 7.1 Hz, 2 H), 7.18 (t, J = 7.4 Hz, 2 H), 7.12–7.04 (m, 2 H), 6.76 (dd, J = 4.0, 1.3 Hz, 1 H), 6.66 (dd, J = 4.1, 2.7 Hz, 1 H), 4.23 (s, 2 H). ^{13}C NMR (100 MHz, CDCl_3): δ 158.7 (d, $J_{\text{C-F}}$ = 243.5 Hz), 155.4, 136.7, 136.1 (d, $J_{\text{C-F}}$ = 11.6 Hz), 127.8, 127.5, 125.6, 124.5, 122.9 (d, $J_{\text{C-F}}$ = 2.2 Hz), 114.0 (d, $J_{\text{C-F}}$ = 22.0 Hz), 113.8 (d, $J_{\text{C-F}}$ = 24.0 Hz), 113.6 (d, $J_{\text{C-F}}$ = 9.0 Hz), 113.4, 112.7, 106.4, 41.4. ^{19}F NMR (377 MHz, CDCl_3): δ –116.8 (s). HRMS (ESI-TOF): m/z $[\text{M} + \text{H}]^+$ calcd for $\text{C}_{18}\text{H}_{14}\text{FN}_2^+$: 277.1135; found: 277.1332.

4-benzyl-7-chloropyrrolo[1,2-a]quinoxaline (3h), purification on a silica gel (petroleum ether/ethyl acetate = 20:1) afforded compound **3h** as a yellow solid (92.2 mg, 63% yield); ^1H NMR (400 MHz, CDCl_3): δ 7.88 (d, J = 2.4 Hz, 1 H), 7.74 (d, J = 1.7 Hz, 1 H), 7.63 (d, J = 8.7 Hz, 1 H), 7.33 (d, J = 8.6 Hz, 3 H), 7.22–7.18 (m, 2 H), 7.14–7.11 (m, 1 H), 6.81 (d, J = 4.5 Hz, 1 H), 6.73–6.72 (m, 1 H), 4.27 (s, 2 H). ^{13}C NMR (100 MHz, CDCl_3): δ 155.4, 136.6, 135.7, 129.1, 128.0, 127.8, 127.5, 126.0, 125.6, 124.8, 124.6, 113.6, 113.5, 112.9, 106.5, 41.4. HRMS (ESI-TOF): m/z $[\text{M} + \text{H}]^+$ calcd for $\text{C}_{18}\text{H}_{14}\text{ClN}_2^+$: 293.0839; found: 293.0837.

4-benzyl-7-bromopyrrolo[1,2-a]quinoxaline (3i), purification on a silica gel (petroleum ether/ethyl acetate = 20:1) afforded compound **3i** as a yellow solid (69.1 mg, 41% yield);

^1H NMR (400 MHz, CDCl_3): δ 7.98 (d, J = 2.3 Hz, 1 H), 7.63 (d, J = 1.5 Hz, 1 H), 7.44 (d, J = 8.8 Hz, 1 H), 7.37 (dd, J = 8.8, 2.3 Hz, 1 H), 7.31 (d, J = 7.6 Hz, 2 H), 7.18 (t, J = 7.5 Hz, 2 H), 7.10 (t, J = 7.3 Hz, 1 H), 6.75 (d, J = 4.1 Hz, 1 H), 6.67–6.65 (m, 1 H), 4.23 (s, 2 H). ^{13}C NMR (100 MHz, CDCl_3): δ 155.3, 136.6, 136.0, 131.1, 128.8, 127.8, 127.5, 125.7, 125.2, 124.6, 116.5, 113.9, 113.5, 113.0, 106.6, 41.4. HRMS (ESI-TOF): m/z $[\text{M} + \text{H}]^+$ calcd for $\text{C}_{18}\text{H}_{14}\text{BrN}_2^+$: 337.0334; found: 337.0333.

*4-benzyl-7-iodopyrrolo[1,2-*a*]quinoxaline (3j)*, purification on a silica gel (petroleum ether/ethyl acetate = 20:1) afforded compound **3i** as a yellow solid (76.8 mg, 40% yield); ^1H NMR (400 MHz, CDCl_3): δ 8.22 (d, J = 2.0 Hz, 1 H), 7.69 (dd, J = 2.8, 1.4 Hz, 1 H), 7.59 (dd, J = 8.6, 2.0 Hz, 1 H), 7.38 (d, J = 8.6 Hz, 1 H), 7.32 (d, J = 7.5 Hz, 2 H), 7.22–7.15 (m, 2 H), 7.11 (t, J = 7.3 Hz, 1 H), 6.78 (dd, J = 4.0, 1.4 Hz, 1 H), 6.70 (dd, J = 4.1, 2.7 Hz, 1 H), 4.24 (s, 2 H). ^{13}C NMR (100 MHz, CDCl_3): δ 155.2, 137.3, 136.6, 136.2, 134.5, 127.8, 127.5, 125.9, 125.7, 124.6, 114.2, 113.5, 113.0, 106.7, 87.1, 41.4. HRMS (ESI-TOF): m/z $[\text{M} + \text{H}]^+$ calcd for $\text{C}_{18}\text{H}_{14}\text{IN}_2^+$: 385.0195; found: 385.0196.

*4-benzyl-9-methylpyrrolo[1,2-*a*]quinoxaline (3k)*, purification on a silica gel (petroleum ether/ethyl acetate = 15:1) afforded compound **3k** as a yellow solid (87.1 mg, 64% yield); ^1H NMR (400 MHz, CDCl_3): δ 8.03 (dd, J = 2.9, 1.4 Hz, 1 H), 7.72 (dd, J = 7.9, 1.8 Hz, 1 H), 7.28 (d, J = 6.8 Hz, 2 H), 7.16–7.10 (m, 3 H), 7.07–7.02 (m, 2 H), 6.72 (dd, J = 4.1, 1.3 Hz, 1 H), 6.59 (dd, J = 4.2, 2.8 Hz, 1 H), 4.21 (s, 2 H), 2.68 (s, 3 H). ^{13}C NMR (100 MHz, CDCl_3): δ 153.7, 137.0, 136.4, 129.6, 127.7, 127.4, 127.1, 126.5, 126.0, 125.4, 124.2, 123.4, 118.8, 111.8, 105.4, 41.3, 22.7. HRMS (ESI-TOF): m/z $[\text{M} + \text{H}]^+$ calcd for $\text{C}_{19}\text{H}_{17}\text{N}_2^+$: 273.1385; found: 273.1390.

*4-Benzyl-9-chloropyrrolo[1,2-*a*]quinoxaline (3l)*. Purification on a silica gel (petroleum ether/ethyl acetate = 15:1) afforded compound **3l** as a yellow solid (95.2 mg, 65% yield); ^1H NMR (400 MHz, CDCl_3): δ 8.90 (dd, J = 2.9, 1.3 Hz, 1 H), 7.72 (dd, J = 8.0, 1.5 Hz, 1 H), 7.27 (dd, J = 8.0, 1.5 Hz, 3 H), 7.15–7.09 (m, 3 H), 7.07–7.03 (m, 1 H), 6.76 (dd, J = 4.2, 1.3 Hz, 1 H), 6.60 (dd, J = 4.2, 2.9 Hz, 1 H), 4.18 (s, 2 H). ^{13}C NMR (100 MHz, CDCl_3): δ 154.6, 137.7, 136.7, 128.5, 127.8, 127.7, 127.4, 125.8, 125.6, 124.4, 123.5, 119.8, 119.8, 112.0, 106.4, 41.2. HRMS (ESI-TOF): m/z $[\text{M} + \text{H}]^+$ calcd for $\text{C}_{18}\text{H}_{14}\text{ClN}_2^+$: 293.0839; found: 293.0844.

*4-benzyl-7,8-dimethylpyrrolo[1,2-*a*]quinoxaline (3m)*, purification on a silica gel (petroleum ether/ethyl acetate = 10:1) afforded compound **3m** as a yellow solid (91.6 mg, 64% yield); ^1H NMR (400 MHz, CDCl_3): δ 7.64 (s, 1 H), 7.62 (s, 1 H), 7.41 (d, J = 5.3 Hz, 1 H), 7.30 (d, J = 8.1 Hz, 2 H), 7.15 (t, J = 7.4 Hz, 2 H), 7.07 (t, J = 7.3 Hz, 1 H), 6.67 (dd, J = 4.0, 1.4 Hz, 1 H), 6.62–6.60 (m, 1 H), 4.23 (s, 2 H), 2.29 (s, 3 H), 2.25 (s, 3 H). ^{13}C NMR (100 MHz, CDCl_3): δ 153.1, 137.2, 135.5, 133.0, 132.8, 128.8, 127.8, 127.4, 125.4, 124.8, 124.2, 113.0, 112.6, 112.2, 105.4, 41.5, 19.1, 18.5. HRMS (ESI-TOF): m/z $[\text{M} + \text{H}]^+$ calcd for $\text{C}_{20}\text{H}_{19}\text{N}_2^+$: 287.1542; found: 287.1540.

*4-benzyl-7,8-difluoropyrrolo[1,2-*a*]quinoxaline (3n)*, purification on a silica gel (petroleum ether/ethyl acetate = 15:1) afforded compound **3n** as a yellow solid (108.8 mg, 76% yield); ^1H NMR (400 MHz, CDCl_3): δ 7.68 (dd, J = 11.0, 8.1 Hz, 1 H), 7.62 (dd, J = 2.7, 1.3 Hz, 1 H), 7.48 (dd, J = 10.5, 7.3 Hz, 1 H), 7.32 (d, J = 6.9 Hz, 2 H), 7.22–7.17 (m, 2 H), 7.14–7.11 (m, 1 H), 6.80 (dd, J = 4.1, 1.3 Hz, 1 H), 6.73 (dd, J = 4.0, 2.8 Hz, 1 H), 4.25 (s, 2 H). ^{13}C NMR (100 MHz, CDCl_3): δ 154.8 (d, $J_{\text{C-F}}$ = 2.9 Hz), 148.3 (dd, $J_{\text{C-F}}$ = 248.7, 14.4 Hz), 146.9 (dd, $J_{\text{C-F}}$ = 245.2, 13.7 Hz), 136.6, 129.9, 127.8, 127.5, 125.7, 124.4, 122.6 (d, $J_{\text{C-F}}$ = 8.7 Hz), 116.2 (d, $J_{\text{C-F}}$ = 19.6 Hz), 113.5, 113.2, 106.6, 101.1 (d, $J_{\text{C-F}}$ = 22.2 Hz), 41.3. ^{19}F NMR (377 MHz, CDCl_3): δ -135.1 (s), -140.2 (s). HRMS (ESI-TOF): m/z $[\text{M} + \text{H}]^+$ calcd for $\text{C}_{18}\text{H}_{13}\text{F}_2\text{N}_2^+$: 295.1041; found: 295.1039.

*4-benzyl-7,8-dichloropyrrolo[1,2-*a*]quinoxaline (3o)*, purification on a silica gel (petroleum ether/ethyl acetate = 25:1) afforded compound **3o** as a yellow solid (106.3 mg, 65% yield); ^1H NMR (400 MHz, CDCl_3): δ 7.94 (s, 1 H), 7.75 (s, 1 H), 7.64 (dd, J = 2.8, 1.3 Hz, 1 H),

7.31 (d, $J = 6.9$ Hz, 2 H), 7.22–7.11 (m, 3 H), 6.80 (dd, $J = 4.0, 1.3$ Hz, 1 H), 6.71 (dd, $J = 4.0, 2.8$ Hz, 1 H), 4.23 (s, 2 H). ^{13}C NMR (100 MHz, CDCl_3): δ 155.6, 136.4, 134.3, 129.6, 129.6, 127.8, 127.6, 127.5, 125.7, 125.4, 124.5, 114.1, 113.8, 113.4, 107.1, 41.4. HRMS (ESI-TOF): m/z $[\text{M} + \text{H}]^+$ calcd for $\text{C}_{18}\text{H}_{13}\text{Cl}_2\text{N}_2^+$: 327.0450; found: 327.0455.

6-benzylindolo[1,2-*a*]quinoxaline (**3p**), purification on a silica gel (petroleum ether/ethyl acetate = 25:1) afforded compound **3p** as a yellow solid (74.1 mg, 48% yield); ^1H NMR (400 MHz, CDCl_3): δ 8.21 (dd, $J = 15.8, 8.6$ Hz, 2 H), 7.89 (dd, $J = 7.9, 1.8$ Hz, 1 H), 7.71 (d, $J = 8.0$ Hz, 1 H), 7.42–7.23 (m, 6 H), 7.17 (t, $J = 7.8$ Hz, 2 H), 7.09 (t, $J = 8.1$ Hz, 1 H), 6.95 (s, 1 H), 4.30 (s, 2 H). ^{13}C NMR (100 MHz, CDCl_3): δ 155.6, 136.6, 134.7, 131.7, 129.2, 128.9, 128.1, 127.9, 127.7, 127.5, 127.0, 125.6, 123.1, 122.9, 121.6, 121.4, 113.5, 113.4, 99.5, 41.6. HRMS (ESI-TOF): m/z $[\text{M} + \text{H}]^+$ calcd for $\text{C}_{22}\text{H}_{17}\text{N}_2^+$: 309.1385; found: 309.1382.

6-*q*-benzyl-3-methylindolo[1,2-*a*]quinoxaline (**3q**), purification on a silica gel (petroleum ether/ethyl acetate = 20:1) afforded compound **3q** as a yellow solid (61.3 mg, 38% yield); ^1H NMR (400 MHz, CDCl_3): δ 8.31 (d, $J = 8.6$ Hz, 1 H), 8.14 (s, 1 H), 7.79 (dd, $J = 16.9, 8.0$ Hz, 2 H), 7.42–7.27 (m, 3 H), 7.29 (t, $J = 7.4$ Hz, 1 H), 7.23–7.06 (m, 4 H), 6.98 (s, 1 H), 4.33 (s, 2 H), 2.51 (s, 3 H). ^{13}C NMR (100 MHz, CDCl_3): δ 154.6, 137.5, 136.7, 132.7, 131.7, 129.1, 128.7, 128.3, 128.0, 127.7, 127.5, 125.6, 124.0, 122.9, 121.6, 121.5, 113.9, 113.6, 99.4, 41.6, 21.1. HRMS (ESI-TOF): m/z $[\text{M} + \text{H}]^+$ calcd for $\text{C}_{23}\text{H}_{19}\text{N}_2^+$: 323.1542; found: 323.1546.

6-Benzyl-7-methylindolo[1,2-*a*]quinoxaline (**3r**). Purification on a silica gel (petroleum ether/ethyl acetate = 15:1) afforded compound **3r** as a yellow solid (56.4 mg, 35% yield); ^1H NMR (400 MHz, CDCl_3): δ 8.44 (t, $J = 7.9$ Hz, 2 H), 7.99 (s, 1 H), 7.88 (d, $J = 8.1$ Hz, 1 H), 7.56 (q, $J = 7.1$ Hz, 2 H), 7.41 (dt, $J = 14.1, 7.1$ Hz, 2 H), 7.27–7.25 (m, 4 H), 7.20 (q, $J = 4.3$ Hz, 1 H), 4.64 (s, 2 H), 2.63 (s, 3 H). ^{13}C NMR (100 MHz, CDCl_3): δ 156.8, 137.9, 132.1, 130.6, 130.0, 129.5, 128.9, 128.6, 128.5, 128.4, 128.2, 126.5, 124.8, 124.0, 123.8, 122.0, 120.7, 114.5, 114.4, 29.7, 11.0. HRMS (ESI-TOF): m/z $[\text{M} + \text{H}]^+$ calcd for $\text{C}_{23}\text{H}_{19}\text{N}_2^+$: 323.1542; found: 323.1543.

4-propylpyrrolo[1,2-*a*]quinoxaline (**3s**), purification on a silica gel (petroleum ether/ethyl acetate = 10:1) afforded compound **3s** as a yellow solid (42.1 mg, 40% yield); ^1H NMR (500 MHz, CDCl_3): δ 7.84 (dd, $J = 7.9, 1.5$ Hz, 1 H), 7.81–7.79 (m, 1 H), 7.73 (d, $J = 8.0$ Hz, 1 H), 7.35 (dtd, $J = 21.0, 7.4, 1.4$ Hz, 2 H), 6.82 (dd, $J = 3.9, 1.2$ Hz, 1 H), 6.75 (dd, $J = 3.8, 2.8$ Hz, 1 H), 2.91 (dd, $J = 8.5, 7.1$ Hz, 2 H), 1.86 (dq, $J = 15.0, 7.4$ Hz, 2 H), 1.00 (t, $J = 7.4$ Hz, 3 H). ^{13}C NMR (125 MHz, CDCl_3): δ 156.4, 135.0, 128.4, 126.2, 125.8, 125.1, 124.0, 113.0, 112.6, 112.4, 105.2, 36.8, 20.9, 13.3. HRMS (ESI-TOF): m/z $[\text{M} + \text{H}]^+$ calcd for $\text{C}_{14}\text{H}_{15}\text{N}_2^+$: 211.1229; found: 211.1233.

(*E*)-4-(prop-1-en-1-yl)pyrrolo[1,2-*a*]quinoxaline (**3t**), purification on a silica gel (petroleum ether/ethyl acetate = 10:1) afforded compound **3t** as a yellow solid (52.1 mg, 40% yield); ^1H NMR (500 MHz, CDCl_3): δ 7.90–7.82 (m, 2 H), 7.77–7.72 (dd, $J = 8.0, 1.0$ Hz, 1 H), 7.42–7.29 (m, 2 H), 7.18–7.09 (qd, $J = 13.5, 7.0$ Hz, 1 H), 6.93–6.90 (dd, $J = 4.0, 1.0$ Hz, 1 H), 6.80 (dd, $J = 4.0, 1.5$ Hz, 1 H), 6.78 (dd, $J = 7.0, 2.5$ Hz, 1 H), 1.98 (dd, $J = 6.8, 1.7$ Hz, 3 H). ^{13}C NMR (125 MHz, CDCl_3): δ 149.2, 135.1, 134.4, 128.6, 126.2, 125.9, 125.7, 124.6, 124.2, 113.3, 112.6, 112.5, 105.0, 17.8. HRMS (ESI-TOF): m/z $[\text{M} + \text{H}]^+$ calcd for $\text{C}_{14}\text{H}_{14}\text{N}_2^+$: 209.1072; found: 209.1071.

2-benzylquinazolin-4(3*H*)-one (**5a**), purification on a silica gel (petroleum ether/ethyl acetate = 2:1) afforded compound **5a** as a white solid (82.7 mg, 70% yield); ^1H NMR (400 MHz, $\text{DMSO-}d_6$): δ 12.43 (s, 1 H), 8.09 (dd, $J = 7.9, 1.6$ Hz, 1 H), 7.78 (ddd, $J = 8.4, 7.0, 1.6$ Hz, 1 H), 7.62 (d, $J = 8.5$ Hz, 1 H), 7.50–7.44 (m, 1 H), 7.39 (d, $J = 7.9$ Hz, 2 H), 7.33 (t, $J = 7.6$ Hz, 2 H), 7.28–7.22 (m, 1 H), 3.95 (s, 2 H). ^{13}C NMR (100 MHz, $\text{DMSO-}d_6$): δ 167.1, 161.2, 154.1, 141.8, 139.6, 134.1, 133.7, 132.2, 132.0, 131.4, 130.9, 126.0, 46.0. HRMS (ESI-TOF): m/z $[\text{M} + \text{H}]^+$ calcd for $\text{C}_{15}\text{H}_{13}\text{ON}_2^+$: 237.1002; found: 237.1005.

2-benzyl-6-methylquinazolin-4(3H)-one (5b), purification on a silica gel (petroleum ether/ethyl acetate = 5:1) afforded compound **5b** as a white solid (92.6 mg, 74% yield). ¹H NMR (400 MHz, DMSO-*d*₆): δ 12.32 (s, 1 H), 7.87 (s, 1 H), 7.59 (dd, *J* = 8.3, 2.2 Hz, 1 H), 7.51 (d, *J* = 8.2 Hz, 1 H), 7.38 (d, *J* = 6.8 Hz, 2 H), 7.32 (t, *J* = 7.5 Hz, 2 H), 7.24 (t, *J* = 7.2 Hz, 1 H), 3.92 (s, 2 H), 2.42 (s, 3H). ¹³C NMR (100 MHz, DMSO-*d*₆): δ 162.3, 155.5, 147.4, 137.1, 136.3, 136.1, 129.3, 129.0, 127.3, 127.2, 125.5, 121.0, 41.2, 21.2. HRMS (ESI-TOF): *m/z* [M + H]⁺ calcd for C₁₆H₁₅ON₂⁺: 251.1178; found: 251.1177.

2-benzyl-6-methoxyquinazolin-4(3H)-one (5c), purification on a silica gel (petroleum ether/ethyl acetate = 1:1) afforded compound **5c** as a white solid (77.3 mg, 58% yield); ¹H NMR (400 MHz, DMSO-*d*₆): δ 12.38 (s, 1 H), 7.57 (d, *J* = 8.8 Hz, 1 H), 7.48 (d, *J* = 2.9 Hz, 1 H), 7.41–7.36 (m, 3 H), 7.32 (d, *J* = 15.0 Hz, 2 H), 7.24 (t, *J* = 7.2 Hz, 1 H), 3.92 (s, 2 H), 3.85 (s, 3 H). ¹³C NMR (100 MHz, DMSO-*d*₆): δ 162.2, 157.8, 154.1, 143.9, 137.2, 129.3, 129.1, 129.0, 127.2, 124.3, 122.0, 106.2, 56.0, 41.1. HRMS (ESI-TOF): *m/z* [M + H]⁺ calcd for C₁₅H₁₅ON₂⁺: 267.1127; found: 267.1123.

2-benzyl-6-fluoroquinazolin-4(3H)-one (5d), purification on a silica gel (petroleum ether/ethyl acetate = 5:1) afforded compound **5d** as a white solid (90.3 mg, 71% yield); ¹H NMR (400 MHz, DMSO-*d*₆): δ 12.60 (s, 1 H), 7.76 (dd, *J* = 8.6, 2.7 Hz, 1 H), 7.71–7.65 (m, 2 H), 7.39 (d, *J* = 6.9 Hz, 2 H), 7.33 (t, *J* = 7.6 Hz, 2 H), 7.25 (t, *J* = 7.3 Hz, 1 H), 3.95 (s, 2 H). ¹³C NMR (100 MHz, DMSO-*d*₆): δ 161.8 (d, *J*_{C-F} = 3.3 Hz), 160.2 (d, *J*_{C-F} = 244.9 Hz), 156.0 (d, *J*_{C-F} = 2.2 Hz), 146.2 (d, *J*_{C-F} = 1.8 Hz), 136.9, 130.2 (d, *J*_{C-F} = 8.0 Hz), 129.4, 129.0, 127.3, 123.3 (d, *J*_{C-F} = 24.0 Hz), 122.4 (d, *J*_{C-F} = 8.4 Hz), 110.8 (d, *J*_{C-F} = 23.3 Hz), 41.1. ¹⁹F NMR (377 MHz, DMSO-*d*₆): δ −114.1 (s). HRMS (ESI-TOF): *m/z* [M + H]⁺ calcd for C₁₅H₁₂OFN₂⁺: 255.0927; found: 255.0928.

2-benzyl-6-chloroquinazolin-4(3H)-one (5e), purification on a silica gel (petroleum ether/ethyl acetate = 5:1) afforded compound **5e** as a white solid (101.55 mg, 75% yield); ¹H NMR (400 MHz, DMSO-*d*₆): δ 12.61 (s, 1 H), 8.01 (d, *J* = 2.5 Hz, 1 H), 7.80 (dd, *J* = 8.8, 2.6 Hz, 1 H), 7.64 (d, *J* = 8.7 Hz, 1 H), 7.38 (d, *J* = 6.8 Hz, 2 H), 7.33 (t, *J* = 7.5 Hz, 2 H), 7.25 (t, *J* = 7.2 Hz, 1 H), 3.95 (s, 2 H). ¹³C NMR (100 MHz, DMSO-*d*₆): δ 161.4, 157.1, 148.1, 136.8, 135.0, 130.9, 129.7, 129.4, 129.0, 127.3, 125.2, 122.5, 41.2. HRMS (ESI-TOF): *m/z* [M + H]⁺ calcd for C₁₅H₁₂OCIN₂⁺: 271.0632; found: 271.0635.

2-benzyl-6-bromoquinazolin-4(3H)-one (5f), purification on a silica gel (petroleum ether/ethyl acetate = 5:1) afforded compound **5f** as a white solid (93.0 mg, 59% yield); ¹H NMR (400 MHz, DMSO-*d*₆): δ 12.65 (s, 1 H), 8.15 (d, *J* = 2.4 Hz, 1 H), 7.92 (dd, *J* = 8.7, 2.4 Hz, 1 H), 7.57 (d, *J* = 8.8 Hz, 1 H), 7.38 (d, *J* = 6.9 Hz, 2 H), 7.33 (t, *J* = 7.5 Hz, 2 H), 7.25 (t, *J* = 7.2 Hz, 1 H), 3.94 (s, 2 H). ¹³C NMR (100 MHz, DMSO-*d*₆): δ 161.2, 157.2, 148.4, 137.7, 136.8, 129.8, 129.4, 129.0, 128.3, 127.3, 122.9, 119.0, 41.2. HRMS (ESI-TOF): *m/z* [M + H]⁺ calcd for C₁₅H₁₂OBrN₂⁺: 315.0127; found: 315.0124.

2-benzyl-7-methylquinazolin-4(3H)-one (5g), purification on a silica gel (petroleum ether/ethyl acetate = 2:1) afforded compound **5g** as a white solid (75.2 mg, 60% yield); ¹H NMR (400 MHz, DMSO-*d*₆): δ 12.31 (s, 1 H), 7.97 (d, *J* = 8.1 Hz, 1 H), 7.47–7.37 (m, 3 H), 7.35–7.20 (m, 4 H), 3.93 (s, 2 H), 2.43 (s, 3 H). ¹³C NMR (100 MHz, DMSO-*d*₆): δ 162.2, 156.5, 149.5, 145.3, 137.1, 129.3, 128.9, 128.0, 127.2, 127.1, 126.0, 118.8, 41.2, 21.8. HRMS (ESI-TOF): *m/z* [M + H]⁺ calcd for C₁₆H₁₅ON₂⁺: 251.1178; found: 251.1175.

2-benzyl-7-fluoroquinazolin-4(3H)-one (5h), purification on a silica gel (petroleum ether/ethyl acetate = 2:1) afforded compound **5h** as a white solid (85.2 mg, 67% yield); ¹H NMR (400 MHz, DMSO-*d*₆): δ 12.54 (s, 1 H), 8.15 (dd, *J* = 8.9, 6.4 Hz, 1 H), 7.42–7.37 (m, 3 H), 7.36–7.30 (m, 3 H), 7.25 (t, *J* = 7.3 Hz, 1 H), 3.95 (s, 2 H). ¹³C NMR (100 MHz, DMSO-*d*₆): δ = 166.2 (d, *J*_{C-F} = 250.7 Hz), 161.6, 158.0, 151.6 (d, *J*_{C-F} = 13.2 Hz), 136.8, 129.4, 129.2, 129.0, 127.3, 118.3 (d, *J*_{C-F} = 1.8 Hz), 115.2 (d, *J*_{C-F} = 23.6 Hz), 112.5 (d, *J*_{C-F} = 21.8 Hz), 41.2.

^{19}F NMR (377 MHz, $\text{DMSO-}d_6$): δ -104.5 (s). HRMS (ESI-TOF): m/z $[\text{M} + \text{H}]^+$ calcd for $\text{C}_{15}\text{H}_{12}\text{OFN}_2^+$: 255.0927; found: 255.0930.

2-benzyl-7-chloroquinazolin-4(3H)-one (**5i**), purification on a silica gel (petroleum ether/ethyl acetate = 2:1) afforded compound **5i** as a white solid (88.1 mg, 65% yield); ^1H NMR (400 MHz, $\text{DMSO-}d_6$): δ 12.58 (s, 1 H), 8.07 (d, $J = 8.4$ Hz, 1 H), 7.66 (d, $J = 2.1$ Hz, 1 H), 7.50 (dd, $J = 8.6, 2.1$ Hz, 1 H), 7.39 (d, $J = 7.0$ Hz, 2 H), 7.33 (t, $J = 7.5$ Hz, 2 H), 7.25 (t, $J = 7.2$ Hz, 1 H), 3.95 (s, 2 H). ^{13}C NMR (100 MHz, $\text{DMSO-}d_6$): δ 161.8, 158.1, 150.5, 139.5, 136.8, 129.4, 129.0, 128.3, 127.3, 127.0, 126.6, 120.1, 41.2. HRMS (ESI-TOF): m/z $[\text{M} + \text{H}]^+$ calcd for $\text{C}_{15}\text{H}_{12}\text{OCIN}_2^+$: 271.0632; found: 271.0630.

2-benzyl-7-bromoquinazolin-4(3H)-one (**5j**), purification on a silica gel (petroleum ether/ethyl acetate = 3:1) afforded compound **5j** as a white solid (100.9 mg, 64% yield); ^1H NMR (400 MHz, $\text{DMSO-}d_6$): δ 12.58 (s, 1 H), 7.99 (d, $J = 8.4$ Hz, 1 H), 7.81 (d, $J = 2.1$ Hz, 1 H), 7.62 (dd, $J = 8.4, 2.0$ Hz, 1 H), 7.39 (d, $J = 6.8$ Hz, 2 H), 7.33 (t, $J = 7.5$ Hz, 2 H), 7.25 (t, $J = 7.2$ Hz, 1 H), 3.95 (s, 2 H). ^{13}C NMR (100 MHz, $\text{DMSO-}d_6$): δ 161.9, 158.1, 150.6, 136.8, 129.7, 129.4, 129.0, 128.5, 128.3, 127.3, 120.4, 41.2. HRMS (ESI-TOF): m/z $[\text{M} + \text{H}]^+$ calcd for $\text{C}_{15}\text{H}_{12}\text{OBrN}_2^+$: 315.0127; found: 315.0131.

2-(4-chlorobenzyl)quinazolin-4(3H)-one (**5k**), purification on a silica gel (petroleum ether/ethyl acetate = 2:1) afforded compound **5k** as a white solid (89.4 mg, 66% yield); ^1H NMR (400 MHz, $\text{DMSO-}d_6$): δ 12.43 (s, 1 H), 8.09 (dd, $J = 7.9, 1.6$ Hz, 1 H), 7.78 (ddd, $J = 8.6, 7.1, 1.6$ Hz, 1 H), 7.60 (dd, $J = 8.3, 1.1$ Hz, 1 H), 7.50–7.45 (m, 1 H), 7.44–7.37 (m, 4 H), 3.95 (s, 2 H). ^{13}C NMR (100 MHz, $\text{DMSO-}d_6$): δ 162.3, 156.1, 149.3, 136.0, 134.9, 132.0, 131.3, 128.9, 127.4, 126.8, 126.2, 121.3, 40.4. HRMS (ESI-TOF): m/z $[\text{M} + \text{H}]^+$ calcd for $\text{C}_{15}\text{H}_{12}\text{OCIN}_2^+$: 271.0632; found: 271.0633.

2-(4-bromobenzyl)quinazolin-4(3H)-one (**5l**), purification on a silica gel (petroleum ether/ethyl acetate = 3:1) afforded compound **5l** as a white solid (99.3 mg, 63% yield); ^1H NMR (400 MHz, $\text{DMSO-}d_6$): δ 12.43 (s, 1 H), 8.09 (d, $J = 9.6$ Hz, 1 H), 7.82–7.73 (m, 1 H), 7.60 (d, $J = 7.4$ Hz, 1 H), 7.53 (d, $J = 8.4$ Hz, 2 H), 7.48 (t, $J = 7.5$ Hz, 1 H), 7.35 (d, $J = 8.5$ Hz, 2 H), 3.93 (s, 2 H). ^{13}C NMR (100 MHz, $\text{DMSO-}d_6$): δ 162.3, 156.0, 149.3, 136.4, 134.9, 131.8, 131.7, 127.4, 126.8, 126.2, 121.3, 120.5, 40.5. HRMS (ESI-TOF): m/z $[\text{M} + \text{H}]^+$ calcd for $\text{C}_{15}\text{H}_{12}\text{OBrN}_2^+$: 315.0127; found: 315.0125.

(E)-2-(prop-1-en-1-yl)quinazolin-4(3H)-one (**5m**). Purification on a silica gel (petroleum ether/ethyl acetate = 1:1) afforded compound **5m** as a white solid (44.7 mg, 48% yield); ^1H NMR (500 MHz, $\text{DMSO-}d_6$): δ 12.17 (s, 1 H), 8.14–8.01 (m, 1 H), 7.82–7.72 (m, 1 H), 7.60 (d, $J = 8.1$ Hz, 1 H), 7.44 (t, $J = 7.5$ Hz, 1 H), 7.21–7.04 (m, 1 H), 6.27 (dd, $J = 15.7, 1.7$ Hz, 1 H), 1.92 (dd, $J = 6.9, 1.5$ Hz, 3 H). ^{13}C NMR (125 MHz, $\text{DMSO-}d_6$): δ 162.3, 151.6, 149.5, 138.7, 134.9, 127.5, 126.4, 126.2, 125.1, 121.4, 18.7. HRMS (ESI-TOF): m/z $[\text{M} + \text{H}]^+$ calcd for $\text{C}_{11}\text{H}_{11}\text{ON}_2^+$: 187.0865; found: 187.0867.

4. Conclusions

To conclude, we disclosed an iodine-mediated one-pot procedure for the synthesis of pyrrolo/indolo[1,2-*a*]quinoxalines and quinazolin-4-ones under metal-free conditions. This methodology tandem the Meinwald rearrangement and annulation process. A series of *N*-heterocycles were obtained with medium to good yields. The protocol has a broad substrate scope, has a simple work-up and was suitable for wide-scale preparation. Furthermore, the obtained products could be further modified to afford promising pharmaceutical reagents. This study injects new vitality into the methodology for the synthesis of *N*-heterocycles. Related research is still in progress in our laboratory.

Author Contributions: Methodology: S.L. and X.L.; validation: X.L., C.D. and L.L.; investigation: S.L. and X.L.; writing—original draft preparation: X.L.; writing—review and editing: B.Y. and C.M. All authors have read and agreed to the published version of the manuscript.

Funding: Shandong Key Research Program (No. 2019JZZY021015) and Zhejiang Xin'an Chemical Group Company Basic Research Project (No. YJG202108).

Institutional Review Board Statement: Not applicable.

Informed Consent Statement: Not applicable.

Data Availability Statement: The supporting data are available in the Supplementary Materials.

Acknowledgments: We are grateful for the financial support from the Shandong Key Research Program (No. 2019JZZY021015) and Zhejiang Xin'an Chemical Group Company Basic Research Project (No. YJG202108). We are also grateful for the Analytical Center for Structural Constituent and the Physical Property of Core Facilities Sharing Platform, Shandong University for their technology and service support.

Conflicts of Interest: The authors declare no conflict of interest.

References

1. Vitaku, E.; Smith, D.T.; Njardarson, J.T. Analysis of the Structural Diversity, Substitution Patterns, and Frequency of Nitrogen Heterocycles among U.S. FDA approved Pharmaceuticals. *J. Med. Chem.* **2014**, *57*, 10257–10274. [CrossRef]
2. Li, R.; Li, B.; Zhang, H.; Ju, C.; Qin, Y.; Xue, X.; Zhao, D. A ring expansion strategy towards diverse azaheterocycles. *Nat. Chem.* **2021**, *13*, 1006–1016. [CrossRef]
3. Zhang, Z.; Zheng, Y.; Sun, Z.; Dai, Z.; Tang, Z.; Ma, J.; Ma, C. Direct Olefination of Fluorinated Quinoxalines via Cross-Dehydrogenative Coupling Reactions: A New Near-Infrared Probe for Mitochondria. *Adv. Synth. Catal.* **2017**, *359*, 2259–2268. [CrossRef]
4. Jonet, A.; Guillon, J.; Mullié, C.; Cohen, A.; Sonnet, P. Synthesis and Antimalarial Activity of New Enantiopure Aminoalcohol pyrrolo [1,2-*a*]quinoxaline. *Med. Chem.* **2018**, *14*, 293–303. [CrossRef]
5. Liu, K.; Li, D.; Zheng, W.; Shi, M.; Chen, Y.; Tang, M.; Yang, T.; Zhao, M.; Deng, D.; Zhang, C.; et al. Discovery, Optimization, and Evaluation of Quinazolinone Derivatives with Novel Linkers as Orally Efficacious Phosphoinositide-3-Kinase Delta Inhibitors for Treatment of Inflammatory Diseases. *J. Med. Chem.* **2021**, *64*, 8951–8970. [CrossRef]
6. Safakish, M.; Hajimahdi, Z.; Aghasadeghi, M.R.; Vahabpour, R.; Zarghi, A. Design, Synthesis, Molecular Modeling and Anti-HIV Assay of Novel Quinazolinone Incorporated Coumarin Derivatives. *Curr. HIV Res.* **2020**, *18*, 41–51.
7. Li, Z.; Zhao, L.; Bian, Y.; Li, Y.; Qu, J.; Song, F. The Antibacterial Activity of Quinazoline and Quinazolinone Hybrids. *Curr. Top. Med. Chem.* **2022**, *22*, 1035–1044. [CrossRef]
8. Wang, Z.; Wang, M.; Yao, X.; Li, Y.; Tan, J.; Wang, L.; Qiao, W.; Geng, Y.; Liu, Y.; Wang, Q. Design, synthesis and antiviral activity of novel quinazolinones. *Eur. J. Med. Chem.* **2012**, *53*, 275–282. [CrossRef]
9. Sakr, A.; Rezaq, S.; Ibrahim, S.M.; Soliman, E.; Baraka, M.M.; Romero, D.G.; Kothayer, H. Design and synthesis of novel quinazolinones conjugated ibuprofen, indoleacetamide, or thioacetohydrazide as selective COX-2 inhibitors: Anti-inflammatory, analgesic and anticancer activities. *J. Enzym. Inhib. Med. Chem.* **2021**, *36*, 1810–1828. [CrossRef]
10. He, L.; Li, H.; Chen, J.; Wu, X.F. Recent Advances in 4(3*H*)-quinazolinone Syntheses. *RSC Adv.* **2014**, *4*, 12065–12077. [CrossRef]
11. El-Subbagh, H.I.; Sabry, M.A. 2-Substituted-mercapto-quinazolin-4(3*H*)-ones as DHFR Inhibitors. *Mini-Rev. Med. Chem.* **2021**, *21*, 2249–2260. [CrossRef]
12. Liu, Q.; Zhang, B.; Wang, Y.; Wang, X.; Gou, S. Discovery of phthalazino [1,2-*b*]-quinazolinone derivatives as multitarget HDAC inhibitors for the treatment of hepatocellular carcinoma via activating the p53 signal pathway. *Eur. J. Med. Chem.* **2022**, *229*, 114058. [CrossRef]
13. Chatterjee, A.; Majumdar, S.G. Alkaloids of *Glycosmis pentaphylla* (Retz.) DC. Part I. *J. Am. Chem. Soc.* **1954**, *76*, 2459–2463. [CrossRef]
14. Cao, L.; Huo, H.; Zeng, H.; Yu, Y.; Lu, D.; Gong, Y. One-Pot Synthesis of Quinazolin-4(3*H*)-ones through Anodic Oxidation and the Related Mechanistic Studies. *Adv. Synth. Catal.* **2018**, *360*, 4764–4773. [CrossRef]
15. Cheeseman, G.W.H.; Tuck, B. The Synthesis of pyrrolo[1,2-*a*]quinoxalines from *N*-(2-acylamino)phenyl-pyrroles. *J. Chem. Soc. C* **1966**, 852–855. [CrossRef]
16. Geng, M.; Huang, M.; Kuang, J.; Fang, W.; Miao, M.; Ma, Y. Application of *N,N*-Dimethylethanolamine as a One-Carbon Synthone for the Synthesis of Pyrrolo [1,2-*a*]quinoxalines, Quinazolin-4-ones, and Benzo [4,5]imidazoquinazolines via [5 + 1] Annulation. *J. Org. Chem.* **2022**, *87*, 14753–14762. [CrossRef]
17. Jayaram, A.; Govindan, K.; Kannan, V.R.; Seenivasan, V.T.; Chen, N.Q.; Lin, W.Y. Iodine-Promoted Oxidative Cyclization of Acylated and Alkylated Derivatives from Epoxides toward the Synthesis of Aza Heterocycles. *J. Org. Chem.* **2023**, *88*, 1749–1761. [CrossRef]

18. Ding, C.; Li, S.; Feng, K.; Ma, C. PEG-400 as a carbon synthon: Highly selective synthesis of quinolines and methylquinolines under metal-free conditions. *Green Chem.* **2021**, *23*, 5542–5548. [CrossRef]
19. Li, S.; Ren, J.; Ding, C.; Wang, Y.; Ma, C. *N,N*-Dimethylformamide as Carbon Synthons for the Synthesis of *N*-Heterocycles: Pyrrolo/Indolo [1,2-*a*]quinoxalines and Quinazolin-4-ones. *J. Org. Chem.* **2021**, *86*, 16848–16857. [CrossRef]
20. Xie, C.; Zhang, Z.; Li, D.; Gong, J.; Han, X.; Liu, X.; Ma, C. Dimethyl Sulfoxide Involved One-Pot Synthesis of Quinoxaline Derivatives. *J. Org. Chem.* **2017**, *82*, 3491–3499. [CrossRef]
21. Liu, H.; Mai, X.; Xian, J.; Liu, S.; Zhang, X.; Li, B.; Chen, X.; Li, Y.; Xie, F. Construction of Spirocyclic Pyrrolo [1,2-*a*]quinoxalines via Palladium-Catalyzed Hydrogenative Coupling of Phenols and Nitroarenes. *J. Org. Chem.* **2022**, *87*, 16449–16457. [CrossRef] [PubMed]
22. Nan, J.; Ma, Q.; Yin, J.; Liang, C.; Tian, L.; Ma, Y. Rh^{III}-Catalyzed formal [5 + 1] cyclization of 2-pyrrolyl/indolylanilines using vinylene carbonate as a C1 synthon. *Org. Chem. Front.* **2021**, *8*, 1764–1769. [CrossRef]
23. Nan, J.; Chen, P.; Gong, X.; Hu, Y.; Ma, Q.; Wang, B.; Ma, Y. Metal-Free C-H [5 + 1] Carbonylation of 2-Alkenyl/Pyrrolylanilines Using Dioxazolones as Carbonylating Reagents. *Org. Lett.* **2021**, *23*, 3761–3766. [CrossRef]
24. He, Z.; Bae, M.; Wu, J.; Jamison, T. Synthesis of Highly Functionalized Polycyclic Quinoxaline Derivatives Using Visible-Light Photoredox Catalysis. *Angew. Chem. Int. Ed.* **2014**, *53*, 14451–14455. [CrossRef]
25. Liu, S.; Liang, J.; Zhang, P.; Li, Z.; Jiao, L.Y.; Jia, W.; Ma, Y.; Szostak, M. Ruthenium-catalyzed divergent deaminative and denitrative C–N cleavages: Facile access to quinoxalines. *Org. Chem. Front.* **2023**, *10*, 22–29. [CrossRef]
26. Liu, X.; Fu, H.; Jiang, Y.; Zhao, Y. A Simple and Efficient Approach to Quinazolinones under Mild Copper-Catalyzed Conditions. *Angew. Chem. Int. Ed.* **2009**, *48*, 348–351. [CrossRef]
27. Huang, D.; Li, X.; Xu, F.; Li, L.; Lin, X. Highly Enantioselective Synthesis of Dihydroquinazolinones Catalyzed by SPINOL-Phosphoric Acids. *ACS Catal.* **2013**, *3*, 2244–2247. [CrossRef]
28. Li, H.; He, L.; Neumann, H.; Beller, M.; Wu, X. Cascade synthesis of quinazolinones from 2-aminobenzonitriles and aryl bromides via palladium-catalyzed carbonylation reaction. *Green Chem.* **2014**, *16*, 1336–1343. [CrossRef]
29. Li, Z.; Dong, J.; Chen, X.; Li, Q.; Zhou, Y.; Yin, S. Metal- and Oxidant-Free Synthesis of Quinazolinones from β -Ketoesters with *o*-Aminobenzamides via Phosphorous Acid Catalyzed Cyclocondensation and Selective C–C Bond Cleavage. *J. Org. Chem.* **2015**, *80*, 9392–9400. [CrossRef]
30. Sharma, R.; Vishwakarma, R.A.; Bharate, S.B. Ligand-Free Copper-Manganese Spinel Oxide-Catalyzed Tandem One-Pot C-H Amidation and *N*-Arylation of Benzylamines: A Facile Access to 2-Arylquinazolin-4(3*H*)-ones. *Adv. Synth. Catal.* **2016**, *358*, 3027–3033. [CrossRef]
31. An, J.; Wang, Y.; Zhang, Z.; Zhao, Z.; Zhang, J.; Wang, F. The Synthesis of Quinazolinones from Olefins, CO, and Amines over a Heterogeneous Ru-clusters/Ceria Catalyst. *Angew. Chem. Int. Ed.* **2018**, *57*, 12308–12312. [CrossRef] [PubMed]
32. Jing, D.; Lu, C.; Chen, Z.; Jin, S.; Xie, L.; Meng, Z.; Su, Z.; Zheng, K. Light-Driven Intramolecular C-N Cross-Coupling via a Long-Lived Photoactive Photoisomer Complex. *Angew. Chem. Int. Ed.* **2019**, *58*, 14666–14672. [CrossRef] [PubMed]
33. Zhang, Z.; Wang, J.; Guo, S.; Fan, J.; Fan, X. *t*-BuOK-Catalyzed Regio- and Stereoselective Intramolecular Hydroamination Reaction Leading to Phthalazinoquinazolinone Derivatives. *J. Org. Chem.* **2023**, *88*, 1282–1291. [CrossRef] [PubMed]
34. Wu, W.; Fan, S.; Wu, X.; Fang, L.; Zhu, J. Cobalt Homeostatic Catalysis for Coupling of Enaminones and Oxadiazolones to Quinazolinones. *J. Org. Chem.* **2023**, *88*, 1945–1962. [CrossRef]
35. Meinwald, J.; Labana, S.S.; Chadha, M.S. Peracid Reactions. III. The Oxidation of Bicyclo [2.2.1]heptadiene. *J. Am. Chem. Soc.* **1963**, *85*, 582–585. [CrossRef]
36. Muller, C.; Horky, F.; Vayer, M.; Golushko, A.; Leboeuf, D.; Moran, J. Synthesis of functionalised isochromans: Epoxides as aldehyde surrogates in hexafluoroisopropanol. *Chem. Sci.* **2023**, *14*, 2983. [CrossRef]
37. Xu, J.; Song, Y.; He, J.; Dong, S.; Lin, L.; Feng, X. Asymmetric Catalytic Vinylogous Addition Reactions Initiated by Meinwald Rearrangement of Vinyl Epoxides. *Angew. Chem. Int. Ed.* **2021**, *60*, 14521–14527. [CrossRef]
38. Mehedi, M.S.A.; Tepe, J.J. Sc(OTf)₃-Mediated One-Pot Synthesis of 2,3-Disubstituted Quinolines from Anilines and Epoxides. *J. Org. Chem.* **2020**, *85*, 6741–6746. [CrossRef]
39. Mehedi, M.S.A.; George, D.E.; Tepe, J.J. Sc(OTf)₃-Mediated One-Pot Synthesis of 3,4-Disubstituted 1*H*-Pyrazoles and 3,5-Disubstituted Pyridines from Hydrazine or Ammonia with Epoxides. *J. Org. Chem.* **2022**, *87*, 16820–16828. [CrossRef]
40. Rao, C.J.; Sudheer, M.; Battula, V.R. Triflic-Acid-Catalyzed Tandem Epoxide Rearrangement and Annulation with Alkynes: An Efficient Approach for Regioselective Synthesis of Naphthalenes. *ChemistrySelect* **2022**, *7*, e20220047. [CrossRef]
41. Ali, S.; Khan, A.T. Ytterbium(III) triflate catalyzed domino reaction of arylamines and styrene oxides: Synthesis of 2-benzyl-3-arylquinoline derivatives. *Tetrahedron Lett.* **2021**, *70*, 152981. [CrossRef]
42. Ali, S.; Khan, A.T. An environmentally benign regioselective synthesis of 2-benzyl-4-arylquinoline derivatives using aryl amines, styrene oxides and aryl acetylenes. *Org. Biomol. Chem.* **2021**, *19*, 8772–8782. [CrossRef] [PubMed]
43. Akyuz, G. Synthesis and urease inhibition studies of some new quinazolinones. *J. Heterocycl. Chem.* **2021**, *58*, 1164–1170. [CrossRef]
44. Purandare, A.V.; Gao, A.; Wan, H.; Somerville, J.; Burke, C.; Seachord, C.; Vaccaro, W.; Wityak, J.; Poss, M.A. Identification of chemokine receptor CCR4 antagonist. *Bioorg. Med. Chem. Lett.* **2005**, *15*, 2669–2672. [CrossRef]
45. Yun, E.S.; Akhtar, M.S.; Mohandoss, S.; Lee, Y.R. Microwave-assisted annulation for the construction of pyrido-fused heterocycles and their application as photoluminescent chemosensors. *Org. Biomol. Chem.* **2022**, *20*, 3397–3407. [CrossRef]

46. Bao, Y.; Yan, Y.; Xu, K.; Su, J.; Zha, Z.; Wang, Z. Copper-catalyzed radical methylation/C–H amination/oxidation cascade for the synthesis of quinazolinones. *J. Org. Chem.* **2015**, *80*, 4736–4742. [CrossRef]
47. Dai, C.; Meschini, F.; Narayanam, J.M.R.; Stephenson, C.R.J. Friedel–Crafts Amidoalkylation via Thermolysis and Oxidative Photocatalysis. *J. Org. Chem.* **2012**, *77*, 4425–4431. [CrossRef]

Disclaimer/Publisher’s Note: The statements, opinions and data contained in all publications are solely those of the individual author(s) and contributor(s) and not of MDPI and/or the editor(s). MDPI and/or the editor(s) disclaim responsibility for any injury to people or property resulting from any ideas, methods, instructions or products referred to in the content.

Article

Target Screen of Anti-Hyperuricemia Compounds from Cortex Fraxini In Vivo Based on ABCG2 and Bioaffinity Ultrafiltration Mass Spectrometry

Xiuxiu Huang [†], Wenqing Dong [†], Xiao Luo, Lu Xu ^{*} and Yinan Wang ^{*}

Jiangsu Key Laboratory of New Drug Research and Clinical Pharmacy, Xuzhou Medical University, 209 Tongshan Road, Xuzhou 221004, China; xxyxyxz@163.com (X.H.); jhuan0926@163.com (W.D.); luoxiao_obu1mo@163.com (X.L.)

^{*} Correspondence: 19851633030@163.com (L.X.); wangyinan@xzhumu.edu.cn (Y.W.);
Tel.: +86-00516-83262138 (Y.W.)

[†] These authors contributed equally to this work.

Abstract: The ATP-binding cassette (ABC) transporter ABCG2 is a significant urate transporter with a high capacity, and it plays a crucial role in the development of hyperuricemia and gout. Therefore, it has the potential to be targeted for therapeutic interventions. Cortex Fraxini, a traditional Chinese medicine (TCM), has been found to possess anti-hyperuricemia properties. However, the specific constituents of Cortex Fraxini responsible for this effect are still unknown, particularly the compound that is responsible for reducing uric acid levels in vivo. In this study, we propose a target screening protocol utilizing bio-affinity ultrafiltration mass spectrometry (BA-UF-MS) to expediently ascertain ABCG2 ligands from the plasma of rats administered with Cortex Fraxini. Our screening protocol successfully identified fraxin as a potential ligand that interacts with ABCG2 when it functions as the target protein. Subsequent investigations substantiated fraxin as an activated ligand of ABCG2. These findings imply that fraxin exhibits promise as a drug candidate for the treatment of hyperuricemia. Furthermore, the utilization of BA-UF-MS demonstrates its efficacy as a valuable methodology for identifying hit compounds that exhibit binding affinity towards ABCG2 within TCMs.

Keywords: hyperuricemia; uric acid; ABCG2; ultrafiltration; Cortex Fraxini; fraxin



Citation: Huang, X.; Dong, W.; Luo, X.; Xu, L.; Wang, Y. Target Screen of Anti-Hyperuricemia Compounds from Cortex Fraxini In Vivo Based on ABCG2 and Bioaffinity Ultrafiltration Mass Spectrometry. *Molecules* **2023**, *28*, 7896. <https://doi.org/10.3390/molecules28237896>

Academic Editors: Tao Liu and Xuexiang Chen

Received: 31 October 2023

Revised: 27 November 2023

Accepted: 28 November 2023

Published: 1 December 2023



Copyright: © 2023 by the authors. Licensee MDPI, Basel, Switzerland. This article is an open access article distributed under the terms and conditions of the Creative Commons Attribution (CC BY) license (<https://creativecommons.org/licenses/by/4.0/>).

1. Introduction

Hyperuricemia, a common disease, can arise from elevated urate synthesis or impaired renal or intestinal excretion [1]. Gout, the clinical manifestation of hyperuricemia, is precipitated by urate deposition [2]. Additionally, gout and hyperuricemia have been linked to various diseases, including chronic kidney disease, hypertension, and metabolic syndrome [3]. An effective approach to managing hyperuricemia involves inhibiting excessive uric acid (UA) production and preventing its build-up in the bloodstream, thereby maintaining a desirable level of serum uric acid (SUA). The elimination of urate primarily occurs through glomerular filtration in the kidney. The ATP-binding cassette (ABC) transporter ABCG2 has been recognized as a significant urate transporter [4,5], exhibiting high expression in both intestinal and renal epithelial cells [6,7]. ABCG2 plays a critical role in the regulation of renal urate overload and extra-renal urate underexcretion, making it a potentially valuable target for pharmacological intervention in the management of hyperuricemia or gout [8,9].

Cortex Fraxini comes from the dry bark of *Fraxinus stylosa* Lingelsh and *Fraxinus rhynchophylla* Hance, and has been utilized in China for the treatment of hyperuricemia [10]. However, the specific active compounds within Cortex Fraxini and their relationship with ABCG2 remain unknown. Since the active ingredients of traditional Chinese medicines (TCMs) are those that can be absorbed into the bloodstream following oral administration, it

is imperative to identify the specific components of medicated plasma of Cortex Fraxini that can regulate ABCG2. Hence, it is imperative to identify the “effective form” of components in Cortex Fraxini that can efficiently, rapidly, and accurately activate ABCG2.

In order to expedite the process of drug discovery, various protein-ligand interaction-based methods have been devised. Among these, the integration of bioaffinity ultrafiltration and LC-MS (BA-UF-MS) has been employed to swiftly screen affinity ligands from intricate mixtures [11]. This approach proves to be time-efficient, cost-effective, and eliminates the need for intricate chemical compound isolation procedures.

This study presents an integrated approach, utilizing BA-UF-MS for the screening of potential ABCG2 ligands from medicated plasma of Cortex Fraxini. Initially, BA-UF-MS enables the swift separation and identification of the hit compound that binds to ABCG2. Subsequently, the activity of the identified hit compound is confirmed through in vitro and in vivo assays. Furthermore, the molecular docking and surface plasmon resonance (SPR) assay were employed to confirm the affinity between the hit compound and ABCG2. As a result, a potent ABCG2 activated ligand was successfully identified from the medicated plasma of Cortex Fraxini. This study represents the first attempt to utilize this integrated method for screening ABCG2 activated ligands from Cortex Fraxini. The overall research framework is depicted in Figure 1. It is anticipated that the implementation of this strategy will expedite the process of natural-product based drug discovery.

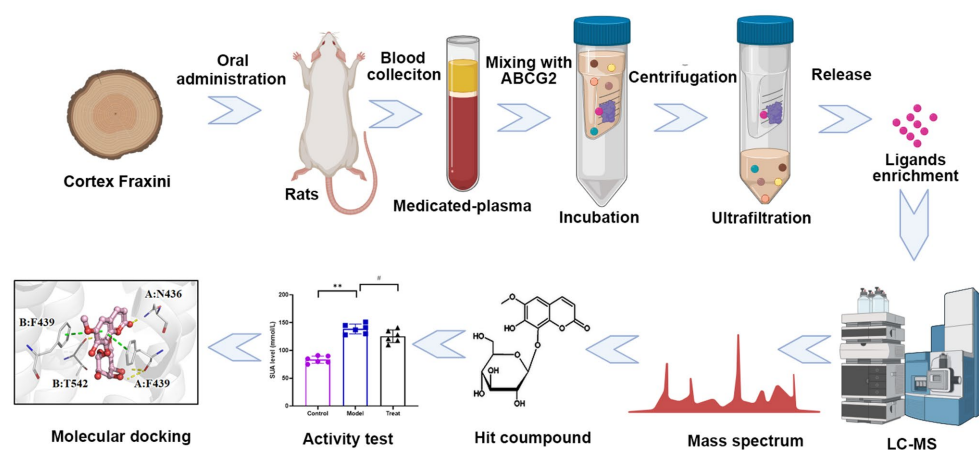


Figure 1. Schematic diagram of ABCG2 ligands screening with BA-UF-MS (# $p < 0.05$, ** $p < 0.05$).

2. Results

2.1. ABCG2 Activated Assay of the Cortex Fraxini Extract

The activity of the Cortex Fraxini extract on ABCG2 was assessed, revealing a significant effect with an EC_{50} value of 35.26 mg/mL as determined by ^{14}C uptake. The ABCG2 activity of the Cortex Fraxini extract had been observed, but the specific bioactive constituents responsible for affecting ABCG2 in medicated plasma of Cortex Fraxini have not been previously identified. Therefore, BA-UF-MS was employed to identify the active constituents that target ABCG2.

2.2. Optimization Conditions for Ligand Screen

Upon incubation of the medicated plasma of Cortex Fraxini with ABCG2, protein-ligand complexes were formed. In order to achieve optimal screening performance with BA-UF-MS, it is necessary to investigate certain important parameters. The protein concentration of ABCG2 directly impacts the screening results. The results depicted in Figure 2A demonstrate that the binding quantity of fumitremorgin C exhibited an upward trend with increasing concentrations of ABCG2 up to 10 mg/mL, beyond which higher concentrations of ABCG2 had a detrimental impact. Furthermore, the duration of incubation influenced the binding quantity of ligands to target proteins. Figure 2B illustrates a substantial increase in the binding quantity of fumitremorgin C to ABCG2 from 5 min to 30 min, with no discernible

changes observed when the incubation time reached 60 min, indicating the saturation of ABCG2 binding at the 30 min mark. Excessive incubation duration may result in a decline in protein activity, consequently leading to a diminished degree of binding [12]. The activity of ABCG2 is influenced by temperature. As depicted in Figure 2C, an incubation temperature of 37 °C exhibited the highest level of binding for fumitremorgin C. The size of the ultrafiltration tube played a significant role, thus necessitating an investigation of ultrafiltration sizes of 10, 30, 50 and 100 kDa. Figure 2D demonstrates that the 10 kDa ultrafiltration tube yielded the highest amount of ligand binding. In conclusion, the optimal screening conditions were determined to be as follows: ABCG2 concentration of 10 mg/mL, incubation time of 30 min, incubation temperature of 37 °C, and 10 kDa of ultrafiltration size.

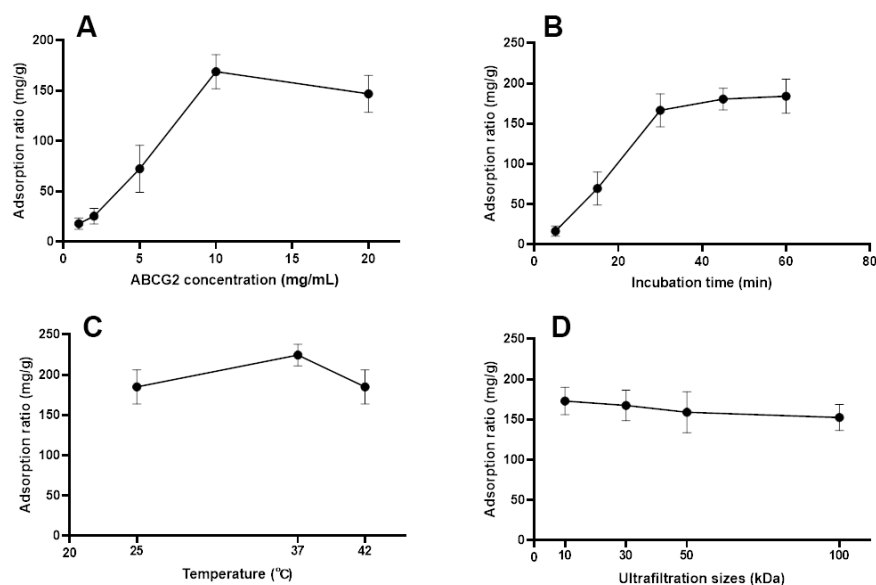


Figure 2. Impacts of parameters on interaction between the ligand and ABCG2. Impact of the ABCG2 concentration (A), incubation time (B), incubation temperature (C) and ultrafiltration size (D) on the binding ability between fumitremorgin C and ABCG2.

2.3. Screen for ABCG2 Ligands Using BA-UF-MS

This experiment involves incubating ABCG2 with the medicated plasma of *Cortex Fraxini*, where ligands with a high affinity interact with the ABCG2 protein. Other components do not exhibit any specific interaction with ABCG2, and thorough washing steps are employed to eliminate low-affinity ligands. During the releasing phase, an organic solvent was employed to liberate binding ligands. Subsequently, the bound compounds were extracted using an organic solution and subjected to analysis via LC-MS. Utilizing the optimized conditions, medicated plasma was screened using BA-UF-MS, and the resulting chromatograms of medicated plasma, eluent solution from ABCG2, and a deactivated control sample solution are presented in Figure 3. By evaluating the peak area, a distinctive peak was observed in the chromatogram of the eluent solution, with a higher peak area compared to that of the control group, indicating favorable specificity. Based on the strategy principle, it was observed that this particular constituent possessed the ability to bind to ABCG2, thereby qualifying it as a potential ligand for ABCG2. The identification of potential active components was accomplished through the utilization of MS fragments and a self-constructed database comprising approximately 4500 compounds derived from natural herbs. Consequently, the compound fraxin was determined to be the hit compound.

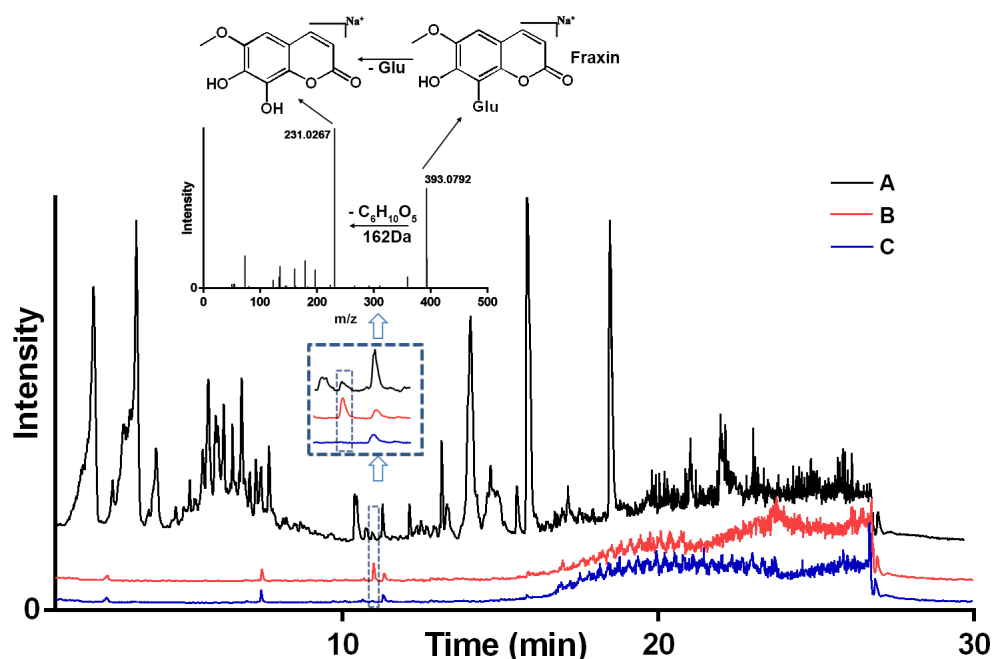


Figure 3. LC-MS chromatograms of the chemical constituents from Cortex Fraxini. (A) medicated plasma; (B) medicated plasma incubated with active ABCG2; (C) medicated plasma incubated with deactivated ABCG2. Glu: Glucose.

2.4. Activity Test of the Hit Compound In Vitro and In Vivo

It is important to note that the binding of a compound to a protein does not necessarily imply its role as an inhibitor or activator, as the compound may exhibit non-specific binding to non-functional sites of the protein [13]. The binding of a compound to a protein does not necessarily indicate whether it functions as an inhibitor or activator, as the compound may bind non-specifically to non-functional sites on the protein. Additional pharmacological investigation is required to determine the activating effect of the hit compound on ABCG2. The activity of fraxin was confirmed to activate ABCG2 in a concentration-dependent manner, as evidenced by the promotion of ABCG2-mediated uptake of ^{14}C -UA with an EC_{50} of $7.55\ \mu\text{M}$, as depicted in Figure 4A. To further validate its efficacy, fraxin was subsequently assessed for its ability to reduce SUA levels in rats. The findings of the study demonstrated that intragastrically administered fraxin led to a significant reduction in the level of SUA in rats ($p < 0.05$), as depicted in Figure 4B. These results were consistent with the outcomes of the target screening.

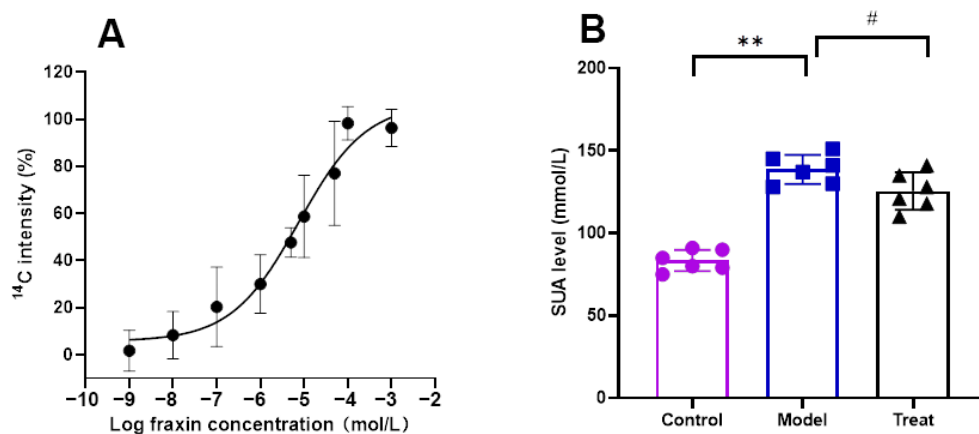


Figure 4. Activity evaluation of hit compound. (A) EC_{50} of fraxin for ABCG2-mediated ^{14}C -UA uptake; (B) SUA-lowering activity of fraxin in model rats (# $p < 0.05$, ** $p < 0.05$).

2.5. Affinity Verification between Fraxin and ABCG2

Molecular docking analysis was employed to investigate the binding sites and interaction between the hit compound and ABCG2. Fraxin exhibited a strong affinity towards the active pocket of ABCG2, as illustrated in Figure 5A, forming hydrogen bonds and π - π stacking with F439, F349, N436, and T542. The binding energy of fraxin with ABCG2 was calculated to be -13.145 kcal/mol. The docking results strongly suggested that fraxin has the potential to act as a ligand for ABCG2. To further validate the binding activity of ABCG2, the K_D value of fraxin was determined using SPR assay. The obtained result indicated that the K_D value for fraxin was calculated as 141.2 μ M (Figure 5B).

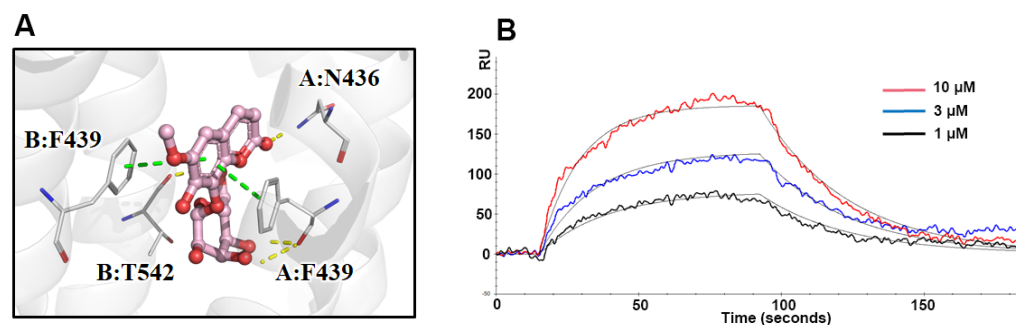


Figure 5. Affinity verification between fraxin and ABCG2. (A) Molecular docking analysis of ABCG2 and fraxin; (B) SPR assay of fraxin and ABCG2.

3. Discussion

ABCG2 is a crucial urate transporter highly expressed in the epithelial cells of the intestine and kidney. This transporter plays a pivotal role in both renal urate overload and extra-renal urate underexcretion. Limited attention is currently devoted to UA-lowering drugs that target sites beyond the kidney. Additionally, numerous components found in TCMs exhibit low bioavailability when orally administered, resulting in limited absorption into the bloodstream and reaching the intended target organs. Conversely, certain components directly impact target sites within the intestine, such as by modulating the gut microbiota to reduce UA levels [14]. Given these considerations, we have selected ABCG2 as the protein target.

Commonly employed drugs for the treatment of hyperuricemia include benzbromarone, allopurinol, and febuxostat. Nevertheless, prolonged administration of these drugs is associated with various adverse effects, such as hepatotoxicity and nephrotoxicity [15]. Consequently, the identification of novel hyperuricemic drugs with reduced toxicity and fewer side effects has become a prominent research area in recent years. TCMs have been widely recognized as a valuable resource for identifying hit compounds in the field of drug discovery [16]. The diverse chemical structures present in these compounds offer a vast pool from which potential leads for drug development and optimization can be selected and refined. Considerable attention has been directed towards exploring the bioactive compounds derived from TCMs, as they hold promise as a novel and safer source for anti-hyperuricemia drug leads.

It is important to note that the pharmacological effects of TCMs primarily rely on the absorption of their components into the bloodstream. However, the oral administration of TCMs results in a significantly low transfer of these components into the blood. Moreover, the presence of numerous dietary and endogenous substances further complicates the identification and separation of the absorbed ingredients from TCMs. Given the intricate nature of the chemical constituents found in natural medicines and the minuscule concentration of their bioactive components within living organisms, the identification of potential target ligands from constituents absorbed into the bloodstream poses a formidable challenge [12]. Traditional approaches to isolating target protein ligands involve separation techniques and bioassay-guided fractionation. However, these conventional methods for screening bioactive compounds from complex systems are both time-consuming and labor-intensive [17].

Consequently, a targeted protein-oriented screening method would serve as an efficient strategy for the identification of active compounds from such intricate systems [18]. The utilization of target screens offers numerous benefits, primarily due to their enhanced speed and convenience in directly capturing target compounds, thereby eliminating the necessity for repetitive separation protocols of non-target analytes [19,20]. Consequently, the implementation of the BA-UF-MS strategy is anticipated to expedite the process of natural-product based drug discovery.

Certain parameters, such as protein concentration, incubation time, incubation temperature, and the size of the ultrafiltration tube depend on the characteristics of ABCG2 and the structure of ligands. The characteristics of ABCG2 are the main factor that influences protein-ligand interactions, due to the ligand structure being variable. Fumitremorgin C, a potent inhibitor, has been identified as a specific ligand for ABCG2. Consequently, it has been selected as the focal point for conditional optimization in order to potentially uncover other bioactive ligands similar to Fumitremorgin C. The correlation between the molecular weight of a protein and the filter size of an ultrafiltration membrane is not absolute. Moreover, the observed molecular size of ABCG2 (72 kDa) in a buffer solution surpasses its theoretical value, and protein interactions can lead to comparable outcomes in ultrafiltration membranes with filter sizes of 50 kDa and 100 kDa.

Cortex Fraxini has been utilized in the management of hyperuricemia and gout, thus presenting a promising opportunity to identify potential therapeutic components from Cortex Fraxini that target hyperuricemia. The assessment of a compound's binding ability to a specific protein is essential in evaluating the biological effects of TCMs [21]. Notably, the Cortex Fraxini extract demonstrated significant activity in ^{14}C -UA uptake experiments, indicating the presence of potential ABCG2 activated ligands within Cortex Fraxini. Employing the BA-UF-MS strategy, fraxin was screened and confirmed to exhibit activity both *in vitro* and *in vivo*, thereby suggesting its potential as an anti-hyperuricemia agent [22].

The identification of ligand compounds primarily depends on their comparison with databases containing natural product standard substances. During the screening process, we analyze and compare the mass spectrometry data, focusing on the most significant specific alterations. The compound exhibiting the highest degree of similarity is determined as fraxin. Furthermore, the compound's structure is confirmed by examining the fragmentation pattern of its mass spectrometry fragments. However, the utilization of lower electron impact energy in the mass spectrometry limits the acquisition of additional secondary fragmentation information. In addition to fraxin, several candidate hit compounds identified in the screening results were not included in this study, necessitating further investigation into their potential for reducing uric acid levels. Moreover, the limitations of the mass spectrometry standard substance library restrict its ability to identify entirely novel hit compounds with unique structural characteristics.

To explore the interaction between the hit compound and ABCG2, we employed molecular docking and SPR assay. Molecular docking, a virtual method influenced by force field, temperature, and pH, provides a theoretical understanding of the receptor-ligand interaction [23]. To complement this, we conducted real experiments and determined the binding affinity between fraxin and ABCG2 to be 141.2 μM using SPR assay. These findings substantiate the mechanistic perspective and validate the accuracy and reliability of the BA-UF-MS strategy.

4. Materials and Methods

4.1. Reagents

Chemical compounds of fumitremorgin C and fraxin were produced from MedChem-Express (Shanghai, China). Cortex Fraxini (Lot: 220509) was purchased from the GuoDa drugstore (Shanghai, China), which was obtained from *Fraxinus rhynchophylla* Hance in Shanxi province, China. HPLC-grade reagents were obtained from Fisher Scientific (Fair Lawn, NJ, USA). All other chemicals were bought from standard commercial sources. Recombinant ABCG2 was purchased from Feiyue Biotechnology Co., Ltd. (Wuhan, China), and

centrifugal ultrafiltration filters with a cutoff membrane were provided by Merck millipore Co., Ltd. (Billerica, MA, USA). ^{14}C -uric acid was purchased from American Radiolabeled Chemicals (St. Louis, MO, USA). Membrane vesicles obtained from ABCG2-overexpressing cells were purchased from SOLVO Biotechnology (Budapest, Hungary).

4.2. Preparation of the Cortex Fraxini Extract

The powdered Cortex Fraxini (1.0 kg) was subjected to ultrasonic extraction using 10 L of 75% ethanol and a power of 500 W for a duration of 1 h. The resulting extracting solution was then centrifuged at a speed of 4000 rpm for a duration of 3 min. Subsequently, the filtrate was concentrated under reduced pressure at a temperature of 50 °C. The remaining solution was then subjected to lyophilization in order to obtain a freeze-dried powder of Cortex Fraxini extract.

4.3. Preparation of Medicated Plasma of Cortex Fraxini

A total of 6 male Sprague Dawley rats, weighing 200 g, were procured from the Experimental Animal Center of Xuzhou Medical University in Xuzhou, China. All experimental procedures were conducted in accordance with the guidelines and regulations set forth by the Medical Ethic Committee of Xuzhou Medical University (NO. L20210226100). The prepared Cortex Fraxini extract, suspended in 0.5% CMC-Na, was administered to the rats via intragastric gavage at a dose of 1.7 g/kg body weight [24]. Blood samples were collected via retro-orbital bleeding at specific time intervals (0.5, 1, 3, 6, 12, and 24 h). Approximately 0.5 mL of blood was collected at each time point and immediately centrifuged at 13,000 rpm for 10 min. The resulting plasma samples from 6 rats were combined and stored at $-80\text{ }^{\circ}\text{C}$ until further analysis.

4.4. Screen of Potential ABCG2 Ligands with BA-UF-MS

The method employed for analysis involved three steps: loading, washing, and releasing [25]. The ABCG2 solution (5 $\mu\text{g}/\text{mL}$) was prepared using a phosphate buffer solution (PBS, 100 mM, pH 7.4). Subsequently, 100 μL of medicated plasma and 100 μL of ABCG2 solution were combined in an EP tube and incubated at 37 °C for 30 min. Following incubation, the formed ABCG2-ligand complexes were filtered through a 10 kDa ultrafiltration (UF) membrane. The target-ligand complexes were retained by centrifugation at 13,000 rpm for 10 min, while unbound compounds in the UF tube were eliminated through 6 rounds of washing with 200 μL of PBS and subsequent centrifugation. Unbound compounds successfully traversed the UF membrane, whereas ligands bound to the ABCG2 protein did not. Consequently, the ABCG2-ligand complexes were isolated and acquired. Subsequently, the attached ligands were liberated by subjecting them to ultrasonication and centrifugation at 13,000 rpm for 10 min, repeated three times. The filtrates from each sample were consolidated for subsequent BA-UF-MS analysis.

To address the issue of nonspecific binding in the ligand screening process, the ABCG2 protein was subjected to denaturation by boiling it in water for a duration of one hour. A control group was established by co-incubating the denatured protein with medicated plasma, followed by conducting the subsequent screening procedure in a similar manner. Subsequently, liquid chromatography, coupled with high-resolution mass spectrometry (LC-HRMS, Orbitrap Exploris 120, Thermo Fisher Scientific, Waltham, MA, USA), was employed to analyze and identify compounds that specifically target ABCG2 within the medicated plasma. By comparing the peak areas of LC-HRMS chromatograms obtained from the experimental and control samples (representing inactive ABCG2), potential ABCG2 ligands were identified and screened within the medicated plasma.

LC-HRMS conditions for compound analysis of Cortex Fraxini were listed as follows. LC analysis was conducted using an UHPLC system equipped with a C18 column (Waters UPLC BEH, 1.7 μm , 2.1 \times 100 mm). The flow rate was set at 0.4 mL/min, and the sample injection volume was 5 μL . The mobile phase consisted of 0.1% formic acid in water (A) and 0.1% formic acid in acetonitrile (B). The elution gradient program involved multiple

linear steps as follows: 0–3.5 min, 95–85% A; 3.5–6 min, 85–70% A; 6–6.5 min, 70–70% A; 6.5–12 min, 70–30% A; 12–12.5 min, 30–30% A; 12.5–18 min, 30–0% A; 18–25 min, 0–0% A; 25–26 min, 0–95% A; 26–30 min, 95–95% A. The MS and MS/MS data were obtained using a mass spectrometer coupled with Xcalibur software (v 4.2), employing the IDA acquisition mode. The mass range during each acquisition cycle was set from 100 to 1500, with the top four ions screened and their corresponding MS/MS data acquired. The sheath gas flow rate was 30 Arb, the aux gas flow rate was 10 Arb, the ion transfer tube temperature was set at 350 °C, and the vaporizer temperature was also set at 350 °C. The full MS resolution was set at 60,000, while the MS/MS resolution was set at 15,000. Collision energy was applied at 16/38/42 in NCE mode, and the spray voltage was set at 5.5 kV (positive).

4.5. Identification of Potential ABCG2 Ligands with LC-HRMS

The identification of potential active components was accomplished through the utilization of MS fragments and a self-constructed database, comprising approximately 4500 compounds derived from natural herbs. The database encompasses a wide range of chemical compounds, including more than 570 distinct alkaloids (such as piperidine alkaloids, quinoline alkaloids, pyridine alkaloids, and quinoline alkaloids), 800 varieties of flavonoids (including isoflavonoids, flavones, dihydrochalcones, and dihydroflavonoids), 1100 types of terpenes (including cyclic sesquiterpenes, lavenderane terpenes, and cyclopentane-cycloene ether terpenes), 360 types of phenylpropanoids (including coumarins, phenylpropanoic acids, and lignans), 50 types of steroids, 60 types of quinones, over 90 types of organic acids, and various other components. The identification of components present in Cortex Fraxini can be achieved by comparing their mass information with a database. Furthermore, the utilization of fragmentation patterns from secondary mass spectrometry can aid in the process of identification.

4.6. Optimization of Experimental Parameters

In order to attain the most favorable screening outcomes, various factors that have the potential to influence the results were examined. These factors encompassed the concentration of ABCG2 (ranging from 1 to 20 mg/mL), the duration of incubation (ranging from 5 to 60 min), the temperature of incubation (25, 37, and 42 °C), and the size of ultrafiltration filters (ranging from 10 to 100 kDa). Fumitremorgin C (a known ligand of ABCG2) was selected as the representative compounds to optimize the screening conditions. The adsorption ratio (mg/g) of fumitremorgin C was used to evaluate optimization procedure, which was calculated as m_a/m_0 , where m_a (mg) represented the mass of adsorptive and subsequently eluted fumitremorgin C, and m_0 (mg) represented the mass of added fumitremorgin C for incubation.

4.7. Study of ^{14}C -UA Uptake by Membrane Vesicles

The evaluation of the ^{14}C -UA uptake of Cortex Fraxini extract or hit compounds was conducted using membrane vesicles obtained from ABCG2-overexpressing cells [26]. In 96-well plates, membrane vesicles, ^{14}C -UA, and a hit compound solution were combined and incubated with PBS buffer for a duration of 30 min at a temperature of 37 °C. The uptake reactions of ^{14}C -UA were initiated by the addition of MgATP, and the membrane vesicles were subsequently washed three times with ice-cold DPBS (Dulbecco's phosphate-buffered saline) in order to terminate the reaction after a period of 5 min. Following filtration through glass fiber filters, the filters were washed three times with ice-cold DPBS. The quantity of substrate present within the filtered vesicles was determined by measuring intracellular radioactivity using a liquid scintillation counter (PerkinElmer, Waltham, MA, USA) subsequent to the addition of scintillant. Each treatment was measured in triplicate.

4.8. Study of SUA-Lowering Effect of the Hit Compound in Hyperuricemic Rats

The hit compound was assessed in a rat model of acute hyperuricemia induced by hypoxanthine and potassium cyanate [27]. Six SD rats were allocated to each of the following

groups: control, hyperuricemic model, and treatment. The hyperuricemic model group rats were administered xanthine intragastrically and potassium oxonate subcutaneously. The treatment group rats were orally administered 10 mg/kg of the hit compound (dissolved in 0.5% CMC-Na) 3 h prior to xanthine and potassium oxonate administration. Blood samples were collected via retro-orbital bleeding after 6 h of hyperuricemia induction. The levels of SUA were assessed using the UA ELISA kit (Bioroyee Co., Ltd., Beijing, China).

4.9. Molecular Docking

Molecular docking was conducted to simulate the process of molecular recognition and determine the binding energies between the hit compound and ABCG2 using PyMOL v1.3 software. The 3D crystal structure of ABCG2 from mitoxantrone (6VXI) was obtained from the Research Collaboratory for Structural Bioinformatics Protein Data Bank (RCSB PDB). The 3D chemical structures of ligand compounds were acquired either from the PubChem website or generated using the ChemDraw software package Pro 12.0. The ligands and ABCG2 were prepared and processed for minimization, and subsequently saved in pdbqt format. Following the selection of specific residues within the pocket region, a CHARMm force field was applied to the ligands and ABCG2 after targeting the grid box [28–30].

4.10. Surface Plasmon Resonance Analysis

The local surface plasmon resonance (LSPR) experiment was performed using an Open-SPR (NicoyaLifesciences, Waterloo, ON, Canada) for the analysis of SPR [31]. The COOH sensor chip was utilized for capture-coupling to immobilize ABCG2 protein (50 µg/mL), and the interaction between ABCG2 and the hit compound was observed at 37 °C. The running buffer utilized in this study was a PBS buffer containing 5% DMSO. Solutions of varying concentrations of the hit compound were sequentially flowed through the chips at a rate of 20 µL/min. Simultaneously, running buffer correction was conducted.

4.11. Statistical Analysis

All experimental data were analyzed using SPSS software (19.0) and recorded as mean ± standard deviation for three replicates. Statistical significance was determined at a threshold of $p < 0.05$.

5. Conclusions

In the current investigation, fraxin was identified from medicated plasma of Cortex Fraxini using a rapid and efficient BA-UF-MS strategy. The bioactivity of fraxin was assessed through in vitro and in vivo experiments, including determination of the EC50 value, evaluation of its SUA lowering effect, analysis of molecular docking scores, and determination of the affinity constant K_D . The findings unequivocally established that fraxin possesses promising bioactivity in reducing UA levels, making it a potential candidate for the treatment of hyperuricemia and gout. In summary, the findings of this study indicate that medicated plasma derived from TCM holds promise as a valuable resource for identifying potential hit compounds. Furthermore, the BA-UF-MS approach proves to be an effective strategy for the discovery of active ingredients from biological samples.

Author Contributions: Conceptualization, X.H.; methodology, W.D.; validation, X.L.; formal analysis, L.X.; investigation, L.X.; resources, L.X.; data curation, L.X.; writing—original draft preparation, Y.W.; writing—review and editing, Y.W.; visualization, Y.W.; supervision, Y.W.; project administration, Y.W.; funding acquisition, Y.W. All authors have read and agreed to the published version of the manuscript.

Funding: This research was funded by the project of scientific and technological development of traditional Chinese medicine in Jiangsu province, grant number MS2021106.

Institutional Review Board Statement: The animal study protocol was approved by the Ethics Committee of Institutional Animal Care and Use Committee of Xuzhou Medical University (protocol code: 202305T008, approval date: 17 May 2023).

Informed Consent Statement: Not applicable.

Data Availability Statement: The data presented in this study are available on request from the corresponding author.

Conflicts of Interest: The authors declare no conflict of interest.

References

1. Johnson, R.J.; Bakris, G.L.; Borghi, C.; Chonchol, M.B.; Feldman, D.; Lanasma, M.A.; Merriman, T.R.; Moe, O.W.; Mount, D.B.; Lozada, L.G.S.; et al. Hyperuricemia, Acute and Chronic Kidney Disease, Hypertension, and Cardiovascular Disease: Report of a Scientific Workshop Organized by the National Kidney Foundation. *Am. J. Kidney Dis.* **2018**, *71*, 851–865. [CrossRef] [PubMed]
2. Bardin, T.; Richette, P. Definition of hyperuricemia and gouty conditions. *Curr. Opin. Rheumatol.* **2014**, *26*, 186–191. [CrossRef] [PubMed]
3. Lanasma, M.A.; Andres-Hernando, A.; Kuwabara, M. Uric acid and hypertension. *Hypertens. Res.* **2020**, *43*, 832–834. [CrossRef]
4. Hoque, K.M.; Dixon, E.E.; Lewis, R.M.; Allan, J.; Gamble, G.D.; Phipps-Green, A.J.; Halperin Kuhns, V.L.; Horne, A.M.; Stamp, L.K.; Merriman, T.R.; et al. The ABCG2 Q141K hyperuricemia and gout associated variant illuminates the physiology of human urate excretion. *Nat. Commun.* **2020**, *11*, 2767. [CrossRef] [PubMed]
5. Woodward, O.M.; Kottgen, A.; Coresh, J.; Boerwinkle, E.; Guggino, W.B.; Kottgen, M. Identification of a urate transporter, ABCG2, with a common functional polymorphism causing gout. *Proc. Natl. Acad. Sci. USA* **2009**, *106*, 10338–10342. [CrossRef]
6. Stiburkova, B.; Pavelcova, K.; Pavlikova, M.; Jesina, P.; Pavelka, K. The impact of dysfunctional variants of ABCG2 on hyperuricemia and gout in pediatric-onset patients. *Arthritis Res. Ther.* **2019**, *21*, 77. [CrossRef]
7. Huls, M.; Brown, C.D.; Windass, A.S.; Sayer, R.; van den Heuvel, J.J.; Heemskerk, S.; Russel, F.G.; Masereeuw, R. The breast cancer resistance protein transporter ABCG2 is expressed in the human kidney proximal tubule apical membrane. *Kidney Int.* **2008**, *73*, 220–225. [CrossRef]
8. Li, Q.; Lin, H.; Niu, Y.; Liu, Y.; Wang, Z.; Song, L.; Gao, L.; Li, L. Mangiferin promotes intestinal elimination of uric acid by modulating intestinal transporters. *Eur. J. Pharmacol.* **2020**, *888*, 173490. [CrossRef]
9. Lu, Y.H.; Chang, Y.P.; Li, T.; Han, F.; Li, C.J.; Li, X.Y.; Xue, M.; Cheng, Y.; Meng, Z.Y.; Han, Z.; et al. Empagliflozin Attenuates Hyperuricemia by Upregulation of ABCG2 via AMPK/AKT/CREB Signaling Pathway in Type 2 Diabetic Mice. *Int. J. Biol. Sci.* **2020**, *16*, 529–542. [CrossRef]
10. Wang, Y.; Zhao, M.; Xin, Y.; Liu, J.; Wang, M.; Zhao, C. ¹H NMR and MS based metabolomics study of the therapeutic effect of Cortex Fraxini on hyperuricemic rats. *J. Ethnopharmacol.* **2016**, *185*, 272–281. [CrossRef]
11. Song, H.P.; Chen, J.; Hong, J.Y.; Hao, H.; Qi, L.W.; Lu, J.; Fu, Y.; Wu, B.; Yang, H.; Li, P. A strategy for screening of high-quality enzyme inhibitors from herbal medicines based on ultrafiltration LC-MS and in silico molecular docking. *Chem. Commun.* **2015**, *51*, 1494–1497. [CrossRef]
12. Dong, X.; Wang, B.; Cao, J.; Zheng, H.; Ye, L.H. Ligand fishing based on bioaffinity ultrafiltration for screening xanthine oxidase inhibitors from citrus plants. *J. Sep. Sci.* **2021**, *44*, 1353–1360. [CrossRef] [PubMed]
13. Li, L.; Kong, J.; Yao, C.H.; Liu, X.F.; Liu, J.H. Rapid identification of urokinase plasminogen activator inhibitors from Traditional Chinese Medicines based on ultrafiltration, LC-MS and in silico docking. *J. Pharm. Biomed. Anal.* **2019**, *164*, 241–248. [CrossRef] [PubMed]
14. Sun, X.; Wen, J.; Guan, B.; Li, J.; Luo, J.; Li, J.; Wei, M.; Qiu, H. Folic acid and zinc improve hyperuricemia by altering the gut microbiota of rats with high-purine diet-induced hyperuricemia. *Front. Microbiol.* **2022**, *13*, 907952. [CrossRef]
15. White, W.B.; Saag, K.G.; Becker, M.A.; Borer, J.S.; Gorelick, P.B.; Whelton, A.; Hunt, B.; Castillo, M.; Gunawardhana, L.; CARES Investigators. Cardiovascular Safety of Febuxostat or Allopurinol in Patients with Gout. *N. Engl. J. Med.* **2018**, *378*, 1200–1210. [CrossRef]
16. Zhang, H.; Xu, C.; Tian, Q.; Zhang, Y.; Zhang, G.; Guan, Y.; Tong, S.; Yan, J. Screening and characterization of aldose reductase inhibitors from Traditional Chinese medicine based on ultrafiltration-liquid chromatography mass spectrometry and in silico molecular docking. *J. Ethnopharmacol.* **2021**, *264*, 113282. [CrossRef]
17. Gaudencio, S.P.; Pereira, F. Dereplication: Racing to speed up the natural products discovery process. *Nat. Prod. Rep.* **2015**, *32*, 779–810. [CrossRef]
18. Ciesla, L.; Moaddel, R. Comparison of analytical techniques for the identification of bioactive compounds from natural products. *Nat. Prod. Rep.* **2016**, *33*, 1131–1145. [CrossRef]
19. Wei, H.; Zhang, X.; Tian, X.; Wu, G. Pharmaceutical applications of affinity-ultrafiltration mass spectrometry: Recent advances and future prospects. *J. Pharm. Biomed. Anal.* **2016**, *131*, 444–453. [CrossRef] [PubMed]
20. Chen, G.; Huang, B.X.; Guo, M. Current advances in screening for bioactive components from medicinal plants by affinity ultrafiltration mass spectrometry. *Phytochem. Anal.* **2018**, *29*, 375–386. [CrossRef]
21. Arai, M.A.; Ishikawa, N.; Tanaka, M.; Uemura, K.; Sugimitsu, N.; Suganami, A.; Tamura, Y.; Koyano, T.; Kowithayakorn, T.; Ishibashi, M. Hes1 inhibitor isolated by target protein oriented natural products isolation (TPO-NAPI) of differentiation activators of neural stem cells. *Chem. Sci.* **2016**, *7*, 1514–1520. [CrossRef] [PubMed]
22. Li, J.M.; Zhang, X.; Wang, X.; Xie, Y.C.; Kong, L.D. Protective effects of cortex fraxini coumarines against oxonate-induced hyperuricemia and renal dysfunction in mice. *Eur. J. Pharmacol.* **2011**, *666*, 196–204. [CrossRef]

23. Zhu, C.; Niu, H.; Nie, A.; Bian, M. Bioactivity-guided separation of potential alpha-glycosidase inhibitor from *clerodendranthus spicatus* based on HSCCC coupled with molecular docking. *Sci. Rep.* **2021**, *11*, 6914. [CrossRef] [PubMed]
24. Wang, Y.; Zhao, M.; Ou, Y.; Zeng, B.; Lou, X.; Wang, M.; Zhao, C. Metabolic profile of esculin in rats by ultra high performance liquid chromatography combined with Fourier transform ion cyclotron resonance mass spectrometry. *J. Chromatogr. B Analyt. Technol. Biomed. Life Sci.* **2016**, *1020*, 120–128. [CrossRef] [PubMed]
25. Luo, S.; Guo, L.; Sheng, C.; Zhao, Y.; Chen, L.; Li, C.; Jiang, Z.; Tian, H. Rapid identification and isolation of neuraminidase inhibitors from mockstrawberry (*Duchesnea indica* Andr.) based on ligand fishing combined with HR-ESI-Q-TOF-MS. *Acta Pharm. Sin. B* **2020**, *10*, 1846–1855. [CrossRef]
26. Taniguchi, T.; Ashizawa, N.; Matsumoto, K.; Saito, R.; Motoki, K.; Sakai, M.; Chikamatsu, N.; Hagihara, C.; Hashiba, M.; Iwanaga, T. Pharmacological Evaluation of Dotinurad, a Selective Urate Reabsorption Inhibitor. *J. Pharmacol. Exp. Ther.* **2019**, *371*, 162–170. [CrossRef]
27. Zhao, T.; Meng, Q.; Sun, Z.; Chen, Y.; Ai, W.; Zhao, Z.; Kang, D.; Dong, Y.; Liang, R.; Wu, T.; et al. Novel Human Urate Transporter 1 Inhibitors as Hypouricemic Drug Candidates with Favorable Druggability. *J. Med. Chem.* **2020**, *63*, 10829–10854. [CrossRef]
28. Akacha, A.; Badraoui, R.; Rebai, T.; Zourgui, L. Effect of extract on methotrexate-induced testicular injury: A biochemical, docking and histological study. *J. Biomol. Struct. Dyn.* **2022**, *40*, 4341–4351. [CrossRef]
29. Alreshidi, M.; Abdhakeem, M.A.; Badraoui, R.; Amato, G.; Caputo, L.; De Martino, L.; Nazzaro, F.; Fratianni, F.; Formisano, C.; De Feo, V.; et al. *Pulicaria incisa* (Lam.) DC. as a Potential Source of Antioxidant, Antibacterial, and Anti-Enzymatic Bioactive Molecules: Phytochemical Constituents, In Vitro and In Silico Pharmacological Analysis. *Molecules* **2023**, *28*, 7439. [CrossRef]
30. Ben Saad, H.; Frikha, D.; Bouallegue, A.; Badraoui, R.; Mellouli, M.; Kallel, H.; Pujo, J.M.; Ben Amara, I. Mitigation of Hepatic Impairment with Polysaccharides from Red Alga *Albidum corallinum* Supplementation through Promoting the Lipid Profile and Liver Homeostasis in Tebuconazole-Exposed Rats. *Pharmaceuticals* **2023**, *16*, 1305. [CrossRef]
31. Hou, Y.; Che, D.; Wei, D.; Wang, C.; Xie, Y.; Zhang, K.; Cao, J.; Fu, J.; Zhou, N.; He, H. Phenothiazine antipsychotics exhibit dual properties in pseudo-allergic reactions: Activating MRGPRX2 and inhibiting the H₁ receptor. *Mol. Immunol.* **2019**, *111*, 118–127. [CrossRef]

Disclaimer/Publisher’s Note: The statements, opinions and data contained in all publications are solely those of the individual author(s) and contributor(s) and not of MDPI and/or the editor(s). MDPI and/or the editor(s) disclaim responsibility for any injury to people or property resulting from any ideas, methods, instructions or products referred to in the content.

Article

A Natural Compound Containing a Disaccharide Structure of Glucose and Rhamnose Identified as Potential N-Glycanase 1 (NGLY1) Inhibitors

Ruijie Liu ^{1,†}, Jingjing Gu ^{2,†}, Yilin Ye ¹, Yuxin Zhang ¹, Shaoxing Zhang ¹, Qiange Lin ¹, Shuying Yuan ³, Yanwen Chen ⁴, Xinrong Lu ⁵, Yongliang Tong ⁵, Shaoxian Lv ⁵, Li Chen ^{5,*} and Guiqin Sun ^{1,*}

¹ School of Medical Technology and Information Engineering, Zhejiang Chinese Medical University, Hangzhou 310053, China; liuruijie523@163.com (R.L.); yyilin995@163.com (Y.Y.); zhangyuxin0005@163.com (Y.Z.); shaoxingz@163.com (S.Z.); linqiange0709@163.com (Q.L.)

² School of Basic Medical Sciences, Zhejiang Chinese Medical University, Hangzhou 310053, China; gjj0824@126.com

³ Department of Clinical Laboratory, Jiaying Maternity and Child Health Care Hospital, Jiaying 314001, China; yuansy1126@163.com

⁴ Central Laboratory, Ningbo Hospital, Renji Hospital, Shanghai Jiao Tong University School of Medicine, Ningbo 315336, China; wlgwzyy@163.com

⁵ Key Laboratory of Medical Molecular Virology (MOE/NHC/CAMS), School of Basic Medical Sciences, Fudan University, Shanghai 200032, China; 20111010058@fudan.edu.cn (X.L.); 22111010078@m.fudan.edu.cn (Y.T.); 23111010078@m.fudan.edu.cn (S.L.)

* Correspondence: lichen_bk@fudan.edu.cn (L.C.); sunguiqin2001@163.com (G.S.); Tel.: +86-021-54237381 (L.C.); +86-0571-86633307 (G.S.)

† These authors contributed equally to this work.

Abstract: N-glycanase 1 (NGLY1) is an essential enzyme involved in the deglycosylation of misfolded glycoproteins through the endoplasmic reticulum (ER)-associated degradation (ERAD) pathway, which could hydrolyze N-glycan from N-glycoprotein or N-glycopeptide in the cytosol. Recent studies indicated that NGLY1 inhibition is a potential novel drug target for antiviral therapy. In this study, structure-based virtual analysis was applied to screen candidate NGLY1 inhibitors from 2960 natural compounds. Three natural compounds, Poliumoside, Soyasaponin Bb, and Saikosaponin B2 showed significantly inhibitory activity of NGLY1, isolated from traditional heat-clearing and detoxifying Chinese herbs. Furthermore, the core structural motif of the three NGLY1 inhibitors was a disaccharide structure with glucose and rhamnose, which might exert its action by binding to important active sites of NGLY1, such as Lys238 and Trp244. In traditional Chinese medicine, many compounds containing this disaccharide structure probably targeted NGLY1. This study unveiled the leading compound of NGLY1 inhibitors with its core structure, which could guide future drug development.

Keywords: N-glycanase 1 (NGLY1); NGLY1 inhibitor; natural compound; structure-based virtual screening



Citation: Liu, R.; Gu, J.; Ye, Y.; Zhang, Y.; Zhang, S.; Lin, Q.; Yuan, S.; Chen, Y.; Lu, X.; Tong, Y.; et al. A Natural Compound Containing a Disaccharide Structure of Glucose and Rhamnose Identified as Potential N-Glycanase 1 (NGLY1) Inhibitors. *Molecules* **2023**, *28*, 7758. <https://doi.org/10.3390/molecules28237758>

Academic Editors: Tao Liu, Xuexiang Chen and Helen Osborn

Received: 23 October 2023

Revised: 13 November 2023

Accepted: 23 November 2023

Published: 24 November 2023



Copyright: © 2023 by the authors. Licensee MDPI, Basel, Switzerland. This article is an open access article distributed under the terms and conditions of the Creative Commons Attribution (CC BY) license (<https://creativecommons.org/licenses/by/4.0/>).

1. Introduction

N-Glycanase 1 (NGLY1) is a de-N-glycosylating enzyme that catalyzes the hydrolysis of the amide bond between the proximal N-acetylglucosamine (GlcNAc) residue and the Asn side chain to which it is attached, removing N-glycans from glycosylated proteins in the cytosol [1–3]. Discovered in 1993, NGLY1 is known to participate in clearing misfolded glycoproteins during the process of glycoprotein synthesis through the endoplasmic reticulum (ER)-associated degradation (ERAD) pathway [4]. NGLY1 deficiency leads to disrupted ERAD function. Histological analysis of *Ngly1*^{-/-} rats demonstrated cytoplasmic ubiquitinated protein accumulation in neurons of the thalamus and spinal cord [5]. In 2014, it was reported that NGLY1 deficiency could lead to NGLY1-congenital disorder

of deglycosylation (CDDG), a disease characterized by developmental delay, intellectual disability, absence of or reduced tears and sweating, abnormal liver function, and motor dysfunction [6–8]. It was noteworthy that NGLY1-CDDG patients were less susceptible to viral infections [9]. Additionally, it has been reported that generated *Ngly1* knockout (*Ngly1*^{−/−}) murine embryonic fibroblasts (MEFs) inhibited vesicular stomatitis virus (VSV) replication [10]. siRNA knockdown of NGLY1 or Z-VAD-FMK (benzyloxycarbonyl-Val-Ala-Asp-fluoromethyl ketone) inhibits NGLY1, restricting the infection of enterovirus 71 (EV71) and coxsackievirus A16 (CA16) in RD cells [11]. Yang et al. [10] also found NGLY1-deficient human and mouse cells, resulting in severely fragmented mitochondria and the activation of cGAS–STING pathways, leading to elevated IFN-stimulated genes (ISGs). A schematic diagram is shown in Figure 1. NGLY1 represents a potential drug target for antiviral therapy. NGLY1 inhibitors screening is an important pathway for discovering potential antiviral lead compounds. Currently, Z-VAD-FMK is reported to inhibit NGLY1 irreversibly by covalently binding to the active site, but it also inhibits pan-caspase [12,13]. Hence, the pursuit of milder NGLY1 inhibitors holds critical significance.

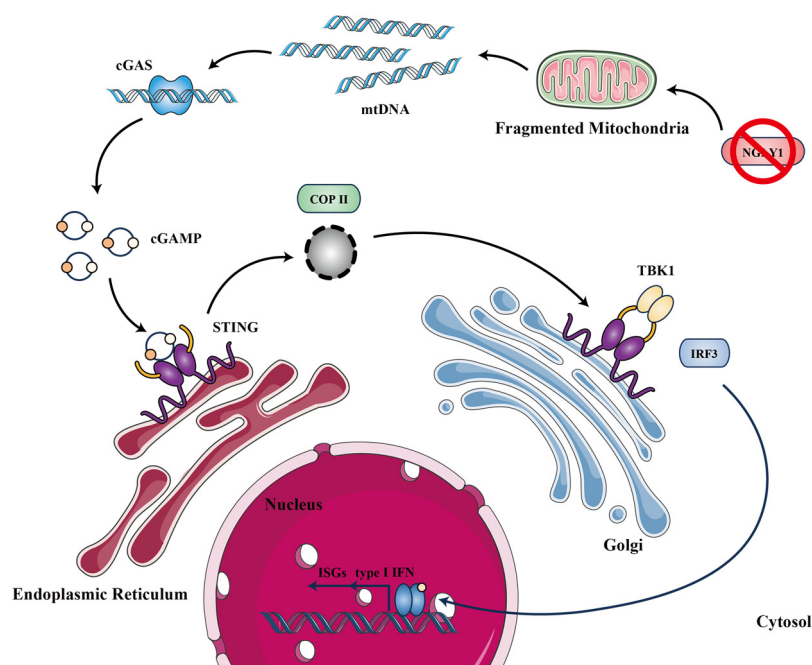


Figure 1. Schematic diagram of antiviral effect by downregulating NGLY1 expression. NGLY1 is an essential enzyme involved in deglycosylation of misfolded glycoproteins. Knocking out the expression of NGLY1 leads to severe mitochondrial fragmentation, causing the release of mitochondrial DNA into the cytoplasm. Innate immune detection of self-DNA by the DNA sensor cGAS activates downstream STING-TBK1-IRF3 signaling cascade, inducing the expression of type I interferons (IFN) and IFN-stimulated genes (ISGs), effectively promoting an antiviral response [10]. mtDNA: mitochondrial DNA; cGAS: cyclic GMP–AMP synthase; cGAMP: 2′3′ cyclic GMP–AMP; STING: stimulator of interferon genes; COP-II: coatamer protein complex II; TBK1: TANK-binding kinase 1; IRF3: interferon regulatory factor 3; type I IFN: type I interferons; ISGs: IFN-stimulated genes.

NGLY1 is a unique protein that plays a role in the ERDA pathway as well as in the activation of key signal proteins such as Nrf1 [3], and its regulation may provide new insights into health and disease. Although efforts have been made on compounds for the regulation of glycosylation from molecule compounds [13] and natural compounds [14], as well as those obtained through synthetic methods [15,16], reports of natural compounds targeting NGLY1 are rare. Commonly used natural compounds from plants, animals, and microorganisms have various beneficial effects on our health, and natural compounds have fewer side effects and are, thus, advantageous for therapeutic purposes [17–19]. One exam-

ple is artemisinin isolated from *artemisia annua* L., which has been used for the treatment of malaria [20]. Similarly, paclitaxel, isolated from *taxus brevifolia*, has been used to treat some malignancies, such as lung, breast, and pancreas cancers [21]. The natural compound has been found to exhibit various effects. Yang et al. [22] found that the natural compound green tea polyphenols exhibited inhibitory effects on proteasomes, suggesting their potential applications in the prevention and treatment of cancers. It also has been reported that two substituted derivatives of the natural compound salacinol showed marginal activity against O-GlcNAcase [23]. Furthermore, many traditional Chinese medicines are known for their heat-clearing and detoxifying properties [24], and natural compounds isolated from these medicines exhibit potential antiviral effects. It has been reported that the natural compound flavonoids acted at different stages of viral infection, such as viral entrance and replication [25]. They had the potential to impede the attachment and entry of viruses into cells, disrupt various stages of viral DNA replication, protein translation, and poly-protein processing [26].

Molecular docking, based on a protein structure, is a method employed to predict the binding modes and affinity of ligands within complexes [27–29]. This approach is crucial in screening ligands within chemical libraries, providing valuable insights into their interactions with biological targets. Consequently, molecular docking studies have emerged as highly accurate and powerful tools for analyzing the interactions between active compounds and potential targets [30,31].

In this study, we employed computer-aided drug screening methods to identify three compounds capable of inhibiting NGLY1 from a library of 2960 natural compounds. The inhibitory effects were further validated through an electrophoretic mobility shift assay. They were isolated from monomers of traditional Chinese medicine for clearing heat and detoxification. We also found that the core structure of NGLY1 inhibitors consists of a disaccharide structure composed of glucose and rhamnose. These compounds might act as lead compounds of NGLY1 inhibitors and may have antiviral effects.

2. Results

2.1. Establishment of a Screening Method for Targeting NGLY1 Lead Compounds

Molecular docking plays a pivotal role in the drug screening process. In this study, we developed a natural lead compound screening method targeting NGLY1. By predicting the three-dimensional structures of NGLY1, we performed molecular docking with 2960 natural compounds derived from plants, animals, or microorganisms. To identify potential inhibitors, we compared the docking scores of these compounds with that of the known NGLY1 inhibitor Z-VAD-FMK. Compounds exhibiting docking scores lower than -4.56 were then selected as primary screening compounds. The enzyme NGLY1 exhibits the same cleavage effect as PNGase F (Figure S1), and the inhibitory effects of the primary screening compounds were validated through an electrophoretic mobility shift assay. We validated the feasibility of this screening method using Z-VAD-FMK, as shown in Figure 2.

The lower binding affinity energy indicates stronger binding affinity. Among the 2960 compounds screened, a total of 215 compounds exhibited docking scores lower than -4.56 . Considering the known biological activities of these compounds, we further narrowed down the selection to 17 compounds associated with glycosylation or possessing anti-inflammatory, antioxidant, and anti-tumor properties (Table S1). Among these 17 compounds, 13 of them contained glycan structures. Therefore, we speculated that compounds with glycan structures might have a higher affinity with NGLY1.

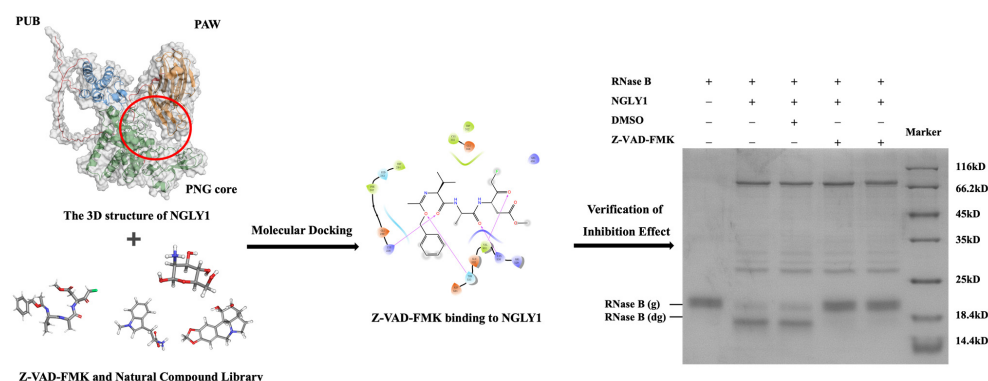


Figure 2. The screening method for targeting NGLY1 lead compounds. Red circle: Location of the receptor pocket. Red arrow: Location of the NGLY1. RNase B (g): N-glycosylated RNase B (NGLY1 is inhibited); RNase B (dg): N-glycosylated RNase B (NGLY1 is not inhibited).

2.2. Verification of Inhibitory Effect of Primary Screening Compounds

The inhibitory effects of primary screening compounds were validated through the electrophoretic mobility shift assay. Specifically, Poliumoside, Soyasaponin Bb, and Saikosaponin B2 demonstrated effective inhibition of NGLY1 activity. The minimum inhibitory concentrations of Z-VAD-FMK, Poliumoside, Soyasaponin Bb, and Saikosaponin B2 were found to be 1 mM, 25 mM, 25 mM, and 50 mM, respectively (Figure 3). It is noteworthy that all three compounds were isolated from traditional heat-clearing and detoxifying Chinese herbs. The strongest dockings of NGLY1 inhibitors and their binding sites, interactions, and distances, are shown in Figure 3 and Table 1. NGLY1 inhibitors mainly bind to amino acids, such as Lys238, Glu239, Trp244, and Glu356, through hydrogen bonding.

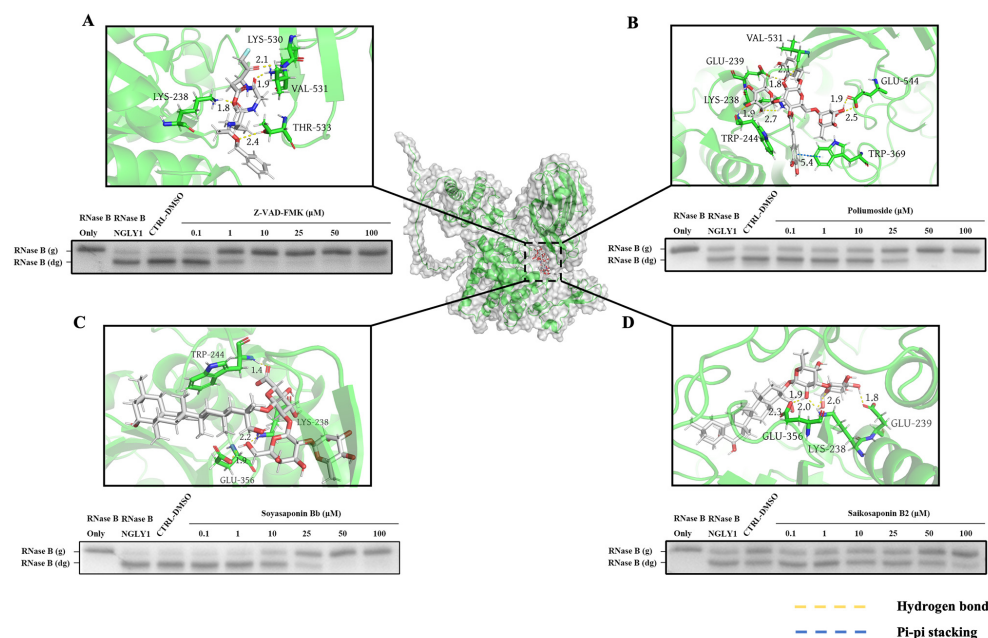


Figure 3. Analysis of interaction mode between NGLY1 inhibitors and NGLY1 protein, and NGLY1 inhibitors' mediated inhibition of NGLY1 activity were tested at various concentrations using the electrophoretic mobility shift assay. (A) Sites of Z-VAD-FMK binding to NGLY1 and Z-VAD-FMK mediated inhibition of NGLY1 activity. (B) Sites of Poliumoside binding to NGLY1 and Poliumoside Bb mediated inhibition of NGLY1 activity. (C) Sites of Soyasaponin Bb binding to NGLY1 and Soyasaponin Bb mediated inhibition of NGLY1 activity. (D) Sites of Saikosaponin B2 binding to NGLY1 and Saikosaponin B2 mediated inhibition of NGLY1 activity. RNase B (g): N-glycosylated RNase B (NGLY1 is inhibited); RNase B (dg): N-glycosylated RNase B (NGLY1 is not inhibited).

Table 1. Molecular docking information of 4 NGLY1 inhibitors.

Compound	Docking Score	Molecular Formula	Weight (g/mol)	Noncovalent Interactions	Lys238	Glu239	Trp244	Lys530	Val531	Thr533	Amino Acid Sites
Z-VAD-FMK	-4.560	C22H30FN3O7	467.494	4 H-bond	Lys238	/	/	/	Val531	Thr533	
Poliumoside	-10.088	C35H46O19	770.734	1 Pi-pi 6 H-bond	Lys238	Glu239	Trp244	/	Val531	/	Glu544
Soyasaponin Bb	-8.497	C48H78O18	943.134	3 H-bond	Lys238	/	Trp244	/	/	/	/
Saikosaponin B2	-6.007	C42H68O13	780.993	5 H-bond	Lys238	Glu239	/	/	/	/	/

2.3. The Analysis of Inhibitory Mechanism of NGLY1 Inhibitor

We compared the chemical structures of Poliumoside, Soyasaponin Bb, and Saikosaponin B2 (Figure 4A) and found that Poliumoside contains D-glucose and L-rhamnose, Soyasaponin Bb contains D-galactose (an enantiomer of D-glucose) and L-rhamnose, and Saikosaponin B2 contains D-glucose and D-fucose (an enantiomer of L-rhamnose). The results illustrated that the natural compounds with a core disaccharide structure of (D-glucose/D-galactose) and (L-rhamnose/D-fucose) may have inhibitory effects on NGLY1. We identified a compound, Rutinose (Figure 4A), which is a disaccharide structure containing D-glucose and L-rhamnose. The electrophoretic mobility shift assay showed that Rutinose inhibited NGLY1 in a dose-dependent manner at high concentrations (Figure 4B). As Poliumoside exhibited the highest potency, and the activity of Rutinose was confirmed, we utilized the disaccharide structure containing glucose and rhamnose as the core structural element for the NGLY1 inhibitor in this study.

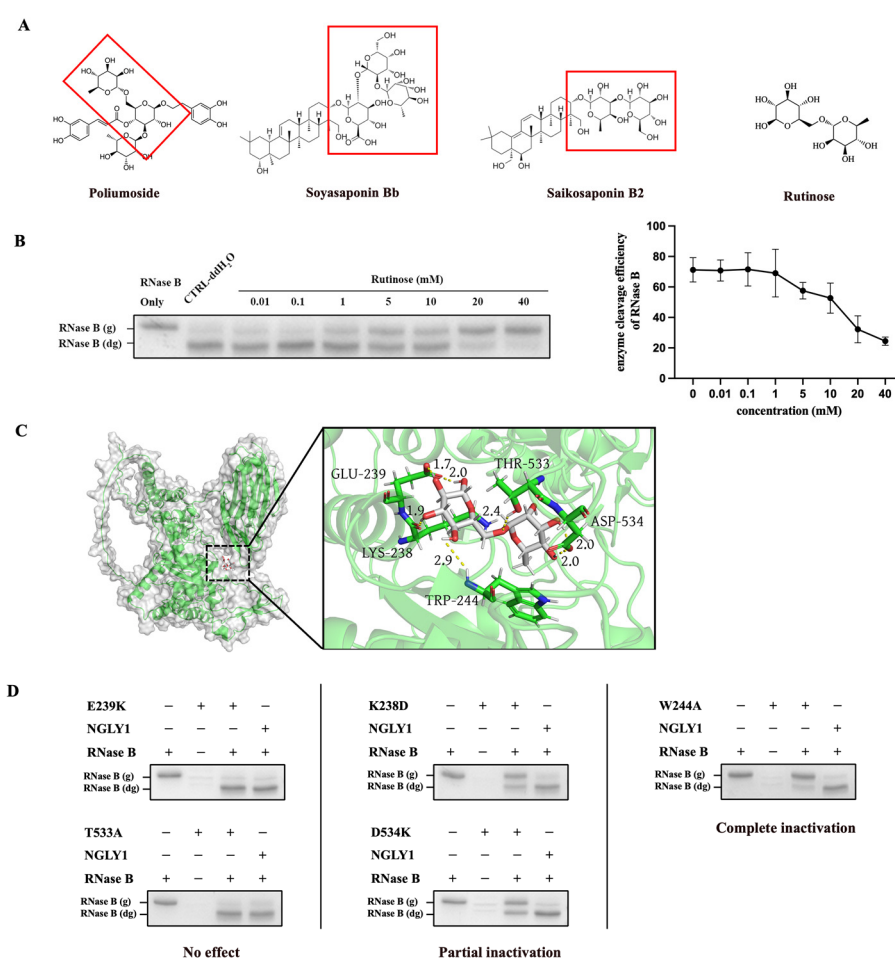


Figure 4. The inhibitory effect of Rutinose as a core structure of Poliumoside, Soyasaponin Bb, and Saikosaponin B2 on NGLY1. (A) Chemical structure of Poliumoside, Soyasaponin Bb, Saikosaponin B2, and Rutinose. (B) Rutinose mediated inhibition of NGLY1 activity. Further quantification of the enzyme cleavage results was performed using Image J (Version 2.1.0) software. (C) Sites of Rutinose binding to NGLY1. (D) The activity of NGLY1 mutants. RNase B (g): N-glycosylated RNase B (NGLY1 is inhibited); RNase B (dg): N-glycosylated RNase B (NGLY1 is not inhibited). Red box: The glycan structure of the compound.

The molecular docking results between Rutinose and NGLY1 showed five binding sites, Lys238, Glu239, Trp244, Thr533, and Asp534 (Figure 4C). Mutations were added to each of the five binding sites, and the results showed that E239K and T533A had no effect on NGLY1 activity, while K238D and D534K mutations led to the partial inactivation of NGLY1. The

W244A mutation resulted in complete inactivation of NGLY1 (Figure 4D). Lys238, Trp244, and Asp534 were important catalytic sites of NGLY1. Poliumoside, Soyasaponin Bb, and Saikosaponin B2 might inhibit NGLY1 by binding to Lys238 or Trp244.

2.4. The Inhibitory Effects of Rutinose as the Core Structural Element for NGLY1 Inhibitor

To validate Rutinose as a core structure for NGLY1 inhibition, we identified two other compounds, Doismin and Rutin, which also contain D-glucose and L-rhamnose in their glycoside portion (Figure 5A,C). Through in vitro enzymatic assays, they were found to inhibit NGLY1 activity as well (Figure 5B,D), but their minimum inhibitory concentration was different. Therefore, we hypothesized that the glycoside composed of glucose and arabinose played a major inhibitory role but exhibited varying inhibitory effects due to different saponin ligands.

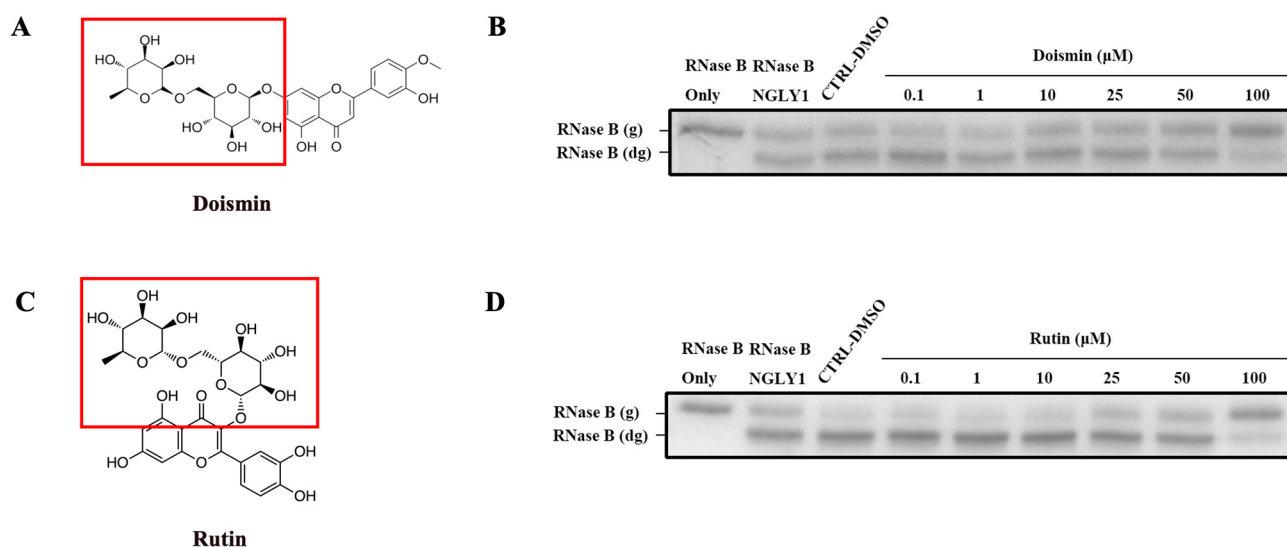


Figure 5. Doismin and Rutin mediated inhibition of NGLY1 activity were tested at various concentrations using the electrophoretic mobility shift assay. (A,C) Chemical structure diagram of Diosmin and Rutin. (B) Diosmin and (D) Rutin mediated inhibition of NGLY1 activity were tested at various concentrations using the electrophoretic mobility shift assay. RNase B (g): N-glycosylated RNase B (NGLY1 is inhibited); RNase B (dg): N-glycosylated RNase B (NGLY1 is not inhibited). Red box: The glycan structure of the compound.

2.5. Toxicity Analysis

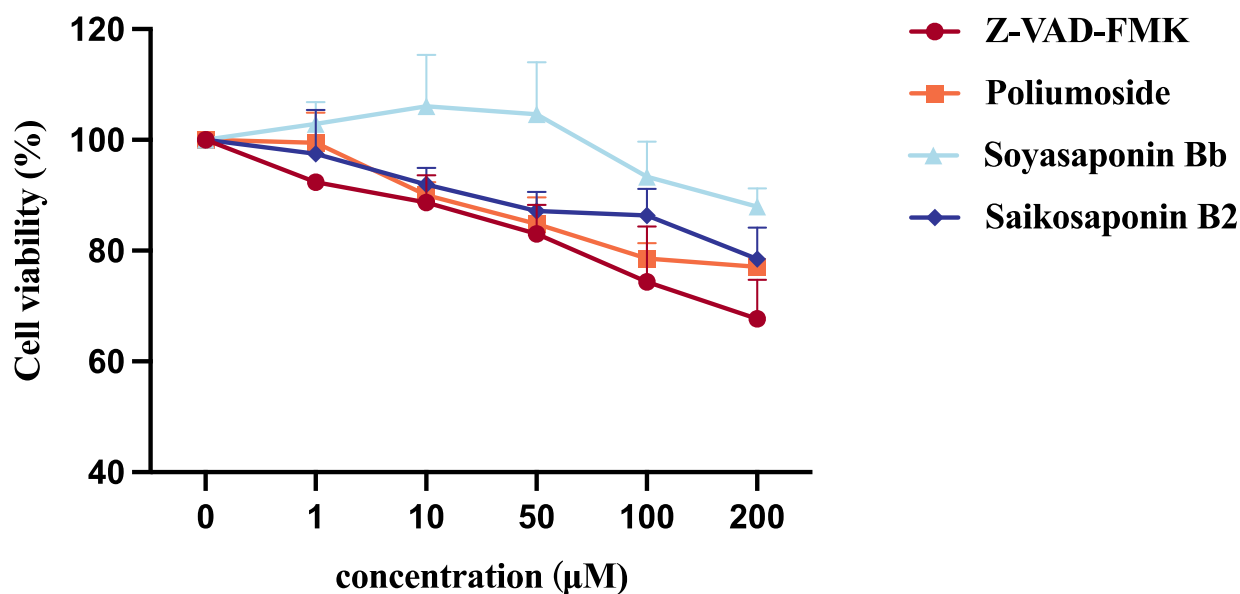
To ensure the safety of candidate drugs, toxicity testing of compounds was an important step. Calculation-based electronic toxicity measurement is widely utilized due to its accuracy and accessibility, providing information on any natural compound [32]. In order to determine the toxicity and adverse effects of the four NGLY1 inhibitors, we used the freely available testing tool ADMETlab 2.0 [33,34]. The website evaluates several toxicological parameters, such as human hepatotoxicity (H-HT), drug-induced liver injury (DILI), skin sensitization, carcinogenicity, eye corrosion, and eye irritation (Table 2). According to ADMETlab 2, Z-VAD-FMK and Poliumoside were highly probable to cause a drug-induced liver injury, with Poliumoside also posing a potential risk of skin allergy. Conversely, Soyasaponin Bb and Saikosaponin B2 exhibited a lower probability of toxicities.

Table 2. Predictive toxicity properties of NGLY1 inhibitors.

Target	H-HT	DILI	Skin Sensitization	Carcinogenicity	Eye Corrosion	Eye Irritation
Z-VAD-FMK	0.377 * (-)	0.924 (+++)	0.401 (-)	0.238 (--)	0.004 (---)	0.01 (---)
Poliumoside	0.375 (-)	0.953 (+++)	0.971 (+++)	0.031 (---)	0.003 (---)	0.311 (-)
Soyasaponin Bb	0.178 (--)	0.044 (---)	0.2 (--)	0.025 (---)	0.003 (---)	0.008 (---)
Saikosaponin B2	0.281 (--)	0.008 (---)	0.053 (---)	0.024 (---)	0.003 (---)	0.006 (---)

*: The value is the probability of being toxic. For the classification endpoints, the prediction probability values are transformed into six symbols: 0–0.1 (---), 0.1–0.3 (--), 0.3–0.5 (-), 0.5–0.7 (+), 0.7–0.9 (++) and 0.9–1.0 (+++). H-HT: human hepatotoxicity; DILI: drug induced liver injury.

Subsequently, we also performed CCK-8 assays of HEK293T cells treated with four NGLY1 inhibitors. After 24 h of compound exposure, Soyasaponin Bb did not significantly impact cell viability and the impact of Poliumoside, Soyasaponin Bb, and Saikosaponin B2 on cell viability was less than that of Z-VAD-FMK (Figure 6). In summary, the compound Soyasaponin Bb demonstrated a higher safety profile compared to Z-VAD-FMK, whereas Poliumoside was predicted to have potential compound toxicity.

**Figure 6.** CCK8 analysis of HEK 293T cells treated with NGLY1 inhibitors for 24 h.

The results were predicted by the ADMETlab 2.0 website (<https://admetmesh.scbdd.com> (accessed on 10 October 2023)), but the actual toxicity of the drugs should be determined through real experiments.

3. Discussion

In this study, we screened three natural compounds that can inhibit NGLY1 activity. Leveraging the predictive structure of NGLY1, we conducted computational virtual screening using a natural compound library. In the initial round of screening, seventeen natural compounds were evaluated, leading to the identification of three promising NGLY1 inhibitors: Poliumoside, Soyasaponin Bb, and Saikosaponin B2. An intriguing revelation emerged upon comparing the chemical structures of these inhibitors. Remarkably, we observed a disaccharide structure composed of glucose and rhamnose, which had been proven to be effective in inhibiting NGLY1 and could serve as a core structural element

for NGLY1 inhibitors. This core disaccharide structure could also serve as a lead structure for the design and development of NGLY1 inhibitors. Based on the molecular interaction analysis, we proposed that Lys238, Trp244, and Asp534 are important catalytic sites of NGLY1. Our findings suggest that NGLY1 inhibitors likely impede its function by binding to Lys238 or Trp244. Consequently, during the screening process, it was crucial to focus on compounds that interact with Lys238 and Trp244, as they may serve as a basis for subsequent drug screening for NGLY1 inhibitors.

Comparatively, Poliumoside, Soyasaponin Bb, and Saikosaponin B2 demonstrated less potent inhibitory effects on NGLY1 when compared to Z-VAD-FMK. However, it is worth noting that these compounds are natural products derived from plants with fewer drug-related side effects. We conducted preliminary toxicity predictions using ADMETLab 2.0 website (<https://admetmesh.scbdd.com> (accessed on 10 October 2023)) and assessed their effects on cellular viability for the three specific compounds, and found that the compounds Soyasaponin Bb demonstrated higher safety profiles compared to Z-VAD-FMK, whereas Poliumoside was predicted to have potential compound toxicity. Further research is necessary to investigate the impact of these compounds on intracellular NGLY1 activity within cells and to conduct metabolomics-based toxicological research, focusing on aspects such as nephrotoxicity, hepatotoxicity, cardiotoxicity, and central nervous system toxicity [35–37].

It has been reported that NGLY1 deficiency could upregulate the expression of ISGs, enhancing the body's innate antiviral capabilities [10,38]. Consequently, NGLY1 inhibitors have the potential to complement traditional antiviral drugs by contributing to an enhanced antiviral response. NGLY1 inhibitors have demonstrated not only antiviral properties but also significant implications in cancer treatment. In the treatment of blood cancers like multiple myeloma (MM) and mantle cell lymphoma (MCL), proteasome inhibitors play a crucial role [39,40]. However, resistance to protease inhibitors primarily arises from the upregulation of proteasome subunit (PSM) levels, with the expression of the PSM gene being regulated by the transcription factor Nuclear Factor, Erythroid 2 Like 1 (NFE2L1 or Nrf1) [39,41]. Importantly, Nrf1 is an N-glycosylated transmembrane protein, and its activation process involves the participation of NGLY1 [42,43]. Tomlin et al. [3] found that inhibiting NGLY1 in cultured cells disrupts Nrf1 function, enhancing the cytotoxicity of protease inhibitors. Notably, NGLY1 is highly expressed in certain human cancer cells, such as melanoma and ovarian cancer, while being low in their corresponding normal tissues like skin and ovary [44]. It has also been reported that the downregulation of NGLY1 results in melanoma cell death and a slowdown in tumor growth [45]. Compounds, like Poliumoside, Soyasaponin Bb, and Saikosaponin, exhibit promising therapeutic potential in various tumor diseases, including melanoma, multiple myeloma, and acute lymphocytic leukemia.

Our future work will encompass a comprehensive assessment of the broad-spectrum antiviral properties associated with NGLY1 inhibitors, employing various types of viruses for thorough evaluation. Additionally, we will also investigate the potential therapeutic utility of NGLY1 inhibitors in the treatment of melanoma, multiple myeloma, and acute lymphocytic leukemia. Current efforts are concentrated on scaffold optimization to refine the molecular structure of the inhibitors, aiming to enhance their inhibitory potential. Dubbu et al. [15] utilized the Prins cyclization to synthesize 2-Deoxy- β -C-aryl/alkyl glycosides, while Chennaiah et al. [16] synthesized vicinal 1,2-azidoacetates catalyzed by TMSOTf, offering a method for structural optimization of NGLY1 inhibitors.

4. Materials and Methods

4.1. Molecular Docking

A three-dimensional structure of NGLY1 was predicted online using AlphaFold2 based on the NGLY1 amino acid sequence (<https://colab.research.google.com/github/sokrypton/ColabFold/blob/main/AlphaFold2.ipynb?pli=1#scrollTo=kOblAo-xetgx> (accessed on 10 January 2022)). The SDF format structures of the natural compound library consist of 2960 compound structures' information obtained from TargetMol (Boston, MA, USA).

NGLY1 consists of three domains: PUB, PNG Core, and PAW. The PNG Core plays the primary catalytic role. Preliminary experiments have shown that mutations of amino acids Trp236, Trp244, Cys283, Leu318, Cys355, Glu356, and Asp386 in the PNG Core domain result in protein inactivation. The receptor pocket was generated with the aforementioned amino acids as the center ($x = 5.47$, $y = 4.28$, $z = 6.22$). The receptor pocket was set as a cubic grid with a side length of 20 Å. Semi-flexible docking was employed. Structural analysis of the docking results was performed using PyMOL (2.5.2) software.

4.2. Construction of NGLY1 Mutant

Plasmid pET28a-NGLY1 (WT) was preserved by our laboratory. All NGLY1 mutants were generated using the reverse complement primers for PCR (Takara, Beijing, China) with the template of pET28a-NGLY1 (WT) plasmid. The constructed pET28a-NGLY1 (WT) plasmid and pET28a-NGLY1 (mutant) plasmid were transformed into *E. coli* BL21 (DE3) (Tiangen, Beijing, China) separately for protein expression. The primers can be found in Table 3.

Table 3. PCR primer sequences for constructing NGLY1 mutants.

Mutant		Primer 5'-3'
K238D	Forward	CACCCAGTGAAAAAATCTTCGTCAAACCAGTGCAAAGCTCCAG
	Reverse	CTGGAGCTTTTGCACCTGGTTTGACGAAGAATTTTTTCACTGGGTG
E239K	Forward	TCACCCAGTGAAAAAATCTTTCTTAAACCAGTGCAAAGCTC
	Reverse	GAGCTTTTGCACCTGGTTTAAAGAAAGAATTTTTTCACTGGGTGA
W244A	Forward	TGCTGCACAAAACGTTATTCACCGCGTGAAAAAATCTTCCTTAAACC
	Reverse	GGTTTAAGGAAGAATTTTTTTCACGCGGTGAATAACGTTTTGTGCAGCA
T533A	Forward	CCATGTGCCAGTCTGCTTCAACTTTTCTGAATATAGATTCCATT
	Reverse	AATGGAATCTATATTCAGAAAAGTTGAAGCAGACTGGCACATGG
D534K	Forward	CAAATATACCATGTGCCACTTTGTTTCAACTTTTCTGAATATAGATTCCATTTTCC
	Reverse	GGAAAATGGAATCTATATTCAGAAAAGTTGAAACAAAGTGGCACATGGTATATTG

4.3. Protein Expression and Purification of NGLY1 and NGLY1 Mutant

Escherichia coli BL21(DE3) cells harboring the NGLY1 and NGLY1 mutant expression plasmid were grown at 37 °C in a Luria-Bertani (LB) medium containing 50 µg/mL kanamycin. When the culture reached OD600 of 0.6–0.8, 1 mM isopropyl β-d-thiogalactoside (IPTG) (Sangon Biotech, Shanghai, China) was added to the medium and incubated further for 12 h at 28 °C.

The frozen cells were resuspended in a lysis buffer (20 mM Tris, 300 mM NaCl, and 10 mM imidazole; pH 7.4) and then disrupted by sonication, and insoluble materials were removed by centrifugation at 12,000 rpm for 30 min at 4 °C. The supernatant was loaded onto a Ni-NTA resin column (1 mL bed volume, Thermo Scientific, Waltham, MA, USA) and incubated for 30 min at 4 °C. The column was washed with lysis buffers and wash buffers (20 mM Tris, 300 mM NaCl, and 25 mM imidazole; pH 7.4), and the protein was eluted with an elution buffer (20 mM Tris, 300 mM NaCl, and 250 mM imidazole; pH 7.4). The purified protein was concentrated using an amicon ultrafiltration concentrator (30kDa, Millipore, MA, USA). The protein concentration was determined by NanoDrop One spectrophotometer (Thermo Scientific, Waltham, MA, USA).

4.4. The Electrophoretic Mobility Shift Assay

The natural compounds were purchased from Targetmol (Boston, MA, USA). Recombinant NGLY1 (2 µg) was incubated with a primary screening compound for 60 min at 37 °C, at which time denatured RNase B (New England Biolabs, Ipswich, MA, USA) (2 µg) was added. The mixture was incubated for 12–16 h at 37 °C before separation by SDS-PAGE (15%) and Coomassie staining. Further quantification was performed using Image J software. RNase B had a molecular weight of ~17 kDa. After NGLY1 mediated deglycosylation,

the molecular weight of RNase B decreased to ~13.7 kDa. RNase B remained at ~17 kDa when NGLY1 activity was inhibited.

4.5. Toxicity Test

The safety profile of natural compounds was analyzed through calculation-based methods. ADMETlab 2.0 (<https://admetmesh.scbdd.com> (accessed on 10 October 2023)) was used to analyze the toxic effects of the NGLY1 inhibitors [33,34]. The ADMETlab 2.0 predicts the human hepatotoxicity (H-HT), drug induced liver injury (DILI), skin sensitization, carcinogenicity, eye corrosion, and eye irritation of the query compounds.

4.6. CCK-8 Analysis of Cell Viability Assay

HEK293T cells were cultured in Dulbecco's modified Eagle's medium (DMEM; Gibco, Shanghai, China) supplemented with 10% fetal bovine serum (FBS; Gibco, NSW, Australia) and 1% penicillin-streptomycin (Beyotime, Beijing, China) at 37 °C with 5% CO₂. 5000 cells were seeded in each well of a 96-well plate. Cell viability was measured using the Cell Counting Kit-8 (Beyotime, Beijing, China) according to the manufacturer's instructions.

5. Conclusions

In conclusion, NGLY1, an essential enzyme involved in the deglycosylation of misfolded glycoproteins through the ERAD pathway, has emerged as a pivotal enzyme with diverse therapeutic potential. Through a comprehensive structure-based virtual analysis of a natural compound library, and by validating the inhibitory effects of compounds using electrophoretic mobility shift assays, we identified three promising NGLY1 inhibitors: Poliumoside, Soyasaponin Bb, and Saikosaponin B2. These compounds were derived from traditional Chinese herbs with heat-clearing and detoxifying properties, displaying inhibitory activity against NGLY1. Preliminary toxicity predictions conducted through computer programs and analysis of cellular toxicity using the CCK-8 assays indicated that Soyasaponin Bb exhibited a higher safety profile in comparison to Z-VAD-FMK, while Poliumoside raised concerns regarding potential compound toxicity.

Moreover, it was revealed that the core structural motif shared by these inhibitors is a disaccharide structure featuring glucose and rhamnose. This structural insight suggested that their mode of action might involve binding to critical active sites of NGLY1, including Lys238 and Trp244, as they might serve as a basis for subsequent drug screening for NGLY1 inhibitors. Furthermore, natural compounds containing a disaccharide structure composed of glucose and rhamnose might also exert inhibitory effects on NGLY1.

Furthermore, NGLY1 inhibitors offer a multifaceted approach to address critical challenges in healthcare. They present a compelling solution to protease inhibitor resistance in blood cancer treatment and hold potential application in the management of melanoma. This study not only highlights the promise of Poliumoside, Soyasaponin Bb, and Saikosaponin B2 as lead compounds for NGLY1 inhibition but also provides a valuable foundation for future drug development efforts in the pursuit of effective antiviral and anticancer therapies.

Supplementary Materials: The following supporting information can be downloaded at: <https://www.mdpi.com/article/10.3390/molecules28237758/s1>. Refs [46–62] are cited in the Supplementary Material.

Author Contributions: Conceptualization, L.C.; methodology, R.L. and Y.Y.; software, S.Z. and Y.Z.; validation, J.G.; formal analysis, Q.L.; investigation, X.L.; data curation, Y.T. and S.L.; writing—original draft preparation, R.L.; writing—review and editing, G.S.; visualization, S.Y. and Y.C.; supervision, L.C.; project administration, G.S.; funding acquisition, G.S. All authors have read and agreed to the published version of the manuscript.

Funding: This research was funded by the Natural Science Foundation of Zhejiang Province (LY20C050002) and through a Research Project of Zhejiang Chinese Medical University (2023GJYY19).

Institutional Review Board Statement: Not applicable.

Informed Consent Statement: Not applicable.

Data Availability Statement: The datasets used and/or analyzed during the current study are available from the corresponding author on reasonable request.

Conflicts of Interest: The authors declare no conflict of interest.

References

1. Srinivasan, B.; Zhou, H.; Mitra, S.; Skolnick, J. Novel small molecule binders of human N-glycanase 1, a key player in the endoplasmic reticulum associated degradation pathway. *Bioorg. Med. Chem.* **2016**, *24*, 4750–4758. [CrossRef] [PubMed]
2. Suzuki, T.; Huang, C.; Fujihira, H. The cytoplasmic peptide: N-glycanase (NGLY1)—Structure, expression and cellular functions. *Gene* **2016**, *577*, 1–7. [CrossRef]
3. Tomlin, F.M.; Gerling-Driessen, U.I.M.; Liu, Y.C.; Flynn, R.A.; Vangala, J.R.; Lentz, C.S.; Clauder-Muenster, S.; Jakob, P.; Mueller, W.F.; Ordoñez-Rueda, D.; et al. Inhibition of NGLY1 Inactivates the Transcription Factor Nrf1 and Potentiates Proteasome Inhibitor Cytotoxicity. *ACS Cent. Sci.* **2017**, *3*, 1143–1155. [CrossRef] [PubMed]
4. Li, X.; Raihan, M.A.; Reynoso, F.J.; He, M. Glycosylation Analysis for Congenital Disorders of Glycosylation. *Curr. Protoc. Hum. Genet.* **2015**, *86*, 17.18.1–17.18.22. [CrossRef] [PubMed]
5. Asahina, M.; Fujinawa, R.; Nakamura, S.; Yokoyama, K.; Tozawa, R.; Suzuki, T. Ngly1^{-/-} rats develop neurodegenerative phenotypes and pathological abnormalities in their peripheral and central nervous systems. *Hum. Mol. Genet.* **2020**, *29*, 1635–1647. [CrossRef] [PubMed]
6. Might, M.; Wilsey, M. The shifting model in clinical diagnostics: How next-generation sequencing and families are altering the way rare diseases are discovered, studied, and treated. *Genet. Med.* **2014**, *16*, 736–737. [CrossRef] [PubMed]
7. Abuduxikuer, K.; Zou, L.; Wang, L.; Chen, L.; Wang, J.S. Novel NGLY1 gene variants in Chinese children with global developmental delay, microcephaly, hypotonia, hypertransaminasemia, alacrimia, and feeding difficulty. *J. Hum. Genet.* **2020**, *65*, 387–396. [CrossRef]
8. Kariminejad, A.; Shakiba, M.; Shams, M.; Namirani, P.; Eghbali, M.; Talebi, S.; Makvand, M.; Jaeken, J.; Najmabadi, H.; Hennekam, R.C. NGLY1 deficiency: Novel variants and literature review. *Eur. J. Med. Genet.* **2021**, *64*, 104146. [CrossRef]
9. Lam, C.; Wolfe, L.; Need, A.; Shashi, V.; Enns, G. NGLY1-Related Congenital Disorder of Deglycosylation. In *GeneReviews*[®]; Adam, M.P., Mirzaa, G.M., Pagon, R.A., Wallace, S.E., Bean, L.J.H., Gripp, K.W., Amemiya, A., Eds.; University of Washington: Seattle, WA, USA, 2018.
10. Yang, K.; Huang, R.; Fujihira, H.; Suzuki, T.; Yan, N. N-glycanase NGLY1 regulates mitochondrial homeostasis and inflammation through NRF1. *J. Exp. Med.* **2018**, *215*, 2600–2616. [CrossRef]
11. Wu, K.X.; Phuektes, P.; Kumar, P.; Goh, G.Y.; Moreau, D.; Chow, V.T.; Bard, F.; Chu, J.J. Human genome-wide RNAi screen reveals host factors required for enterovirus 71 replication. *Nat. Commun.* **2016**, *7*, 13150. [CrossRef]
12. Misaghi, S.; Pacold, M.E.; Blom, D.; Ploegh, H.L.; Korbel, G.A. Using a small molecule inhibitor of peptide: N-glycanase to probe its role in glycoprotein turnover. *Chem. Biol.* **2004**, *11*, 1677–1687. [CrossRef] [PubMed]
13. Needs, S.H.; Bootman, M.D.; Grotzke, J.E.; Kramer, H.B.; Allman, S.A. Off-target inhibition of NGLY1 by the polycaspase inhibitor Z-VAD-fmk induces cellular autophagy. *FEBS J.* **2022**, *289*, 3115–3131. [CrossRef] [PubMed]
14. Bhamhani, S.; Kondhare, K.R.; Giri, A.P. Diversity in Chemical Structures and Biological Properties of Plant Alkaloids. *Molecules* **2021**, *26*, 3374. [CrossRef] [PubMed]
15. Dubbu, S.; Chennaiah, A.; Verma, A.K.; Vankar, Y.D. Stereoselective synthesis of 2-deoxy-β-C-aryl/alkyl glycosides using Prins cyclization: Application in the synthesis of C-disaccharides and differently protected C-aryl glycosides. *Carbohydr. Res.* **2018**, *468*, 64–68. [CrossRef] [PubMed]
16. Chennaiah, A.; Bhowmick, S.; Vankar, Y.D. Conversion of glycals into vicinal-1,2-diazides and 1,2-(or 2,1)-azidoacetates using hypervalent iodine reagents and Me₃SiN₃. Application in the synthesis of N-glycopeptides, pseudo-trisaccharides and an iminosugar. *RSC Adv.* **2017**, *7*, 41755–41762. [CrossRef]
17. Yamasaki, S.; Asakura, M.; Neogi, S.B.; Hinenoya, A.; Iwaoka, E.; Aoki, S. Inhibition of virulence potential of *Vibrio cholerae* by natural compounds. *Indian J. Med. Res.* **2011**, *133*, 232–239.
18. Zhang, L.; Song, J.; Kong, L.; Yuan, T.; Li, W.; Zhang, W.; Hou, B.; Lu, Y.; Du, G. The strategies and techniques of drug discovery from natural products. *Pharmacol. Ther.* **2020**, *216*, 107686. [CrossRef]
19. Guo, X.; Yin, X.; Liu, Z.; Wang, J. Non-Alcoholic Fatty Liver Disease (NAFLD) Pathogenesis and Natural Products for Prevention and Treatment. *Int. J. Mol. Sci.* **2022**, *23*, 15489. [CrossRef]
20. Ma, N.; Zhang, Z.; Liao, F.; Jiang, T.; Tu, Y. The birth of artemisinin. *Pharmacol. Ther.* **2020**, *216*, 107658. [CrossRef]
21. Yu, D.L.; Lou, Z.P.; Ma, F.Y.; Najafi, M. The interactions of paclitaxel with tumour microenvironment. *Int. Immunopharmacol.* **2022**, *105*, 108555. [CrossRef]
22. Yang, H.; Landis-Piwowar, K.R.; Chen, D.; Milacic, V.; Dou, Q.P. Natural compounds with proteasome inhibitory activity for cancer prevention and treatment. *Curr. Protein Pept. Sci.* **2008**, *9*, 227–239. [CrossRef] [PubMed]
23. Choubdar, N.; Bhat, R.G.; Stubbs, K.A.; Yuzwa, S.; Pinto, B.M. Synthesis of 2-amido, 2-amino, and 2-azido derivatives of the nitrogen analogue of the naturally occurring glycosidase inhibitor salacinol and their inhibitory activities against O-GlcNAcase and NagZ enzymes. *Carbohydr. Res.* **2008**, *343*, 1766–1777. [CrossRef] [PubMed]


24. Zhen, D.; Xuan, T.Q.; Hu, B.; Bai, X.; Fu, D.N.; Wang, Y.; Wu, Y.; Yang, J.; Ma, Q. Pteryxin attenuates LPS-induced inflammatory responses and inhibits NLRP3 inflammasome activation in RAW264.7 cells. *J. Ethnopharmacol.* **2022**, *284*, 114753. [CrossRef] [PubMed]
25. Badshah, S.L.; Faisal, S.; Muhammad, A.; Poulson, B.G.; Emwas, A.H.; Jaremko, M. Antiviral activities of flavonoids. *Biomed. Pharmacother.* **2021**, *140*, 111596. [CrossRef] [PubMed]
26. Ahmad, A.; Kaleem, M.; Ahmed, Z.; Shafiq, H. Therapeutic potential of flavonoids and their mechanism of action against microbial and viral infections—A review. *Food Res. Int.* **2015**, *77*, 221–235. [CrossRef]
27. Śledź, P.; Cafilisch, A. Protein structure-based drug design: From docking to molecular dynamics. *Curr. Opin. Struct. Biol.* **2018**, *48*, 93–102. [CrossRef]
28. Ballante, F.; Kooistra, A.J.; Kampen, S.; de Graaf, C.; Carlsson, J. Structure-Based Virtual Screening for Ligands of G Protein-Coupled Receptors: What Can Molecular Docking Do for You? *Pharmacol. Rev.* **2021**, *73*, 527–565. [CrossRef]
29. Kitchen, D.B.; Decornez, H.; Furr, J.R.; Bajorath, J. Docking and scoring in virtual screening for drug discovery: Methods and applications. *Nat. Rev. Drug Discov.* **2004**, *3*, 935–949. [CrossRef]
30. Zhang, L.; Xu, J.; Guo, J.; Wang, Y.; Wang, Q. Elucidation of Pharmacological Mechanism Underlying the Anti-Alzheimer's Disease Effects of Evodia rutaecarpa and Discovery of Novel Lead Molecules: An In Silico Study. *Molecules* **2023**, *28*, 5846. [CrossRef]
31. Lu, F.; Luo, G.; Qiao, L.; Jiang, L.; Li, G.; Zhang, Y. Virtual Screening for Potential Allosteric Inhibitors of Cyclin-Dependent Kinase 2 from Traditional Chinese Medicine. *Molecules* **2016**, *21*, 1259. [CrossRef]
32. Luo, L.; Zhong, A.; Wang, Q.; Zheng, T. Structure-Based Pharmacophore Modeling, Virtual Screening, Molecular Docking, ADMET, and Molecular Dynamics (MD) Simulation of Potential Inhibitors of PD-L1 from the Library of Marine Natural Products. *Mar. Drugs* **2021**, *20*, 29. [CrossRef] [PubMed]
33. Xiong, G.; Wu, Z.; Yi, J.; Fu, L.; Yang, Z.; Hsieh, C.; Yin, M.; Zeng, X.; Wu, C.; Lu, A.; et al. ADMETlab 2.0: An integrated online platform for accurate and comprehensive predictions of ADMET properties. *Nucleic Acids Res.* **2021**, *49*, W5–W14. [CrossRef]
34. Alkahtani, H.M.; Almehezia, A.A.; Al-Omar, M.A.; Obaidullah, A.J.; Zen, A.A.; Hassan, A.S.; Aboulthana, W.M. In Vitro Evaluation and Bioinformatics Analysis of Schiff Bases Bearing Pyrazole Scaffold as Bioactive Agents: Antioxidant, Anti-Diabetic, Anti-Alzheimer, and Anti-Arthritic. *Molecules* **2023**, *28*, 7125. [CrossRef] [PubMed]
35. Chen, D.Q.; Chen, H.; Chen, L.; Tang, D.D.; Miao, H.; Zhao, Y.Y. Metabolomic application in toxicity evaluation and toxicological biomarker identification of natural product. *Chem. Biol. Interact.* **2016**, *252*, 114–130. [CrossRef] [PubMed]
36. Rendedula, D.; Doddipalla, R.; Shaik, H.; Gupta, H.P.; Godugu, D.; Kristipati, R.R.; Mudiam, M.K.R. Multiplatform Metabolomics to Understand the Imidacloprid-Induced Toxicity in Drosophila. *Chem. Res. Toxicol.* **2023**, *36*, 1574–1583. [CrossRef] [PubMed]
37. Zhou, J.; Chen, B.; Cai, Z. Metabolomics-based approach for assessing the toxicity mechanisms of dibutyl phthalate to abalone (*Haliotis diversicolor supertexta*). *Environ. Sci. Pollut. Res. Int.* **2015**, *22*, 5092–5099. [CrossRef]
38. Decout, A.; Katz, J.D.; Venkatraman, S.; Ablasser, A. The cGAS-STING pathway as a therapeutic target in inflammatory diseases. *Nat. Rev. Immunol.* **2021**, *21*, 548–569. [CrossRef] [PubMed]
39. Manasanch, E.E.; Orłowski, R.Z. Proteasome inhibitors in cancer therapy. *Nat. Rev. Clin. Oncol.* **2017**, *14*, 417–433. [CrossRef]
40. Dou, Q.P.; Zonder, J.A. Overview of proteasome inhibitor-based anti-cancer therapies: Perspective on bortezomib and second generation proteasome inhibitors versus future generation inhibitors of ubiquitin-proteasome system. *Curr. Cancer Drug Targets* **2014**, *14*, 517–536. [CrossRef]
41. Radhakrishnan, S.K.; Lee, C.S.; Young, P.; Beskow, A.; Chan, J.Y.; Deshaies, R.J. Transcription factor Nrf1 mediates the proteasome recovery pathway after proteasome inhibition in mammalian cells. *Mol. Cell* **2010**, *38*, 17–28. [CrossRef]
42. Radhakrishnan, S.K.; den Besten, W.; Deshaies, R.J. p97-dependent retrotranslocation and proteolytic processing govern formation of active Nrf1 upon proteasome inhibition. *eLife* **2014**, *3*, e01856. [CrossRef]
43. Suzuki, T.; Yoshida, Y. Ever-expanding NGLY1 biology. *J. Biochem.* **2022**, *171*, 141–143. [CrossRef] [PubMed]
44. Uhlén, M.; Björling, E.; Agaton, C.; Szizyarto, C.A.; Amini, B.; Andersen, E.; Andersson, A.C.; Angelidou, P.; Asplund, A.; Asplund, C.; et al. A human protein atlas for normal and cancer tissues based on antibody proteomics. *Mol. Cell. Proteom.* **2005**, *4*, 1920–1932. [CrossRef]
45. Zolekar, A.; Lin, V.J.T.; Mishra, N.M.; Ho, Y.Y.; Hayatshahi, H.S.; Parab, A.; Sampat, R.; Liao, X.; Hoffmann, P.; Liu, J.; et al. Stress and interferon signalling-mediated apoptosis contributes to pleiotropic anticancer responses induced by targeting NGLY1. *Br. J. Cancer* **2018**, *119*, 1538–1551. [CrossRef] [PubMed]
46. Yu, S.Y.; Lee, I.S.; Jung, S.H.; Lee, Y.M.; Lee, Y.R.; Kim, J.H.; Sun, H.; Kim, J.S. Caffeoylated phenylpropanoid glycosides from *Brandisia hancei* inhibit advanced glycation end product formation and aldose reductase in vitro and vessel dilation in larval zebrafish in vivo. *Planta Med.* **2013**, *79*, 1705–1709. [CrossRef]
47. Zhu, L.; Fu, R.; Liu, X.; He, Y.; Wang, B.; Ma, T. Soyasaponin Bb Protects Rat Hepatocytes from Alcohol-Induced Oxidative Stress by Inducing Heme Oxygenase-1. *Pharmacogn. Mag.* **2016**, *12*, 302–306.
48. Jiang, K.; Lu, Q.; Li, Q.; Ji, Y.; Chen, W.; Xue, X. Astragaloside IV inhibits breast cancer cell invasion by suppressing Vav3 mediated Rac1/MAPK signaling. *Int. Immunopharmacol.* **2017**, *42*, 195–202. [CrossRef] [PubMed]
49. Li, H.; Zhu, J.; Xu, Y.W.; Mou, F.F.; Shan, X.L.; Wang, Q.L.; Liu, B.N.; Ning, K.; Liu, J.J.; Wang, Y.C.; et al. Notoginsenoside R1-loaded mesoporous silica nanoparticles targeting the site of injury through inflammatory cells improves heart repair after myocardial infarction. *Redox Biol.* **2022**, *54*, 102384. [CrossRef]

50. Wu, L.; Li, Q.; Liu, Y. Polyphyllin D induces apoptosis in K562/A02 cells through G2/M phase arrest. *J. Pharm. Pharmacol.* **2014**, *66*, 713–721. [CrossRef]
51. Li, S.; Li, X.; He, F.; Jiao, R.; Zhang, S.; Li, Z. Amarogentin promotes osteoblast differentiation in oestrogen-deficiency-induced osteoporosis rats by modulating the Nrf-2/MAPK/ERK signalling pathway. *Arch. Med. Sci.* **2023**, *19*, 452–457. [CrossRef]
52. Siraj, F.M.; SathishKumar, N.; Kim, Y.J.; Kim, S.Y.; Yang, D.C. Ginsenoside F2 possesses anti-obesity activity via binding with PPAR γ and inhibiting adipocyte differentiation in the 3T3-L1 cell line. *J. Enzym. Inhib. Med. Chem.* **2015**, *30*, 9–14. [CrossRef] [PubMed]
53. Liu, S.; Shen, H.; Li, J.; Gong, Y.; Bao, H.; Zhang, J.; Hu, L.; Wang, Z.; Gong, J. Loganin inhibits macrophage M1 polarization and modulates sirt1/NF- κ B signaling pathway to attenuate ulcerative colitis. *Bioengineered* **2020**, *11*, 628–639. [CrossRef] [PubMed]
54. Li, C.; Deng, C.; Pan, G.; Wang, X.; Zhang, K.; Dong, Z.; Zhao, G.; Tan, M.; Hu, X.; Shi, S.; et al. Lycorine hydrochloride inhibits cell proliferation and induces apoptosis through promoting FBXW7-MCL1 axis in gastric cancer. *J. Exp. Clin. Cancer Res.* **2020**, *39*, 230. [CrossRef]
55. Lin, L.T.; Chung, C.Y.; Hsu, W.C.; Chang, S.P.; Hung, T.C.; Shields, J.; Russell, R.S.; Lin, C.C.; Li, C.F.; Yen, M.H.; et al. Saikosaponin b2 is a naturally occurring terpenoid that efficiently inhibits hepatitis C virus entry. *J. Hepatol.* **2015**, *62*, 541–548. [CrossRef] [PubMed]
56. Song, Z.; Xu, X. Advanced research on anti-tumor effects of amygdalin. *J. Cancer Res. Ther.* **2014**, *10* (Suppl. S1), 3–7.
57. Matsuzaki, Y.; Koyama, M.; Hitomi, T.; Yokota, T.; Kawanaka, M.; Nishikawa, A.; Germain, D.; Sakai, T. Arctiin induces cell growth inhibition through the down-regulation of cyclin D1 expression. *Oncol. Rep.* **2008**, *19*, 721–727. [CrossRef] [PubMed]
58. Jang, S.A.; Hwang, Y.H.; Yang, H.; Ryuk, J.A.; Gu, D.R.; Ha, H. Ethanolic extract of *Pyrrhosia lingua* (Thunb.) Farw. ameliorates OVX-induced bone loss and RANKL-induced osteoclastogenesis. *Biomed. Pharmacother.* **2022**, *147*, 112640. [CrossRef]
59. Manciu, F.S.; Guerrero, J.; Bennet, K.E.; Chang, S.Y.; Rahman, M.; Martinez Lopez, L.V.; Chantigian, S.; Castellanos, M.; Manciu, M. Assessing Nordihydroguaiaretic Acid Therapeutic Effect for Glioblastoma Multiforme. *Sensors* **2022**, *22*, 2643. [CrossRef]
60. Yamashita, N.; Taga, C.; Ozawa, M.; Kanno, Y.; Sanada, N.; Kizu, R. Camalexin, an indole phytoalexin, inhibits cell proliferation, migration, and mammosphere formation in breast cancer cells via the aryl hydrocarbon receptor. *J. Nat. Med.* **2022**, *76*, 110–118. [CrossRef]
61. Tan, C.; Zhu, W.; Lu, Y. Aloin, cinnamic acid and sophorcarpidine are potent inhibitors of tyrosinase. *Chin. Med. J.* **2002**, *115*, 1859–1862.
62. Cao, B.; Zhao, R.Y.; Li, H.H.; Xu, X.M.; Cui, H.; Deng, H.; Chen, L.; Wei, B. Oral administration of asparagine and 3-indolepropionic acid prolongs survival time of rats with traumatic colon injury. *Mil. Med. Res.* **2022**, *9*, 37. [CrossRef]

Disclaimer/Publisher’s Note: The statements, opinions and data contained in all publications are solely those of the individual author(s) and contributor(s) and not of MDPI and/or the editor(s). MDPI and/or the editor(s) disclaim responsibility for any injury to people or property resulting from any ideas, methods, instructions or products referred to in the content.

Article

Transition-Metal-Free One-Pot Synthesis of Fused Benzofuranamines and Benzo[*b*]thiophenamines

Ran Liu ¹, Lili Lv ², Bingchuan Yang ^{1,3,4,5,*}, Ziyi Gu ¹, Chenglong Li ⁶, Xueyan Lv ⁴, Chengcheng Ding ⁴, Xianqiang Huang ¹ and Dong Yuan ^{3,*} 

¹ School of Chemistry and Chemical Engineering, Liaocheng University, Liaocheng 252000, China; liuranbjt@163.com (R.L.); 19816255672@163.com (Z.G.); hxq@lcu.edu.cn (X.H.)

² China Petroleum Planning and Engineering Institute, Dongying 257237, China; lvlili@petrochina.com.cn

³ College of Chemistry and Chemical Engineering, Qilu Normal University, Jinan 250013, China

⁴ School of Chemistry and Chemical Engineering, Shandong University, Jinan 250100, China;

lxy17852267584@163.com (X.L.); 202220349@mail.sdu.edu.cn (C.D.)

⁵ The Department of Chemistry, University of South Florida, 4202 East Fowler Avenue, Tampa, FL 33620, USA

⁶ Shandong Weijiao Holding Group Co., Ltd., Weifang 262404, China; lichenglong@sdcoker.com

* Correspondence: yangbingchuan@lcu.edu.cn (B.Y.); yuandong@126.com (D.Y.)

Abstract: A series of benzofuran and benzo[*b*]thiophen derivatives was synthesized via a transition-metal-free one-pot process at room temperature. This one-pot protocol enables the synthesis of compounds with high reaction efficiency, mild conditions, simple methods, and a wide-ranging substrate scope. Regioselective five-membered heterocycles were constructed in good-to-excellent yields.

Keywords: one-pot synthesis; transition metal-free; benzofuranamines; benzo[*b*]thiophenamines; C-C coupling



Citation: Liu, R.; Lv, L.; Yang, B.; Gu, Z.; Li, C.; Lv, X.; Ding, C.; Huang, X.; Yuan, D. Transition-Metal-Free One-Pot Synthesis of Fused Benzofuranamines and Benzo[*b*]thiophenamines. *Molecules* **2023**, *28*, 7738. <https://doi.org/10.3390/molecules28237738>

Academic Editors: Tao Liu and Xuexiang Chen

Received: 17 October 2023

Revised: 17 November 2023

Accepted: 20 November 2023

Published: 23 November 2023



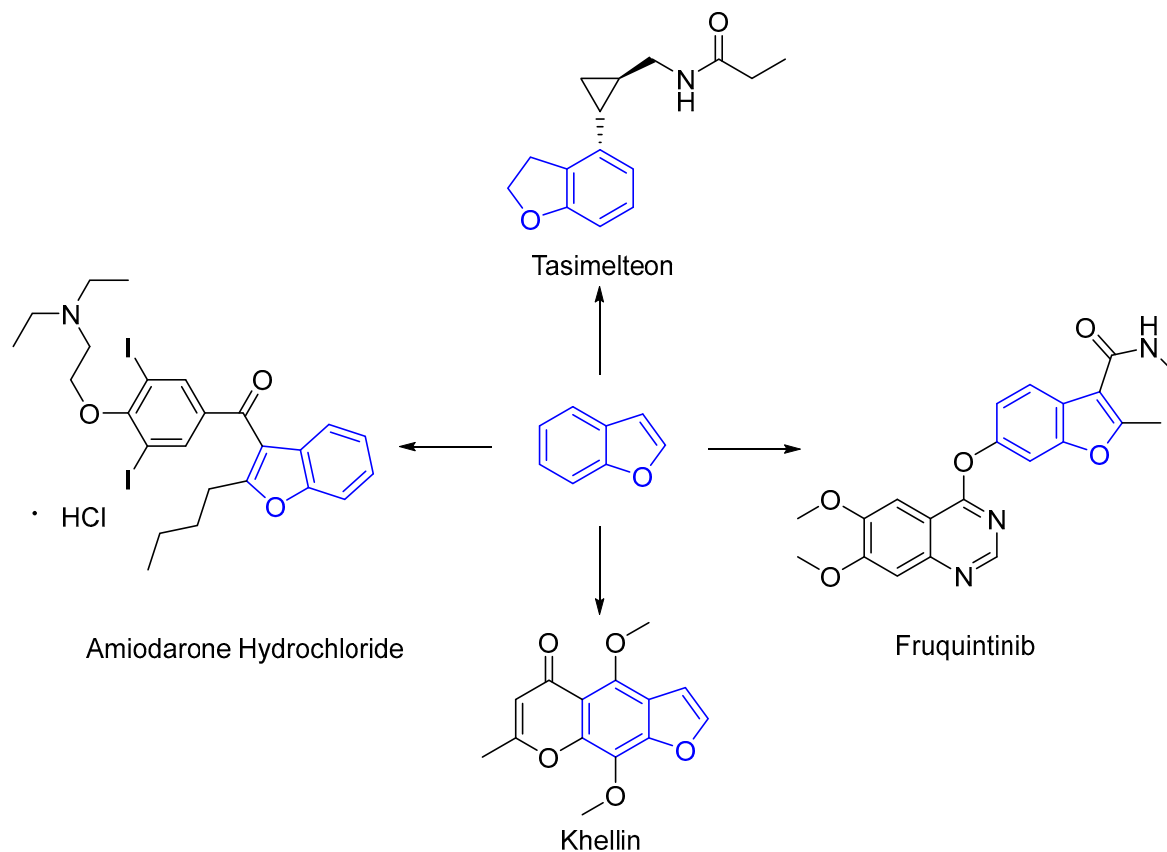
Copyright: © 2023 by the authors. Licensee MDPI, Basel, Switzerland. This article is an open access article distributed under the terms and conditions of the Creative Commons Attribution (CC BY) license (<https://creativecommons.org/licenses/by/4.0/>).

1. Introduction

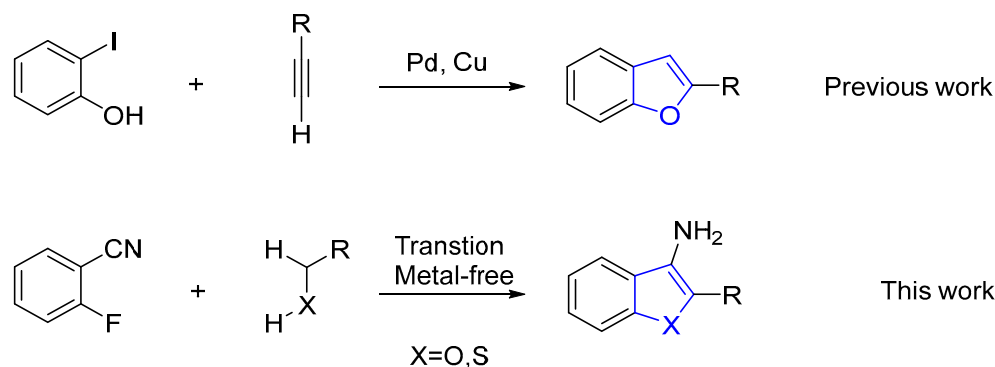
Benzofuran and benzo[*b*]thiophen derivatives have attracted considerable interest given their outstanding medicinal and biological properties [1,2]. Compounds with benzofuran functionalities have been widely employed to cure different kinds of diseases [3–6]. For example, Tasimelteon [7] is a small-molecule melatonin receptor agonist used to treat non-24-hour sleep disorders in patients with total blindness. Amiodarone hydrochloride [8,9] is a third class of antiarrhythmic drugs widely used for the treatment and prevention of arrhythmia and has a direct dilation effect on coronary arteries and peripheral vessels. Fruquintinib [10,11] can inhibit the formation of tumor neovascularization and eventually exert a tumor growth inhibition effect. It is a highly selective inhibitor of tumor angiogenesis. Khellin [12] is a micranochromone that has antiproliferative activity in vitro; meanwhile, it also has antispasmodic and coronary diastolic effects (Scheme 1). Fused benzofuran and benzothiophen also have antimicrobial, anti-inflammatory, antihypertensive, and analgesic activities [13].

As a result, all kinds of methods have been developed for the construction of benzofuran and benzothiophen derivatives [14]. Classical methods for the synthesis of these derivatives are described in the literature. Zhang's group [15] developed a palladium-catalyzed aryldifluoroalkylation method that involves the reaction of 1,6-enynes with ethyl difluoroiodoacetate and arylboronic acids, thereby achieving the desired derivatives. Jiang's group [16] developed a palladium-catalyzed fluoroalkylative cyclization of olefins with the formation of C_{sp3}–CF₂ and C–O/N bonds in one step to obtain difluoroalkylated 2,3-dihydrobenzofuran and indolin derivatives. In the synthesis of 2,3-disubstituted benzofuran, the Sonogashira coupling reaction [17] can be completed with a one-step reaction. It is prepared by coupling–cyclizing o-iodophenol with a terminal alkyne in the presence of powder potassium-fluoride-doped alumina and a mixture of powder palladium, cuprous

iodide, and tri-phenylphosphine. However, these methods still suffer from some drawbacks, such as vigorous reaction conditions and multiple steps (Scheme 2). In this context, the development of a novel synthetic method to fulfill the atom economy and achieve great efficiency is highly desired [18–20].

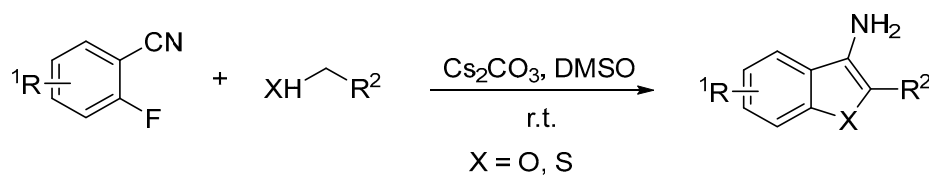


Scheme 1. Structures of some biologically important benzofurans.



Scheme 2. Attempts to synthesize benzofuran and benzothiophen derivatives in previous work and this work.

A one-step synthetic route would be a very useful improvement [21,22]. We focused on the development of the direct synthesis of heterocyclic systems using tandem reactions. Herein, we report an efficient and convergent one-pot synthetic strategy approach to benzofuran and benzothiophen derivatives under mild conditions. Benzofuran and benzothiophen scaffolds were obtained through the reaction of 2-fluorobenzonitriles and substituted alcohol at room temperature (Scheme 3).



Scheme 3. Synthesis of benzofuran-3-amines and benzo[*b*]thiophen-3-amines.

2. Results

To obtain the optimized conditions, 2-fluorobenzonitrile, **1a**, and 1-hydroxypropan-2-one, **2a**, were chosen as models. As shown in Table 1, the reaction base, solvent, and time were investigated. The reaction proceeded with different bases in DMSO at room temperature, and Cs_2CO_3 provided the highest yields (Table 1, entry 5). In weak basic systems such as K_2CO_3 or K_3PO_4 at room temperature, no desired product, **3a**, was obtained (Table 1, entries 1,3). When we used the organic base Et_3N in the reaction, no desired compound, **3a**, was detected either. In constructing **3a**, Cs_2CO_3 performed much better than KOH and *t*-BuOK, with a yield of 76% (Table 1, entries 5–7). The investigation of the solvent proved that the yields of the product in DMSO were higher than in CH_3CN , THF, and DMF with the same base system (Table 1, entries 5, 9, 10, 11). Finally, we chose Cs_2CO_3 in DMSO as the most efficient system to accomplish the synthesis of the benzofuran derivatives, **3** (Table 1, entry 5).

Table 1. Optimization of conditions ^a.

Entry	Base	Solvent	T (°C)	Time (h)	Yield (%) ^b
1	K_2CO_3	DMSO	r.t.	4	n.d.
2	K_2CO_3	DMSO	60	6	6
3	K_3PO_4	DMSO	r.t.	4	n.d.
4	K_3PO_4	DMSO	60	6	18
5	Cs_2CO_3	DMSO	r.t.	4	76
6	KOH	DMSO	r.t.	4	36
7	<i>t</i> -BuOK	DMSO	r.t.	1	56
8	Et_3N	DMSO	r.t.	5	n.d.
9	Cs_2CO_3	THF	r.t.	4	n.d.
10	Cs_2CO_3	CH_3CN	r.t.	4	n.d.
11	Cs_2CO_3	DMF	r.t.	4	n.d.

^a Reaction conditions: 2-fluorobenzonitrile, **1a** (1.0 equiv.); 1-hydroxypropan-2-one, **2a** (1.0 equiv.); base (3.0 equiv.).

^b Isolated yields. n.d.: not detected.

To explore the range of this methodology, various primary alcohols were studied (Table 2) under the selected reaction condition (Scheme 2). The structures of products **3a–3q** are shown in Figure 1. As shown in Table 2, both ketone and ester led to the formation of bicyclic products with high yields. However, 2-fluorobenzonitrile with strong electron-withdrawing groups (Table 2, entry 6, 7, 16, 17) obtained better yields than the non-substituted derivatives, and 2,4-difluorobenzonitrile obtained the best reaction yield of all the halogen-substituted scaffolds (Table 2, entry 3–5).

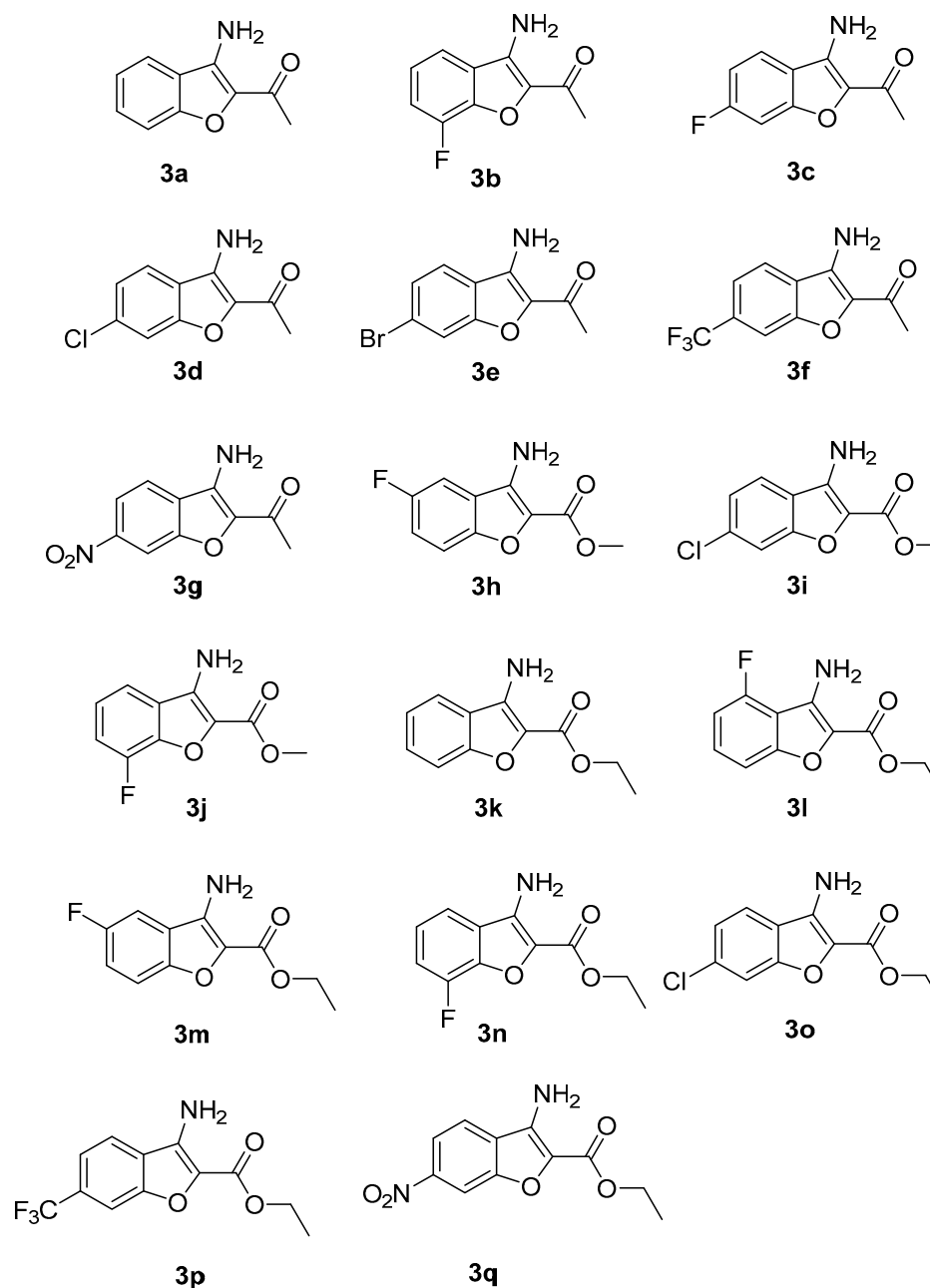
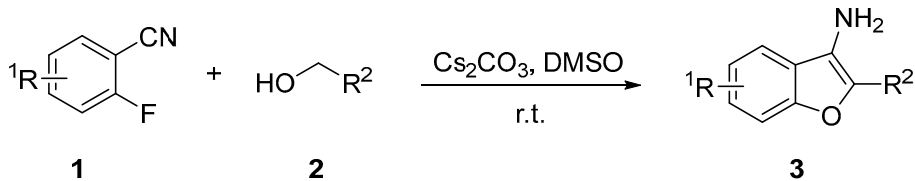


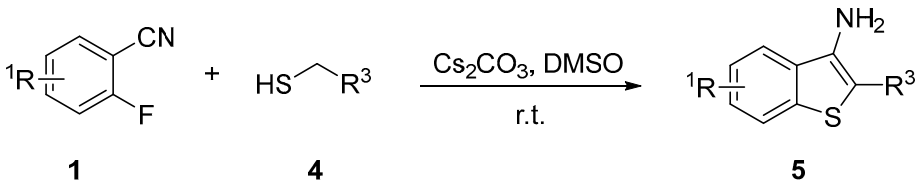
Figure 1. Structures of the desired compounds, 3a–3q.

Additionally, a steric hindrance affected the reaction very slightly. Ethyl 2-hydroxyacetate (Table 2, entry 11–17) also obtained a high yield of 3.

As shown in Table 3, a variety of substituted methanethiols, 4, were used to expand the applicability of this methodology. Substituted 2-fluorobenzonitrile bearing methoxyl obtained a low yield of 31% in the reaction (Table 3, entry 9), whereas 2-fluorobenzonitrile with electron-withdrawing groups obtained higher yields (Table 3, entries 6–8). The steric hindrance affected the reaction very slightly, and butyl 2-hydroxyacetate also provided a high yield of 5 (Table 3, entry 4).

Table 2. Synthesis of benzofuran-3-amines ^a.


Entry	R ¹	R ²	Time (h)	Product	Yield (%) ^b
1	H	-COCH ₃	6	3a	76
2	3-F	-COCH ₃	6	3b	80
3	4-F	-COCH ₃	5	3c	82
4	4-Cl	-COCH ₃	6	3d	78
5	4-Br	-COCH ₃	6	3e	56
6	4-CF ₃	-COCH ₃	6	3f	90
7	4-NO ₂	-COCH ₃	6	3g	81
8	5-F	-COOCH ₃	6	3h	77
9	4-Cl	-COOCH ₃	6	3i	72
10	3-F	-COOCH ₃	6	3j	78
11	H	-COOCH ₂ CH ₃	6	3k	71
12	6-F	-COOCH ₂ CH ₃	6	3l	73
13	5-F	-COOCH ₂ CH ₃	6	3m	80
14	3-F	-COOCH ₂ CH ₃	6	3n	81
15	4-Cl	-COOCH ₂ CH ₃	6	3o	74
16	4-CF ₃	-COOCH ₂ CH ₃	6	3p	90
17	4-NO ₂	-COOCH ₂ CH ₃	6	3q	87

^a Reaction conditions: 2-fluorobenzonitrile, **1** (1.0 equiv.); primary alcohols, **2** (1.0 equiv.); Cs₂CO₃ (3.0 equiv.).^b Isolated yields.**Table 3.** Synthesis of benzo[*b*]thiophen-3-amines ^a.


Entry	R ¹	R ³	Time (h)	Product	Yield (%) ^b
1	3-F	-COCH ₃	6	5a	78
2	H	-COOCH ₃	6	5b	76
3	H	-COOCH ₂ CH ₃	5	5c	74
4	H	-COOCH ₂ CH ₂ CH ₂ CH ₃	6	5d	77
5	H	-ph	6	5e	85
6	5-F	-COCH ₃	6	5f	75
7	3-F	-COCH ₃	6	5g	76
8	5-F	-COOCH ₃	6	5h	75
9	4-OMe	-COOCH ₂ CH ₃	6	5i	31

^a Reaction conditions: 2-fluorobenzonitrile, **1** (1.0 equiv.); α-substituted methanethiol, **4** (1.0 equiv.); Cs₂CO₃ (3.0 equiv.). ^b Isolated yields.

Aromatic substituted methanethiol also obtained a high yield of **5** (Table 3, entry 5). The structures of products **5a–5i** are shown in Figure 2.

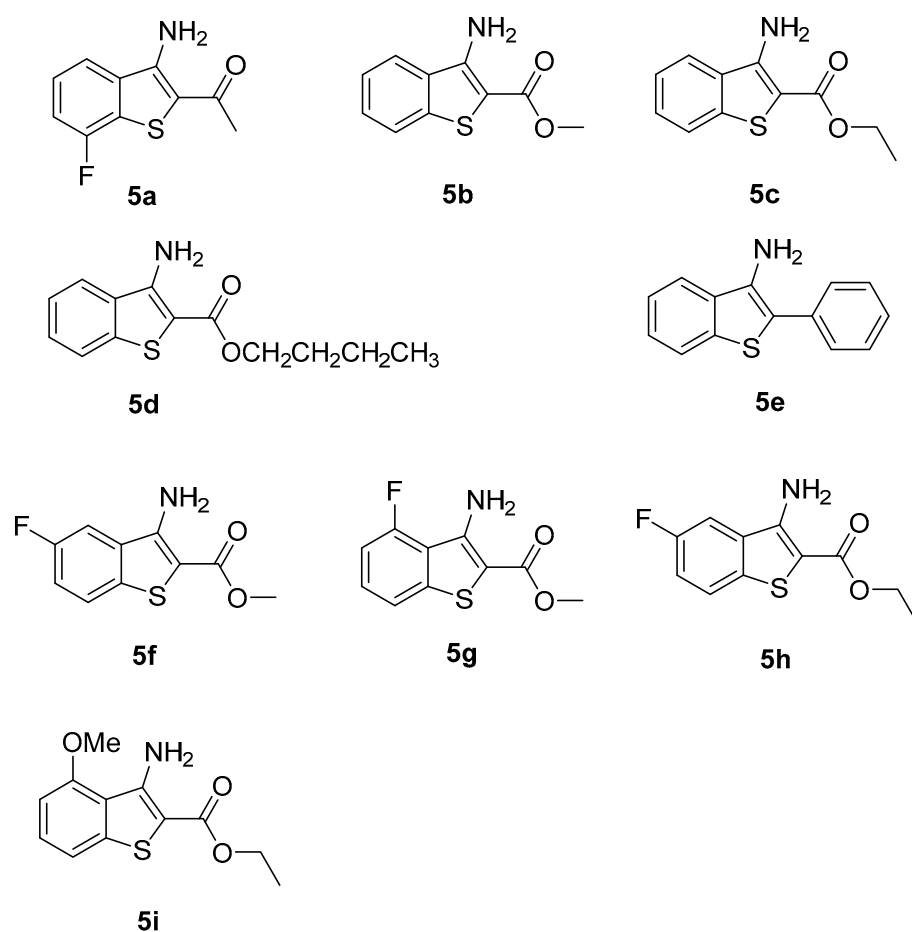
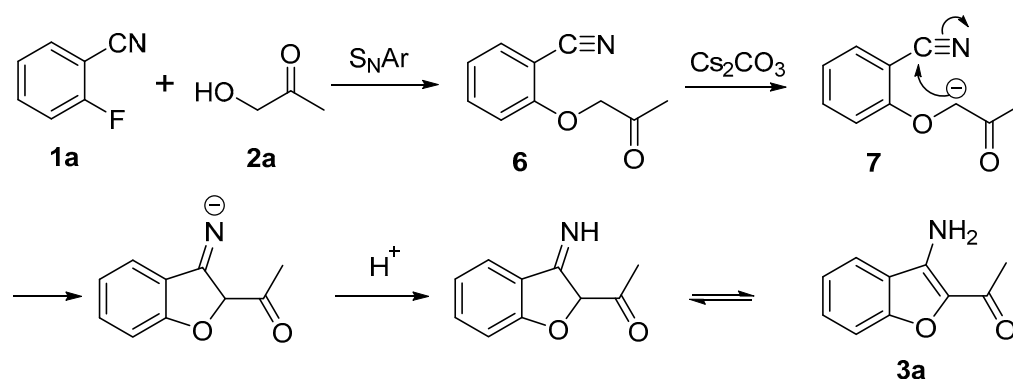


Figure 2. Structures of the desired compounds, 5a–5i.

Based on our previous work [23], a plausible reaction mechanism is presented in Scheme 4. Compounds **1a** and **2a** undergo nucleophilic aromatic substitution, providing compound **6**. In the presence of Cs_2CO_3 , the carbanion, **7**, that forms attacks the nitrile group, leading to cyclization and imine anion formation. Then, proton addition and tautomerism lead to the corresponding product, **3a**.



Scheme 4. Plausible mechanism of the formation of **3a**.

To demonstrate the structure of benzothiazole, the molecular configuration of product **5g** was determined through X-ray crystallographic analysis (Figure 3).

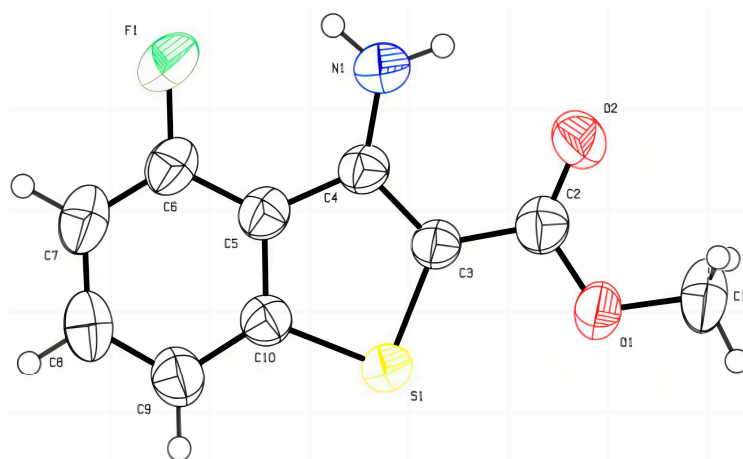


Figure 3. X-ray structure of compound **5g**.

3. Experimental Section

3.1. General

^1H and ^{13}C NMR spectra were recorded with a 300 spectrometer or a 400 spectrometer in CDCl_3 . HRMS spectra were determined with a Q-TOF spectrograph. Compounds **3a–3q** and **5a–5i** were prepared according to the literature. Other reagents (Adamas) were commercially available and were used without further purification. All reactions were monitored via thin-layer chromatography (TLC). For the NMR spectrum of compounds see the Supplementary Materials.

3.2. General Experimental Procedure for 1-(3-Aminobenzofuran-2-yl)ethan-1-one (**3a**)

To a solution of DMSO (15 mL), 2-fluorobenzonitrile, **1a** (0.12 g, 1.0 mmol); propionic acid, **2a** (0.037 g, 0.5 mmol); and Cs_2CO_3 (0.98 g, 3.0 mmol) were added and stirred for 1 h at room temperature; then, more propionic acid, **2a** (0.037 g, 0.5 mmol), was added and stirred at r.t. over 4 h. Brine (40 mL) was poured into the solution, and the mixture was extracted with CH_2Cl_2 (3×40 mL). The organic layers were combined and dried by over-anhydrous Na_2SO_4 . The product was purified via flash chromatography on silica gel (Hexane/EtOAc = 5:1). Compound **3a** was obtained as a white solid (mp: 175–176 °C, 0.13 g, 76% yield). ^1H NMR (CDCl_3 , 300 MHz): δ 7.59–7.56 (m, 1H), 7.52–7.46 (m, 1H), 7.42–7.40 (d, $J = 8.1$ Hz, 1H), 7.26–7.21 (m, 1H), 5.59 (s, 2H), 2.50 (s, 3H); ^{13}C NMR (CDCl_3 , 75 MHz): δ 189.8, 154.0, 138.5, 135.4, 129.4, 122.2, 121.3, 120.3, 112.6, 25.9; FT-HRMS (ESI) calcd for $\text{C}_{10}\text{H}_9\text{NO}_2$ [(M + H) $^+$]: 176.0667; found, 176.0691.

3.3. General Experimental Procedure for 1-(3-Amino-7-fluorobenzo[b]thiophen-2-yl)ethan-1-one (**5a**)

This compound was prepared in the same way as described for **3a** by using 2,3-difluorobenzonitrile (0.14 g, 1.0 mmol), 1,2-difluoro-4-nitrobenzene **4a** (0.09 g, 1.0 mmol), and Cs_2CO_3 (0.98 g, 3.0 mmol) in DMSO (15 mL) at room temperature. The product was purified via flash chromatography on silica gel (hexane/EtOAc = 5:1) to obtain **5a** (mp: 245–246 °C, 0.16 g, 78% yield) as a pale yellow solid. ^1H NMR (CDCl_3 , 400 MHz): δ 7.88 (s, 1H), 7.48 (t, $J = 8.8$ Hz, 2H), 5.88 (s, 2H), 3.89 (s, 3H); ^{13}C NMR (CDCl_3 , 75 MHz): δ 165.6, 147.9, 141.3, 128.8 ($J_{\text{C,F}} = 267$ Hz), 125.9, 122.4 ($J_{\text{C,F}} = 22$ Hz), 51.4; FT-HRMS (ESI) calcd for $\text{C}_{10}\text{H}_8\text{FNOS}$ [(M + H) $^+$]: 210.0344; found, 210.0567.

3.4. X-ray Crystal Structure Analysis of Compound **5g** [24,25]

Single crystals of **5g** suitable for X-ray crystal analysis were obtained via recrystallization from a hexane/ CH_2Cl_2 mixed solvent. Intensity data were collected at 293 K with an X-ray diffractometer with Mo $\text{K}\alpha$ radiation ($\lambda = 0.71073$ Å) and a graphite monochromator. A total of 1137 reflections were measured at a maximum 2θ angle of 50.0°, of which 1781 were independent reflections ($R_{\text{int}} = 0.0406$). The structure was determined with direct

methods (SHELXS-97)²² and refined by using full-matrix least-squares on F^2 (SHELEXL-97)²². The crystal data are as follows: $C_{10}H_8FNO_2S$; $F_W = 225.03$; crystal size, $0.12 \times 0.10 \times 0.10 \text{ mm}^3$; monoclinic, $P21/c$, $a = 13.7929(8) \text{ \AA}$, $b = 3.9422(3) \text{ \AA}$; $c = 22.5228(15) \text{ \AA}$; $V = 991.90(12) \text{ \AA}^3$; $Z = 4$. The refinement converged to $R_1 = 0.0637$, $wR_2 = 0.1604$ ($I > 2\sigma(I)$).

3.5. Characterization Data

1-(3-Amino-7-fluorobenzofuran-2-yl)ethan-1-one (**3b**): 155 mg (80% yield), white solid, mp: 188–189 °C; 1H NMR ($CDCl_3$, 300 MHz): δ 7.35 (dd, $J = 1.5, 7.5$ Hz, 1H), 7.25–7.14 (m, 2H), 5.31 (s, 1H), 2.53 (s, 3H); ^{13}C NMR ($CDCl_3$, 75 MHz): δ 190.0, 148.6 ($J_{C,F} = 249$ Hz), 141.4 ($J_{C,F} = 13$ Hz), 138.1, 136.1, 124.8, 122.8 ($J_{C,F} = 6$ Hz), 115.7, 115.1 ($J_{C,F} = 16$ Hz), 25.97; FT-HRMS (ESI) calcd for $C_{10}H_8FNO_2 [(M + H)^+]$: 194.0573; found, 194.0625.

1-(3-Amino-6-fluorobenzofuran-2-yl)ethan-1-one (**3c**): 158 mg (82% yield), white solid, mp: 188–189 °C; 1H NMR ($CDCl_3$, 400 MHz): δ 7.56 (t, $J = 8.0$ Hz, 1H), 6.79–6.71 (m, 2H), 4.70 (s, 2H), 3.83 (s, 3H); ^{13}C NMR ($CDCl_3$, 100 MHz): δ 163.1, 159.7 ($J_{C,F} = 257$ Hz), 157.9 ($J_{C,F} = 11$ Hz), 129.70, 109.3, 106.7, 98.5 ($J_{C,F} = 23$ Hz), 89.6 ($J_{C,F} = 16$ Hz), 26.0; FT-HRMS (ESI) calcd for $C_{10}H_8FNO_2 [(M + H)^+]$: 194.0573; found, 194.0653

1-(3-Amino-6-chlorobenzofuran-2-yl)ethan-1-one (**3d**): 163 mg (78% yield), white solid, mp: 217–219 °C; 1H NMR ($CDCl_3$, 400 MHz): δ 7.50 (d, $J = 8.4$ Hz, 1H), 7.44 (d, $J = 1.6$ Hz, 1H), 7.24 (dd, $J = 1.6, 8.4$ Hz, 1H), 5.58 (s, 2H), 2.50 (s, 3H); ^{13}C NMR ($CDCl_3$, 100 MHz): δ 189.7, 153.9, 137.8, 135.4, 123.3, 120.9, 120.0, 113.1, 110.0, 25.9; FT-HRMS (ESI) calcd for $C_{10}H_8ClNO_2 [(M + H)^+]$: 211.0214; found, 211.0265.

1-(3-Amino-6-bromobenzofuran-2-yl)ethan-1-one (**3e**): 142 mg (56% yield), white solid, mp: 247–249 °C; 1H NMR ($CDCl_3$, 400 MHz): δ 7.61 (d, $J = 1.2$ Hz, 1H), 7.45 (d, $J = 8.4$ Hz, 1H), 7.37 (dd, $J = 1.6, 8.4$ Hz, 1H), 5.56 (s, 2H), 2.49 (s, 3H); ^{13}C NMR ($CDCl_3$, 100 MHz): δ 189.8, 154.0, 137.8, 135.6, 125.9, 123.1, 121.1, 120.3, 116.1, 26.0; FT-HRMS (ESI) calcd for $C_{10}H_8BrNO_2 [(M + H)^+]$: 254.9718; found, 254.9816.

1-(3-Amino-6-(trifluoromethyl)benzofuran-2-yl)ethan-1-one (**3f**): 219 mg (90% yield), white solid, mp: 203–204 °C; 1H NMR ($CDCl_3$, 400 MHz): δ 7.70 (d, $J = 8.8$ Hz, 2H), 7.50 (d, $J = 8.4$ Hz, 1H), 5.60 (s, 2H), 2.53 (s, 3H); ^{13}C NMR ($CDCl_3$, 100 MHz): δ 190.3, 152.8, 137.1, 136.6, 131.5 ($J_{C,F} = 32$ Hz), 130.8 ($J_{C,F} = 33$ Hz), 125.3, 124.1, 122.6, 119.0 ($J_{C,F} = 3$ Hz), 110.3 ($J_{C,F} = 4$ Hz), 26.1; FT-HRMS (ESI) calcd for $C_{11}H_8F_3NO_2 [(M + H)^+]$: 244.0541; found, 244.0645.

1-(3-Amino-6-nitrobenzofuran-2-yl)ethan-1-one (**3g**): 178 mg (81% yield), white solid, mp none; 1H NMR ($CDCl_3$, 400 MHz): δ 8.35 (d, $J = 1.6$ Hz, 1H), 8.16 (dd, $J = 2.0, 8.4$ Hz, 1H), 7.72 (d, $J = 8.8$ Hz, 1H), 5.59 (s, 2H), 2.56 (s, 3H); ^{13}C NMR ($CDCl_3$, 100 MHz): δ 190.5, 152.3, 148.3, 138.2, 136.5, 126.4, 120.6, 117.5, 109.1, 26.2; FT-HRMS (ESI) calcd for $C_{10}H_8N_2O_4 [(M + H)^+]$: 221.0518; found, 221.0589.

Methyl 3-amino-5-fluorobenzofuran-2-carboxylate (**3h**): 161 mg (77% yield), white solid, mp: 180–182 °C; 1H NMR ($CDCl_3$, 400 MHz): δ 7.40–7.34 (m, 1H), 7.23 (d, $J = 8.0$ Hz, 1H), 6.90–6.86 (m, 1H), 5.21 (s, 2H), 3.96 (s, 3H); ^{13}C NMR ($CDCl_3$, 100 MHz): δ 163.4, 161.5, 157.3 ($J_{C,F} = 250$ Hz), 129.4 ($J_{C,F} = 9$ Hz), 111.1 ($J_{C,F} = 18$ Hz), 108.7 ($J_{C,F} = 5$ Hz), 107.8 ($J_{C,F} = 18$ Hz), 51.5; FT-HRMS (ESI) calcd for $C_{10}H_8FNO_3 [(M + H)^+]$: 210.0522; found, 210.0539.

Methyl 3-amino-6-chlorobenzofuran-2-carboxylate (**3i**): 173 mg (72% yield), white solid, mp: 210–211 °C; 1H NMR ($CDCl_3$, 400 MHz): δ 7.49–7.45 (m, 2H), 7.24 (dd, $J = 1.6, 8.4$ Hz, 1H), 4.99 (s, 2H), 3.97 (s, 3H); ^{13}C NMR ($CDCl_3$, 100 MHz): δ 161.6, 153.9, 138.2, 134.9, 125.9, 123.3, 120.4, 120.2, 113.0, 110.0, 103.1, 51.6; FT-HRMS (ESI) calcd for $C_{10}H_8ClNO_3 [(M + H)^+]$: 227.0163; found, 227.0195.

Methyl 3-amino-7-fluorobenzofuran-2-carboxylate (**3j**): 164 mg (78% yield), white solid, mp: 180–182 °C; 1H NMR ($CDCl_3$, 400 MHz): δ 7.35–7.32 (m, 1H), 7.22–7.17 (m, 2H), 5.02 (s, 2H), 3.97 (s, 3H); ^{13}C NMR ($CDCl_3$, 100 MHz): δ 161.7, 148.4 ($J_{C,F} = 250$ Hz), 141.4 ($J_{C,F} = 13$ Hz),

138.6, 126.2, 125.0 ($J_{C,F} = 3$ Hz), 123.0 ($J_{C,F} = 6$ Hz), 115.2 ($J_{C,F} = 4$ Hz), 114.7 ($J_{C,F} = 16$ Hz), 51.6; FT-HRMS (ESI) calcd for $C_{10}H_8FNO_3 [(M + H)^+]$: 210.0522; found, 210.0598.

Ethyl 3-aminobenzofuran-2-carboxylate (**3k**): 146 mg (71% yield), white solid, mp: 179–180 °C; 1H NMR ($CDCl_3$, 300 MHz): δ 7.57–7.54 (m, 1H), 7.46–7.44 (m, 2H), 7.27–7.22 (m, 2H), 4.96 (s, 1H), 4.45 (q, $J = 6.9$ Hz, 2H), 1.44 (t, $J = 6.9$ Hz, 3H); ^{13}C NMR ($CDCl_3$, 75 MHz): δ 161.67, 154.02, 130.91, 128.85, 128.77, 125.56, 122.30, 121.67, 119.59, 112.66, 65.58, 60.46, 30.59, 29.71, 19.19, 14.66, 13.72; FT-HRMS (ESI) calcd for $C_{11}H_{11}NO_3 [(M + H)^+]$: 206.0772; found, 206.0785.

Ethyl 3-amino-4-fluorobenzofuran-2-carboxylate (**3l**): 162 mg (73% yield), white solid, mp: 192–193 °C; 1H NMR ($CDCl_3$, 400 MHz): δ 7.39–7.34 (m, 1H), 7.24 (d, $J = 8.4$ Hz, 1H), 6.88 (dd, $J = 8.0, 9.6$ Hz, 1H), 5.19 (s, 2H), 4.44 (q, $J = 7.2$ Hz, 2H), 1.44 (t, $J = 7.2$ Hz, 3H); ^{13}C NMR ($CDCl_3$, 100 MHz): δ 161.4, 157.3 ($J_{C,F} = 250$ Hz), 155.2, 129.3 ($J_{C,F} = 7$ Hz), 111.1 ($J_{C,F} = 20$ Hz), 108.8 ($J_{C,F} = 5$ Hz), 107.7, ($J_{C,F} = 18$ Hz), 60.5, 14.6; FT-HRMS (ESI) calcd for $C_{11}H_{10}FNO_3 [(M + H)^+]$: 224.0678; found, 224.0693.

Ethyl 3-amino-5-fluorobenzofuran-2-carboxylate (**3m**): 179 mg (80% yield), white solid, mp: 192–193 °C; 1H NMR ($CDCl_3$, 400 MHz): δ 7.44 (d, $J = 8.0$ Hz, 1H), 7.37–7.32 (m, 1H), 6.94 (dd, $J = 8.0, 9.6$ Hz, 1H), 6.31 (s, 2H), 4.34 (q, $J = 7.2$ Hz, 2H), 1.38 (t, $J = 7.2$ Hz, 3H); ^{13}C NMR ($CDCl_3$, 100 MHz): δ 165.2, 159.6 ($J_{C,F} = 250$ Hz), 147.6, 142.1, 128.8 ($J_{C,F} = 9$ Hz), 120.3 ($J_{C,F} = 14$ Hz), 119.2 ($J_{C,F} = 4$ Hz), 109.3 ($J_{C,F} = 20$ Hz), 97.6, 60.4, 14.49; FT-HRMS (ESI) calcd for $C_{11}H_{10}FNO_3 [(M + H)^+]$: 224.0678; found, 224.0695.

Ethyl 3-amino-7-fluorobenzofuran-2-carboxylate (**3n**): 181 mg (81% yield), white solid, mp: 192–193 °C; 1H NMR ($CDCl_3$, 400 MHz): δ 7.34–7.32 (m, 1H), 7.22–7.17 (m, 2H), 5.00 (s, 2H), 4.45 (q, $J = 7.2$ Hz, 2H), 1.44 (t, $J = 7.2$ Hz, 3H); ^{13}C NMR ($CDCl_3$, 100 MHz): δ 161.4, 148.4 ($J_{C,F} = 250$ Hz), 141.4 ($J_{C,F} = 13$ Hz), 138.4, 126.5, 125.1 ($J_{C,F} = 3$ Hz), 122.8 ($J_{C,F} = 6$ Hz), 115.1 ($J_{C,F} = 4$ Hz), 114.5 ($J_{C,F} = 15$ Hz), 60.6, 14.5; FT-HRMS (ESI) calcd for $C_{11}H_{10}FNO_3 [(M + H)^+]$: 224.0678; found, 224.0689.

Ethyl 3-amino-6-chlorobenzofuran-2-carboxylate (**3o**): 177 mg (74% yield), white solid, mp: 221–222 °C; 1H NMR ($CDCl_3$, 400 MHz): δ 7.47 (d, $J = 8.8$ Hz, 2H), 7.24 (dd, $J = 2.0, 8.4$ Hz, 1H), 4.97 (s, 2H), 4.44 (q, $J = 7.2$ Hz, 2H), 1.44 (t, $J = 7.2$ Hz, 3H); ^{13}C NMR ($CDCl_3$, 100 MHz): δ 161.4, 153.9, 134.7, 123.3, 120.3, 113.0, 60.6, 14.6; FT-HRMS (ESI) calcd for $C_{11}H_{10}ClNO_3 [(M + H)^+]$: 241.0320; found.

Ethyl 3-amino-6-(trifluoromethyl)benzofuran-2-carboxylate (**3p**): 246 mg (90% yield), white solid, mp: 207–208 °C; 1H NMR ($CDCl_3$, 400 MHz): δ 7.73 (s, 1H), 7.68 (d, $J = 8.4$ Hz, 1H), 7.50 (d, $J = 8.4$ Hz, 1H), 5.02 (s, 2H), 4.46 (q, $J = 7.2$ Hz, 2H), 1.45 (t, $J = 7.2$ Hz, 3H); ^{13}C NMR ($CDCl_3$, 100 MHz): δ 161.3, 152.8, 137.5, 131.1, 130.8, 130.3 ($J_{C,F} = 30$ Hz), 128.0, 127.3, 125.3, 124.4, 122.6, 120.4, 119.1 ($J_{C,F} = 3$ Hz), 110.2 ($J_{C,F} = 4$ Hz), 60.8, 14.6; FT-HRMS (ESI) calcd for $C_{12}H_{10}F_3NO_3 [(M + H)^+]$: 274.0646; found, 274.0686.

Ethyl 3-amino-6-nitrobenzofuran-2-carboxylate (**3q**): 218 mg (87% yield), white solid, mp none; 1H NMR ($CDCl_3$, 400 MHz): δ 7.68 (d, $J = 1.2$ Hz, 1H), 7.52 (d, $J = 8.4$ Hz, 1H), 7.20 (dd, $J = 1.6, 8.4$ Hz, 1H), 5.88 (s, 2H), 4.35 (q, $J = 7.2$ Hz, 2H), 1.38 (t, $J = 7.2$ Hz, 3H); ^{13}C NMR ($CDCl_3$, 100 MHz): δ 165.2, 162.6, 147.7, 140.9, 134.4, 129.8, 124.7, 122.9, 122.0, 99.8, 60.6, 14.5; FT-HRMS (ESI) calcd for $C_{11}H_{10}N_2O_5 [(M + H)^+]$: 251.0623; found, 251.0635.

Methyl 3-aminobenzo[*b*]thiophene-2-carboxylate (**5b**): 157 mg (76% yield), pale yellow solid, mp: 224–225 °C; 1H NMR ($CDCl_3$, 300 MHz): δ 7.73 (d, $J = 8.1$ Hz, 1H), 7.63 (d, $J = 7.8$ Hz, 1H), 7.49–7.44 (m, 1H), 7.39–7.34 (m, 1H), 5.80 (s, 2H), 3.89 (s, 3H); ^{13}C NMR ($CDCl_3$, 75 MHz): δ 165.9, 148.5, 140.0, 131.3, 128.2, 123.9, 123.4, 121.2, 99.0, 51.5; FT-HRMS (ESI) calcd for $C_{10}H_9NO_2S [(M + H)^+]$: 208.0388; found, 208.0398.

Ethyl 3-aminobenzo[*b*]thiophene-2-carboxylate (**5c**): 164 mg (74% yield), pale yellow solid, mp: 235–237 °C; 1H NMR ($CDCl_3$, 300 MHz): δ 7.72 (d, $J = 8.1$ Hz, 1H), 7.63 (d, $J = 8.1$ Hz, 1H), 7.49–7.43 (m, 1H), 7.39–7.34 (m, 1H), 5.61 (s, 1H), 4.36 (q, $J = 7.2$ Hz, 2H), 1.39 (t, $J = 7.2$ Hz, 3H); ^{13}C NMR ($CDCl_3$, 75 MHz): δ 165.6, 148.3, 140.0, 131.5, 128.1, 123.8,

123.4, 121.2, 99.5, 60.4, 14.5; FT-HRMS (ESI) calcd for $C_{11}H_{11}NO_2S$ [(M + H)⁺]: 222.0544; found, 222.0609.

Butyl 3-aminobenzo[*b*]thiophene-2-carboxylate (**5d**): 192 mg (77% yield), pale yellow solid, mp: 258–259 °C; ¹H NMR (CDCl₃, 300 MHz): δ 7.73–7.66 (m, 2H), 7.48–7.42 (m, 1H), 7.38–7.33 (m, 1H), 5.26 (s, 2H), 4.30 (t, *J* = 6.6 Hz, 2H), 1.80—1.69 (m, 2H), 1.54–1.41 (m, 2H), 0.98 (t, *J* = 7.5 Hz, 3H); ¹³C NMR (CDCl₃, 75 MHz): δ 165.6, 147.9, 140.0, 131.5, 128.2, 123.9, 123.4, 121.2, 100.0, 64.3, 30.9, 19.3, 13.8; FT-HRMS (ESI) calcd for $C_{13}H_{15}NO_2S$ [(M + H)⁺]: 250.0857; found, 250.0903.

2-Phenylbenzo[*b*]thiophen-3-amine (**5e**): 191 mg (85% yield), pale yellow solid, mp: 253–255 °C; ¹H NMR (CDCl₃, 300 MHz): δ 7.78 (dd, *J* = 1.5, 6.9 Hz, 1H), 7.64–7.57 (m, 3H), 7.49–7.44 (m, 2H), 7.42–7.29 (m, 3H), 4.07 (s, 2H); ¹³C NMR (CDCl₃, 75 MHz): δ 137.6, 134.5, 134.3, 133.6, 129.2, 128.4, 127.0, 124.8, 123.9, 122.7, 119.9, 115.6; FT-HRMS (ESI) calcd for $C_{14}H_{11}NS$ [(M + H)⁺]: 226.0646; found, 226.0649.

Methyl 3-amino-5-fluorobenzo[*b*]thiophene-2-carboxylate (**5f**): 169 mg (75% yield), pale yellow solid, mp: 237–238 °C; ¹H NMR (CDCl₃, 400 MHz): δ 7.67 (dd, *J* = 4.8, 8.8 Hz, 1H), 7.30 (dd, *J* = 2.4, 8.8 Hz, 1H), 7.25–7.21 (m, 1H), 5.83 (s, 2H), 3.90 (s, 3H); ¹³C NMR (CDCl₃, 100 MHz): δ 165.6, 160.4 (*J*_{C,F} = 242 Hz), 147.8, 136.4, 135.2, 132.2 (*J*_{C,F} = 8 Hz), 130.7, 124.8 (*J*_{C,F} = 8 Hz), 117.2 (*J*_{C,F} = 25 Hz), 109.9, 106.9 (*J*_{C,F} = 23 Hz), 101.2, 51.7; FT-HRMS (ESI) calcd for $C_{10}H_8FNO_2S$ [(M + H)⁺]: 226.0293; found, 226.0356.

Methyl 3-amino-4-fluorobenzo[*b*]thiophene-2-carboxylate (**5g**): 171 mg (76% yield), pale yellow solid, mp: 237–238 °C; ¹H NMR (CDCl₃, 400 MHz): δ 7.44 (d, *J* = 8.0 Hz, 1H), 7.37–7.32 (m, 1H), 7.17 (t, *J* = 8.8 Hz, 1H), 5.92 (s, 2H), 3.90 (s, 3H); ¹³C NMR (CDCl₃, 100 MHz): δ 165.6, 157.9 (*J*_{C,F} = 246 Hz), 148.3, 134.5 (*J*_{C,F} = 10 Hz), 127.1 (*J*_{C,F} = 20 Hz), 125.4 (*J*_{C,F} = 7 Hz), 117.1, 117.0, 113.2 (*J*_{C,F} = 18 Hz), 99.9, 53.4, 51.7; FT-HRMS (ESI) calcd for $C_{10}H_8FNO_2S$ [(M + H)⁺]: 226.0293; found, 226.0348.

Ethyl 3-amino-5-fluorobenzo[*b*]thiophene-2-carboxylate (**5h**): 179 mg (75% yield), pale yellow solid, mp: 249–250 °C; ¹H NMR (CDCl₃, 400 MHz): δ 7.67 (dd, *J* = 4.8, 8.8 Hz, 1H), 7.30 (dd, *J* = 2.0, 8.8 Hz, 1H), 7.25–7.21 (m, 1H), 5.80 (s, 2H), 4.36 (q, *J* = 7.2 Hz, 2H), 1.40 (t, *J* = 7.2 Hz, 3H); ¹³C NMR (CDCl₃, 100 MHz): δ 165.3, 160.4 (*J*_{C,F} = 242 Hz), 147.6, 135.2, 132.3 (*J*_{C,F} = 8 Hz), 124.8 (*J*_{C,F} = 9 Hz), 117.1 (*J*_{C,F} = 25 Hz), 106.9 (*J*_{C,F} = 23 Hz), 60.6, 14.5; FT-HRMS (ESI) calcd for $C_{11}H_{10}FNO_2S$ [(M + H)⁺]: 240.0450; found, 240.0468.

Ethyl 3-amino-4-methoxybenzo[*b*]thiophene-2-carboxylate (**5i**): 78 mg (31% yield), pale yellow solid, mp: 282–283 °C; ¹H NMR (CDCl₃, 400 MHz): δ 7.37–7.28 (m, 1H), 7.24 (d, *J* = 4.0 Hz, 1H), 6.75 (s, 2H), 6.71–6.64 (m, 1H), 4.32 (q, *J* = 8.0 Hz, 2H), 2.62 (s, 3H), 1.37 (t, *J* = 8.0 Hz, 3H); ¹³C NMR (CDCl₃, 100 MHz): δ 165.5, 157.7, 148.8, 142.0, 129.0, 120.9, 115.8, 104.0, 60.0, 55.6, 14.5; FT-HRMS (ESI) calcd for $C_{12}H_{13}NO_3S$ [(M + H)⁺]: 252.0650; found, 252.0687.

4. Conclusions

In conclusion, a variety of benzofuran and benzo[*b*]thiophen derivatives was synthesized in good-to-excellent yields via Smiles rearrangement. At room temperature, an efficient and simple method was used to construct regioselective five-membered heterocycles. The outstanding features of this approach are mild conditions and transition-metal-free one-pot synthesis. This green and clean synthetic methodology has potential applications in the synthesis of biologically and medicinally relevant compounds. Our team is currently conducting more research to widen the applications of this technology.

Supplementary Materials: The following supporting information can be downloaded at: <https://www.mdpi.com/article/10.3390/molecules28237738/s1>, Table S1: Details of Crystal Structure Determination for **5g**; Figure S1: X-ray structure of compound **5g**; Figure S2: ¹H NMR and ¹³C NMR spectra of compound **3a**; Figure S3: ¹H NMR and ¹³C NMR spectra of compound **3b**; Figure S4: ¹H NMR and ¹³C NMR spectra of compound **3c**; Figure S5: ¹H NMR and ¹³C NMR spectra of

compound **3d**; Figure S6: ^1H NMR and ^{13}C NMR spectra of compound **3e**; Figure S7: ^1H NMR and ^{13}C NMR spectra of compound **3f**; Figure S8: ^1H NMR and ^{13}C NMR spectra of compound **3g**; Figure S9: ^1H NMR and ^{13}C NMR spectra of compound **3h**; Figure S10: ^1H NMR and ^{13}C NMR spectra of compound **3i**; Figure S11: ^1H NMR and ^{13}C NMR spectra of compound **3j**; Figure S12: ^1H NMR and ^{13}C NMR spectra of compound **3k**; Figure S13: ^1H NMR and ^{13}C NMR spectra of compound **3l**; Figure S14: ^1H NMR and ^{13}C NMR spectra of compound **3m**; Figure S15: ^1H NMR and ^{13}C NMR spectra of compound **3n**; Figure S16: ^1H NMR and ^{13}C NMR spectra of compound **3o**; Figure S17: ^1H NMR and ^{13}C NMR spectra of compound **3p**; Figure S18: ^1H NMR and ^{13}C NMR spectra of compound **3q**; Figure S19: ^1H NMR and ^{13}C NMR spectra of compound **5a**; Figure S20: ^1H NMR and ^{13}C NMR spectra of compound **5b**; Figure S21: ^1H NMR and ^{13}C NMR spectra of compound **5c**; Figure S22: ^1H NMR and ^{13}C NMR spectra of compound **5d**; Figure S23: ^1H NMR and ^{13}C NMR spectra of compound **5e**; Figure S24: ^1H NMR and ^{13}C NMR spectra of compound **5f**; Figure S25: ^1H NMR and ^{13}C NMR spectra of compound **5g**; Figure S26: ^1H NMR and ^{13}C NMR spectra of compound **5h**; Figure S27: ^1H NMR and ^{13}C NMR spectra of compound **5i**.

Author Contributions: Investigation, C.D., L.L., D.Y. and Z.G.; methodology, B.Y. and X.H.; project administration, C.L.; supervision, X.L.; writing—original draft, R.L. All authors have read and agreed to the published version of the manuscript.

Funding: We are grateful to the National Innovation and Entrepreneurship Training Program for College Students (CXC2023105, S202210447044, 202210447015) for financial support of this research.

Institutional Review Board Statement: Not applicable.

Informed Consent Statement: Not applicable.

Data Availability Statement: The data used to support the findings of this study are available from the corresponding author upon request.

Conflicts of Interest: Author Chenglong Li was employed by the Shandong Weijiao Holding Group Co., Ltd. The remaining authors declare that the research was conducted in the absence of any commercial or financial relationships that could be construed as a potential conflict of interest.

References


1. Nevagi, R.J.; Dighe, S.N.; Dighe, S.N. Biological and medicinal significance of benzofuran. *Eur. J. Med. Chem.* **2015**, *97*, 561–581. [CrossRef]
2. Keri, R.S.; Chand, K.; Budagumpi, S.; Somappa, S.B.; Patil, S.A.; Nagaraja, B.A. An overview of benzo [*b*] thiophene-based medicinal chemistry. *Eur. J. Med. Chem.* **2017**, *138*, 1002–1033. [CrossRef] [PubMed]
3. Khanam, H.; Shamsuzzaman. Bioactive Benzofuran derivatives: A review. *Eur. J. Med. Chem.* **2015**, *97*, 483–504. [CrossRef] [PubMed]
4. Miao, Y.; Hu, Y.; Yang, J.; Liu, T.; Sun, J.; Wang, X. Natural source, bioactivity and synthesis of benzofuran derivatives. *RSC Adv.* **2019**, *9*, 27510–27540. [CrossRef] [PubMed]
5. de Brito, D.H.A.; Almeida-Neto, F.W.Q.; Ribeiro, L.R. Synthesis, structural and spectroscopic analysis, and antiproliferative activity of chalcone derivate (E)-1-(4-aminophenyl)-3-(benzo [*b*] thiophen-2-yl) prop-2-en-1-one in *Trypanosoma cruzi*. *J. Mol. Struct.* **2022**, *1253*, 132197. [CrossRef]
6. Algso, M.A.S.; Kivrak, A. New strategy for the synthesis of 3-ethynyl-2-(thiophen-2-yl) benzo [*b*] thiophene derivatives. *Chem. Pap.* **2019**, *73*, 977–985. [CrossRef]
7. Dhillon, S.; Clarke, M. Tasimelteon: First global approval. *Drugs* **2014**, *74*, 505–511. [CrossRef]
8. Mhoumadi, A.; Elkhatab, M.; Prillieux, S.; Dumas, J.; Collas, F.; Louvain, N.; Fraisse, B.; Espeau, P. Characterization of the heat behavior of amiodarone hydrochloride. *Thermochim. Acta* **2022**, *708*, 179121. [CrossRef]
9. McGovern, B.; Garan, H.; Kelly, E.; Ruskin, J.N. Adverse reactions during treatment with amiodarone hydrochloride. *Br. Med. J. (Clin. Res. Ed.)* **1983**, *287*, 175–180. [CrossRef]
10. Shirley, M. Fruquintinib: First global approval. *Drugs* **2018**, *78*, 1757–1761. [CrossRef]
11. Li, J.; Qin, S.; Xu, R.H. Effect of fruquintinib vs placebo on overall survival in patients with previously treated metastatic colorectal cancer: The FRESCO randomized clinical trial. *JAMA* **2018**, *319*, 2486–2496. [CrossRef]
12. Valkova, S.; Trashlieva, M.; Christova, P. Treatment of vitiligo with local khellin and UVA: Comparison with systemic PUVA. *Clin. Exp. Dermatol.* **2004**, *29*, 180–184. [CrossRef] [PubMed]
13. Berrade, L.; Aisa, B.; Ramirez, M.J.; Galiano, S.; Guccione, S.; Moltzau, L.R.; Levy, F.O.; Nicoletti, F.; Battaglia, G.; Molinaro, G.; et al. Novel Benzo[*b*]thiophene Derivatives as New Potential Antidepressants with Rapid Onset of Action. *J. Med. Chem.* **2011**, *54*, 3086–3090. [CrossRef] [PubMed]

14. Liu, Z.; Xia, Y.; Zhou, S.; Wang, L.; Zhang, Y.; Wang, J. Pd-catalyzed cyclization and carbene migratory insertion: New approach to 3-vinylindoles and 3-vinylbenzofurans. *Org. Lett.* **2013**, *15*, 5032–5035. [CrossRef] [PubMed]
15. Zhang, P.; Wang, C.; Cui, M.; Du, M.; Li, W.; Jia, Z.; Zhao, Q. Synthesis of difluoroalkylated benzofuran, benzothiophene, and indole derivatives via palladium-catalyzed cascade difluoroalkylation and arylation of 1, 6-enynes. *Org. Lett.* **2020**, *22*, 1149–1154. [CrossRef]
16. Liao, J.; Fan, L.; Guo, W.; Zhang, Z.; Li, J.; Zhu, C.; Ren, Y.; Wu, W.; Jiang, H. Palladium-Catalyzed Fluoroalkylative Cyclization of Olefins. *Org. Lett.* **2017**, *19*, 1008–1011. [CrossRef] [PubMed]
17. Kuram, M.R.; Bhanuchandra, M.; Sahoo, A.K. Direct access to benzo [b] furans through Palladium-catalyzed oxidative annulation of phenols and unactivated internal alkynes. *Angew. Chem. Int. Ed.* **2013**, *52*, 4607–4612. [CrossRef] [PubMed]
18. Huang, X.; Rong, N.; Li, P.; Shen, G.; Li, Q.; Xin, N.; Cui, C.; Cui, J.; Yang, B.; Li, D.; et al. AIBN-promoted synthesis of bibenzo [b][1, 4] thiazines by the condensation of 2, 2'-dithiodianiline with methyl aryl ketones. *Org. Lett.* **2018**, *20*, 3332–3336. [CrossRef]
19. Wang, D.; Lu, Q.; Li, Z.; Fang, C.; Liu, R.; Yang, B.; Shen, G. "One-Pot" CuCl₂-Mediated Condensation/C–S Bond Coupling Reactions to Synthesize Dibenzothiazepines by Bi-Functional-Reagent N, N'-Dimethylethane-1, 2-Diamine. *Molecules* **2022**, *27*, 7392. [CrossRef]
20. Liu, G.; Liu, S.; Li, Z.; Chen, C.; Li, J.; Zhang, Y.; Shen, G.; Yang, B.; Hu, X.; Huang, X. Metal-and oxidant-free electrochemically promoted oxidative coupling of amines. *RSC Adv.* **2022**, *12*, 118–122. [CrossRef]
21. Khan, I.; Zaib, S.; Ibrar, A. New frontiers in the transition-metal-free synthesis of heterocycles from alkynoates: An overview and current status. *Org. Chem. Front.* **2020**, *7*, 3734–3791. [CrossRef]
22. Suleymanov, A.A.; Scopelliti, R.; Fadaei Tirani, F.; Severin, K. One-Pot Synthesis of Trisubstituted Triazenes from Grignard Reagents and Organic Azides. *Org. Lett.* **2018**, *20*, 3323–3326. [CrossRef] [PubMed]
23. Li, Y.; Zhan, C.; Yang, B.; Cao, X.; Ma, C. A one-pot transition-metal-free tandem process to 1, 4-benzodiazepine scaffolds. *Synthesis* **2013**, *45*, 111–117.
24. Crystal Data for **5g**: See the Supporting Information. CCDC 2285416 (**5g**) Contains the Supplementary Crystallographic Data for This Paper. These Data Can Be Obtained Free of Charge from The Cambridge Crystallographic Data Centre. Available online: www.ccdc.cam.ac.uk/data_request/cif (accessed on 31 July 2023).
25. Sheldrick, G.M. *SHELX-97. Program for the Refinement of Crystal Structure*; University of Göttingen: Göttingen, Germany, 1997.

Disclaimer/Publisher's Note: The statements, opinions and data contained in all publications are solely those of the individual author(s) and contributor(s) and not of MDPI and/or the editor(s). MDPI and/or the editor(s) disclaim responsibility for any injury to people or property resulting from any ideas, methods, instructions or products referred to in the content.

Article

Structural Characterization and Immunoenhancing Properties of Polysaccharide CPTM-P1 from *Taxus media*

Jiangtao Fan ^{1,2,†}, Xiong Huang ^{1,2,†}, Mengke Dou ^{1,2}, Shuqin Tang ^{1,2}, Gang Wang ^{1,3}, Yijun Fan ¹, Aoxue Luo ¹, Gang Wang ^{1,2,*} and Yong Wang ^{1,2,*} 

¹ National Forestry and Grassland Southwest Engineering Technology Research Centre of Taxus, Sichuan Agricultural University, Dujiangyan 611800, China; jiangtao_fan@163.com (J.F.); huangdoctor226@163.com (X.H.); dmkl5836@163.com (M.D.); tangshuqin2021@163.com (S.T.); wg@cdut.edu.cn (G.W.); yijunfan@163.com (Y.F.); aoxueluo@sina.com (A.L.)

² College of Forestry, Sichuan Agricultural University, Chengdu 611130, China

³ College of Geography and Planning, Chengdu University of Technology, Chengdu 611130, China

* Correspondence: wanggang@sicau.edu.cn (G.W.); wangyong2015@sicau.edu.cn (Y.W.)

† These authors contributed equally to this work.

Abstract: Polysaccharides extracted from *Taxus media* through an aqueous method were further refined by removing proteins via the Sevag technique and purified by dialysis. The separation of these polysaccharides was accomplished using a DEAE-cellulose chromatography column, yielding two distinct fractions, named CPTM-P1 and CPTM-P2. Notably, CPTM-P1 emerged as the primary polysaccharide component within *Taxus media*. Consequently, a comprehensive analysis focusing exclusively on CPTM-P1 was undertaken. The molecular weight of CPTM-P1 was established through gel permeation chromatography (GPC), and its monosaccharide composition was deciphered using HPLC-MS. The structure was further elucidated through nuclear magnetic resonance (NMR) spectroscopy. The molecular weight of CPTM-P1 was determined to be 968.7 kDa. The monosaccharide composition consisted of galactose (Gal), arabinose (Ara), galacturonic acid (Gal-UA), glucose (Glc), rhamnose (Rha), xylose (Xyl), mannose (Man), fucose (Fuc), glucuronic acid (Glc-UA), and ribose (Rib). The proportional distribution of these components was 30.53%, 22.00%, 5.63%, 11.67%, 11.93%, 1.69%, 8.50%, 1.23%, 5.63%, and 1.17%, respectively. This confirmed CPTM-P1 as an acidic heteropolysaccharide with a glycuronic acid backbone. Moreover, CPTM-P1 showed immunoenhancing properties, effectively augmenting the secretion of nitric oxide and cytokines (TNF- α , IL-1 β , and IL-6). Additionally, it significantly enhances the phagocytic capacity of RAW264.7 cells. These findings underscore the potential application of these polysaccharides in functional foods and pharmaceuticals, providing a solid scientific basis for further exploration and utilization of *Taxus media* polysaccharides.

Keywords: *Taxus media*; polysaccharide; structural characterization; immunoenhancing properties



Citation: Fan, J.; Huang, X.; Dou, M.; Tang, S.; Wang, G.; Fan, Y.; Luo, A.; Wang, G.; Wang, Y. Structural Characterization and Immunoenhancing Properties of Polysaccharide CPTM-P1 from *Taxus media*. *Molecules* **2024**, *29*, 1370. <https://doi.org/10.3390/molecules29061370>

Academic Editor: George Grant

Received: 2 January 2024

Revised: 14 March 2024

Accepted: 15 March 2024

Published: 19 March 2024



Copyright: © 2024 by the authors. Licensee MDPI, Basel, Switzerland. This article is an open access article distributed under the terms and conditions of the Creative Commons Attribution (CC BY) license (<https://creativecommons.org/licenses/by/4.0/>).

1. Introduction

Polysaccharides, complex biopolymers consisting of 10 or more monosaccharides linked by glycosidic bonds, stand as some of nature's most prevalent molecules [1]. Research on polysaccharides is expanding due to their potent anti-tumor [2], hypoglycemic [3], antioxidant [4], anti-allergic [5], and immunomodulatory [6] effects, and their capacity to shield cells from inflammatory cytokines [7]. The evaluation of polysaccharides' immunomodulatory capabilities often involves measuring cytokine levels released by macrophages following polysaccharide stimulation [8,9]. Research has underscored polysaccharides' capacity to stimulate macrophages, enhance phagocytosis, and trigger a broad spectrum of cytokine production, including interleukins (IL-1 β , IL-6, IL-8), tumor necrosis factor (TNF- α), and nitric oxide (NO). Specifically, IL-1 β is produced by activated immune cells, playing a crucial role in driving immune and inflammatory responses, including

fever induction, immune cell activation, and inflammation mediation. IL-6, a key marker of acute inflammation, is secreted by various cells and is pivotal in immune regulation, inflammation, cell growth, and differentiation. IL-8, primarily released by macrophages and endothelial cells, acts as a chemoattractant that directs white blood cells, especially neutrophils, to inflammation sites, playing a significant role in both inflammation and immune regulation [10,11]. Consequently, these actions reinforce the organism's immune response [10–13]. Certain plant polysaccharides are capable of augmenting the secretion of nitric oxide (NO) and cytokine synthesis of cytokines, thereby enhancing the efficacy of macrophages in combating pathogenic microorganisms and tumors [14]. Nitric oxide is a key effector molecule produced by macrophages, which upon activation, release various chemotactic factors and cytokines crucial for activating immune responses and modulating the immune system [15]. Activated macrophages play an important role in TNF- α generating, serving as a pivotal cytokine in anti-tumor immune responses and an essential indicator of macrophage activity [16]. IL-6 plays a versatile role in immune defense, underscoring the complex interactions within the immune system [17].

The plant kingdom boasts a rich diversity of polysaccharides. Previous studies have successfully isolated polysaccharides from a variety of plants, including *Ziziphus jujuba* [18], *Astragalus membranaceus* [19], *Panax ginseng* [4], and persimmon [7], demonstrating their potent immunomodulatory and outstanding antioxidant activities in vitro. In the genus *Taxus*, significant research efforts have yielded notable findings. Complex water-soluble polysaccharide (T1) and a singular polysaccharide component (CPTC-2) were isolated from the branches and leaves of *Taxus chinensis* [20,21]. Additionally, TCFPs, a polysaccharide from *T. chinensis* fruits, exhibited significant tumor growth inhibition [22]. Two novel water-soluble polysaccharides with anticancer properties, TMP70S-1 and TMP70W, were identified in the branches and leaves of *Taxus yunnanensis* [23,24]. *Taxus cuspidata* yielded four polysaccharides (Pe1, Pe2, Pe3, and Pe4), with Pe4 exhibiting the strongest anti-tumor and glucosidase inhibitory properties [25]. Moreover, these studies also revealed that *Taxus* polysaccharides exhibit minimal toxic side effects and potent pharmacological effects. They can reduce the dosage of chemotherapy drugs, thereby lowering the toxic side effects of chemotherapy. As a result, they present themselves as promising adjunctive medications for clinical chemotherapy in cancer patients, showcasing excellent prospects for medicinal use [22–25]. Despite these advancements, research into the unique polysaccharides found in *Taxus media* branches and leaves, particularly their immunoenhancing properties, remains unpublished, presenting a gap in the development of therapeutic polysaccharides.

This study focused on analyzing the molecular weight, monosaccharide composition, and glycan chain structure of CPTM-P1. Additionally, it aimed to explore its immunoenhancing properties using RAW 264.7 macrophage cells. This dual approach seeks to deepen our understanding of CPTM-P1's structural and biological characteristics.

2. Results and Discussion

2.1. Isolation and Purification of Polysaccharides from *T. media*

Through a process of staged elution with a NaCl solution, two distinct polysaccharide components were obtained, named CPTM-P1 and CPTM-P2, as illustrated in Figure 1. CPTM-P1 was isolated using a wash with 0.1 M NaCl, while CPTM-P2 was separated using 0.2 M NaCl. Among these components, CPTM-P1 constitutes the largest fraction and is identified as the predominant polysaccharide in *T. media*. Consequently, the focus of this study will be primarily on CPTM-P1, aiming to delve into the structural characteristics and immuno-enhancing properties of this polysaccharide. CPTM-CP, the crude polysaccharide extract from *T. media*, serves as the basis for isolating these components.

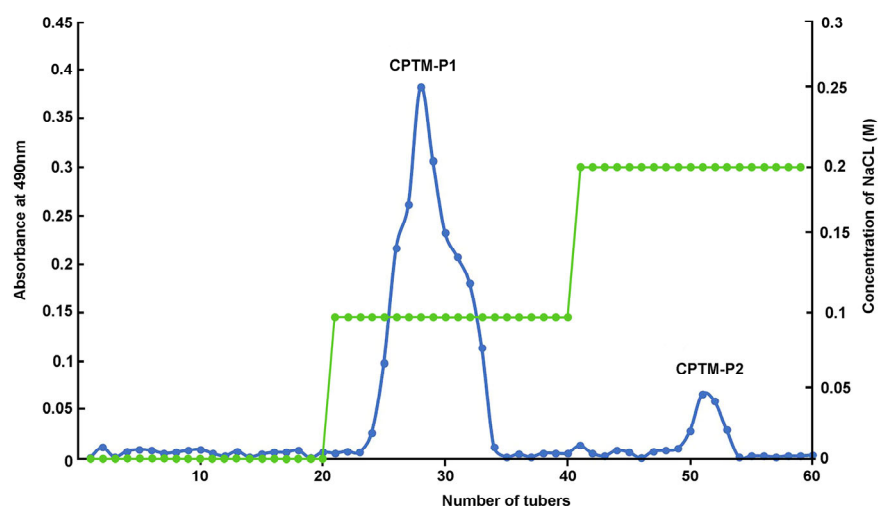


Figure 1. Chromatography of eluted crude polysaccharide (CPTM-CP) on a DEAE-cellulose column (26 mm × 300 mm). CPTM-P1 eluted with 0.1 M NaCl; CPTM-P2 eluted with 0.2 M NaCl.

2.2. Analysis of Structural Characteristics of Polysaccharides

2.2.1. Molecular Weight Analysis

The molecular weight (Mw) of polysaccharides plays a critical role in defining their properties, which largely depend on their molecular dimensions [26]. Typically, the distribution of Mw is represented by an average value. The Mw and purity of polysaccharide samples were determined using Gel Permeation Chromatography (GPC) and analyzed with Empower software (v3.8.0), as shown in Figure 2. This analysis revealed that CPTM-P1 has a molecular weight of 968.7 kDa, a polydispersity index (PDI) of 1.126, and a purity of 79%. It has been demonstrated that polysaccharides with different molecular weights possess distinct biological functions. For example, fucoidan with a lower molecular weight (<50 kDa) exhibits stronger immunomodulatory effects compared to those with a higher molecular weight (>100 kDa) [27,28]. Similarly, the high molecular weight polysaccharide from persimmon, DK-H (>345 kDa), shows enhanced physiological effects, including antioxidative, anti-inflammatory, and anti-wrinkle properties, unlike its low molecular weight counterpart, DK-L (<1 kDa) [7].

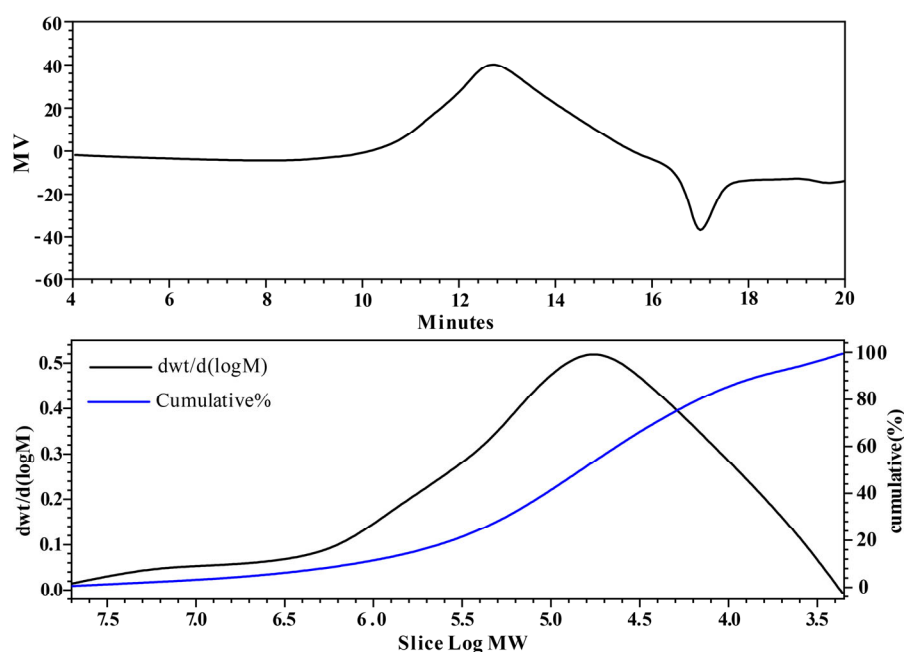


Figure 2. Analysis of CPTM-P1 polysaccharide by GPC.

Research has consistently shown that polysaccharides with higher molecular weights tend to have greater pharmacological efficacy than those with lower molecular weights [29,30]. However, it is imperative to acknowledge that certain low molecular weight polysaccharides (<10 or 30 kDa) have been reported to lack biological activity under specific circumstances [31]. The polysaccharide CPTM-P1 (968.7 kDa) investigated in this study exhibits a greater molecular weight in comparison to the *T. chinensis* polysaccharide CPTC-2 (73.53 kDa), and the *T. yunnanensis* polysaccharides TMP70W (36.94 kDa) and TMP70S-1 (17.37 kDa). This molecular weight difference suggests the potential for heightened biological activity in CPTM-P1 [20,23,24]. In summary, the molecular weight of polysaccharides assumes an important role in shaping their biological activities.

2.2.2. Infrared Spectrum Analysis

Fourier-transform infrared (FT-IR) spectroscopy is an essential technique in organic and polymer chemistry, allowing for the quantitative analysis of specific compounds through infrared spectroscopy [32]. This method was employed to examine the functional groups and sugar chain structure of CPTM-P1. The FT-IR spectrum of CPTM-P1, depicted in Figure 3, features a pronounced broad peak between $3600\text{--}3200\text{ cm}^{-1}$, indicative of the stretching vibrations of hydroxyl (--OH) groups within the sugar units. This observation suggests the presence of both intermolecular and intramolecular hydrogen bonds. The weak C–H absorption seen between $3000\text{--}2800\text{ cm}^{-1}$, coupled with an absorption peak in the $1400\text{--}1200\text{ cm}^{-1}$ range signaling C–H bending vibrations, confirms that CPTM-P1 is a polysaccharide. Typically, saccharide hydrates display characteristic absorption peaks within $1665\text{--}1635\text{ cm}^{-1}$, a feature also observed in the CPTM-P1 polysaccharide spectrum. Moreover, distinct peaks at 1223 cm^{-1} and 1078 cm^{-1} signify the presence of pyran rings in CPTM-P1's structure. Furthermore, a peak at 746 cm^{-1} delineates the α -configuration of this polysaccharide, providing insights into its molecular architecture.

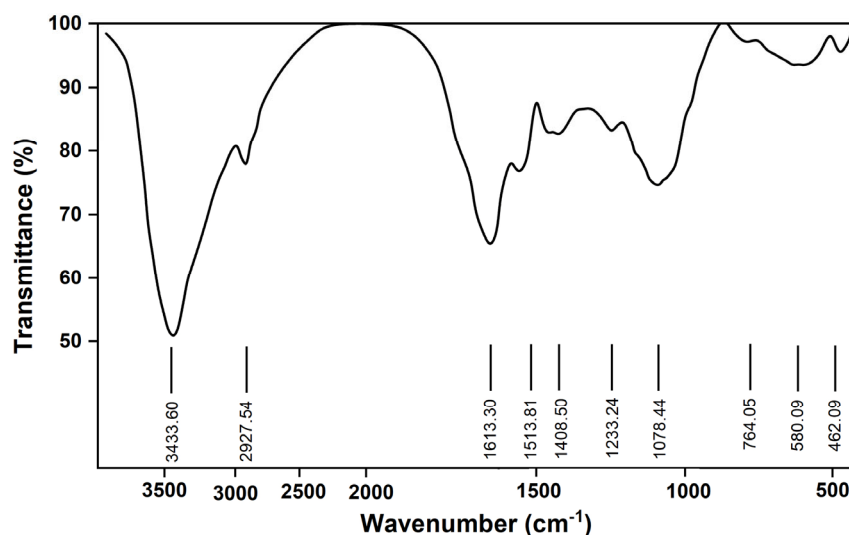


Figure 3. FTIR analysis of CPTM–P1 polysaccharide from *T. media*.

2.2.3. Monosaccharide Analysis

Ten different monosaccharides were identified in CPTM-P1. Which included Fuc, Ara, Rha, Gal, Glc, Xyl, Man, Rib, Gal-UA, and Glc-UA. Fru, Gul-UA, and Man-UA were not detected (Table 1). Notably, Gal emerged as the most predominant constituent. Following Gal, Gal-UA exhibited a content of 27.42 mg/g, while Ara demonstrated a concentration of 26.24 mg/g, and Rha exhibited a measure of 14.23 mg/g. Similarly, Glc and Man registered values of 13.92 mg/g and 10.14 mg/g, respectively. Conversely, the remaining monosaccharides were characterized by diminutive peak areas, indicating the relatively

marginal abundance of their respective CPTM-P1 polysaccharide constituents (less than 10 mg/g).

Table 1. Monosaccharide composition of CPTM–P1.

Monosaccharide	Content (mg/g)	Percentage (%)
Gal	36.42	30.53
Ara	26.24	22.00
Rha	14.23	5.63
Glc	13.92	11.67
Gal-UA	27.42	11.93
Xyl	2.01	1.69
Fuc	1.47	8.5
Man	10.14	1.23
Rib	1.4	5.63
Glc-UA	6.72	1.17

Research has established a strong correlation between the structural features and pharmacological activities of polysaccharides [33]. Complex carbohydrates include galacturonic and gluturonic acids in their structure [34]. Findings suggest that Gal-UA may have anti-inflammatory effects and play a role in immune response regulation. Additionally, the amount of Ara in polysaccharides is positively associated with their immune activity [35]. CPTM-P1 contains elevated levels of both Gal-UA and Ara, which could potentially account for the observed immune activity of CPTM-P1. The presence of glyoxylate residues has the capacity to alter the physicochemical properties and solubility of associated polysaccharide couplings, thereby influencing the activity of plant polysaccharides [36]. Fractions characterized by a higher glyoxalate content demonstrate heightened antioxidant activity. Specifically, ZSP3c and ZSP4b, featuring the highest glyoxalate content among date polysaccharide fractions, exhibit the most robust in vitro antioxidant activity [37]. Galactose also influences the immune-modulating activity of polysaccharides; research has identified galactose in *A. membranaceus* polysaccharides as the primary factor responsible for immune-regulatory activity [38]. Another study has shown that polysaccharides with a higher galactose (Gal) content exhibit superior immune-modulating activity [39]. CPTM-P1 also has a significant galactose content, suggesting its activity may be closely related to its glyoxalate and galactose levels. Furthermore, pumpkin polysaccharides, which include glucuronic acid, show that higher concentrations of glucuronic acid correlate with increased biological activity. Among pumpkin polysaccharides, WPP2, which has the highest glyoxalate content, demonstrated superior activity compared to WPP0, WPP1, and WPP3 [40]. However, CPTM-P1 contains an equal amount of galacturonic and glucuronic acids, possibly contributing to its immunomodulatory properties. Polysaccharides in plants exist in a variety of forms, such as pectic polysaccharides. Pectic polysaccharides usually contain components such as Galactose (Gal), Arabinose (Ara), Galacturonic acid (Gal-UA), etc., so, based on the composition of the monosaccharides, we hypothesized that the CPTM-P1 polysaccharides might belong to the category of pectic polysaccharides. In plant cell walls, various substances, including cellulose, hemicellulose, and pectin, are present [41]. Although our study's crude polysaccharide extract includes a mix of cellulose, hemicellulose, and starch, the active polysaccharides isolated and purified did not react with Congo red for cellulose or iodine for starch, excluding them as cellulose, pectin, or starch components.

2.2.4. Nuclear Magnetic Resonance (NMR) Analysis

To delve deeper into the molecular architecture of CPTM-P1, a detailed nuclear magnetic resonance (NMR) spectroscopy analysis was performed. Figure 4 shows the ^1H NMR and ^{13}C NMR spectra of CPTM-P1. In the ^1H NMR spectrum, most of the signals appeared in the range of 4.8–5.5 ppm. Typically, an anomeric signal above 4.9 ppm indicates an

α -configuration, whereas a signal falling below 4.9 ppm indicates a β -configuration [42,43]. Evidently, the allosteric signal in CPTM-P1's ^1H spectrum is located around 5.0 ppm (Figure 4A). Therefore, CPTM-P1 has an α -configuration. In the ^{13}C spectrum, resonances within 50–85 ppm correspond to carbons at positions C-2 to C-6 (Figure 4B). Characteristic signals arising from the carboxyl groups are discernible within the spectral region of 165–180 ppm. Specifically, the distinct peaks at 177.848 ppm and 167.858 ppm in CPTM-P1's carbon spectrum indicate $-\text{CO}$ signals inherent to the $-\text{COOH}$ moiety. This resonance pattern serves to confirm the presence of uronic acids within the molecular composition of CPTM-P1; a deduction further substantiated by the findings of HPLC-MS analysis. It is well known that the type of glycosidic linkage plays a crucial role in determining the immunomodulatory activity of polysaccharides [44]. For example, the anti-inflammatory efficacy of *Poria cocos* polysaccharides has been linked to a 1,3- α -d-Galp backbone and 1,6- α -d-Galp branches [45]. Although the sugar chains in CPTM-P1 exhibit similarities, future research must investigate the specific linkage patterns within CPTM-P1 and their influence on immunomodulatory activity.

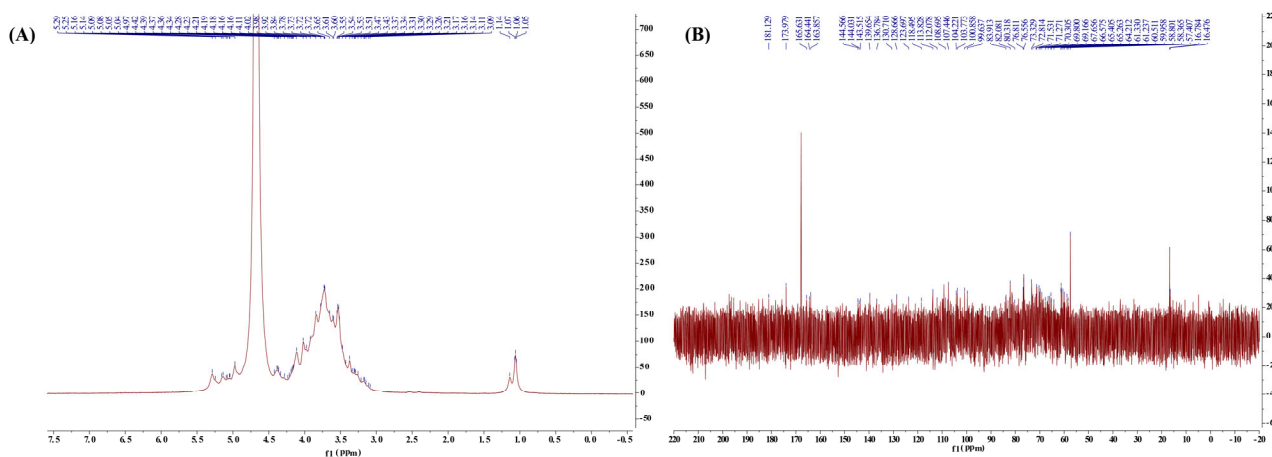


Figure 4. NMR analysis results. (A) is the ^1H NMR of CPTM-P1, (B) is ^{13}C NMR of CPTM-P1.

Drawing upon the existing literature [46–48], our deductions ascertain the principal occurrence of the indicated glycan chains within the constitution of CPTM-P1 (refer to Table 2). However, due to the constraints imposed by the finite data yielded by NMR, certain glycan chains characterized by lower prevalence could not be definitively resolved.

Table 2. Chemical shifts in the ^1H NMR and ^{13}C NMR of CPTM-P1.

Glycosyl Residues	Chemical Shift H/C (ppm)					
	H ₁ /C ₁	H ₂ /C ₂	H ₃ /C ₃	H ₄ /C ₄	H ₅ /C ₅	H ₆ /C ₆
α -D-Galp-(1→	5.12/99.52	3.80/68.68	3.89/69.37	4.024/70.36	4.12/70.69	3.71/61.36
→6)- α -D-Glcp-(1→	5.12/99.52	3.62/76.71	3.71/73.72	3.55/70.36	3.96/70.69	4.07/67.01
→1-(α -L-Rhap-(2→	5.30/95.47	4.14/76.71	3.96/69.37	3.40/73.37	3.80/68.88	1.14/16.78
→1)- α -L-Araf-(5→	5.12/107.54	4.14/78.74	4.07/76.71	4.18/82.08	3.96/68.88	-
α -D-Manp-(1→	5.12/99.52	4.07/70.36	3.87/70.69	3.71/68.68	3.78/73.72	4.02/61.33
→2)- α -D-Manp-(1→	5.30/99.52	4.07/78.74	4.00/70.69	3.67/68.68	3.71/73.72	3.80/61.33
→4)- α -GalpA-(1→	4.99/99.52	3.89/70.69	4.12/73.37	4.36/78.74	4.68/73.77	177.848
α -D-GlcAp-(-1→	5.30/99.52	3.62/73.72	3.71/76.71	3.55/73.72	4.02/73.37	-

2.2.5. SEM Analysis Results

Utilizing Scanning Electron Microscopy (SEM) enables the acquisition of high-resolution data on surface topography, providing detailed insights into the particle size, shape, and surface characteristics of polysaccharides. This information is pivotal for understanding the spatial arrangement and structural details of these biomolecules [39,40]. Consequently, SEM

was used to examine the structure and spatial organization of the CPTM-P1 surface. The SEM images (Figure 5) reveal that the CPTM-P1 polysaccharide surface is predominantly smooth and features convex, semi-circular particles within a notable layered structure. This observation suggests that the polysaccharide's branched monomers are intricately intertwined, predominantly existing in states of aggregation and coiling.

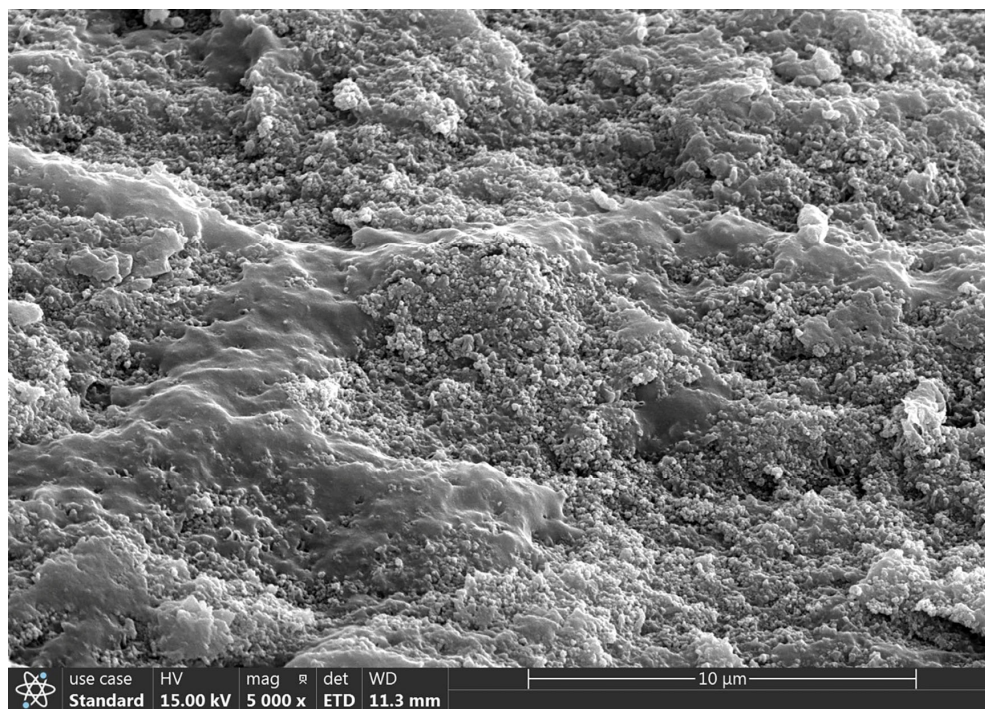


Figure 5. Morphology observation of CPTM–P1 polysaccharide under SEM.

2.3. Effect of CPTM-P1 on RAW264.7 Cell Immunoreactivity

2.3.1. Effect of CPTM-P1 on RAW264.7 Cell Proliferation

The effects of CPTM-P1 on RAW264.7 cells proliferation are shown in Figure 6A. When compared to the control group (CK), the stimulation of RAW264.7 cell proliferation by CPTM-P1 exhibited a trend of increase in line with rising concentrations, peaking at 1.0 mg/mL. However, there were no statistically significant differences between the experimental groups at varying concentrations and the control group ($p > 0.05$). This finding supports the conclusion that CPTM-P1, within a concentration range up to 4.0 mg/mL, does not show cytotoxic effects on RAW264.7 cells. The optimal conditions for polysaccharide intervention are often established by evaluating their effects on cell viability [49]. The investigation revealed that within the concentration range of 0.25–4 mg/mL, there existed a direct relationship between the concentration and the proliferation rate of RAW 264.7 cells, reaching its zenith at 1.0 mg/mL. Notably, even at the highest concentration of 4 mg/mL, no statistically significant distinction was discerned between the control group and the experimental group. These results indicate that, within a specific concentration range, CPTM-P1 does not induce cytotoxic effects on RAW 264.7 cells.

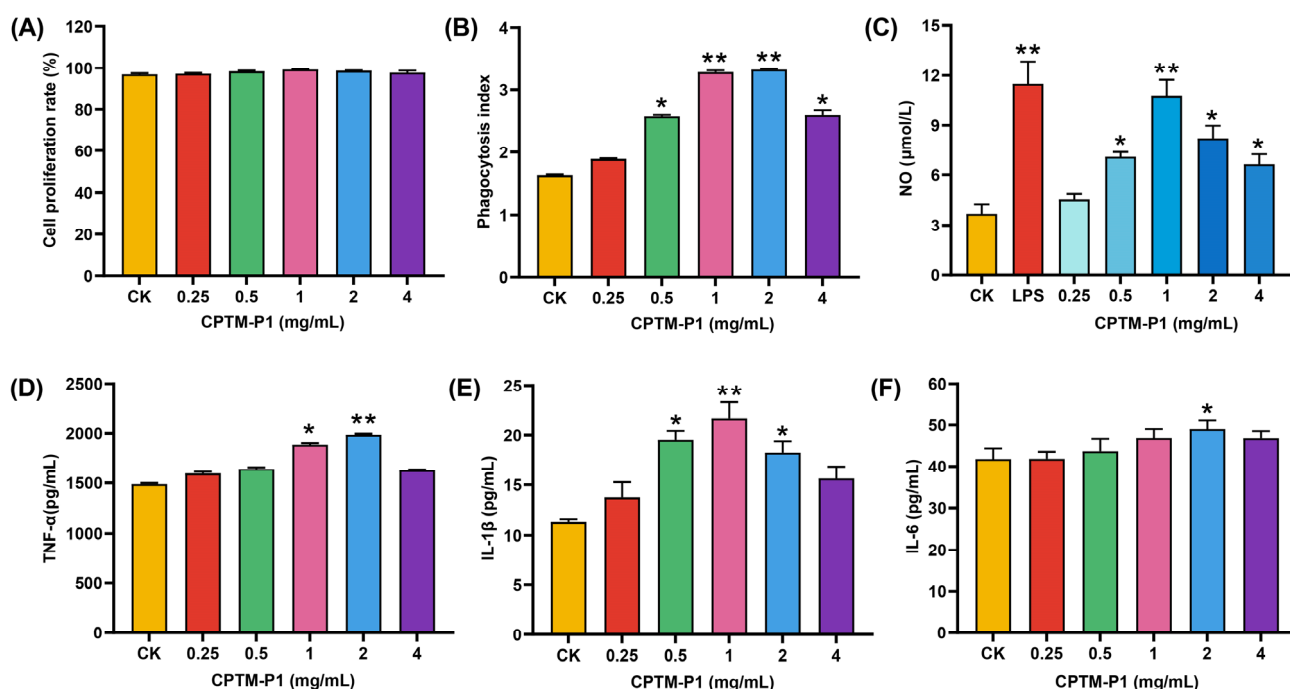


Figure 6. (A) Effects of different concentrations of CPTM–P1 on the proliferation of RAW264.7 cells; (B) effect of CPTM–P1 on phagocytosis of RAW264.7 cells; (C) detection of NO release from RAW264.7 cells in response to CPTM–P1, the concentration of LPS was 0.5 $\mu\text{g/mL}$. ELISA detection of (D) TNF- α , (E) IL-1 β and (F) IL-6. * indicated $p < 0.05$; ** indicated $p < 0.01$.

2.3.2. Effect of CPTM-P1 on RAW264.7 Cell Phagocytosis

Data on the impact of different polysaccharide concentrations on RAW264.7 cell phagocytosis is presented in Figure 6B. The findings underscore that all concentrations of the polysaccharide CPTM-P1 elicited a discernible enhancement in the phagocytic efficacy of RAW264.7 cells. The cellular phagocytic activity reached its zenith at a concentration of 2.0 mg/mL ($p < 0.01$), followed by a modest decline in phagocytic activity.

2.3.3. CPTM-P1 Effect on NO, TNF- α , IL-1 β , and IL-6 Production

Activated macrophages perform dual functions: they secrete cytokines and synthesize nitric oxide (NO). In this research, we further explored NO secretion by RAW264.7 cells activated with the polysaccharide CPTM-P1 and LPS, as shown in Figure 6C. Notably, LPS significantly elevated NO levels in RAW264.7 cells. The introduction of varying concentrations of CPTM-P1 led to increase NO secretion, with the effect intensifying at higher polysaccharide concentrations. This increase was most significant at 1.0 mg/mL, equating the effect to that of the LPS positive control. Beyond this concentration, a slight decline in NO production was noted.

The study also examined the effects of CPTM-P1 on the secretion of TNF- α , IL-1 β , and IL-6 by RAW264.7 cells, considering the critical roles these cytokines play in inter-cellular communication, immune cell regulation, and inflammatory responses (Figure 6D–F). The data reveal that varying CPTM-P1 concentrations differently influenced TNF- α , IL-1 β , and IL-6 levels in the cell culture supernatant. A pattern emerged where cytokine concentrations initially increased and then decreased, with TNF- α and IL-6 peaking at 2.0 mg/mL ($p < 0.05$), and IL-1 β peaking at 1.0 mg/mL ($p < 0.05$). Past these peaks, a slight decrease in cytokine levels was observed. These results collectively suggest that CPTM-P1 enhances the immunomodulatory capacity of RAW264.7 cells by stimulating the secretion of TNF- α , IL-1 β , and IL-6.

One study shows that lipopolysaccharides (LPS) trigger immune stress can incite immune stress by stimulating host immune cells to produce nitric oxide (NO) and cytokines,

including tumor necrosis factor- α (TNF- α), interleukin-1 β (IL-1 β), and interleukin-6 (IL-6) [50]. Due to their capability to release NO, activated RAW264.7 cells are frequently used to evaluate the immunomodulatory activity of compounds [27]. Thus, LPS-treated RAW 264.7 cells served as a positive control for assessing the immunomodulatory potential of CPTM-P1. Significantly, CPTM-P1 induced NO release from RAW 264.7 cells and increased levels of TNF- α , IL-1 β , and IL-6, indicating that CPTM-P1 can activate macrophages and elicit immune responses akin to LPS. This aligns with observations of polysaccharides from sweet cherry, berries, *Cucurbita moschata*, and lavender, which also modulate immune function by activating macrophages [51–54]. While CPTM-P1's immunomodulatory effects are confirmed, further investigation into its mechanistic pathways is necessary.

2.4. Endotoxin Contamination

Extracting polysaccharides from plants carries a risk of endotoxin contamination, which can falsely enhance immune stimulation assays due to the potent macrophage activation by endotoxins [55,56]. To confirm that CPTM-P1's immunomodulatory effects were not due to endotoxin contamination, we treated CPTM-P1 with polymyxin B and evaluated its activity in RAW264.7 cells. As depicted in Figure 7, the solution of lipopolysaccharide (LPS) (0.5 $\mu\text{g}/\text{mL}$), after passing through a polymyxin B affinity column, exhibited a nearly complete reduction in nitric oxide-induced activity. This suggests that the polymyxin B affinity column effectively absorbed almost all of the LPS. However, the CPTM-P1 solution (1 mg/mL) passed through the polymyxin B affinity column did not exhibit a significant reduction in nitric oxide-induced activity. To eliminate the potential interference of unknown substances in the CPTM-P1 solution with the formation of the polymyxin B complex, CPTM-P1 was mixed with LPS, passed through a polymyxin B affinity column, and then assessed for nitric oxide-induced activity in RAW264.7 cells. The results, as shown in Figure 7, indicate that the column effectively eliminated LPS from the mixture, confirming that CPTM-P1's immunomodulatory effects are not due to endotoxin contamination.

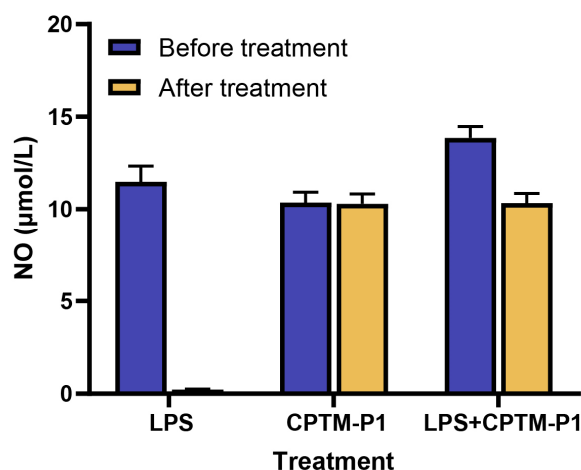


Figure 7. Effects of polymyxin B treatment. LPS (0.5 $\mu\text{g}/\text{mL}$), CPTM-P1 (1 mg/mL), or an LPS (0.5 $\mu\text{g}/\text{mL}$) and CPTM-P1 (1 mg/mL) mixture was added to the polymyxin B-affinity column, incubated overnight at 4 $^{\circ}\text{C}$, eluted from the column by centrifugation, and then added to the cultures of RAW264.7 cells (final, 1:80 dilution) for 2 days. The amounts of nitric oxide were measured using a Griess reagent.

3. Materials and Methods

3.1. Materials and Chemicals

Branches and leaves of *Taxus media* were collected in November 2022 from Xudu Garden, Dujiangyan, Sichuan, China, and were authenticated by Professor Xiaohong Chen from Sichuan Agricultural University. The specimens were archived at the National Forestry and Grassland Administration Southwest Engineering Technology Research Center for

Taxus at Sichuan Agricultural University. The MTT kit, along with mouse TNF- α , IL-1 β , and IL-6 ELISA kits, were acquired from Beijing Solabao (Beijing, China). RPMI 1640 medium and phosphate-buffered saline (PBS) for cell immunoreactivity assays were sourced from Thermo Fisher Scientific (Waltham, MA, USA), while trypsin and penicillin were obtained from Wistent (Saint-Jean-Baptiste, QC, Canada). Fetal bovine serum (FBS) was procured from Lanzhou Bailing Company (Lanzhou, China). DEAE-cellulose was purchased from (Sigma Chemical, St. Louis, MO, USA). Kormas Brilliant Blue G-250 and Trifluoroacetic acid (TFA) were purchased from (Chengdu Kelong Chemical Company, Chengdu, China). The Congo red reagent and iodine solution were purchased from Beijing Solebo. Monosaccharide standards including fucose (Fuc), arabinose (Ara), rhamnose (Rha), galactose (Gal), glucose (Glc), xylose (Xyl), mannose (Man), fructose (Fru), ribose (Rib), galacturonic acid (Gal-UA), glucuronic acid (Glc-UA), mannuronic acid (Man-UA), and guluronic acid (Gul-UA) were obtained from the Sigma-Aldrich Chemical Co. (St. Louis, MO, USA).

3.2. General Methods

Determination of CPTM-CP total sugars was conducted by the phenol-sulphuric acid method using glucose as a standard [7]. An HP-GPC system with tandem UltrahydrogelTM2000 and UltrahydrogelTM250 columns was used to analyze the molecular weight of CPTM-P1. A Fourier-transform IR spectrophotometer (Perkin-Elmer Corp., Waltham, MA, USA) was used to scan FTIR spectra. A Thermo ICS5000 (Thermo Fisher Scientific Corp., USA) ion chromatography system with a Dionex CarboPac PA20 (150 \times 3.0 mm, 10 μ m) liquid chromatography column was used for HPLC-MS.

3.3. Extraction, Isolation, and Purification of CPTM-P1

Three hundred grams of powdered *Taxus media* branches and leaves were initially treated with petroleum ether and 80% ethanol to remove fat-soluble substances, alcohol-soluble impurities, monosaccharides, and oligosaccharides. This was followed by triple water extractions to eliminate remaining impurities. Proteins were then removed using Sevag reagent (n-butanol: chloroform = 1:4). This procedure was repeated until the supernatant no longer exhibited absorption peaks at 260 and 280 nm, indicating complete protein removal, thereby allowing progression to the next phase. The extract was mixed with anhydrous ethanol and left to precipitate overnight at 4 $^{\circ}$ C. The resulting precipitate was collected, sequentially washed with ethanol, acetone, ethyl acetate, and anhydrous ethanol, then dissolved in distilled water, decolorized with activated charcoal, filtered, and finally collected. A freeze dryer was employed to produce the crude polysaccharide. A 1.000 g sample of CPTM-CP was dissolved in 40 mL of distilled water and filtered through a 0.45-micrometer membrane. The filtrate was then applied to a DEAE-cellulose column (2.6 \times 30 cm). The column underwent washing with water and two concentrations of sodium chloride, maintaining a flow rate of 1 mL/min at room temperature. After washing, two distinct polysaccharide fractions, CPTM-P1 and CPTM-P2, were isolated via phased elution. The DEAE profile was analyzed using the phenol-sulfuric acid method. The entire extraction and purification process is detailed in Figure 8.

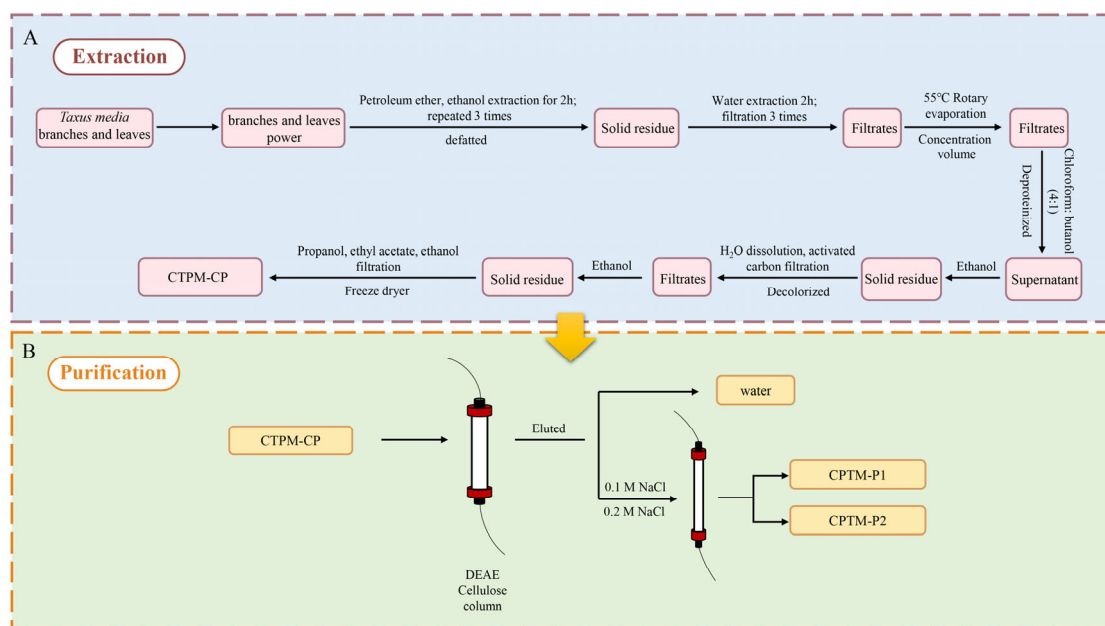


Figure 8. Extraction and purification flowchart of CPTM–P1 from *Taxus media*. (A) is the extraction flowchart, and (B) is the purification flowchart.

3.4. Analysis of Gel Permeation Chromatograph (GPC)

For GPC analysis, a total of 5.0 mg of the sample was dissolved in ddH₂O for GPC analysis. The analysis was conducted using a Waters ultra-hydrophilic linear column (300 × 7.8 mm) at room temperature, with 0.2 M phosphoric acid buffer for elution at a flow rate of 0.70 mL/min. The standard reference for calibration ranged from dextran molecules of 2500 Da to 2,000,000 Da [43].

3.5. Monosaccharide Analysis

A 5 mg sample of the CPTM-P1 polysaccharide was hydrolyzed with trifluoroacetic acid (TFA) at 121 °C for two hours. Post-hydrolysis, the sample was washed with methanol two to three times, dried under a stream of nitrogen gas, and reconstituted in sterile water for analysis. Ion chromatography was used to analyze the monosaccharide fraction after adding sterile water to the dry powder. The liquid chromatography column used was a Dionex™ CarboPac™ PA20 (150 × 3.0 mm, 10 μm). The injection volume was 5 μL. The chromatographic conditions were: mobile phase A (0.1 M NaOH), mobile phase B (0.1 M NaOH, 0.2 M NaAc), flow rate 0.5 mL/min; column temperature 30 °C; elution gradient: 0 min A-phase/B-phase (95:5 v/v), 30 min A-phase/B-phase (80:20 v/v), 30.1 min A-phase/B-phase (60:40 v/v), 45 min A-phase/B-phase (30.1 min A-phase/B-phase). (30 min A-phase/B-phase, 80:20 v/v, 30.1 min A-phase/B-phase, 45 min A-phase/B-phase, 45.1 min A-phase/B-phase, 60 min A-phase/B-phase, 95:5 v/v). The monosaccharide standards, including fucose (Fuc), arabinose (Ara), rhamnose (Rha), galactose (Gal), glucose (Glc), xylose (Xyl), mannose (Man), fructose (Fru), ribose (Rib), galacturonic acid (Gal-UA), glucuronic acid (Glc-UA), mannuronic acid (Man-UA), and guluronic acid (Gul-UA), were obtained from the Sigma-Aldrich Chemical Co. (St. Louis, MO, USA). The identification and quantification of different sugars were achieved, respectively, by comparing the retention time and peak area with those of monosaccharide standards.

3.6. Fourier-Transform Infrared (FT-IR) Analysis

For the FT-IR analysis, purified CPTM-P1 was mixed with potassium bromide (KBr) powders in a 1:20 weight ratio (*w/w*), ground thoroughly, and pressed into thin pellets. These were then analyzed using a Fourier Transform Infrared Spectrophotometer (Perkin-Elmer Corp., USA) across a frequency range of 500–4000 cm^{−1} to record the FT-IR spectra.

3.7. Nuclear Magnetic Resonance Spectroscopy (NMR) Analysis

NMR spectroscopy, known for its high-resolution capability in elucidating molecular structures, was utilized to examine CPTM-P1 in detail. Fifty milligrams of CPTM-P1 were dissolved in 0.5 mL of deuterium oxide (D₂O) and lyophilized three times. The lyophilized sample was redissolved in 0.5 mL of D₂O and analyzed in an NMR tube using a Bruker AVANCE IIIHD 600 spectrometer (Bruker, Rheinstetten, Germany) at 600 MHz for both ¹H-NMR and ¹³C-NMR at 25 °C. Acetone served as the internal standard for ¹³C NMR, with chemical shifts reported in parts per million (ppm).

3.8. Scanning Electron Microscope (SEM) Analysis

For SEM analysis, the dried CPTM-P1 polysaccharide underwent ion sputtering to ensure electron conductivity. The coated sample was examined under a scanning electron microscope set to an acceleration voltage of 15 kV and magnifications ranging from 1000 to 10,000×. This SEM analysis facilitated a detailed observation and documentation of the poly-saccharide's surface characteristics.

3.9. Measurement of Anti-Inflammatory Activity In Vitro

3.9.1. Culture of RAW264.7 Cells

RAW264.7 cells were sourced from Procell Life Science & Technology (Wuhan, China). The cells were cultured in Dulbecco's modified Eagle's medium (DMEM, Gibco, Beijing, China) supplemented with 10% (*v/v*) fetal bovine serum (FBS, Biological Industries, Bioind, Kibbutz Beit, Israel), 100 U/mL penicillin, and 100 µg/mL streptomycin. The cell culture was maintained at 37 °C in a 5% CO₂ atmosphere.

3.9.2. RAW264.7 Cell Proliferation and Phagocytic Capacity Analysis

RAW264.7 cells in the logarithmic growth phase were diluted and plated in 96-well plates at a density of 6×10^4 cells per well, with 100 µL of cell suspension per well. The blank control received fresh medium only. Each concentration gradient had triplicate wells. After 24 h of incubation at 37 °C in 5% CO₂, the supernatant was discarded, and wells were treated with 100 µL of varying concentrations (0.25, 0.5, 1, 2, and 4 mg/mL) of the polysaccharide CPTM-P1 solution, while controls received fresh medium. Following an additional 24-hour incubation, cell proliferation was assessed using the MTT assay, with optical density (OD) measured at 490 nm. For phagocytic capacity analysis, cells were washed with phosphate-buffered saline (PBS) and stained with 0.075% neutral red for 1 h. After staining, wells were rinsed with PBS and lysed with an ethanol acetate solution (1:1 *v/v*), left overnight at room temperature. The OD was measured at 492 nm to evaluate the cells' phagocytic capacity.

3.9.3. Analysis of RAW264.7 Cell's Secretion Ability of TNF- α , IL-1 β , IL-6, and NO

Macrophages, maintained in a favorable growth condition at a density of 6×10^4 cells/mL, were subjected to incubation with 0.5 µg/mL of lipopolysaccharide (LPS) along with various concentrations of CPTM-P1 (0.25, 0.5, 1, 2, and 4 µg/mL) as a positive control. This incubation process took place at 37 °C for a duration of 24 h. The culture supernatant was collected, and the levels of TNF- α , IL-1 β , and IL-6 were determined using an enzyme-linked immunosorbent assay (ELISA). The content of nitric oxide (NO) in the RAW264.7 cell culture supernatant was assessed using the Griess method.

3.10. Removal of Endotoxin

To mitigate the potential impact of endotoxin contamination on the immunomodulatory activity of CPTM-P1, Affi-Prep Polymyxin Matrix (BIO-RAD, Hercules, CA, USA) was employed to remove potential endotoxin contaminants in CPTM-P1. Initially, 1 mL of Affi-Prep Polymyxin Matrix was packed into a Bio-spin column (BIO-RAD) and centrifuged at $300 \times g$ for 3 min. Subsequently, 1 mL of CPTM-P1 (1 mg/mL), LPS (0.5 µg/mL), or a mixture of CPTM-P1 (1 mg/mL) and LPS (0.5 µg/mL) was added. After overnight incuba-

tion at 4 °C, the liquid eluted under the same centrifugation conditions was collected from the recovered chromatography column, which was performed in three biological replicates.

3.11. Statistical Analysis

Statistical analysis was performed using IBM SPSS version 27.0. Each experiment was independently conducted three times, with results expressed as mean \pm standard deviation. Differences between groups were evaluated using a one-way analysis of variance (ANOVA), with statistical significance set at $p < 0.05$ or $p < 0.01$.

4. Conclusions

In this study, we successfully isolated and purified a *Taxus media* polysaccharide, CPTM-P1, and meticulously characterized its molecular attributes (Figure 1). Employing high-performance gel permeation chromatography (HP-GPC) and high-performance liquid chromatography-mass spectrometry (HPLC-MS), we ascertained CPTM-P1's molecular weight to be 968.7 kDa, with a composition rich in monosaccharides like galactose (Gal), galacturonic acid (Gal-UA), and arabinose (Ara). Nuclear magnetic resonance (NMR) spectroscopy further detailed the structural intricacies of CPTM-P1's sugar chains. The pronounced immunomodulatory activity of CPTM-P1 was highlighted by its capacity to enhance the secretion of nitric oxide (NO), tumor necrosis factor-alpha (TNF- α), interleukin-1 β (IL-1 β), and interleukin-6 (IL-6), without dampening macrophage function. This underscores CPTM-P1's favorable safety profile. Ultimately, CPTM-P1 emerges as a promising candidate for immuno-modulatory applications, boasting low toxicity and significant potential for use in functional foods or pharmaceutical products.

Author Contributions: J.F. and X.H.: investigation, conceptualization, writing—original draft. M.D. and S.T.: methodology, software, data curation. G.W. (Gang Wang 1) and A.L.: investigation, methodology. Y.F.: visualization, resources. G.W. (Gang Wang 2) and Y.W.: writing—review and editing, conceptualization, supervision. All authors have read and agreed to the published version of the manuscript.

Funding: This research was funded by Forestry and Grassland Science and Technology Popularization Demonstration Project of the Central Finance ([2023]9) and Sichuan Province Innovative Talent Funding Project for Postdoctoral Fellows (2322999070).

Institutional Review Board Statement: Not applicable.

Informed Consent Statement: Not applicable.

Data Availability Statement: Dataset available on request from the authors.

Conflicts of Interest: The authors declare that they have no known competing financial interests or personal relationships that could have appeared to influence the work reported in this paper.

References

1. Liu, F.; Wang, R.; Chen, Y.; Geng, R.; Gao, H.; Wang, F.; Liu, X.; Li, W. Structural characterization of a pectic polysaccharide from laoshan green tea and its inhibitory effects on the production of NO, TNF- α and IL-6. *Nat. Prod. Res.* **2023**, *37*, 1797–1805. [CrossRef] [PubMed]
2. Xin, T.; Zhang, F.; Jiang, Q.; Chen, C.; Huang, D.; Li, Y.; Shen, W.; Jin, Y. Extraction, purification and antitumor activity of a water-soluble polysaccharide from the roots of *Polygala tenuifolia*. *Carbohydr. Polym.* **2012**, *90*, 1127–1131. [CrossRef] [PubMed]
3. Li, B.; Xu, H.; Wang, X.; Wan, Y.; Jiang, N.; Qi, H.; Liu, X. Antioxidant and antihyperlipidemic activities of high sulfate content purified polysaccharide from *Ulva pertusa*. *Int. J. Biol. Macromol.* **2020**, *146*, 756–762. [CrossRef] [PubMed]
4. Chen, F.; Huang, G. Antioxidant activity of polysaccharides from different sources of ginseng. *Int. J. Biol. Macromol.* **2019**, *125*, 906–908. [CrossRef] [PubMed]
5. Oka, S.; Okabe, M.; Tsubura, S.; Mikami, M.; Imai, A. Properties of fucoidans beneficial to oral healthcare. *Odontology* **2020**, *108*, 34–42. [CrossRef] [PubMed]
6. Fan, L.; Ding, S.; Ai, L.; Deng, K. Antitumor and immunomodulatory activity of water-soluble polysaccharide from *Inonotus obliquus*. *Carbohydr. Polym.* **2012**, *90*, 870–874. [CrossRef]
7. Hwang, K.C.; Shin, H.Y.; Kim, W.J.; Seo, M.S.; Kim, H. Effects of a high-molecular-weight polysaccharides isolated from korean persimmon on the antioxidant, anti-inflammatory, and antiwrinkle activity. *Molecules* **2021**, *26*, 1600. [CrossRef] [PubMed]

8. Schepetkin, I.A.; Danilets, M.G.; Ligacheva, A.A.; Trofimova, E.S.; Selivanova, N.S.; Sherstoboev, E.Y.; Krivoshechekov, S.V.; Gulina, E.I.; Brazovskii, K.S.; Kirpotina, L.N.; et al. Immunomodulatory activity of polysaccharides isolated from *Saussurea salicifolia* L. and *Saussurea frolovii* Ledeb. *Molecules* **2023**, *28*, 6655. [CrossRef]
9. Wang, N.; Zhang, X.; Wang, S.; Guo, Q.; Li, Z.; Liu, H.; Wang, C. Structural characterisation and immunomodulatory activity of polysaccharides from white asparagus skin. *Carbohydr. Polym.* **2020**, *227*, 115314. [CrossRef]
10. Lee, J.S.; Kwon, D.S.; Lee, K.R.; Park, J.M.; Ha, S.; Hong, E.K. Mechanism of macrophage activation induced by polysaccharide from *Cordyceps militaris* culture broth. *Carbohydr. Polym.* **2015**, *120*, 29–37. [CrossRef]
11. Yu, Q.; Nie, S.; Wang, J.; Yin, P.; Huang, D.; Li, W.; Xie, M. Toll-like receptor 4-mediated ROS signaling pathway involved in ganoderma atrum polysaccharide-induced tumor necrosis factor- α secretion during macrophage activation. *Food Chem. Toxicol.* **2014**, *66*, 14–22. [CrossRef]
12. Wang, M.; Yang, X.B.; Zhao, J.W.; Lu, C.J.; Zhu, W. Structural characterization and macrophage immunomodulatory activity of a novel polysaccharide from *Smilax glabra* Roxb. *Carbohydr. Polym.* **2017**, *156*, 390–402. [CrossRef] [PubMed]
13. Ma, L.; Jiao, K.; Luo, L.; Xiang, J.; Fan, J.; Zhang, X.; Yi, J.; Zhu, W. Characterization and macrophage immunomodulatory activity of two polysaccharides from the flowers of *Paeonia suffruticosa* Andr. *Int. J. Biol. Macromol.* **2019**, *124*, 955–962. [CrossRef] [PubMed]
14. Ferreira, S.S.; Passos, C.P.; Madureira, P.; Vilanova, M.; Coimbra, M.A. Structure–function relationships of immunostimulatory polysaccharides: A review. *Carbohydr. Polym.* **2015**, *132*, 378–396. [CrossRef] [PubMed]
15. Xu, X.; Yan, H.; Zhang, X. Structure and immuno-stimulating activities of a new heteropolysaccharide from *Lentinula edodes*. *J. Agr. Food Chem.* **2012**, *60*, 11560–11566. [CrossRef] [PubMed]
16. Liao, W.; Luo, Z.; Liu, D.; Ning, Z.; Yang, J.; Ren, J. Structure characterization of a novel polysaccharide from *Dictyophora indusiata* and its macrophage immunomodulatory activities. *J. Agr. Food Chem.* **2015**, *63*, 535–544. [CrossRef] [PubMed]
17. Schepetkin, I.A.; Xie, G.; Kirpotina, L.N.; Klein, R.A.; Jutila, M.A.; Quinn, M.T. Macrophage immunomodulatory activity of polysaccharides isolated from *Opuntia polyacantha*. *Int. Immunopharmacol.* **2008**, *8*, 1455–1466. [CrossRef] [PubMed]
18. Yang, Y.; Qiu, Z.; Li, L.; Vidyarthi, S.K.; Zheng, Z.; Zhang, R. Structural characterization and antioxidant activities of one neutral polysaccharide and three acid polysaccharides from *Ziziphys jujuba* cv. *Hamidazao*: A comparison. *Carbohydr. Polym.* **2021**, *261*, 117879. [CrossRef]
19. Chen, G.; Jiang, N.; Zheng, J.; Hu, H.; Yang, H.; Lin, A.; Hu, B.; Liu, H. Structural characterization and anti-inflammatory activity of polysaccharides from *Astragalus membranaceus*. *Int. J. Biol. Macromol.* **2023**, *241*, 124386. [CrossRef]
20. Wu, M.; Zhang, F.; Yu, Z.; Lin, J.; Yang, L. Chemical characterization and in vitro antitumor activity of a single-component polysaccharide from *Taxus chinensis* var. *mairei*. *Carbohydr. Polym.* **2015**, *133*, 294–301. [CrossRef]
21. Wu, M.; Wu, Y.; Zhou, J.; Pan, Y. Structural characterisation of a water-soluble polysaccharide with high branches from the leaves of *Taxus chinensis* var. *mairei*. *Food Chem.* **2009**, *113*, 1020–1024. [CrossRef]
22. Zhao, C.; Li, Z.; Li, C.; Yang, L.; Yao, L.; Fu, Y.; He, X.; Shi, K.; Lu, Z. Optimized extraction of polysaccharides from *Taxus chinensis* var. *mairei* fruits and its antitumor activity. *Int. J. Biol. Macromol.* **2015**, *75*, 192–198. [CrossRef]
23. Yan, C.; Yin, Y.; Zhang, D.; Yang, W.; Yu, R. Structural characterization and invitroantitumor activity of a novel polysaccharide from *Taxus yunnanensis*. *Carbohydr. Polym.* **2013**, *96*, 389–395. [CrossRef]
24. Yin, Y.; Yu, R.; Yang, W.; Yuan, F.; Yan, C.; Song, L. Structural characterization and anti-tumor activity of a novel heteropolysaccharide isolated from *Taxus yunnanensis*. *Carbohydr. Polym.* **2010**, *82*, 543–548. [CrossRef]
25. Jiang, P.; Zhang, Q.; Zhao, Y.; Xiong, J.; Wang, F.; Zhang, T.; Zhang, C. Extraction, purification, and biological activities of polysaccharides from branches and leaves of *Taxus cuspidata* S. et Z. *Molecules* **2019**, *24*, 2926. [CrossRef]
26. Zeng, P.; Li, J.; Chen, Y.; Zhang, L. The structures and biological functions of polysaccharides from traditional Chinese herbs. *Prog. Mol. Biol. Transl. Sci.* **2019**, *163*, 423–444. [PubMed]
27. Wu, N.; Wen, Z.; Xiang, X.; Huang, Y.; Gao, Y.; Qu, Y. Immunostimulative activity of low molecular weight chitosans in RAW264.7 macrophages. *Mar. Drugs* **2015**, *13*, 6210–6225. [CrossRef] [PubMed]
28. Apostolova, E.; Lukova, P.; Baldzhieva, A.; Katsarov, P.; Nikolova, M.; Iliev, I.; Peychev, L.; Trica, B.; Oancea, F.; Delattre, C.; et al. Immunomodulatory and anti-inflammatory effects of fucoidan: A review. *Polymers* **2020**, *12*, 2338. [CrossRef] [PubMed]
29. Zhu, Y.; Yao, Y.; Gao, Y.; Hu, Y.; Shi, Z.; Ren, G. Suppressive effects of barley β -Glucans with different molecular weight on 3T3-L1 adipocyte differentiation. *J. Food Sci.* **2016**, *81*, H786–H793. [CrossRef] [PubMed]
30. Yoo, H.J.; You, D.; Lee, K. Characterization and immunomodulatory effects of high molecular weight fucoidan fraction from the sporophyll of *Undaria pinnatifida* in cyclophosphamide-induced immunosuppressed mice. *Mar. Drugs* **2019**, *17*, 447. [CrossRef] [PubMed]
31. Flórez-Fernández, N.; Torres, M.D.; González-Muñoz, M.J.; Domínguez, H. Potential of intensification techniques for the extraction and depolymerization of fucoidan. *Algal Res.* **2018**, *30*, 128–148. [CrossRef]
32. Fan, Y.; Ma, J.; Wang, G.; Li, X.; Liu, Y.; Xu, E.; Luo, A. Ultrasonic extraction, structural modification and gastric mucosal cells protective activity of a polysaccharide from *Dendrobium denneanum*. *Arab. J. Chem.* **2023**, *16*, 105033. [CrossRef]
33. Wang, Y.; Han, J.; Yue, Y.; Wu, Y.; Zhang, W.; Xia, W.; Wu, M. Purification, structure identification and immune activity of a neutral polysaccharide from *Cynanchum auriculatum*. *Int. J. Biol. Macromol.* **2023**, *237*, 124142. [CrossRef] [PubMed]
34. Wu, H.; Zhu, J.; Diao, W.; Wang, C. Ultrasound-assisted enzymatic extraction and antioxidant activity of polysaccharides from pumpkin (*Cucurbita moschata*). *Carbohydr. Polym.* **2014**, *113*, 314–324. [CrossRef] [PubMed]

35. Wei, N.; Wang, X.; Wu, Y.; Liu, L.; Zhao, Y.; Zhao, R. Comparative study on anti-inflammatory effect of polysaccharides from vinegar-baked *Radix Bupleuri* using different methods. *ACS Omega* **2023**, *8*, 29253–29261. [CrossRef] [PubMed]
36. Ji, X.; Peng, Q.; Yuan, Y.; Shen, J.; Xie, X.; Wang, M. Isolation, structures and bioactivities of the polysaccharides from jujube fruit (*Ziziphus Jujuba* Mill.): A review. *Food Chem.* **2017**, *227*, 349–357. [CrossRef] [PubMed]
37. Ji, X.; Yan, Y.; Hou, C.; Shi, M.; Liu, Y. Structural characterization of a galacturonic acid-rich polysaccharide from *Ziziphus jujuba* cv. *Muzao*. *Int. J. Biol. Macromol.* **2020**, *147*, 844–852. [CrossRef] [PubMed]
38. Cai, Y.; Si, Z.; Jiang, Y.; Ye, M.; Wang, F.; Yang, X.; Yu, J.; Gao, X.; Liu, W. Structure-activity relationship of low molecular weight astragalus membranaceus polysaccharides produced by *Bacteroides*. *Carbohydr. Polym.* **2023**, *316*, 121036. [CrossRef] [PubMed]
39. Wu, J.; Li, C.; Bai, L.; Wu, J.; Bo, R.; Ye, M.; Huang, L.; Chen, H.; Rui, W. Structural differences of polysaccharides from *Astragalus* before and after honey processing and their effects on colitis mice. *Int. J. Biol. Macromol.* **2021**, *182*, 815–824. [CrossRef]
40. Li, F.; Zhao, J.; Wei, J.; Jiao, X.; Li, Q. Holistic review of polysaccharides isolated from pumpkin: Preparation methods, structures and bioactivities. *Int. J. Biol. Macromol.* **2021**, *193*, 541–552. [CrossRef]
41. Zhou, S.; Huang, G. Extraction, structural analysis and antioxidant activity of aloe polysaccharide. *J. Mol. Struct.* **2023**, *1273*, 134379. [CrossRef]
42. Luo, A.; Ge, Z.; Fan, Y.; Luo, A.; Chun, Z.; He, X. In vitro and in vivo antioxidant activity of a water-soluble polysaccharide from *Dendrobium denneanum*. *Molecules* **2011**, *16*, 1579–1592. [CrossRef] [PubMed]
43. Luo, A.; He, X.; Zhou, S.; Fan, Y.; He, T.; Chun, Z. In vitro antioxidant activities of a water-soluble polysaccharide derived from *Dendrobium nobile* Lindl. Extracts. *Int. J. Biol. Macromol.* **2009**, *45*, 359–363. [CrossRef] [PubMed]
44. Liang, J.; Zhao, M.; Xie, S.; Peng, D.; An, M.; Chen, Y.; Li, P.; Du, B. Effect of steam explosion pretreatment on polysaccharide isolated from *Poria cocos*: Structure and immunostimulatory activity. *J. Food Biochem.* **2022**, *46*, e14355. [CrossRef] [PubMed]
45. Lu, M.K.; Cheng, J.J.; Lin, C.Y.; Chang, C.C. Purification, structural elucidation, and anti-inflammatory effect of a water-soluble 1,6-branched 1,3- α -D-galactan from cultured mycelia of *Poria cocos*. *Food Chem.* **2010**, *118*, 349–356. [CrossRef]
46. Shakhmatov, E.G.; Makarova, E.N. Structure of KON-extractable polysaccharides of tree greenery of from Siberian fir *Abies sibirica* Ledeb. *Carbohydr. Polym.* **2022**, *276*, 118794. [CrossRef] [PubMed]
47. Liu, G.; Kamilijiang, M.; Abuduwaili, A.; Zang, D.; Abudukelimu, N.; Liu, G.; Yili, A.; Aisa, H.A. Isolation, structure elucidation, and biological activity of polysaccharides from *Saussurea involucreata*. *Int. J. Biol. Macromol.* **2022**, *222*, 154–166. [CrossRef] [PubMed]
48. Jiang, Y.; Shang, Z.; Lv, X.; Du, M.; Ma, L.; Hou, G.; Chen, J.; Wang, C.; Zhao, F. Structure elucidation and antitumor activity of a water soluble polysaccharide from *Hemicentrotus pulcherrimus*. *Carbohydr. Polym.* **2022**, *292*, 119718. [CrossRef]
49. Lin, P.; Chen, L.; Huang, X.; Xiao, F.; Fu, L.; Jing, D.; Wang, J.; Zhang, H.; Sun, L.; Wu, Y. Structural characteristics of polysaccharide GP2a in *Gardenia jasminoides* and its immunomodulatory effect on macrophages. *Int. J. Mol. Sci.* **2022**, *23*, 11279. [CrossRef]
50. Cavaillon, J. Exotoxins and endotoxins: Inducers of inflammatory cytokines. *Toxicon* **2018**, *149*, 45–53. [CrossRef]
51. Huang, L.; Zhao, J.; Wei, Y.; Yu, G.; Li, F.; Li, Q. Structural characterization and mechanisms of macrophage immunomodulatory activity of a pectic polysaccharide from *Cucurbita moschata* Duch. *Carbohydr. Polym.* **2021**, *269*, 118288. [CrossRef] [PubMed]
52. Georgiev, Y.N.; Paulsen, B.S.; Kiyohara, H.; Ciz, M.; Ognyanov, M.H.; Vasicek, O.; Rise, F.; Denev, P.N.; Yamada, H.; Lojek, A.; et al. The common lavender (*Lavandula angustifolia* Mill.) Pectic polysaccharides modulate phagocytic leukocytes and intestinal Peyer's patch cells. *Carbohydr. Polym.* **2017**, *174*, 948–959. [CrossRef] [PubMed]
53. Cao, J.; Tang, D.; Wang, Y.; Li, X.; Hong, L.; Sun, C. Characteristics and immune-enhancing activity of pectic polysaccharides from sweet cherry (*Prunus avium*). *Food Chem.* **2018**, *254*, 47–54. [CrossRef]
54. Wang, H.; Bi, H.; Gao, T.; Zhao, B.; Ni, W.; Liu, J. A homogalacturonan from *Hippophae rhamnoides* L. Berries enhance immunomodulatory activity through TLR4/MyD88 pathway mediated activation of macrophages. *Int. J. Biol. Macromol.* **2018**, *107*, 1039–1045. [CrossRef] [PubMed]
55. Pugh, N.D.; Tamta, H.; Balachandran, P.; Wu, X.; Howell, J.; Dayan, F.E.; Pasco, D.S. The majority of in vitro macrophage activation exhibited by extracts of some immune enhancing botanicals is due to bacterial lipoproteins and lipopolysaccharides. *Int. Immunopharmacol.* **2008**, *8*, 1023–1032. [CrossRef]
56. Gertsch, J.; Viveros-Paredes, J.M.; Taylor, P. Plant immunostimulants—Scientific paradigm or myth? *J. Ethnopharmacol.* **2011**, *136*, 385–391. [CrossRef]

Disclaimer/Publisher's Note: The statements, opinions and data contained in all publications are solely those of the individual author(s) and contributor(s) and not of MDPI and/or the editor(s). MDPI and/or the editor(s) disclaim responsibility for any injury to people or property resulting from any ideas, methods, instructions or products referred to in the content.

MDPI AG
Grosspeteranlage 5
4052 Basel
Switzerland
Tel.: +41 61 683 77 34

Molecules Editorial Office
E-mail: molecules@mdpi.com
www.mdpi.com/journal/molecules



Disclaimer/Publisher's Note: The title and front matter of this reprint are at the discretion of the . The publisher is not responsible for their content or any associated concerns. The statements, opinions and data contained in all individual articles are solely those of the individual Editors and contributors and not of MDPI. MDPI disclaims responsibility for any injury to people or property resulting from any ideas, methods, instructions or products referred to in the content.



Academic Open
Access Publishing

mdpi.com

ISBN 978-3-7258-1705-4